

Investigation of a

turbulent wake

in an adverse pressure gradient  
using

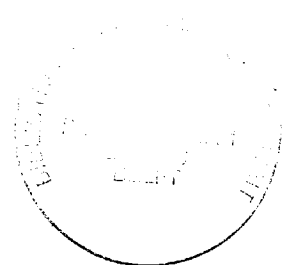
laser Doppler  
anemometry

Mark J. Tummers

7-2000  
3042000 3400

INVESTIGATION OF A TURBULENT WAKE TR311  
IN AN ADVERSE PRESSURE GRADIENT  
USING LASER DOPPLER ANEMOMETRY

PROEFSCHRIFT



ter verkrijging van de graad van doctor  
aan de Technische Universiteit Delft,  
op gezag van de Rector Magnificus prof.ir. K.F. Wakker  
in het openbaar te verdedigen ten overstaan van een commissie,  
door het College voor Promoties aangewezen,

op dinsdag 9 november 1999 te 16.00 uur

door

Mark Jeroen TUMMERS

ingenieur luchtvaart- en ruimtevaarttechniek  
geboren te Amsterdam

Dit proefschrift is goedgekeurd door de promotor:  
Prof.dr.ir. J.L. van Ingen

Samenstelling promotiecommissie:

Rector Magnificus	voorzitter
Prof.dr.ir. J.L. van Ingen	Technische Universiteit Delft, promotor
Prof.dr.ir. P.G. Bakker	Technische Universiteit Delft
Prof.Dr.Dipl.-Ing. K. Hanjalić	Technische Universiteit Delft
Prof.dr.ir. F.T.M. Nieuwstadt	Technische Universiteit Delft
Prof.Dr.-Ing. C. Tropea	Technische Universität Darmstadt, Duitsland
Ir. D.M. Passchier	Technische Universiteit Delft
Dr.ir. R.A.W.M. Henkes	Shell International Oil Products

Ir. D.M. Passchier heeft als begeleider in belangrijke mate aan de totstandkoming van het proefschrift bijgedragen.

Copyright © 1999 by M.J. Tummers, Delft, The Netherlands.

All rights reserved. No part of this publication may be reproduced, stored in a retrieval system or transmitted in any form or by any means, electronic, mechanical, photocopying, recording or otherwise, without the prior written permission of the publisher.

Publisher: Delft University of Technology  
Faculty of Aerospace Engineering  
P.O. Box 5058  
2600 GB Delft  
The Netherlands  
Tel: +31 15 2781455  
Fax: +31 15 2781822

ISBN 90-5623-069-7

# Summary

The main objective of the present investigation is to gain a better understanding of the complex flow in the near wake of a flat plate subjected to an adverse pressure gradient. To realize this objective a combined experimental and numerical investigation is carried out. A three-component LDA (3D LDA) is used to acquire data on mean velocities, Reynolds stresses and triple-velocity correlations. LDA was also used for the measurement of power spectra and spatial correlation functions. These data were used for a detailed comparison between the experiments and the numerical predictions based on the Reynolds-averaged Navier Stokes equations. Two turbulence models were employed: a  $k - \epsilon$  model and a differential Reynolds-stress transport model. The comparison between the experiments and the numerical predictions aided the interpretation of the experimental results and enabled the tracing of deficiencies in the turbulence models for computations in the wake in adverse pressure gradient.

The use of a 3D LDA for measurements in a turbulent flow is hampered by three error sources. A general configuration for the 3D LDA is suggested that eliminates the three error sources. Furthermore, the random sampling in LDA gives rise to problems such as velocity bias and large statistical scatter in the measured autocorrelation functions and power spectra. An experimental investigation confirmed the existence of the velocity bias and it was shown that the effects of the velocity bias can be compensated for by the use of weighting factors that are based on the inverse of the velocity. The problem of the large statistical scatter in the measured autocorrelation functions (and power spectra) was partly solved by the introduction of a "locally scaled" version of the slotting method (and a variable-windowing technique).

The experiments in the trailing-edge flow of the flat plate in an adverse pressure gradient indicated a rapid growth of the shear-layer thickness, a large increase of the turbulence kinetic energy in the streamwise direction and the presence of a backflow region some distance downstream of the trailing edge. The balance of the turbulence kinetic energy equation in the near wake showed that the dissipation decreased in the downstream direction while the production of turbulence kinetic energy remained at a high level. The power spectra measured in the near wake revealed the presence of a significant amount of turbulence kinetic energy in the (very) low frequency range.

Neither the  $k - \epsilon$  model nor the differential Reynolds stress model were able to reproduce the measured mean flow reversal and the large increase of the turbulence kinetic energy on the wake centreline. Both turbulence models predicted too much dissipation in the near wake. It is shown that this is the result of a deficiency in the transport equations for the dissipation, which are similar in both turbulence models. The transport equations for the dissipation respond to the high level of production of turbulence kinetic energy by maintaining a high level of dissipation. However, this is an incorrect response, because a significant part of the produced kinetic energy remains in the low frequency range and is not dissipated in the near wake.

# Contents

<b>Summary</b>	<b>iii</b>
<b>Nomenclature</b>	<b>ix</b>
<b>1 Introduction</b>	<b>1</b>
1.1 Background of the Investigation . . . . .	1
1.1.1 High-lift systems in aircraft aerodynamics . . . . .	1
1.1.2 Free separation in flows about multi-element airfoils . . . . .	3
1.2 Objectives of the Investigation . . . . .	5
1.3 Outline of the Thesis . . . . .	5
<b>2 Turbulent Flows</b>	<b>7</b>
2.1 Basics of Turbulent Flows . . . . .	7
2.1.1 Equations of motion . . . . .	7
2.1.2 Reynolds-averaged Navier-Stokes equations . . . . .	8
2.1.3 Reynolds-stress transport equations . . . . .	9
2.1.4 Turbulence modeling . . . . .	10
2.1.5 Correlations and spectra . . . . .	12
Spatial correlations and length scales . . . . .	12
Autocorrelation and time scales . . . . .	14
Taylor's hypothesis . . . . .	15
2.1.6 Turbulent boundary layers and wakes . . . . .	16
The boundary-layer approximation . . . . .	16
Turbulent boundary layers . . . . .	18
Self-preserving wakes . . . . .	19
2.2 Turbulent Near Wakes . . . . .	20
2.2.1 Characteristics of the near wake . . . . .	20
2.2.2 Calculation of the near wake of a flat plate . . . . .	23
<b>3 Laser Doppler Anemometry</b>	<b>29</b>
3.1 Introduction . . . . .	29
3.2 Basic Principles of LDA . . . . .	30
3.2.1 Doppler frequency . . . . .	30
3.2.2 Heterodyne detection . . . . .	32

3.2.3	Directional ambiguity . . . . .	33
3.2.4	Fringe model . . . . .	34
3.2.5	Amplitude bias . . . . .	35
3.2.6	Particle characteristics . . . . .	37
3.2.7	Signal processor . . . . .	38
3.3	The Three-Component LDA . . . . .	40
3.3.1	Introduction . . . . .	40
3.3.2	Orthogonality requirement . . . . .	40
3.3.3	Virtual particles . . . . .	42
3.3.4	Geometry bias . . . . .	43
<b>4</b>	<b>Research on the LDA Sampling Process</b> . . . . .	<b>47</b>
4.1	Introduction . . . . .	47
4.2	Velocity Bias . . . . .	48
4.2.1	Correction methods . . . . .	49
	Sampling techniques . . . . .	50
	Weighting factors . . . . .	51
4.2.2	Relationship between velocity bias and mean data rate . . . . .	54
4.2.3	Detection methods . . . . .	55
4.2.4	Experimental investigation of the velocity bias . . . . .	57
	Velocity bias and mean data rate . . . . .	57
	Bias detection methods . . . . .	59
	Correction methods . . . . .	60
4.2.5	Concluding remarks . . . . .	61
4.3	Spectral Analysis of LDA Data . . . . .	62
4.3.1	Spectral estimation using the correlation method . . . . .	63
4.3.2	Improved spectral estimation . . . . .	64
	Local normalization of the slotted covariance function . . . . .	65
	Variation of the window width with frequency . . . . .	66
4.3.3	Application to simulated data . . . . .	66
4.3.4	Performance of the new estimator . . . . .	67
4.3.5	Lifting the model restrictions . . . . .	69
	Effects of uncorrelated noise . . . . .	70
	Effects of velocity bias on the autocorrelation function . . . . .	72
	Effects of spatial averaging . . . . .	74
	Experiment on the effects of spatial averaging on the acf . . . . .	76
4.3.6	Concluding remarks . . . . .	77
<b>5</b>	<b>Investigation of the Adverse Pressure Gradient Wake</b> . . . . .	<b>79</b>
5.1	Experimental Investigation . . . . .	79
5.1.1	Wind tunnel and model . . . . .	79
5.1.2	Flow quality . . . . .	81
5.1.3	Optical arrangements and instrumentation . . . . .	82
	Set-up 1: single-point statistics . . . . .	82
	Set-up 2: autocorrelation functions . . . . .	85

	Set-up 3: two-point statistics . . . . .	85
5.1.4	Additional instrumentation . . . . .	86
5.1.5	Measuring programme and data reduction . . . . .	86
5.2	Numerical Investigation . . . . .	88
	Low-Reynolds-number $k - \epsilon$ model . . . . .	88
	Reynolds-stress transport model . . . . .	89
	Numerical procedure . . . . .	92
<b>6</b>	<b>Results of the Investigation of the Wake</b>	<b>95</b>
6.1	Results of the Single-Point Measurements . . . . .	95
6.1.1	Pressure distribution . . . . .	95
6.1.2	Mean-flow characteristics . . . . .	96
	Mean-velocity components and integral parameters . . . . .	96
	Skin-friction data . . . . .	98
	Centreline velocity . . . . .	100
6.1.3	Turbulence quantities . . . . .	102
	Reynolds stresses . . . . .	102
	Reynolds-stress anisotropy . . . . .	104
	Triple-velocity correlations . . . . .	104
	Balance of the momentum equation . . . . .	105
	Balance of the kinetic-energy equation . . . . .	107
6.2	Numerical Results . . . . .	108
6.2.1	Mean velocity and kinetic energy . . . . .	110
6.2.2	Effect of the $S_{\epsilon 4}$ term in the RSTM . . . . .	111
6.2.3	Prediction of the Reynolds-stress anisotropy . . . . .	113
6.2.4	Predictions of Reynolds shear stress and kinetic energy . . . . .	113
6.2.5	The computed kinetic-energy balances . . . . .	115
6.2.6	Concluding remarks on the computations . . . . .	117
6.3	Results of the Spatial Correlation Measurements . . . . .	117
6.3.1	Correlation values for small separations . . . . .	117
6.3.2	Determination of Taylor length scales . . . . .	118
6.3.3	Variation of Taylor length scales in streamwise direction . . . . .	119
6.4	Spectral Measurements . . . . .	120
6.4.1	Small-scale characteristics of the autocorrelation function . . . . .	120
6.4.2	Spectral density functions in the wake . . . . .	121
6.5	Discussion . . . . .	124
<b>7</b>	<b>Conclusions</b>	<b>129</b>
	Conclusions regarding the flow . . . . .	129
	Conclusions regarding the measurement technique . . . . .	130
<b>A</b>	<b>Alignment of the 3-D LDA</b>	<b>133</b>

<b>B</b>	<b>Generation of Simulated Data</b>	<b>137</b>
B.1	Introduction . . . . .	137
B.2	Poisson Distributed Sampling Times . . . . .	137
B.3	Generation of AR(2) Data . . . . .	138
B.4	The Shinozuka Method . . . . .	139
B.5	Simulated Data and Velocity Bias . . . . .	140
B.5.1	Generation of Biased Velocity Data . . . . .	141
B.5.2	Generation of Particle Transit Times . . . . .	141
<b>C</b>	<b>Measurement of Spatial Correlation Functions using LDA</b>	<b>143</b>
C.1	Introduction . . . . .	143
C.2	Problems Related to the Measurement of Spatial Correlation Functions . . . . .	144
C.2.1	The cylinder wake . . . . .	144
Experimental set-up . . . . .	144	
Effects of uncorrelated noise and overlapping pinhole images . . . . .	145	
C.2.2	The flat plate wake . . . . .	147
Experimental set-up . . . . .	147	
Effect of overlapping measuring volumes . . . . .	147	
The correlation-geometry bias . . . . .	151	
C.2.3	The backwards facing step flow . . . . .	153
Experimental set-up . . . . .	153	
Increased spatial resolution . . . . .	153	
Effects of the time-coincidence window . . . . .	154	
Effect of the lag times between the samples . . . . .	155	
C.2.4	Influence of spatial averaging . . . . .	156
C.3	Concluding Remarks . . . . .	157
	<b>Bibliography</b>	<b>159</b>
	<b>Samenvatting</b>	<b>167</b>
	<b>Dankwoord</b>	<b>168</b>
	<b>Curriculum Vitae</b>	<b>169</b>



# Nomenclature

Symbol	Description	Unit
$A$	amplitude of Doppler burst, Eq (3.19)	V
$A_p$	projected area of measuring volume, Fig. 4.1	m <sup>2</sup>
$B_w$	bandwidth of BSA processor	Hz
$C$	coefficient in Reichardt's mean-velocity distribution, Eq (2.57)	
$C_f$	skin friction coefficient, $C_f = 2\tau_w/(\rho U_e^2)$	
$C_p$	static pressure coefficient, $C_p = 2(\bar{p} - \bar{p}_{ref})/(\rho U_{ref}^2)$	
$C_1$	length scale ratio for one-dimensional case, Eq (4.59)	
$C_3$	length scale ratio for three-dimensional case, Eq (4.60)	
$C_\mu$	closure coefficient, Eq (2.18)	
$C_{\epsilon_1}$	closure coefficient, Eq (2.21)	
$C_{\epsilon_2}$	closure coefficient, Eq (2.21)	
$E_i$	plane light wave, Eq (3.1)	V/m
$E_{i_0}$	amplitude of plane light wave, Eq (3.1)	V/m
$E_s$	spherical light wave, Eq (3.2)	V/m
$F$	velocity defect function, Eq (2.55)	
$F_{int}$	Klebanov intermittency function, Eq (2.17)	
$G$	wake function, Eq (2.58)	
$H$	shape factor, $H = \delta^*/\theta$	
$H(k\Delta\tau)$	number of cross products per slot, Eq (4.26)	
$I$	intensity of light in overlap region of laser beams, Eq (3.15)	W/m <sup>2</sup>
$J(k\Delta\tau)$	local variance of velocity fluctuations, Eq (4.33)	m <sup>2</sup> /s <sup>2</sup>
$L$	flow length scale for $x$ -direction	m
$L_{11}$	integral length scale, Eq (2.25)	m
$M$	number of particles per unit volume, Eq (4.2)	
$M$	number of slots, Eq (4.26)	
$N$	number of velocity samples	
$N_c$	number of cycles in Doppler burst	
$N_{int}$	number of divisions of time axis, Eq (4.20)	
$P(\Delta z)$	probability density function of $\Delta z$ , Eq (4.55)	m <sup>-1</sup>
$R_{ij}(\Delta\vec{x})$	spatial covariance function, Eq (2.22)	m <sup>2</sup> /s <sup>2</sup>
$R_{va}(\tau)$	volume-averaged autocovariance function, Eq (4.52)	m <sup>2</sup> /s <sup>2</sup>
$R_\theta$	Reynolds number at trailing edge, $R_\theta = U_e\theta/\nu$	
$R(t_1, t_2)$	(temporal) autocovariance function, Eq (2.35)	m <sup>2</sup> /s <sup>2</sup>
$Re_t$	turbulent Reynolds number, $Re_t = k^2/(\epsilon\nu)$	
$\hat{R}(k\Delta\tau)$	slotted autocovariance function, Eq (4.26)	m <sup>2</sup> /s <sup>2</sup>
$S$	radiant sensitivity, Eq (3.8)	
$S(\omega)$	(normalised) spectral density function of velocity fluctuations $u'$ , Eq (4.25)	s
$S_1$	spectral estimator, Eq (4.31)	s

$S_2$	spectral estimator, Eq (4.38)	s
$S_\delta$	spectral density where variance of $S_1$ (or $S_2$ ) exceeds the value $\delta^2 S^2(\omega)$	s
$T$	measuring time	s
$T_s$	time constant of photomultiplier, Eq (3.8)	s
$T_u$	integral time scale, Eq (2.37)	s
$U_e$	mean velocity at edge of shear layer, Eq (2.46)	m/s
$U_{ref}$	reference velocity	m/s
$a$	constant in one-dimensional spectrum, Eq (2.34)	
$a$	constant in Eq (2.59)	
$a_{sp}$	structural parameter, $a_{sp} = -\overline{u'v'_s}/k$	
$c$	speed of light, $c \approx 3.0 \times 10^8$ m/s in vacuum	m/s
$c$	constant in Eq (4.32)	
$d$	diameter of measuring volume	m
$d_f$	fringe distance, Eq (3.15)	m
$d_p$	diameter of particle, Eq (3.21)	m
$\vec{e}_i$	unit vector for direction of incident laser beam, Fig. 3.1	
$\vec{e}_d$	unit vector for direction of detector, Fig. 3.1	
$f_c$	centre frequency of BSA processor	Hz
$f_D$	Doppler frequency, Eq (3.7)	Hz
$f_s$	frequency shift, Eq (3.13)	Hz
$f_{sam}$	sampling frequency of BSA processor, $f_{sam} = 1/t_{sam}$	Hz
$f_w$	frequency of scattered light at detector, Eq (3.5)	Hz
$f_0$	frequency of laser light, $f_0 = c/\lambda_0$	Hz
$g$	function, Eq (2.63)	
$k$	turbulence kinetic energy per unit mass, $k = \overline{u'_i u'_i}/2$	$\text{m}^2/\text{s}^2$
$k$	wave number, $k =  \vec{k} $	$\text{m}^{-1}$
$k_1$	$x_1$ -component of wave vector $\vec{k}$	$\text{m}^{-1}$
$k_0$	wave number of laser light, $k_0 = 2\pi/\lambda_0$	$\text{m}^{-1}$
$\vec{k}$	wave vector, $\vec{k} = (k_1, k_2, k_3)$	
$l$	flow length scale for $y$ -direction	m
$l$	length of measuring volume	m
$l_0$	wake halve width, Eq (2.58)	m
$m$	average number of samples per time interval, Eq (4.20)	
$n$	coordinate normal to plate surface	m
$n(t)$	noise error in instantaneous velocity, Eq (4.41)	m/s
$n_{rec}$	record length of BSA processor	
$p$	static pressure, Eq (2.6)	$\text{N}/\text{m}^2$
$p(z)$	probability density function of $z$ , Eq (4.53)	$\text{m}^{-1}$
$p(\Delta t)$	probability density function of $\Delta t$ , Eq (4.1)	$\text{s}^{-1}$
$p'$	fluctuating static pressure, Eq (2.6)	$\text{N}/\text{m}^2$
$\bar{p}$	mean static pressure, Eq (2.6)	$\text{N}/\text{m}^2$
$\bar{p}_e$	mean static pressure at edge of shear layer, Eq (2.45)	$\text{N}/\text{m}^2$
$r$	radius of curvature, Eq (6.13)	m

$\vec{r}_d$	location of detector, Fig. 3.1	
$s$	coordinate along plate surface normal to $z$	m
$s(\omega)$	spectral density function of velocity fluctuations $u'$ , Eq (2.39)	s
$s_{ij}$	rate of strain tensor, Eq (2.4)	s <sup>-1</sup>
$s_r$	arithmetic average of $(u_i^2 + v_i^2 + w_i^2)^{1/2}$ -values, Eq (4.18)	m/s
$t$	time	s
$t_i$	arrival time of $i$ -th particle	s
$t_s$	sampling interval, Fig. 4.2	s
$t_{sam}$	sampling interval of BSA processor, $t_{sam} = 1/f_{sam}$	s
$\bar{u}_{cl}$	mean velocity on centreline	m/s
$u_{cor}$	mean velocity corrected for velocity bias, Eq (4.23)	m/s
$u_f$	velocity of fluid, Eq (3.21)	m/s
$u_i$	instantaneous velocity in $x_i$ -direction, Eq (2.6)	m/s
$u_l$	arithmetic average of velocities on $l$ -th time interval, Eq (4.20)	m/s
$u_p$	velocity of particle, Eq (3.21)	m/s
$u_r$	arithmetic average of velocity samples, $u_r = N^{-1} \sum_{i=1}^N u_i$	m/s
$u_T$	time averaged velocity, Eq (2.7)	m/s
$u_0$	maximum velocity defect in wake, Eq (2.58)	m/s
$u_\tau$	friction velocity, $u_\tau = (\tau_w/\rho)^{1/2}$	m/s
$u^+$	dimensionless mean velocity, $u^+ = \bar{u}/u_\tau$	
$u'_{rms}$	root-mean-square value $u'$	m/s
$u'_i$	fluctuating velocity in $x_i$ -direction, Eq (2.6)	m/s
$\frac{u'_m(t)}{u'^2}$	measured velocity fluctuation, Eq (4.41)	m/s
$\bar{u}_i$	mean velocity in $x_i$ -direction, Eq (2.6)	m/s
$-\frac{u'_i v'_j}{u'^2}$	(kinematic) Reynolds stress tensor	m <sup>2</sup> /s <sup>2</sup>
$-\frac{u' v'_j}{u'^2}$	(kinematic) Reynolds shear stress	m <sup>2</sup> /s <sup>2</sup>
$-\frac{u' v'_s}{u'^2}$	(kinematic) Reynolds shear stress in streamline coordinates, Eq (6.5)	m <sup>2</sup> /s <sup>2</sup>
$v_b$	velocity component measured by "blue" channel, Eq (3.23)	m/s
$v_g$	velocity component measured by "green" channel, Eq (3.23)	m/s
$v_p$	primary velocity component	m/s
$v_v$	velocity component measured by "violet" channel, Eq (3.23)	m/s
$\frac{v'_v}{v'^2}$	variance of velocity fluctuations $v'$	m <sup>2</sup> /s <sup>2</sup>
$\vec{v}$	velocity vector	
$w$	lag window function, Eq (4.31)	
$\frac{w}{w'^2}$	variance of velocity fluctuations $w'$	m <sup>2</sup> /s <sup>2</sup>
$x$	streamwise coordinate	m
$x(t)$	input signal of photomultiplier, Eq (3.9)	
$x_0$	virtual origin of $x$ -coordinate, Eq (2.59)	m
$y$	lateral coordinate	m
$y(t)$	output signal of photomultiplier, Eq (3.8)	V
$y^+$	dimensionless $y$ -coordinate, $y^+ = yu_\tau/\nu$	
$z$	spanwise coordinate	m

## Greek symbols

$\Delta t_i$	interarrival time, $\Delta t_i = t_{i+1} - t_i$	s
$\Delta u$	amount of correction, $\Delta u = u_r - u_{cor}$	m/s
$\Delta x$	spatial separation in $x$ -direction, Eq (2.24)	m
$\Delta x_1$	spatial separation in $x_1$ -direction, Eq (2.24)	m
$\Delta \vec{x}$	spatial separation vector, Eq (2.22)	
$\Delta \rho$	discontinuity in measured autocorrelation function, Eq (4.44)	
$\Delta \tau$	slot width, $\Delta \tau = \tau_{m0}/(M - 1)$	s
$\Phi$	phase of spherical wave at detector, Eq (3.5)	rad
$\Phi_{ij}(\vec{k})$	three-dimensional spectrum, Eq (2.31)	$\text{m}^3/\text{s}^2$
$\alpha$	closure coefficient in Cebeci-Smith model, $\alpha = 0.0168$	
$\alpha$	angle between velocity vector and $x$ -axis, Eq (3.12)	rad
$\alpha$	angle between $x$ -axis and projection of $v_p$ on $xy$ -plane, Fig. 3.7	rad
$\alpha_1$	parameter in $AR(2)$ spectral density function, Eq (4.39)	rad/s
$\alpha_2$	parameter in $AR(2)$ spectral density function, Eq (4.39)	$\text{rad}^2/\text{s}^2$
$\beta$	angle between $v_p$ and $xy$ -plane, Fig. 3.7	rad
$\beta$	trailing edge angle, Fig. 2.4	rad
$\beta_1$	parameter in Heisenberg spectral density function, Eq (4.40)	rad/s
$\beta_2$	parameter in Heisenberg spectral density function, Eq (4.40)	rad/s
$\gamma$	angle between mean velocity vector and $x$ -axis, Eq (6.13)	rad
$\delta$	shear layer thickness	m
$\delta$	constant in $S_\delta$	
$\delta_{ij}$	Kronecker delta function	
$\delta^*$	displacement thickness, Eq (2.50)	m
$\epsilon$	dissipation of $k$ per unit mass, Eq (2.13)	$\text{m}^2/\text{s}^3$
$\epsilon_c$	comparison	
$\eta$	Kolmogorov length scale, $\eta = (\nu^3/\epsilon)^{1/4}$	m
$ \eta $	amplitude ratio, Eq (3.22)	
$\theta$	momentum thickness, Eq (2.51)	m
$\theta$	crossing angle of incident laser beams, Eq (3.12)	rad
$\kappa$	Von Karman constant	
$\lambda$	expected number of particles per unit time, Eq (4.2)	$\text{s}^{-1}$
$\lambda_x$	Taylor length scale of velocity fluctuations $u'$ with spatial separation in $x$ -direction, Eq (2.29)	m
$\lambda_m$	Meyers' time scale, $T/N_{int}$	s
$\lambda_t$	Taylor time scale of velocity fluctuations $u'$ , Eq (2.38)	s
$\lambda_0$	wavelength of laser light, $\lambda_0 = c/f_0$	m
$\mu$	dynamic viscosity	kg/m/s
$\nu$	kinematic viscosity, $\nu (= \mu/\rho)$	$\text{m}^2/\text{s}$
$\nu$	mean data rate, $\nu = N/T$	Hz
$\nu_t$	eddy viscosity, Eq (2.14)	$\text{m}^2/\text{s}$
$\rho_A$	correlation coefficient for Adams' method, Eq (4.18)	

$\rho_M$	correlation coefficient for Meyers' method, Eq (4.20)	
$\rho_{ij}(\Delta\vec{x})$	spatial correlation function, Eq (2.23)	
$\rho_f$	density of fluid, Eq (3.21)	kg/m <sup>3</sup>
$\rho_p$	density of particle, Eq (3.21)	kg/m <sup>3</sup>
$\rho_{11}(\Delta x)$	spatial correlation function of velocity fluctuations $u'_1$ with spatial separation in $x_1$ -direction, Eq (2.24)	
$\rho(\tau)$	(temporal) autocorrelation function, Eq (2.36)	
$\hat{\rho}(k\Delta\tau)$	slotted autocorrelation function (standard), Eq (4.29)	
$\tilde{\rho}(k\Delta\tau)$	slotted autocorrelation function (local scaling), Eq (4.34)	
$\tilde{\rho}_c(k\Delta\tau)$	noise-corrected value of $\tilde{\rho}(k\Delta\tau)$ , Eq (4.45)	
$\sigma_r$	density ratio, $\sigma_r = \rho_p/\rho_f$	
$\sigma^2$	theoretical variance of $u_r$ values, Eq (4.22)	m <sup>2</sup> /s <sup>2</sup>
$\sigma_k$	closure coefficient, Eq (2.20)	
$\sigma_s$	scattering efficiency, Eq (3.2)	
$\sigma_{ij}$	stress tensor (in Newtonian fluid), Eq (2.3)	
$\sigma_\epsilon$	closure coefficient, Eq (2.21)	
$\tau$	lag time	s
$\tau_{m0}$	maximum lag time, Eq (4.26)	s
$\tau_w$	wall shear stress, Eq (2.49)	N/m <sup>2</sup>
$\tau_w$	time-coincidence window	s
$v$	Kolmogorov velocity scale, $v = (\nu\epsilon)^{1/4}$	m/s
$\phi_i$	initial phase of plane light wave, Eq (3.1)	rad
$\phi_{11}(k_1)$	one-dimensional spectrum, Eq (2.32)	m <sup>3</sup> /s <sup>2</sup>
$\omega$	radial frequency	rad/s
$\omega_i$	weighting factor for $i$ -th velocity sample, Eq (4.5)	

Abbreviations

acf	autocorrelation function
apg	adverse pressure gradient
BBO	Basset Boussinesq Oseen
BSA	Burst Spectrum Analyzer
DNS	Direct Numerical Simulation
FFT	Fast Fourier Transform
HWA	Hot Wire Anemometry
LDA	Laser Doppler Anemometry
NS	Navier Stokes
RANS	Reynolds Averaged Navier Stokes
RSTM	Reynolds Stress Transport Model
scf	spatial correlation function
sdf	spectral density function
SNR	Signal-to-Noise Ratio
TSI	Thermo Systems Inc.



# Chapter 1

## Introduction

### 1.1 Background of the Investigation

#### 1.1.1 High-lift systems in aircraft aerodynamics

The wing of a transport aircraft is designed to give optimum performance during cruise flight because this is generally the longer part of the flight. Here, optimum performance means that the required lift coefficient for cruise flight is achieved with a minimum of drag. However, the resulting wing is usually not well suited to generate sufficient lift at low speed as needed during take off and landing. To generate high lift at low speed the shape of the wing is adapted in flight by means of a mechanical high-lift system comprising trailing-edge flaps and, sometimes, leading-edge slats. A practical high-lift system is a complex mechanism that significantly contributes to the weight and cost of an airplane. Manufacturers aim to reduce the weight and cost by improving the aerodynamic efficiency of the high-lift system. Extensive research in high-lift aerodynamics is required to achieve better low-speed performance in terms of shorter landing and take-off distances, an increased payload and a reduction of noise in areas surrounding airports.

The increased camber and the larger chordwise extent of a multi-element airfoil will increase the lift. However, as discussed by Smith [1975], the main contribution to the lift increase stems from the successful manipulation of the pressure distribution by the “gaps” between the different airfoil elements. Smith’s classical paper greatly contributed to the understanding of the physics of the flow around a multi-element airfoil. However, more than 20 years later the aerodynamic design of a high-lift system still poses a challenging problem. Major causes for this are the various viscous phenomena that affect the flow around a multi-element airfoil, see e.g. Butter [1984] or Meredith [1992]. A number of these viscous phenomena are listed below and illustrated in Fig. 1.1.

- The large suction peak on the most forward element may cause local supersonic flow, even if the free-stream Mach number is as low as 0.2. The shock wave interacts with the boundary layer on the slat.
- Near the sharp edge of a cavity the boundary layer is forced to separate and a

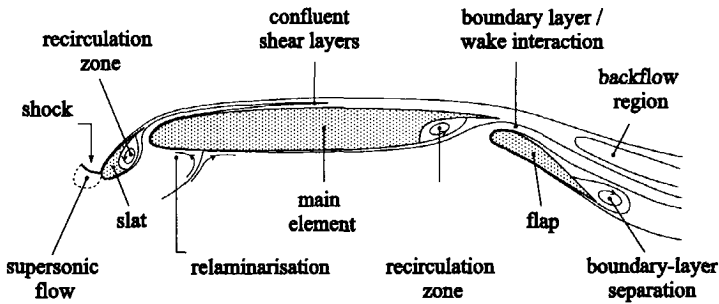


Figure 1.1: Viscous phenomena that affect the flow around a multi-element airfoil.

recirculation zone is formed in the cavity.

- Near the leading edge of the main element the turbulent boundary layer may relaminarize as a result of strong favourable pressure gradients.
- At high angles of attack, the slat wake may become confluent with the boundary layer on the main element. The wake of the main element may interact with the boundary layer that develops on the flap.
- Due to the large effective camber the shear layers are strongly curved, giving rise to significant static-pressure variations across the shear layers.
- Strong adverse pressure gradients promote the growth of wakes and boundary layers, and can lead to flow separation.

Considering the complexity of the different flow phenomena, and their possible interactions, it is not surprising that the numerical prediction of the flow around a multi-element airfoil is extremely difficult. Modern computational methods based on the Reynolds-averaged Navier-Stokes equations can accurately predict the lift up to moderate angles of attack, provided the flow remains attached, whereas the drag cannot be predicted accurately. At higher angles of attack, i.e. near the maximum-lift conditions, the computational methods fail to predict correctly either the lift or the drag as discussed by Adair and Horne [1989]. A decade later the situation is essentially still the same. The improvement of the existing calculation methods requires not only advances in grid generation and numerical schemes, but, perhaps even more important, it also requires turbulence models that properly describe the different phenomena that are essential to the flow around high-lift systems. In turn, this requires a better understanding of the physics of these flow phenomena, which can be achieved by studying isolated features of these phenomena. Experimental investigations of elementary flows, such as a turbulent boundary layer that separates from a wall [Simpson et al. 1981], [Simpson 1989], the development of a curved wake [Ramjee et al. 1987] or the flow over a backward-facing step [Eaton and Johnston 1981], can provide insight into the different flow phenomena.



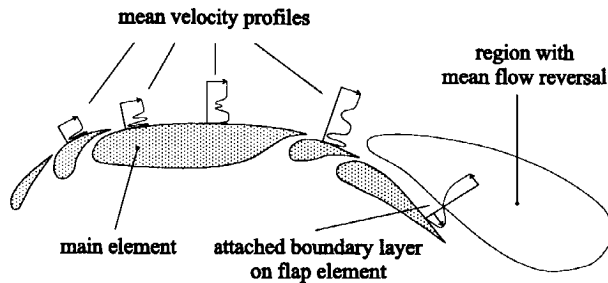


Figure 1.2: Illustration of free-separation in the flow around a multi-element airfoil as observed by Petrov [1980].

### 1.1.2 Free separation in flows about multi-element airfoils

The present investigation of the adverse pressure gradient wake, to be described in detail in Chapter 5, is related to one particular feature of high-lift aerodynamics, i.e. the development of the wake of the main element in the pressure field that is induced by the flap. An accurate numerical prediction of the near wake of the main element is highly desirable because it has a significant effect on the lift, especially at high incidence. However, as was shown by Adair and Horne [1989] and Nakayama et al. [1990], this wake is extremely complex owing to the combined effects of curvature, asymmetry, crosswise and streamwise pressure gradients and the interaction between the wake and the boundary layer on the flap. In a most interesting series of wind-tunnel tests on a multi-element airfoil, Petrov [1980] showed that the wake of the main element can exhibit a region with mean-flow reversal that is detached from the surfaces of the various elements, see Fig. 1.2. Petrov called this phenomenon “detached separation,” because the backflow region is separated from the surfaces of the elements by a relatively thin zone that consists of an attached boundary layer and a region of potential flow. Perhaps “free separation” is a better label, because “detachment” usually refers to the location in a separating turbulent boundary-layer where the wall-shear stress vanishes [Simpson et al. 1981].

The free-separation phenomenon is interesting since it does not occur in flows about single-element airfoils where separation takes place on the surface of the airfoil. Contrary to conventional wisdom, the stall of a multi-element airfoil is not always caused by boundary-layer separation on the flap or the aft portion of the main element. The stall can also occur when a zone of reversed flow in the wake of the main airfoil rapidly widens and propagates upstream. In fact, due to the thickening of this main-airfoil wake, the boundary-layer separation on the flap, which occurred at moderate angles of attack in Petrov’s experiment, disappeared with increasing incidence. Consequently, the flow on the flap and on the main element remained fully attached during the stall. This was also reported by, for example, Johnston and Horton [1986].

To the author’s knowledge, there are no detailed investigations of the free-separation phenomenon, despite its practical significance in high-lift aerodynamics or other technical applications in which free shear layers are subjected to severe streamwise pressure gradients. An exception is the experiment performed by Hill et al. [1963], who investigated the

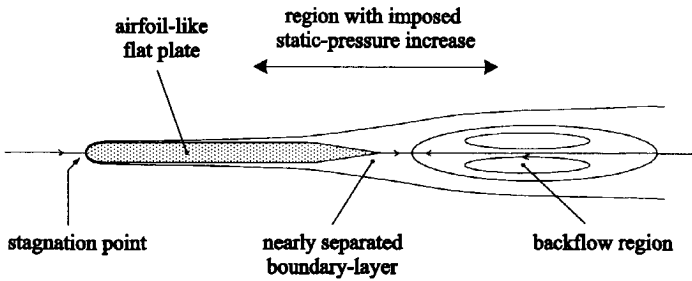


Figure 1.3: The mean flow around an airfoil-like flat plate with an imposed adverse pressure gradient in the streamwise direction.

effects of streamwise pressure gradients on the decay of wakes. They subjected the wake of a thick plate with a streamlined nose to adverse pressure gradients of various strengths by means of a diffusing wind-tunnel section with variable side walls. The wake generating body was placed in the test section of a wind tunnel with its trailing edge close to the entrance of the diffusing section. For all pressure gradients considered, the maximum velocity defect of the wake profile that entered the diffuser was  $(U_e - \bar{u}_{cl}) \approx 0.4U_e$ , in which  $U_e$  is the edge velocity and  $\bar{u}_{cl}$  is the mean velocity at the centreline of the wake. The experiments of Hill et al. [1963] showed that the maximum velocity defect in an adverse pressure gradient wake decreases at a slower rate than in the constant pressure wake of the same body. For a sufficiently strong pressure gradient, the maximum velocity defect increased rather than decreased, so that a zone of reversed mean flow developed in the central portion of the wake. This backflow region is not attached to the surface of the wake generating body. For all but the largest pressure gradient, i.e. the one that caused the mean-flow reversal, Hill et al. were able to predict the mean flow reasonably well with a simple calculation method based on von Kármán's integral momentum equation and an eddy viscosity that is uniform across the wake. However, they could not indicate whether the turbulence was predicted accurately, because the measurements were limited to time-averaged values of velocity and pressure.

The present investigation can be considered as a follow-up of the study carried out by Hill et al. [1963]. The present investigation concentrates on the development of the near wake of an "airfoil-like" flat plate that is subjected to a strong adverse pressure gradient, see Fig. 1.3. The pressure distribution was tuned such that the boundary layer at the trailing edge of the plate was close to separation. This simulates the trailing-edge flow on the suction side of an airfoil near maximum lift. A zone with mean-flow reversal occurred some distance downstream of the trailing edge of the plate. As in the experiment of Hill et al. [1963], the recirculation zone is not attached to the surface of the plate, so that it can be considered a simulation of free separation in the flow about a multi-element airfoil. In addition to mean velocities and mean pressures, turbulence quantities, such as Reynolds stresses, triple-velocity correlations and power spectra of streamwise velocity fluctuations, were measured in both the boundary layer and in the near wake of the plate.

## 1.2 Objectives of the Investigation

The primary objective of the present investigation is to gain better understanding of the complex turbulent flow that results when a strong adverse pressure gradient is imposed on the wake of an "airfoil-like" flat plate. The underlying assumption is that the improved understanding of the decelerating wake will ultimately improve the tools for the numerical prediction of flows about multi-element airfoils. To achieve the objective, a combined experimental and numerical investigation is carried out, although the emphasis will be on experimentation. Great effort is made to produce reliable experimental data on mean velocities, Reynolds stresses, triple-velocity correlations, and more complex turbulence statistics, such as spectral densities and spatial correlation functions. Numerical predictions are compared to the results of the experiment to investigate the suitability of several turbulence models for computations in wakes subjected to a severe adverse pressure gradient.

As discussed in Section 1.1.2, the wake of the flat plate is expected to exhibit mean-flow reversal when it is subjected to a sufficiently strong adverse pressure gradient. Also, turbulent velocity fluctuations may cause instantaneous flow reversal in this wake. Laser Doppler Anemometry (LDA) is needed to perform reliable measurements in such a highly turbulent flow. Although the mean flow about the plate is two-dimensional, the turbulence is a three-dimensional phenomenon. A special LDA will therefore be used to measure the three components of the velocity simultaneously. However, the three component LDA (3-D LDA) is not a standard instrument and, hence, there is little experience with its operation as compared to a one- or two-component LDA. As a consequence, extensive research is required to overcome the problems associated with the use of the instrument. One of the secondary objectives of the present investigation is to explain these problems and discuss possible solutions, resulting in practical guidelines for the operation of the 3-D LDA.

Irrespective of the number of components that is measured, the random nature of the LDA sampling process is a source of problems. LDA measures the velocity of particles that pass through the overlap region of intersecting laser beams. The sampling times are random because the particles are randomly distributed in space. Two effects of the random sampling are thoroughly investigated: (1) the correlation between the sampling process and the instantaneous velocity, commonly referred to as the velocity bias, and (2) the high statistical scatter of spectral estimates in the high-frequency range. Both effects may cause severe problems when inferring turbulence statistics from the LDA velocity samples. The explanation of these problems and the presentation of possible solutions is another secondary objective of the investigation.

## 1.3 Outline of the Thesis

Chapter 2 is concerned with the basics of turbulent flows. Section 2.1 focuses on the Reynolds-averaged equations of motion for incompressible turbulent flows, the Reynolds-stress modelling and several statistical quantities, like power spectral densities and correlation functions. This is followed by a summary of the main characteristics of turbulent

boundary layers and wakes. Section 2.2 considers the near wake of a flat plate without an imposed pressure gradient. This flow provides a reference for the investigation of the near wake in adverse pressure gradient.

Chapters 3 and 4 are devoted to the laser Doppler measurement technique. Chapter 3 starts with the basic principles of LDA, followed by a discussion of the problems related to the use of a 3-D LDA. Chapter 4 discusses the results of an investigation of the LDA sampling process.

Details on the experimental and the numerical investigation of the adverse-pressure-gradient wake are given in Chapter 5. Section 5.1 describes the wind tunnel, the model and the various optical configurations of the LDA. The measurement programme is also described. Details on the two turbulence models that are used to compute the wake, i.e. a standard  $k - \epsilon$  model and a (differential) Reynolds-stress transport model, are given in Section 5.2.

Chapter 6 gives the results of the investigation of the adverse-pressure-gradient wake. Section 6.1 presents and analyzes the main experimental results on the mean velocities, the integral parameters, the Reynolds stresses and the triple-velocity correlations. Section 6.2 presents a comparison between the experimental results and the numerical predictions of the two turbulence models. The findings of the spatial correlation measurements and the spectral measurements are discussed in Section 6.3 and Section 6.4, respectively. The discrepancies found between the experiment and the calculations are discussed in Section 6.5.

Finally, the general conclusions of the investigation are given in Chapter 7.

# Chapter 2

## Turbulent Flows

Chapter 2 is split into two sections. The aim of the first section is to introduce a number of tools that are common in turbulence research. Perhaps it is fair to say that the aim is even more limited: only those tools are introduced that are needed in later chapters as part of the combined experimental and numerical investigation of the adverse pressure gradient wake. For an introduction to turbulence the reader is referred to textbooks such as those by Tennekes and Lumley [1972], Townsend [1976] and Hinze [1975]. The second section concentrates on one particular turbulent flow, namely the wake of a flat plate in zero pressure gradient. Clearly, this flow is of importance, because it can be seen as a reference when studying the effects of the adverse pressure gradient on the wake.

### 2.1 Basics of Turbulent Flows

#### 2.1.1 Equations of motion

The equations of motion for a turbulent flow can be derived from the conservation of mass and momentum. For an incompressible flow with constant density, the conservation of mass is expressed by the continuity equation

$$\frac{\partial u_i}{\partial x_i} = 0, \tag{2.1}$$

where  $u_i$  is the instantaneous velocity component in the  $x_i$ -direction. In Eq (2.1) the usual summation convention applies, i.e. a term containing a repeated suffix is summed over all three values of the suffix. The tensor notation will be used here and in subsequent chapters for compactness. Sometimes, the  $x,y,z$  form will be used when it appears to be more convenient.

The conservation of momentum for a constant density flow is expressed by

$$\rho \left( \frac{\partial u_i}{\partial t} + u_j \frac{\partial u_i}{\partial x_j} \right) = \frac{\partial \sigma_{ij}}{\partial x_j} \quad (i = 1, 2, 3) \tag{2.2}$$

where  $\rho$  is the fluid density and  $\sigma_{ij}$  is the stress tensor. The term between brackets on the left-hand side is the acceleration of a fluid element, whereas the term on the right-hand side represents the forces acting on that fluid element. In a Newtonian fluid the stress tensor is given by

$$\sigma_{ij} = -p\delta_{ij} + 2\mu s_{ij} , \quad (2.3)$$

where  $p$  is the hydrodynamic pressure,  $\delta_{ij}$  is the Kronecker delta,  $\mu$  is the dynamic viscosity and  $s_{ij}$  is the rate of strain tensor given by

$$s_{ij} = \frac{1}{2} \left( \frac{\partial u_i}{\partial x_j} + \frac{\partial u_j}{\partial x_i} \right) . \quad (2.4)$$

Note that the viscous stress  $2\mu s_{ij}$  is assumed to be proportional to the rate of strain  $s_{ij}$ , which is a flow property, and the dynamic viscosity  $\mu$ , which is a fluid property. Combining Eq (2.1) through Eq (2.4) yields the well known Navier-Stokes equations (NS equations) for a flow with constant density

$$\frac{\partial u_i}{\partial t} + u_j \frac{\partial u_i}{\partial x_j} = -\frac{1}{\rho} \frac{\partial p}{\partial x_i} + \nu \frac{\partial^2 u_i}{\partial x_j \partial x_j} \quad (i = 1, 2, 3) \quad (2.5)$$

where  $\nu (= \mu/\rho)$  is the kinematic viscosity, which is assumed to be constant. The NS equations and the continuity equation, together with the boundary conditions and the initial conditions, are generally considered to describe the turbulent motion in all its temporal and spatial detail. The NS equations can therefore be seen as an exact model for the turbulence, but this interpretation is of little practical use since there is no exact solution to the NS equations. Although direct numerical simulations (DNS) can be seen as good approximations of exact solutions, DNS for complex geometries or high Reynolds numbers is beyond the capacity and speed of existing computers, and this will remain so in the foreseeable future. As a consequence, engineering practice heavily relies on experimental data, which in general are expensive to obtain, and on numerical solutions of the *Reynolds-averaged* NS equations (RANS equations).

### 2.1.2 Reynolds-averaged Navier-Stokes equations

The instantaneous velocity  $u_i$  and the instantaneous pressure  $p$  are random processes in the sense that their instantaneous values fluctuate in time and cannot be predicted (see, for example, Priestley [1981]). However, the velocity and the pressure can be described in terms of probability. This leads to the introduction of mean values. Reynolds [1895] introduced the decomposition of the instantaneous turbulence quantities in a mean value and a fluctuating component, i.e.

$$u_i = \bar{u}_i + u'_i \quad (i = 1, 2, 3) \quad \text{and} \quad p = \bar{p} + p' . \quad (2.6)$$

In these expressions, the overbar denotes ensemble averaging and the fluctuating component is denoted by a prime. The ensemble average is defined as the arithmetic average over infinitely many realizations of a particular experiment. It is the most general type of averaging and it allows for time-dependent mean turbulence quantities in instationary

processes. However, if the turbulence is assumed to be ergodic, which implies stationarity, then the ensemble average can be replaced by a simple time average, such as

$$u_{i,T} = \lim_{T \rightarrow \infty} \frac{1}{T} \int_{-T/2}^{T/2} u_i(t) dt. \quad (2.7)$$

At this moment, however, no assumptions will be made about the stationarity of the turbulence. Applying the Reynolds averaging to the continuity equation results in

$$\frac{\partial \overline{u_i}}{\partial x_i} = 0, \quad (2.8)$$

which has the same form as the continuity equation for the instantaneous velocity, Eq (2.1). The Reynolds-averaged NS equations are given by

$$\frac{\partial \overline{u_i}}{\partial t} + \overline{u_j} \frac{\partial \overline{u_i}}{\partial x_j} = -\frac{1}{\rho} \frac{\partial \overline{p}}{\partial x_i} + \nu \frac{\partial^2 \overline{u_i}}{\partial x_j \partial x_j} - \frac{\partial \overline{u'_i u'_j}}{\partial x_j} \quad (i = 1, 2, 3). \quad (2.9)$$

The difference between the Reynolds averaged and the instantaneous NS equations is the appearance of the velocity correlations  $\overline{u'_i u'_j}$ . These correlations originate from the non-linear convection terms in the NS equations in conjunction with the Reynolds averaging. The quantity  $-\overline{\rho u'_i u'_j}$  is known as the Reynolds-stress tensor. This symmetrical tensor has six independent components that, in addition to the three mean-velocity components  $\overline{u_i}$  and the mean pressure  $\overline{p}$ , are unknowns in the Reynolds-averaged NS equations. In order to close the set of equations, appropriate expressions for the Reynolds stresses have to be devised, an activity known as "turbulence modeling." In essence, the turbulence model replaces the information that is lost during the averaging of the equations of motion.

### 2.1.3 Reynolds-stress transport equations

To gain insight into the Reynolds stresses it is helpful to consider the so-called Reynolds-stress transport equations. These equations can be derived by taking moments of the NS equations, see e.g. Wilcox [1993]. To be more precise: adding the product of the velocity fluctuation  $u'_i$  and the  $x_j$ -component of the NS equation to the product of  $u'_j$  and the  $x_i$ -component of the NS equation yields, after averaging:

$$\begin{aligned} \frac{\partial \overline{u'_i u'_j}}{\partial t} + \overline{u_l} \frac{\partial \overline{u'_i u'_j}}{\partial x_l} = & - \left( \overline{u'_i u'_l} \frac{\partial \overline{u_j}}{\partial x_l} + \overline{u'_j u'_l} \frac{\partial \overline{u_i}}{\partial x_l} \right) + \frac{1}{\rho} \overline{p'} \left( \frac{\partial u'_i}{\partial x_j} + \frac{\partial u'_j}{\partial x_i} \right) \\ & + \frac{\partial}{\partial x_l} \left[ -\overline{u'_i u'_j u'_l} - \frac{1}{\rho} \overline{p' u'_i} \delta_{jl} - \frac{1}{\rho} \overline{p' u'_j} \delta_{il} + \nu \frac{\partial \overline{u'_i u'_j}}{\partial x_l} \right] - 2\nu \frac{\partial \overline{u'_i}}{\partial x_l} \frac{\partial \overline{u'_j}}{\partial x_l}. \end{aligned} \quad (2.10)$$

A detailed physical interpretation of the different terms can be found in, for example, Bradshaw [1976]. The formulation of the transport equation does not solve the basic problem of determining the Reynolds stresses, because Eq (2.10) contains many (22) new unknown correlations. This is not surprising, since the procedure that is followed to derive Eq (2.10), i.e. taking moments of the NS equations followed by Reynolds averaging,

does not supply any new information. Eventually, empirical information in the form of a turbulence model is needed to replace the information that is lost as a result of the Reynolds averaging.

Before turning to turbulence modeling, attention will be directed to a special case of the Reynolds-stress transport equation that follows by setting  $i = j$  in Eq (2.10) and dividing the result by 2. This yields the transport equation for the turbulence kinetic energy per unit mass,  $k$ , defined as

$$k = \frac{1}{2} \overline{u'_i u'_i} = \frac{1}{2} (\overline{u'^2} + \overline{v'^2} + \overline{w'^2}). \quad (2.11)$$

The transport equation for  $k$  reads

$$\underbrace{\frac{\partial k}{\partial t}}_{\text{advection}} + \underbrace{\overline{u_i} \frac{\partial k}{\partial x_i}}_{\text{production}} = \underbrace{\frac{\partial}{\partial x_i} \left[ -\overline{u'_i u'_i} \frac{\partial \overline{u_i}}{\partial x_i} - \frac{1}{\rho} \overline{p' u'_i} + \nu \frac{\partial k}{\partial x_i} \right]}_{\text{transport}} - \underbrace{\nu \frac{\partial u'_i}{\partial x_i} \frac{\partial u'_i}{\partial x_i}}_{\text{dissipation}} \quad (2.12)$$

The equation's left-hand side is the sum of an unsteady term and the advection. It represents the change of the kinetic energy when moving with the mean flow. The first term on the right-hand side is known as production. It is the work of the Reynolds stresses against the mean strain and represents the transfer of energy from the mean flow to the turbulence. The second term on the right-hand side is the spatial transport of turbulence. It can be split into three contributions: transport by velocity fluctuations ( $-\overline{u'_i u'_i} \partial \overline{u_i} / \partial x_i$ ), by pressure fluctuations ( $-\overline{p' u'_i} / \rho$ ) and by viscosity ( $\nu \partial k / \partial x_i$ ). The last term in Eq (2.12) is the dissipation per unit mass, i.e. the transfer of the turbulence kinetic energy into heat. It is usually denoted by the Greek symbol  $\epsilon$ :

$$\epsilon = \nu \frac{\partial u'_i}{\partial x_i} \frac{\partial u'_i}{\partial x_i}. \quad (2.13)$$

Both the turbulence kinetic energy  $k$  and the dissipation  $\epsilon$  appear in the well known  $k - \epsilon$  turbulence model as will be discussed below.

### 2.1.4 Turbulence modeling

The Reynolds stresses are frequently modeled as

$$-\overline{u'_i u'_j} = \nu_t \left( \frac{\partial \overline{u_i}}{\partial x_j} + \frac{\partial \overline{u_j}}{\partial x_i} \right) - \frac{2}{3} k \delta_{ij}, \quad (2.14)$$

where  $\nu_t$  is the “eddy viscosity”. The term with  $\delta_{ij}$  is included in Eq (2.14) to obtain the correct value of the trace of the Reynolds stress tensor. The assumption that the Reynolds stresses are proportional to the mean rate of strain is known as the Boussinesq approximation. A comparison between Eq (2.3), Eq (2.4) and Eq (2.14) shows that this approximation mimics the behaviour of the viscous stresses. Dimensional analysis of Eq (2.14) shows that

$$\nu_t \sim \mathcal{U} \mathcal{L}, \quad (2.15)$$



where  $U$  is a velocity scale and  $\mathcal{L}$  is a length scale. For a two-dimensional flow, Eq (2.14) can be written as

$$\nu_t \equiv \frac{-\overline{u'v'}}{\partial\bar{u}/\partial y + \partial\bar{v}/\partial x}. \quad (2.16)$$

This suggests that, in general, the scales  $U$  and  $\mathcal{L}$  depend on both mean flow and turbulence quantities. The popular Cebeci-Smith turbulence model [Cebeci and Smith 1974] expresses the eddy viscosity in mean-flow quantities only. In this model, the eddy viscosity in, for example, the outer region of the turbulent boundary layer or in the turbulent wake is given by

$$\nu_t = \alpha U_e \delta^* F_{int}, \quad (2.17)$$

where  $\alpha (= 0.0168)$  is a closure coefficient,  $U_e$  is the mean velocity at the edge of the boundary layer and  $\delta^*$  is the displacement thickness as defined by Eq (2.50). Furthermore,  $F_{int}$  is an empirical function that takes into account the effects of the intermittent behaviour of the flow. On the other hand, the well known  $k - \epsilon$  model, see e.g. Launder and Sharma [1974], expresses the eddy viscosity exclusively in turbulence quantities. It uses  $U = k^{1/2}$  and  $\mathcal{L} = k^{3/2}/\epsilon$  yielding

$$\nu_t = C_\mu \frac{k^2}{\epsilon}, \quad (2.18)$$

where  $C_\mu$  is a closure coefficient. The  $k - \epsilon$  model uses a modeled transport equation for the kinetic energy  $k$ , reading

$$\frac{\partial k}{\partial t} + \bar{u}_j \frac{\partial k}{\partial x_j} = -\overline{u'_i u'_j} \frac{\partial \bar{u}_i}{\partial x_j} + \frac{\partial}{\partial x_j} \left[ \left( \nu + \frac{\nu_t}{\sigma_k} \right) \frac{\partial k}{\partial x_j} \right] - \epsilon. \quad (2.19)$$

A comparison between the modeled equation and the exact transport equation for  $k$ , Eq (2.12), shows that the triple-velocity correlations and the pressure-velocity correlations are taken together and are modeled as a "gradient-diffusion process," i.e.

$$\frac{1}{2} \overline{u'_i u'_i u'_i} + \frac{1}{\rho} \overline{p' u'_i} = -\frac{\nu_t}{\sigma_k} \frac{\partial k}{\partial x_i}, \quad (2.20)$$

where  $\sigma_k$  is a closure coefficient. The remaining unknown in Eq (2.19) is the dissipation  $\epsilon$ . It is possible to derive an exact transport equation for  $\epsilon$  from the NS equations, see Wilcox [1993] for details. However, the  $\epsilon$ -equation that is used in the  $k - \epsilon$  model shows only qualitative resemblance to the exact transport equation, so that the latter is not given here. In the  $k - \epsilon$  model the transport equation for  $\epsilon$  usually has the following form

$$\frac{\partial \epsilon}{\partial t} + \bar{u}_j \frac{\partial \epsilon}{\partial x_j} = -C_{\epsilon_1} \frac{\epsilon}{k} \overline{u'_i u'_j} \frac{\partial \bar{u}_i}{\partial x_j} + \frac{\partial}{\partial x_j} \left[ \left( \nu + \frac{\nu_t}{\sigma_\epsilon} \right) \frac{\partial \epsilon}{\partial x_j} \right] - C_{\epsilon_2} \frac{\epsilon^2}{k}, \quad (2.21)$$

where  $C_{\epsilon_1}$ ,  $C_{\epsilon_2}$  and  $\sigma_\epsilon$  are closure coefficients. The basic mechanisms that govern the transport of kinetic energy, i.e. advection, production, transport and dissipation, are also recognized in the modeled equation for  $\epsilon$ . The first term on the equation's right-hand side expresses that the dissipation increases in response to a high production of turbulence

kinetic energy, whereas the third term acts as a sink to decrease the dissipation levels in case of zero production.

After specification of the boundary conditions and the initial conditions, the system of partial differential equations that form the  $k - \epsilon$  model is ready to be solved. Some details on the numerical procedure for the computations in a turbulent wake are given in Section 5.2. There, the values of the closure coefficients will also be specified.

Turbulence models based on the Boussinesq eddy viscosity, Eq (2.14), are found to be unreliable in cases such as boundary-layer separation or flows over curved surfaces, see, for example, Wilcox [1993]. It seems more natural for these situations to describe the Reynolds-stresses with a transport equation, such as Eq (2.10). However, as mentioned before, the Reynolds-stress transport equations contain many unknowns that have to be modelled to solve the set of equations. Details on a turbulence model based on the Reynolds-stress transport equation are given in Section 5.2.

### 2.1.5 Correlations and spectra

In the previous sections, turbulence was described in terms of single-point statistics, which are averages defined in one point in time or in one point in space. However, single-point statistics do not always give sufficient insight into the structure of turbulence. The simplest statistical quantities to describe the turbulence structure are two-point correlations from which several turbulence length scales can be derived. These are briefly described below.

#### Spatial correlations and length scales

The simultaneous measurement of the fluctuating velocity component at two locations in space enables the construction of the spatial covariance function

$$R_{ij}(\Delta\vec{x}) = \overline{u'_i(\vec{x})u'_j(\vec{x} + \Delta\vec{x})}, \quad (2.22)$$

where, for simplicity, it is assumed that the turbulence is homogeneous, so that  $R_{ij}$  depends on the spatial separation  $\Delta\vec{x}$  only. It is common practice to present  $R_{ij}$  in a normalized form, yielding the spatial correlation function (scf)

$$\rho_{ij}(\Delta\vec{x}) = \frac{\overline{u'_i(\vec{x})u'_j(\vec{x} + \Delta\vec{x})}}{(\overline{u'_i(\vec{x})^2} \overline{u'_j(\vec{x} + \Delta\vec{x})^2})^{1/2}}. \quad (2.23)$$

The scf  $\rho_{ij}(\Delta\vec{x})$  has 27 components which makes it tedious to discuss (and to measure). In a drastic simplification, the present discussion will be limited to the longitudinal correlation  $\rho_{11}(\Delta x_1, 0, 0)$ , i.e.

$$\rho_{11}(\Delta x_1, 0, 0) \equiv \rho_{11}(\Delta x) = \frac{\overline{u'(x)u'(x + \Delta x)}}{(\overline{u'(x)^2} \overline{u'(x + \Delta x)^2})^{1/2}}, \quad (2.24)$$

where, for convenience,  $u'_1$  and  $\Delta x_1$  are replaced by  $u'$  and  $\Delta x$ , respectively. In turbulence research the spatial correlation  $\rho_{11}(\Delta x)$  is frequently used to determine a number of length scales of the flow. The integral length scale,  $L_{11}$ , defined as

$$L_{11} = \int_0^\infty \rho_{11}(\Delta x) d\Delta x, \quad (2.25)$$

can be seen as a typical length scale for the large, energy-containing eddies of the turbulence. After some manipulation of Eq (2.24) it can be shown that [Hinze 1975]

$$\frac{d^2 \rho_{11}(\Delta x)}{d\Delta x^2} \Big|_{\Delta x=0} = -\frac{(\overline{\partial u' / \partial x})^2}{u'^2}. \quad (2.26)$$

This means that the curvature of  $\rho_{11}(\Delta x)$  at zero spatial separation contains information on the small length scales of the turbulence, because the gradient of a velocity fluctuation as appearing in Eq (2.26) is dominated by small scales. Consider the Taylor-series expansion of  $\rho_{11}(\Delta x)$  around zero spatial separation

$$\rho_{11}(\Delta x) = \rho_{11}(0) + \frac{\partial \rho_{11}(\Delta x)}{\partial \Delta x} \Big|_{\Delta x=0} \Delta x + \frac{1}{2} \frac{\partial^2 \rho_{11}(\Delta x)}{\partial \Delta x^2} \Big|_{\Delta x=0} \Delta x^2 + \dots \quad (2.27)$$

It follows from Eq (2.24) that  $\rho_{11}(0) = 1$ . Furthermore, the second term on the right-hand side of Eq (2.27) is zero because  $\rho_{11}(\Delta x)$  is an even function. Combining Eq (2.26) and Eq (2.27) yields

$$\rho_{11}(\Delta x) = 1 - \frac{(\overline{\partial u' / \partial x})^2}{2u'^2} \Delta x^2 + \dots = 1 - \left( \frac{\Delta x}{\lambda_x} \right)^2 + \dots, \quad (2.28)$$

where we have introduced the Taylor length scale  $\lambda_x$ , defined as

$$\lambda_x^2 \equiv \frac{2\overline{u'^2}}{(\overline{\partial u' / \partial x})^2}. \quad (2.29)$$

The Taylor length scale  $\lambda_x$  is the value of  $\Delta x$  where the osculating parabola  $1 - (\Delta x / \lambda_x)^2$  intersects the spatial separation axis.

The curvature of the scf at zero separation contains information on  $(\overline{\partial u' / \partial x})^2$ . Such a quantity is related to the dissipation of the turbulence kinetic energy. It appears as an unknown in the transport equation for the turbulence kinetic energy, see Eq (2.12). This provides a clue on how to measure the dissipation of  $k$ . The basic idea is to measure the shape of the appropriate scf for very small values of the separation vector  $\Delta \vec{x}$ . (The adjective "appropriate" refers to the choice of the suffices  $ij$  and the orientation of the separation vector  $\Delta \vec{x}$  in Eq (2.23) such that the desired correlation is obtained.) Then the curvature of the measured scf at zero separation is determined in the form of a Taylor length scale, which effectively determines the value of a correlation such as  $(\overline{\partial u' / \partial x})^2$ . Multiplied with the kinematic viscosity,  $\nu$ , this yields a contribution to the dissipation of  $k$ .

The direct measurement of the dissipation of  $k$  by means of the "correlation approach" is not without problems. As can be seen from Eq (2.13), the total dissipation involves contributions from a large number of terms. Consequently, an equally large number of scfs must be measured. However, in locally isotropic flow the dissipation of  $k$  is given by [Hinze 1975]

$$\epsilon = 15 \nu \left( \frac{\overline{\partial u'}}{\partial x} \right)^2, \quad (2.30)$$

so that only one spatial correlation function has to be determined. Other issues related to the correlation approach for the direct measurement of dissipation of turbulence kinetic energy are discussed in Appendix C.

Instead of the spatial covariance  $R_{ij}(\Delta\vec{x})$  itself, it is more usual in turbulence research to consider the Fourier transform of  $R_{ij}(\Delta\vec{x})$ . This yields the three-dimensional spectrum  $\Phi_{ij}(\vec{k})$  defined as

$$\Phi_{ij}(\vec{k}) = \frac{1}{(2\pi)^3} \iiint_{-\infty}^{\infty} R_{ij}(\Delta\vec{x}) e^{-i\vec{k}\Delta\vec{x}} d\Delta\vec{x}, \quad (2.31)$$

where  $\vec{k}$  is the wave vector and  $k \equiv |\vec{k}|$  is the wave number, so that  $\vec{k}/k$  represents the propagation direction of the wave. To facilitate the interpretation of  $\Phi_{ij}$ , the wave number  $k$  may be related to the size of the turbulent eddies, in the sense that high values of  $k$  correspond to small eddies, and vice versa. In theory  $\Phi_{ij}$  is well suited to describe the spatial structure of turbulence, but in (measurement) practice it is too complex to handle. In experimental studies it is more convenient to study one-dimensional spectra, such as the Fourier transform of  $R_{11}(\Delta x)$

$$\phi_{11}(k_1) = \frac{1}{2\pi} \int_{-\infty}^{\infty} R_{11}(\Delta x) e^{-i k_1 \Delta x} d\Delta x, \quad (2.32)$$

where  $k_1$  is the  $x_1$ -component of the wave vector  $\vec{k}$ . The small scales (high wave numbers) are mainly responsible for the dissipation of energy. Typical length and velocity scales of the dissipating eddies are the Kolmogorov scales  $\eta = (\nu^3/\epsilon)^{1/4}$  and  $v = (\nu\epsilon)^{1/4}$ , respectively. These are the smallest length scale and velocity scale of the turbulence. Dimensional analysis suggests that the one-dimensional spectrum  $\phi_{11}$  in the high wave number region is given by

$$\phi_{11}(k_1) = v^2 \eta f(\eta k_1). \quad (2.33)$$

A well known result in turbulence states that for sufficiently high Reynolds number there is a range of wave numbers where viscous effects are not important and the turbulent eddies are isotropic. In this "inertial subrange" the one-dimensional spectrum has the following appearance

$$\phi_{11}(k_1) = a \epsilon^{2/3} k_1^{-5/3}. \quad (2.34)$$

Experiments suggest that the constant  $a$  is about 0.26.

### Autocorrelation and time scales

Time resolved measurements (or DNS data) of, for example, the fluctuating velocity component in the  $x_1$ -direction allow for the computation of the (temporal) autocovariance function,  $R$ , defined as

$$R(t_1, t_2) = \overline{u'_1(t_1)u'_1(t_2)} = \overline{u'(t_1)u'(t_2)}, \quad (2.35)$$

where  $u'_1$  is replaced by  $u'$  for convenience. For stationary turbulence,  $R(t_1, t_2)$  depends only on the lag time  $\tau = t_2 - t_1$ . It is common practice to normalize  $R(\tau)$  with  $R(0) \equiv \overline{u'^2}$ . This yields the autocorrelation function (acf):

$$\rho(\tau) = \frac{R(\tau)}{R(0)} = \frac{\overline{u'(t)u'(t+\tau)}}{\overline{u'^2}}. \quad (2.36)$$

In terms of signal-processing,  $\rho(\tau)$  measures the similarity between a realization of  $u'(t)$  and the same realization shifted over time  $\tau$ . Therefore, it is said that  $\rho(\tau)$  represents the "memory" of the process  $u'(t)$ . In analogy to the scf, the autocorrelation function  $\rho(\tau)$  can be used to determine a number of time scales of the turbulence, such as the integral time scale,  $T_u$ , defined as

$$T_u = \int_0^{\infty} \rho(\tau) d\tau, \quad (2.37)$$

and the Taylor time scale,  $\lambda_t$ , defined as

$$\lambda_t^2 \equiv \frac{2\overline{u'^2}}{(\partial u'/\partial t)^2}. \quad (2.38)$$

The inverse of  $\lambda_t$  is a measure for the highest frequencies that are present in the fluctuating velocity  $u'(t)$ . In practice,  $\lambda_t$  can be determined from the curvature of a measured acf at zero lag time. This procedure is followed in Section 6.4 for measurements in a turbulent wake.

As in case of the spatial covariance function  $R_{ij}(\Delta\vec{x})$ , it is possible to Fourier transform the autocovariance function  $R(\tau)$ . This yields the spectral density function (sdf), defined as

$$s(\omega) = \frac{1}{2\pi} \int_{-\infty}^{\infty} R(\tau) e^{-i\omega\tau} d\tau = \frac{1}{\pi} \int_0^{\infty} R(\tau) \cos(\omega\tau) d\tau. \quad (2.39)$$

The quantity  $s(\omega) d\omega$  can be interpreted as the contribution to  $\overline{u'^2}$  of components with frequencies between  $\omega$  and  $\omega + d\omega$ . It follows directly from the definition of the sdf that its low-frequency range is related to the large scale structure, because  $s(0) = \overline{u'^2} T_u / \pi$ . The interpretation of the sdf is aided by the close relation that exists between the Fourier transforms of  $R_{11}(\Delta x)$  and  $R(\tau)$  for flows with low turbulence intensity. This relation is known as Taylor's hypothesis.

### Taylor's hypothesis

In theoretical studies on turbulence there is usually more emphasis on the spatial dependency of the turbulence quantities than on the temporal dependency. On the other hand, most experimental research concerns Eulerian measurements where a quantity is measured as a function of time at a fixed location in space. Often, the time-dependent signal is converted into a space-dependent signal using Taylor's hypothesis, which can be expressed in mathematical terms as [Hinze 1975]

$$\frac{\partial}{\partial t} = -\bar{u} \frac{\partial}{\partial x}, \quad (2.40)$$

where  $\bar{u}$  is the mean velocity. Taylor's hypothesis is valid only if the mean velocity is large compared to the mean level of the velocity fluctuations, i.e.  $\bar{u}^2 \gg \overline{u'^2}$ . According to Taylor's hypothesis the temporal fluctuations at a fixed point in space are caused by the passage of a turbulence velocity field that remains unaltered during the time of passage. The latter condition is known as "frozen turbulence." With the help of Taylor's hypothesis, the sdf  $s(\omega)$ , defined by Eq (2.39), can be interpreted as a one-dimensional spectrum  $\phi_{11}(k_1)$

$$s(\omega/\bar{u}) = \phi_{11}(k_1). \quad (2.41)$$

Similarly, the acf  $\rho(\tau)$ , defined by Eq (2.36), can be interpreted as a spatial correlation  $\rho_{11}(\Delta x)$  by means of the substitution  $\tau = \Delta x/\bar{u}$ , i.e.

$$\rho(\tau\bar{u}) = \rho_{11}(\Delta x). \quad (2.42)$$

Also, the Taylor length scale  $\lambda_x$  is related to the Taylor time scale  $\lambda_t$  as  $\lambda_x = \lambda_t \bar{u}$ .

## 2.1.6 Turbulent boundary layers and wakes

### The boundary-layer approximation

For turbulent boundary layers and wakes it is often assumed that the change of flow quantities in the mean-flow direction ( $x$ -direction) is much smaller than that in the lateral direction, the  $y$ -direction. This can be expressed in mathematical terms as

$$\frac{\partial}{\partial x} \ll \frac{\partial}{\partial y}. \quad (2.43)$$

Alternatively, one may say that the length scale ( $L$ ) for flow variations in the  $x$ -direction is much larger than that in the  $y$ -direction ( $l$ ), i.e.  $L \gg l$ . This is known as the "boundary-layer" approximation, sometimes called the "thin shear-layer" approximation to underline that its validity is not restricted to boundary layers along fixed walls, but that it is also valid for turbulent wakes, and certain other flows, such as jets and thermal plumes. The boundary-layer approximation can be used to simplify the Reynolds-averaged equations of motion for turbulent boundary layers and wakes. In case these flows are two-dimensional, Eq (2.9) with  $i = 2$  simplifies to (see Tennekes and Lumley [1972] for details)

$$0 = -\frac{1}{\rho} \frac{\partial \bar{p}}{\partial y} - \frac{\partial \overline{v'^2}}{\partial y}. \quad (2.44)$$

For convenience the tensor notation is replaced by the  $x, y$ -notation. The above equation states that the lateral pressure gradient is determined only by the gradient of the Reynolds stress  $\overline{v'^2}$  in  $y$ -direction. Integration of Eq (2.44) yields

$$\bar{p} + \rho \overline{v'^2} = \bar{p}_e(x), \quad (2.45)$$

where the subscript  $e$  refers to conditions at the edge of the turbulent shear layer. Clearly,  $\bar{p}_e$  is related to the velocity just outside the shear layer,  $U_e$ , by

$$U_e \frac{dU_e}{dx} = -\frac{1}{\rho} \frac{d\bar{p}_e}{dx}. \quad (2.46)$$

Eq (2.45) can be used to obtain the following approximation to the Reynolds-averaged momentum equation for the  $x$ -direction

$$\bar{u} \frac{\partial \bar{u}}{\partial x} + \bar{v} \frac{\partial \bar{u}}{\partial y} = -\frac{1}{\rho} \frac{d\bar{p}_e}{dx} - \frac{\partial(\overline{u'^2} - \overline{v'^2})}{\partial x} - \frac{\partial \overline{u'v'}}{\partial y} + \nu \frac{\partial^2 \bar{u}}{\partial y^2}. \quad (2.47)$$

The term  $\partial(\overline{u'^2} - \overline{v'^2})/\partial x$  is often small and is, therefore, often neglected as part of the thin shear-layer approximation. However, the term cannot be neglected in, for example, boundary layers subjected to adverse pressure gradients near separation. A useful relation can be derived by integrating Eq (2.47) and the continuity equation, Eq (2.8), across a boundary layer from  $y = 0$  (wall) to  $y = +\infty$ . After some manipulation, see e.g. Hinze [1975], the Von Kármán integral momentum equation is obtained, reading

$$\frac{d\theta}{dx} + (2 + H) \frac{dU_e}{dx} \frac{\theta}{U_e} = \frac{\tau_w}{\rho U_e^2} + \frac{1}{U_e^2} \frac{d}{dx} \int_0^\infty (\overline{u'^2} - \overline{v'^2}) dy, \quad (2.48)$$

where  $\tau_w$  is the shear stress at the wall, given by

$$\tau_w = \mu \left. \frac{\partial \bar{u}}{\partial y} \right|_{y=0}. \quad (2.49)$$

The displacement thickness  $\delta^*$  and the momentum thickness  $\theta$  are characteristics of the mean-velocity profile, and defined as

$$\delta^* = \int_0^\infty \left(1 - \frac{\bar{u}}{U_e}\right) dy \quad (2.50)$$

and

$$\theta = \int_0^\infty \frac{\bar{u}}{U_e} \left(1 - \frac{\bar{u}}{U_e}\right) dy. \quad (2.51)$$

Furthermore,  $H(\equiv \delta^*/\theta)$  is known as the “shape factor” of the mean-velocity profile. The integral momentum equation, Eq (2.48), is also valid for the wake if the integrals in Eqs (2.50) and (2.51) are evaluated from  $y = -\infty$  to  $y = +\infty$  and if  $\tau_w$  is set to zero.

The boundary-layer approximation can also be applied to the transport equation for the turbulence kinetic energy, Eq (2.12). This yields (for a stationary flow)

$$\bar{u} \frac{\partial k}{\partial x} + \bar{v} \frac{\partial k}{\partial y} = -\overline{u'v'} \frac{\partial \bar{u}}{\partial y} + \frac{\partial}{\partial y} \left[ -\frac{1}{2}(\overline{u'^2 v'} + \overline{v'^3} + \overline{w'^2 v'}) - \frac{1}{\rho} \overline{p'v'} + \nu \frac{\partial k}{\partial y} \right] - \epsilon \quad (2.52)$$

Note that the production consists of “shear-stress production” only, and that the streamwise derivative of the transport term is neglected. The expression for the dissipation  $\epsilon$  is unaltered under the boundary-layer approximation, and is given by Eq (2.13).

It should be mentioned that the boundary-layer approximations are valid only if the ratio  $l/L$  is sufficient small. For a constant-pressure turbulent wake, experiments, e.g. Andreopoulos and Bradshaw [1980], suggest that the boundary-layer approximation is accurate. However, it is unlikely that the approximations are still accurate for wakes with a large pressure increase in the streamwise direction. The adverse pressure gradient is expected to enhance the spreading of the wake so that the streamlines are no longer nearly parallel to the  $x$ -axis. This suggests an increase of the ratio  $l/L$  as compared to the turbulent wake in zero pressure gradient.

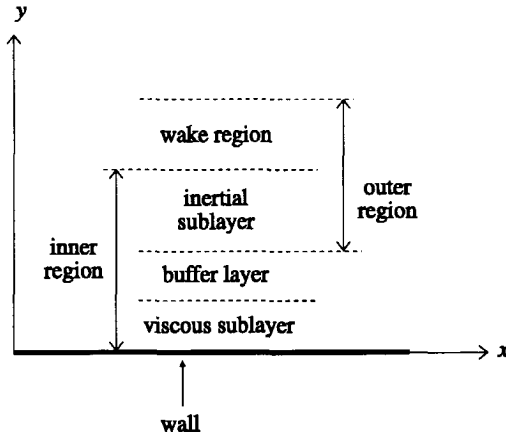


Figure 2.1: Different scaling regions in the boundary layer.

### Turbulent boundary layers

A characteristic that makes turbulent boundary layers generally more complicated than turbulent far wakes is the fact that a boundary layer consist of different regions, each with distinct scales. This complication has its origin in the fluid viscosity that imposes the *no-slip condition* on a solid wall, a condition that is clearly absent in a turbulent wake. Figure 2.1 illustrates the different regions in the boundary layer. In the region close to the wall the viscosity is important and a suitable length scale is formed by  $\nu/u_\tau$ . The friction velocity  $u_\tau$  ( $u_\tau \equiv (\tau_w/\rho)^{1/2}$ , where  $\tau_w$  is the wall shear stress) is a relevant velocity scale. The mean velocity in the inner region can be described by the “law-of-the-wall” [Tennekes and Lumley 1972]

$$u^+ = f(y^+) \quad \text{with} \quad u^+ \equiv \frac{\bar{u}}{u_\tau} \quad \text{and} \quad y^+ \equiv \frac{yu_\tau}{\nu}, \quad (2.53)$$

where  $f$  does not depend on the streamwise coordinate  $x$ . The law-of-the-wall expresses that the flow near the wall is independent of the large-scale motion in the outer region of the boundary layer. Close to the wall the Reynolds stresses are negligible compared to the viscous stresses, and the law-of-the-wall takes the following form

$$u^+ = y^+ \quad \text{for} \quad y^+ < 3. \quad (2.54)$$

The region where Eq (2.54) is valid is called the “viscous sublayer.”

The boundary-layer thickness,  $\delta$ , is an appropriate length scale for the larger part of the turbulent boundary layer, except close to the wall. The friction velocity  $u_\tau$  can still be used as a velocity scale in the outer region. The mean-velocity profile in the outer region of the boundary layer may be expressed in defect form

$$\frac{U_e - \bar{u}}{u_\tau} = F\left(\frac{y}{\delta}\right), \quad (2.55)$$



where  $U_e$  is the mean velocity outside the boundary layer. Eq (2.55) is called a "defect law" if  $F$  does not depend on the streamwise coordinate  $x$ , so that the mean-velocity profile has the same functional form at different streamwise locations.

The "inertial sublayer" is the region of the boundary layer where both the defect law and the law-of-the-wall are valid. It follows from Eq (2.55) and Eq (2.53) that the mean-velocity profile in the inertial sublayer is given by [Tennekes and Lumley 1972]

$$u^+ = \frac{1}{\kappa} \ln y^+ + C, \quad (2.56)$$

where  $\kappa$  is the Von Kármán constant the value of which is approximately 0.41. Depending on the experiment, the value of the coefficient  $C$  ranges between 5.0 and 5.5 for smooth surfaces. In the inertial sublayer the Reynolds stresses are much larger than the viscous stresses, so that the latter can be neglected. In between the inertial sublayer and the viscous sublayer one finds the "buffer layer", where the viscous stresses and the Reynolds stresses have comparable magnitude.

A frequently used expression for the mean-velocity distribution in the inner region is due to Reichardt [1951]

$$u^+ = \frac{1}{\kappa} \ln (1 + \kappa y^+) + \frac{C\kappa - \ln \kappa}{\kappa} \left( 1 - e^{-\frac{y^+}{11}} - \frac{y^+}{11} e^{-0.33y^+} \right). \quad (2.57)$$

This expression reduces to the linear mean-velocity profile, Eq (2.54), for small values of  $y^+$  while for large values of  $y^+$  the mean-velocity distribution of Eq (2.56) is obtained. Eq (2.57) can be conveniently used to determine the friction velocity,  $u_\tau$ , from experimental data using a method introduced by Clauser [1954]. In this method the theoretical mean-velocity distribution, Eq (2.57), is matched to the experimental data in the inner region by variation of  $u_\tau$ . The matching is usually carried out by visual inspection of a so called "Clauser plot" in which both the experimental and the theoretical mean-velocity distributions are plotted against  $\ln(y^+)$ .

### Self-preserving wakes

The distributions of the mean velocity and turbulence quantities in a turbulent wake change in downstream direction. For large distances behind the wake-generating body, it is often assumed that the flow development is "self-preserving," also referred to as "self-similar." In that case the variation of, for example, the mean velocity in the wake is assumed to have the following form

$$\frac{U_e - \bar{u}}{u_0(x)} = G \left( \frac{y}{l_0(x)} \right), \quad (2.58)$$

in which  $u_0(x)$  is a velocity scale, e.g. the maximum velocity defect, and  $l_0(x)$  is a transverse length scale, e.g. the wake width at half the maximum velocity defect. Eq (2.58) expresses that the lateral distribution of  $\bar{u}$  has the same functional form at different streamwise locations, i.e. the universal function  $G$  is independent of  $x$ . The streamwise development of the distribution is accounted for by the dependence of  $u_0$  and  $l_0$  on  $x$ . Substitution of the expressions for self-preserving development, such as Eq (2.58), in the

equations of motion relates the different universal functions and imposes conditions on the dependence of  $u_0$  and  $l_0$  on  $x$ . However, a complete discussion of self-similarity of a wake is not within the scope of this chapter; it is discussed in detail in several textbooks on turbulence. It suffices here to mention the necessary conditions for self-preservation of a wake with small velocity defect. In the case that the edge velocity,  $U_e$ , is proportional to  $(x - x_0)^a$ , where  $x_0$  is some virtual origin and  $a$  is a constant, the velocity scale  $u_0$  and the length scale  $l_0$  should behave as (see Townsend [1976])

$$u_0(x) \propto (x - x_0)^{-\frac{1}{2} - \frac{1}{2}a} \quad \text{and} \quad l_0(x) \propto (x - x_0)^{\frac{1}{2} - \frac{3}{2}a}. \quad (2.59)$$

In a zero streamwise pressure gradient ( $a = 0$ ) the above expressions simplify to the following well-known result

$$u_0(x) \propto (x - x_0)^{-\frac{1}{2}} \quad \text{and} \quad l_0(x) \propto (x - x_0)^{\frac{1}{2}}. \quad (2.60)$$

The behaviour of the scales  $u_0$  and  $l_0$  as given by the above expressions is confirmed by several experiments, such as those by Pot [1979] and Andreopoulos and Bradshaw [1980].

Of considerable importance is the downstream distance from the wake-generating body beyond which the wake has reached the self-preserving state. For the wake of a flat plate this issue was addressed by Ramaprian et al. [1982]. After a careful analysis of the available experimental data, they concluded that the mean velocity reached the self-preserving state at  $x/\theta \approx 25$ , where  $\theta$  is the momentum thickness of the wake (which is constant in a zero pressure gradient wake). Turbulence quantities generally require much longer downstream distances before self-similar development is attained. The observation that the mean velocity reaches an asymptotic state at  $x/\theta \approx 25$  has, perhaps somewhat arbitrary, led to the labeling "far wake" for  $x/\theta \gg 25$ , while the region  $x/\theta \ll 25$  is known as the "near wake". The near wake will be discussed in some detail in the following section.

## 2.2 Turbulent Near Wakes

### 2.2.1 Characteristics of the near wake

When a boundary layer moves past the trailing edge of a streamlined body, there is a sudden change in the boundary conditions due to the removal of the no-slip condition. The flow adjusts itself to the new boundary conditions, and then transforms into the far wake at large distances beyond the trailing edge. Both the turbulent boundary layer and the far wake have been the subject of numerous experimental and numerical investigations. But investigations into these flows are unlikely to give information on the way the boundary layer evolves into the far wake. By definition, the transformation from the boundary layer into the far wake takes place in the near wake.

The near wake of a streamlined body, such as an airfoil or a flat plate, consists of two regions, which are commonly referred to as the "outer wake" and the "inner wake", see Fig. 2.2. Both regions have distinct velocity and length scales, not unlike the turbulent boundary layer. The outer wake is the part of the near wake that is unaffected by the sudden change of the boundary conditions at the trailing edge ( $x = 0$ ). The outer wake

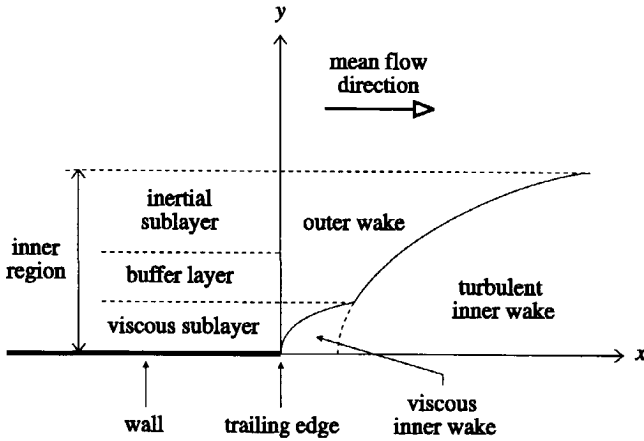


Figure 2.2: Definition of the different scaling regions in the near wake. The  $y$ -direction is not drawn to scale. (Adapted from Alber [1980].)

can be seen as the remnant of the velocity distribution in the boundary layer that is convected downstream by the mean flow. Chevray and Kovaszny [1969] were the first to report the observation that only the centre portion of the near wake changes, while the outer wake remains practically the same. For the zero-pressure-gradient case Chevray and Kovaszny [1969] also noted the very small spreading of the near wake beyond the initial distributions of the boundary layer at the trailing edge. As indicated by Andreopoulos and Bradshaw [1980] this is actually the result of two opposing effects. First, there is the natural growth of the outer region of the boundary layer when it moves downstream of the trailing edge into the wake. Secondly, there is a rapid increase in  $x$  of the mean velocity near the centre line. This rapid acceleration of the mean velocity in the inner wake, to be discussed shortly, induces an inflow towards the centre of the wake. For a constant-pressure wake the two opposing effects apparently cancel each other, thereby causing negligible growth of the near wake.

The inner wake is the region of the near wake in the direct vicinity of the trailing edge where the flow changes rapidly in both lateral and streamwise direction. In the inner wake the mean velocity distribution scales with the same length and velocity scales that are used in the law-of-the-wall region of the boundary layer, i.e.,  $u_\tau$  is a characteristic velocity and  $\nu/u_\tau$  is a characteristic length. According to Alber [1980] the value of  $u_\tau$  at the trailing edge should be used<sup>1</sup>. The inner wake is divided into two regions, namely the “viscous inner wake” and the “turbulent inner wake” as illustrated in Fig 2.2. Alber [1980] derived approximate solutions for the mean velocity in, and the thickness of, both regions of the inner wake. In the viscous inner wake the viscous stresses dominate the Reynolds stresses so that the latter can be ignored. The viscous inner wake grows into the remnants of the viscous sublayer of the original boundary layer. The region extends in streamwise

<sup>1</sup>Note that Alber’s choice for the relevant value of  $u_\tau$  is reasonable in case an “infinitely thin” plate is considered, but is likely to cause problems when the aft portion of the wake generating body is shaped in such a way that  $u_\tau$  rapidly changes towards the trailing edge.

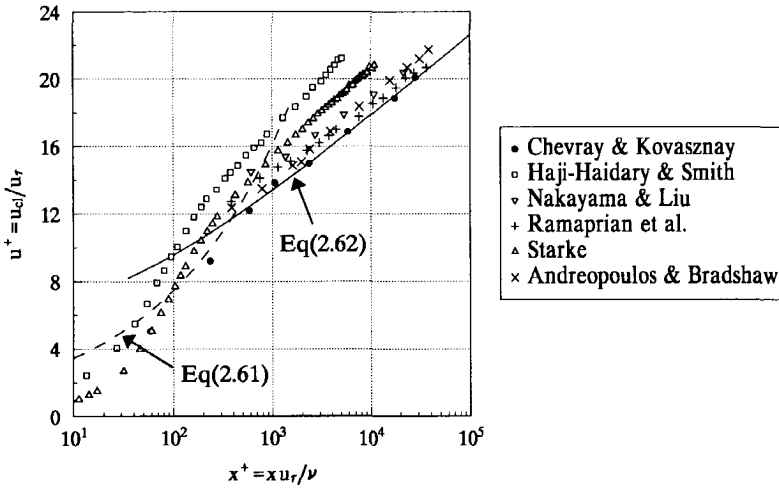


Figure 2.3: Dimensionless centreline velocity for the zero-pressure-gradient wake.

direction from the trailing edge ( $x = 0$ ) up to  $x \approx 100 \nu / u_\tau$ . The inner wake's centreline velocity behaves as

$$\frac{\bar{u}_{cl}}{u_\tau} = 1.611 \left( \frac{x u_\tau}{\nu} \right)^{1/3}, \quad (2.61)$$

where the subscript  $cl$  denotes conditions on the centreline. The thickness of the viscous inner wake also increases proportional to  $x^{1/3}$ . Furthermore, Alber [1980] reasoned that once the viscous inner wake has consumed the viscous sublayer, a turbulent inner wake will develop in the region of the convected turbulent boundary layer where Reynolds stresses are not negligible compared to viscous stresses. Assuming that the eddy viscosity near the centreline varied linearly in  $y$ , Alber [1980] derived the following expression for the centreline velocity in the turbulent inner wake

$$\frac{\bar{u}_{cl}}{u_\tau} = \frac{1}{\kappa} [\ln g(x u_\tau / \nu) - \gamma] + C, \quad (2.62)$$

where  $\kappa = 0.41$ ,  $C = 5.0$ ,  $\gamma = 0.5772$  and the function  $g(x)$  is implicitly defined by

$$g(x) [\ln g(x) - 1] = \kappa^2 x. \quad (2.63)$$

Alber determined the values of  $\kappa$  and  $C$  from a matching of Chevray and Kovaszny's mean-velocity distribution at the trailing edge to the mean-velocity profile in the inertial sublayer, Eq (2.56).

It is interesting to compare Alber's predictions to the results of several other experiments in the near wakes of flat plates. Figure 2.3 shows the predicted mean velocity along the centreline in dimensionless form. The dashed line in Fig. 2.3 is the centreline velocity in the viscous part of the near wake, Eq (2.61), whereas the full line represents the centreline velocity in the turbulent part given by Eq (2.62). Also shown in Fig. 2.3

are the results of various experiments in flat-plate wakes. Starke's results [Starke 2000] are somewhat special because they were obtained in the wake of the same plate as used in the experiment described later in this thesis. The agreement between Eq (2.61) and the experimental data is poor. To the author's knowledge there are no experiments that support the validity of Eq (2.61). A close examination of Starke's data reveals that the centreline velocity is nearly linear in  $x$  for small trailing-edge distances. In other words: the centreline velocity behaves nearly as  $\bar{u}_{cl} \propto x$  instead of  $\bar{u}_{cl} \propto x^{1/3}$ . This is in agreement with the findings of Haji-Haidari and Smith [1988].

In the logarithmic region there is excellent agreement between Alber's theory and the measurements of Chevray and Kovaszny [1969]. The data of Andreopoulos and Bradshaw [1980] indicate a slightly larger slope and intercept. The experiments of Starke and Haji-Haidari and Smith reveal even larger slopes in the logarithmic region, whereas the data of Ramaprian et al. [1982] are unique in the sense that these data indicate a slope that is slightly smaller than that of Alber.

It is clear from Fig. 2.3 that the different experiments on flat plate wakes do not indicate a unique set of values for  $\kappa$  and  $C$ . It should be noted that the investigation of Nakayama and Liu [1990] revealed a correlation between the Reynolds number based on the momentum thickness of the boundary layer at the trailing edge,  $R_\theta$ , and the value of the intercept  $C$ . They found that an increase of  $R_\theta$  generally resulted in an increase of  $C$ . However, Table 2.1 shows that this  $R_\theta$ -effect alone cannot explain the differences observed in Fig. 2.3. It is therefore likely that another effect exists. Table 2.1 also gives the angles of the tapered trailing edges for various experiments. Chevray and Kovaszny [1969] apparently used an extremely "thin" flat plate with an included angle at the trailing edge of  $0.13^\circ$ . On the other hand, Starke [2000] and Haji-Haidari and Smith [1988] used "thick" flat plates with trailing-edge angles of  $8.9^\circ$  and  $8.0^\circ$ , respectively.

It is obvious that the pressure distribution in the tapered part of the trailing edge will differ from that of a plate with "zero" thickness. Figure 2.4 sketches the inviscid static-pressure distribution along the plate surface (solid line) and along a streamline some distance away from the surface (dashed line). The taper induces an adverse pressure gradient in the trailing-edge region of the boundary layer. This reduces the friction velocity,  $u_\tau$ , thereby increasing the slope of the velocity distribution in the logarithmic region. In the direct vicinity of the trailing edge there is an even larger adverse pressure gradient, causing a further reduction of the friction velocity. Interestingly, there is a strong favourable pressure gradient over some distance in the wake, which induces an additional acceleration of the centreline velocity.

### 2.2.2 Calculation of the near wake of a flat plate

Patel and Scheuerer [1982] have calculated the wake of a flat plate in zero pressure gradient. Numerical solutions of the Reynolds-averaged Navier-Stokes equations (under boundary-layer approximation) were obtained by using a standard  $k - \epsilon$  turbulence model. To assess the performance of the  $k - \epsilon$  model for computations in both the near and the far wake, Patel and Scheuerer compared the numerical solutions with several sets of experimental data. Far downstream of the trailing edge, say  $x/\theta > 350$ , the comparison with the far-wake data of Pot [1979] indicated that the  $k - \epsilon$  model underpredicts the

Investigation	$\beta$ [°]	$R_\theta$
Chevray & Kovaszny	0.13	1582
Andreopoulos & Bradshaw	1.8	13600
Ramaprian et al.	1.5	5220
Nakayama & Liu	2.4	2747
Haji-Haidari & Smith	8.0	13600
Starke	8.9	1400

Table 2.1: The trailing-edge angle  $\beta$  and the Reynolds number  $R_\theta$  at the trailing edge for various experiments.

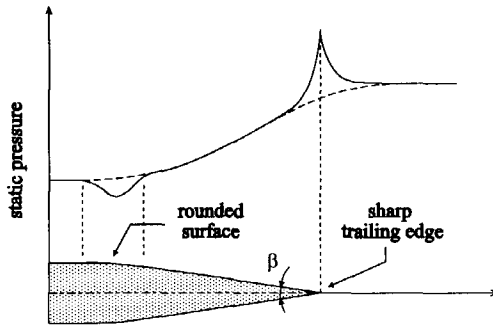


Figure 2.4: Effects of taper on the static-pressure distribution. The full line represents the static-pressure distribution on the plate surface and along the wake centreline. The dashed line is the static-pressure distribution along a streamline some distance away from the plate.

spreading rate of the far wake. This, however, is a well-known defect of the  $k - \epsilon$  model. Figures 2.5 and 2.6 show important results of the comparison with the near-wake data of Ramaprian et al. [1982] and Andreopoulos and Bradshaw [1980], respectively. Both figures illustrate that the calculated values of the maximum velocity defect,  $u_0$ , the wake half-width,  $l_0$ , and the shape factor,  $H$ , are in good agreement with the experimental data for the range of trailing-edge distances covered by the experiments. Later, these conclusions were confirmed by the findings of a more detailed investigation of the trailing-edge region by Patel and Chen [1987].

More recently, Tummers et al. [1997] computed the nominally zero-pressure-gradient near wake of a tapered flat plate using both a  $k - \epsilon$  model [Launder and Sharma 1974] and a differential Reynolds-stress transport model (RSTM) [Hanjalić et al. 1992]. These computations were based on the elliptic formulation of the RANS-equations (no boundary-layer approximation). The same near wake was also investigated experimentally by Starke [2000] using the same experimental facility and wake-generating flat plate as in the experiment described in Section 5.1. It is important to note that the trailing edge of this plate has a relatively large taper angle. As discussed in Section 2.2.1, the pressure field induced by the taper has significant effects on the flow field in the trailing-edge region. One cannot exclude beforehand the possibility that the “internal” pressure varia-

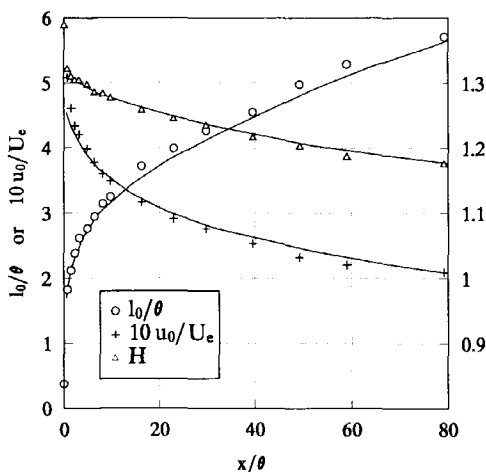


Figure 2.5: Comparison between calculations of Patel and Scheuerer [1982] and the experiments of Ramaprian et al. [1982]. (Taken from Patel and Scheuerer [1982]).

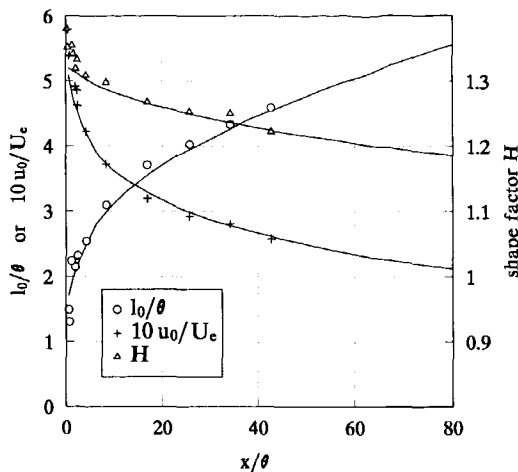


Figure 2.6: Comparison between calculations of Patel and Scheuerer [1982] and the experiments of Andreopoulos and Bradshaw [1980]. (Taken from Patel and Scheuerer [1982]).

tions caused by the tapering form a complication for the turbulence models that prevents successful prediction of this trailing-edge flow. However, it will be shown below that this is not the case.

Figure 2.7 depicts the measured and the computed centreline velocity in the wake of the tapered plate. The turbulent kinetic energy on the centreline and the maximum value of the turbulent kinetic energy at various  $x$ -stations are shown in Fig. 2.8. Both graphs indicate good agreement between the experiments and the numerical predictions.

The streamwise development of the displacement thickness  $\delta^*$  and the momentum thickness  $\theta$  are given in Fig. 2.9. The values of  $\delta^*$  and  $\theta$  for both the measured and computed mean-velocity profiles were determined from the definitions given by Eqs (2.50) and (2.51), respectively. The upper (lower) limit in the integrals defining  $\delta^*$  and  $\theta$  was chosen as the largest (smallest)  $y$ -coordinate of the measurement grid at each  $x$ -station<sup>2</sup>. The computations accurately reproduce the measured decrease of the momentum thickness from  $\theta = 4.7$  mm at the trailing edge to  $\theta = 3.3$  mm further downstream. At first glance, it appears surprising that the momentum thickness varies significantly in the nominally zero-pressure-gradient wake. However, the variation of the momentum thickness can be easily explained from the computed static-pressure distribution in the near wake that is plotted in Fig. 2.10.  $C_p$  is the static-pressure coefficient as will be defined in Section 6.1. The graph confirms that the static pressure is practically constant at the outer edge of

<sup>2</sup>Strictly speaking the concept of the "integral parameters" is valid only in flows without lateral pressure gradients (boundary-layer approximation). Although extensions to flows with lateral pressure gradients are known (e.g. Lock [1981] and Lock and Firmin [1982]), the above procedure is followed, thereby accepting that the thus determined values of  $\delta^*$  and  $\theta$  do not have the original physical interpretation.

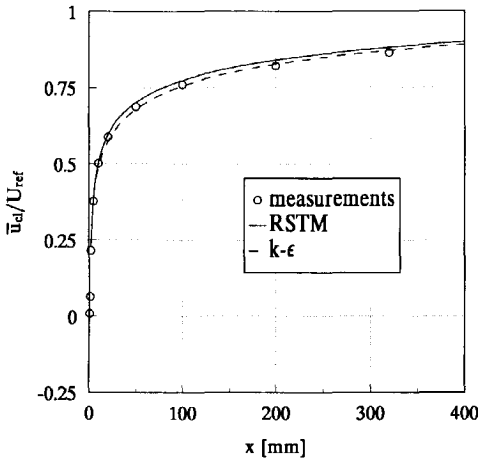


Figure 2.7: The centreline velocity  $\bar{u}_{cl}$  for the wake in zero pressure gradient. [Tummers et al. 1997]

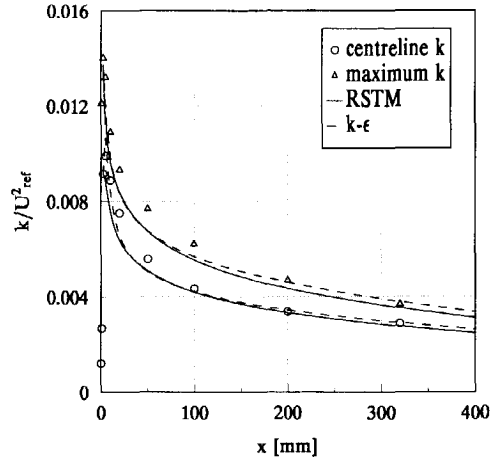


Figure 2.8: The turbulent kinetic energy  $k$  for the wake in zero pressure gradient. [Tummers et al. 1997]

the computational domain ( $y = 80$  mm). This boundary condition followed from static-pressure measurements. The static pressure is also practically constant across the wake far downstream of the trailing edge. There, the very small static-pressure variations in  $y$ -direction are caused by the variation of the Reynolds stress  $\overline{v'^2}$  with  $y$ , in agreement with the Reynolds-averaged momentum equation for the  $y$ -direction. However, owing to the tapering of the trailing edge of the plate, there are significant pressure gradients in both lateral and streamwise direction near the trailing edge. The taper causes an increase of the static pressure in the boundary layer when moving towards the trailing edge. This explains the relatively high value of the shape factor ( $H = 1.55$ ) of the mean-velocity profile at the trailing edge in Starke's experiment [Starke 2000]. The static pressure reaches a local maximum at the trailing edge and then relaxes in the wake. As a result, the near wake is subjected to a favourable pressure gradient even though the static pressure is practically constant at the outer edge at  $y = 80$  mm. The favourable pressure gradient induced by the tapering is responsible for the decrease of the momentum thickness. Note that this phenomenon could not have been predicted when the boundary-layer approximation to the RANS-equations had been used for the computations in the near wake.

The above discussion can be summarized as follows. The near wake of a flat plate in a nominally zero pressure gradient can be accurately computed using either a standard  $k - \epsilon$  model or a RSTM. Furthermore, it has been shown that both turbulence models can cope with the internal pressure variations caused by the tapering of the trailing edge.



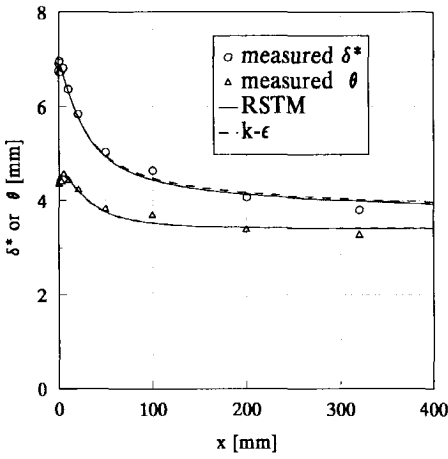


Figure 2.9: The displacement thickness  $\delta^*$  and the momentum thickness  $\theta$  for the wake in zero pressure gradient. [Tummers et al. 1997]

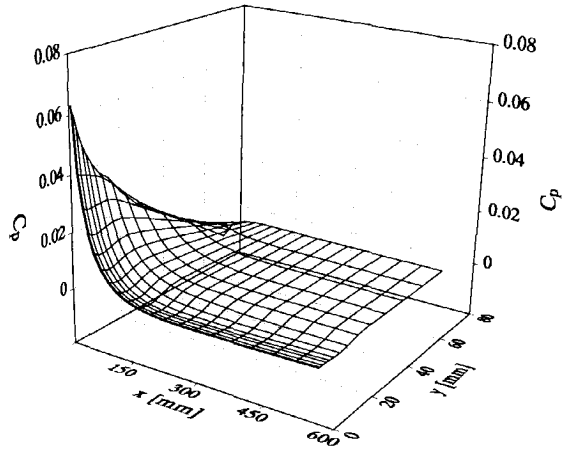


Figure 2.10: The static-pressure distribution in the near wake, as found from the Reynolds-stress transport model. [Tummers et al. 1997]



## Chapter 3

# Laser Doppler Anemometry

Sections 3.1 and 3.2 briefly summarize the basic principles of laser Doppler anemometry (LDA). For a more comprehensive treatment of these principles, the reader is referred to standard text books such as those by Durst et al. [1976], Durrani and Greated [1977], Somerscales [1981] and Absil [1995]. Aspects of LDA that are typical for a three-component system are described in some detail in Section 3.3, since, to the author's knowledge, these are not treated in the standard literature. Readers who are familiar with all this may proceed to the next chapter.

### 3.1 Introduction

In LDA the Doppler-shift is determined of light scattered by a small particle that moves with the flow. This Doppler-shift provides a measure for the velocity of the particle, and, therefore, for the flow velocity. Since the introduction of the technique by Yeh and Cummins [1964] the use of LDA has become widespread in both research and industrial applications. The main advantage of the technique over conventional measuring techniques, such as hot-wire anemometry (HWA) and pressure probes, is that it does not require a physical probe in the flow, i.e. it is a non-intrusive technique. Therefore, the flow is not disturbed during a measurement. Other advantages of the technique are:

- The Doppler frequency is a measure for the velocity *component* in a direction that is determined by the geometry of the optical arrangement;
- There is a linear relationship between the Doppler frequency and the velocity, resulting in a single calibration factor. The calibration factor depends only on the geometry of the optical arrangement and the frequency of the light source, and is independent of the flow properties;
- The LDA combines a good spatial resolution with a high temporal resolution. Especially for multi-component measurements, the spatial resolution of LDA is superior to that of HWA;

- The technique is directionally sensitive which means that it is able to measure flow reversal.

The combination of the different items makes the technique ideally suited for measurements in turbulent flows. Both the magnitude and the direction of the instantaneous velocity vector can be measured. It does not only give accurate information on relatively simple statistics, such as mean velocities and Reynolds stresses, but the non-intrusive nature also enables the measurement of more complex quantities such as spatial correlation functions.

The list of advantages is impressive, it resembles the specification of an ideal measuring instrument. However, it is not difficult to list some serious drawbacks of LDA:

- LDA samples the velocity when a particle transits the measuring volume, i.e. the region in space where the measurements are taken. Since the particles are randomly distributed in space, the sampling times are random as well. The random nature of the sampling process precludes the use of many standard data-processing methods (such as the fast Fourier transform (FFT) algorithm) for the spectral analysis of the turbulent velocity fluctuations;
- The processing of the randomly sampled data is further complicated by the dependence of the sampling process on the flow velocity. This phenomenon is known as the velocity bias [McLaughlin and Tiederman 1973]. Erroneous statistics will result if the velocity bias is ignored during the processing of the data;
- LDA measures the velocity of small particles that move with the flow. Since the quantity of interest is the fluid velocity, the relationship between the particle velocity and the fluid velocity must be known.

However, the main disadvantage lies in the complexity of the measuring technique. The complexity not only results in relatively high cost of purchasing an LDA system, it also requires an experienced operator who is familiar with all the peculiarities of the measuring technique.

## 3.2 Basic Principles of LDA

### 3.2.1 Doppler frequency

The Doppler effect forms the basis of LDA. Light scattered by a small moving particle undergoes a shift in frequency. This frequency shift is called the Doppler frequency and it is related to the velocity of the particle. Below, the relationship between the Doppler frequency and the velocity is derived.

Consider Fig. 3.1 which shows a light source that generates a plane light wave with frequency  $f_0$ . The direction of propagation of the plane wave is given by the unit vector  $\vec{e}_i$ . In complex notation the plane wave is given by

$$E_i(\vec{x}) = E_{i0} e^{-i(2\pi f_0 t - k_0 \vec{e}_i \cdot \vec{x} + \phi_i)}, \quad (3.1)$$

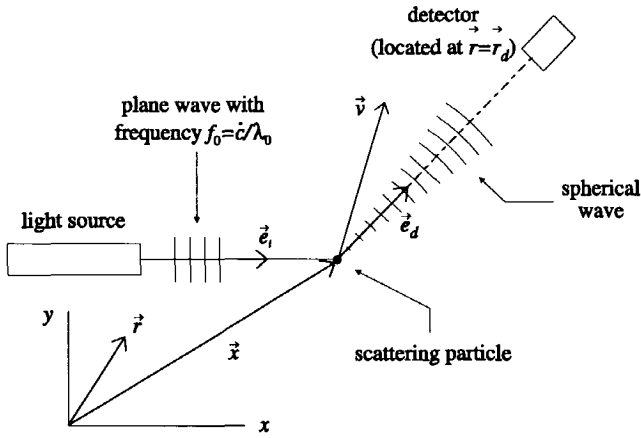


Figure 3.1: The light-scattering configuration.

where  $\phi_i$  is the initial phase and  $k_0 = 2\pi/\lambda_0$  is the wave number. The wavelength  $\lambda_0$  is related to the frequency of the light source as  $\lambda_0 = c/f_0$  where  $c$  is the speed of light. A particle passing through the plane wave scatters light in all directions and some of the light will be received by a detector. The orientation of the detector is determined by the unit vector  $\vec{e}_d$ , and the detector is located at  $\vec{r} = \vec{r}_d$ . The spherical wave emitted by the particle may be represented by [Goldstein 1983]:

$$E_s(\vec{r} - \vec{x}) = \frac{E_{s0}\sigma_s}{|\vec{r} - \vec{x}|} e^{-i(2\pi f_s t - k_s |\vec{r} - \vec{x}| + \phi_s)}, \quad (3.2)$$

where  $\sigma_s$  depends on the scattering characteristics of the particle. At the particle ( $\vec{r} = \vec{x}$ ) it follows from Eq (3.1) and Eq (3.2) that

$$2\pi f_0 t - k_0 \vec{e}_i \vec{x} + \phi_i = 2\pi f_s t + \phi_s. \quad (3.3)$$

This yields the following expression for the phase  $\Phi$  of the spherical wave at the detector ( $\vec{r} = \vec{r}_d$ )

$$\begin{aligned} \Phi &= 2\pi f_0 t + \phi_i - k_0 \vec{e}_i \vec{x} - k_s |\vec{r}_d - \vec{x}| \\ &= 2\pi f_0 t + \phi_i - k_0 \vec{e}_i \vec{x} - k_s \left( R - \vec{e}_d \frac{d\vec{x}}{dt} t \right), \end{aligned} \quad (3.4)$$

where it is assumed that at time  $t = 0$  the distance between the particle and the detector is  $R$ . Furthermore,  $d\vec{x}/dt \equiv \vec{v}$  is the velocity vector of the particle at  $t = 0$ . The frequency of the scattered light as seen by the detector,  $f_w$ , is proportional to the time derivative of  $\Phi$ , i.e.

$$2\pi f_w = \frac{d\Phi}{dt} = 2\pi f_0 + \vec{v} \cdot (k_s \vec{e}_d - k_0 \vec{e}_i). \quad (3.5)$$

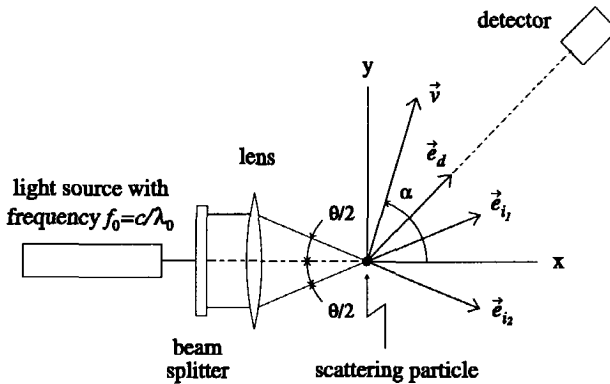


Figure 3.2: The optical arrangement for the dual-beam heterodyne LDA.

If the velocity of the particle is small compared to the speed of light, it can be assumed that  $k_0 \approx k_s$  in Eq (3.5), so that the frequency of the scattered light at the detector,  $f_w$ , becomes

$$f_w = f_0 + \frac{\vec{v}(\vec{e}_d - \vec{e}_i)}{\lambda_0}. \quad (3.6)$$

The second term on the right-hand side of Eq (3.6) is known as the Doppler frequency. It contains information on the component of the velocity in the direction of the vector  $\vec{e}_d - \vec{e}_i$ . This vector is determined by the geometry of the optical arrangement of the LDA.

### 3.2.2 Heterodyne detection

It is the task of the detector to generate an output signal from which the Doppler frequency  $f_D$  can be determined. The direct measurement of the Doppler frequency requires a very high resolution of the detector, because the Doppler frequency is much smaller than the frequency of light; typically  $f_D/f_0 \approx 10^{-13}$ . In the low-velocity range, say  $|\vec{v}| < 300$  m/s, the Doppler frequency can be determined with an “optical mixing” or “heterodyne” technique in conjunction with a square-law detector. The essence of heterodyning is that when two light waves with slightly different frequencies,  $f_{w_1}$  and  $f_{w_2}$ , are mixed on the surface of a square-law detector, the output signal oscillates with the difference frequency  $f_{w_1} - f_{w_2}$ . Because of its superior signal-to-noise ratio, the most widely used optical configuration is the dual-beam heterodyne configuration. Figure 3.2 shows the optical arrangement for the dual-beam configuration. Eq (3.6) can be applied to both incident beams, resulting in

$$\left. \begin{aligned} f_{w_1} &= f_0 + \vec{v}(\vec{e}_d - \vec{e}_{i_1})/\lambda_0 \\ f_{w_2} &= f_0 + \vec{v}(\vec{e}_d - \vec{e}_{i_2})/\lambda_0 \end{aligned} \right\} \Rightarrow f_D \equiv f_{w_2} - f_{w_1} = \frac{\vec{v}(\vec{e}_{i_1} - \vec{e}_{i_2})}{\lambda_0}. \quad (3.7)$$

The unit vectors  $\vec{e}_{i_1}$  and  $\vec{e}_{i_2}$  indicate the direction of the incident beams, and the Doppler frequency  $f_D$  is now defined as the difference between  $f_{w_1}$  and  $f_{w_2}$ . Inspection of Eq (3.7) shows that  $f_D$  is a measure for the velocity component in the direction of  $\vec{e}_{i_1} - \vec{e}_{i_2}$ . The Doppler frequency is independent of the orientation of the detector with respect to the incident beams, which enables the use of large apertures to collect more scattered light.

When a particle passes through the overlap region of the incident beams, i.e. the so-called measuring volume, it scatters light in all directions. A square-law detector, usually a photomultiplier tube, then receives light with two slightly different frequencies,  $f_{w_1}$  and  $f_{w_2}$ . The relationship between the output signal  $y(t)$  and the input signal  $x(t)$  of a photomultiplier is given by [Somerscales 1981]

$$y(t) = \frac{S}{T_s} \int_{t-T_s/2}^{t+T_s/2} x(t')^2 dt', \quad (3.8)$$

where  $T_s$  is the time constant of the photomultiplier and the constant  $S$  represents the radiant sensitivity. According to Eq (3.5) the input signal can be written as

$$x(t) = a_1 \cos(2\pi f_{w_1} t + \phi_1) + a_2 \cos(2\pi f_{w_2} t + \phi_2), \quad (3.9)$$

where  $\phi_1 - \phi_2$  is the phase difference between the two light waves. The phase difference is assumed to be constant, which indicates the need for a coherent light source such as a laser. On combining Eqs (3.7) through (3.9) the following expression for the output signal of the photomultiplier is obtained (assuming  $T_s f_{w_1} \gg 1$  and  $T_s f_{w_2} \gg 1$ )

$$y(t) = \frac{1}{2} S a_1^2 a_2^2 + S a_1 a_2 \frac{|\sin(\pi f_D T_s)|}{\pi f_D T_s} \cos(2\pi f_D t + \phi_1 - \phi_2). \quad (3.10)$$

For small values of the time constant  $T_s$ , say  $T_s \approx 10^{-9}$  s, Eq (3.10) reduces to the following well-known expression for the output signal of the photomultiplier

$$y(t) = \frac{1}{2} S a_1^2 a_2^2 + S a_1 a_2 \cos(2\pi f_D t + \phi_1 - \phi_2). \quad (3.11)$$

The first term on the equation's right-hand side is known as the pedestal; it is the result of the spatial distribution of the light intensity in the overlap region of both beams. The second term, called the Doppler burst, carries the desired information, because it oscillates with the Doppler frequency  $f_D$ .

### 3.2.3 Directional ambiguity

Referring to Fig. 3.2, it is easy to see that the expression for the Doppler frequency, Eq (3.7), can be rewritten as

$$f_D = \frac{\vec{v}(\vec{e}_{i_1} - \vec{e}_{i_2})}{\lambda_0} = \frac{2 \sin(\theta/2)}{\lambda_0} |\vec{v}| \sin \alpha, \quad (3.12)$$

where  $\theta$  is the angle between the unit vectors  $\vec{e}_{i_1}$  and  $\vec{e}_{i_2}$ , i.e.  $\theta$  is the crossing angle of the incident laser beams. Furthermore,  $\alpha$  is the angle between the velocity vector and the  $x$ -axis. The frequency difference  $f_D$  can be positive or negative depending on the value

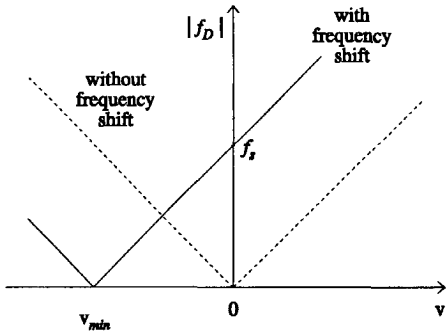


Figure 3.3: The effect of frequency shift on the relationship between the particle velocity and the frequency of the photomultiplier output signal.

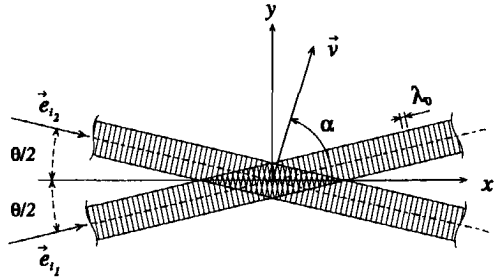


Figure 3.4: The interference of two plane light waves.

of  $\alpha$ . However, the output of the photomultiplier cannot distinguish between positive and negative values of  $f_D$  because  $\cos(-f_D) = \cos(f_D)$ . As a result, the LDA in its basic form is unable to determine the sign of the velocity. The insensitivity to the direction of the particle velocity is usually referred to as the “directional ambiguity.” The common method to remove this ambiguity is frequency shifting. In that case the frequency of one of the incident beams in Fig. 3.2 is shifted by a constant value  $f_s$ . This can be achieved with an acousto-optic Bragg cell. Due to the frequency shift the relationship between Doppler frequency and particle velocity becomes (assuming  $f_s \ll f_0$ )

$$f_D = f_s + \frac{2 \sin(\theta/2)}{\lambda_0} |\vec{v}| \sin \alpha, \quad (3.13)$$

as illustrated in Fig. 3.3. If the shift frequency  $f_s$  is chosen larger than the Doppler frequency that corresponds to the smallest anticipated velocity in the flow,  $v_{min}$ , each value of  $|f_D|$  is uniquely related to one velocity value, and, as a consequence, the directional ambiguity is removed. In practice, one usually sets the shift frequency  $f_s$  about two times larger than the Doppler frequency that corresponds to  $v_{min}$  [Tropea 1986].

### 3.2.4 Fringe model

An alternative procedure to derive the relationship between the Doppler frequency and the velocity for the dual-beam LDA, Eq (3.12), is given by the “fringe model,” which is due to Rudd [1969]. The fringe model is often used to visualize different aspects of the dual-beam configuration, such as the nature of the detector output signals in case the incident beams are improperly aligned [Durst and Stevenson 1979]. It also gives an interpretation of the proportionality constant between the Doppler frequency and the velocity in Eq (3.12). However, the fringe model should be considered with some reserve, because it is incorrect in the sense that it ignores the fact that heterodyning takes place on the surface of the photomultiplier and not at the particle, see Durst [1982]. However,



most of the predictions of the fringe model are in accordance with the Doppler theory, as will be shown below.

If the incident beams shown in Fig. 3.4 are properly aligned, their wavefronts are nearly plane in the overlap region, so that the light waves can be described with Eq (3.1). The intensity of the light in the overlap region of both beams is then given by

$$\begin{aligned} I &= (E_{1_0} + E_{2_0})(E_{1_0}^* + E_{2_0}^*) \\ &= E_{1_0}^2 + E_{2_0}^2 + 2E_{1_0}E_{2_0} \cos(2k_0y \sin(\theta/2) + \phi_1 - \phi_2), \end{aligned} \quad (3.14)$$

where  $\theta$  is the angle between the unit vectors  $\vec{e}_{i_1}$  and  $\vec{e}_{i_2}$ ,  $y$  is a coordinate in the direction of  $\vec{e}_{i_1} - \vec{e}_{i_2}$  and  $\phi_1 - \phi_2$  is the phase difference between the two light waves. According to Eq (3.14) the intensity varies periodically in  $y$ , and the distance between two consecutive lines of constant intensity in the interference pattern is given by

$$d_f = \frac{\lambda_0}{2 \sin(\theta/2)}. \quad (3.15)$$

The quantity  $d_f$  is known as the fringe distance, and inspection of Eq (3.12) reveals that it is the inverse of the proportionality constant between the Doppler frequency and the velocity. A small particle passing through the interference pattern with a velocity component in the  $y$ -direction of  $v (= |\vec{v}| \sin \alpha)$ , scatters light with an intensity that is proportional to the local value of  $I$ . The intensity of the scattered light then oscillates with frequency

$$\frac{v}{d_f} = \frac{2 \sin(\theta/2)}{\lambda_0} |\vec{v}| \sin \alpha. \quad (3.16)$$

It follows from a comparison with Eq (3.12) that this is identical to the Doppler frequency.

The fringe model can also be used to visualize the effects of applying a frequency shift to remove the directional ambiguity. If in Fig. 3.4 the frequency of one of the beams, say beam 1, is increased with a value  $f_s$ , the intensity of the light in the overlap region becomes

$$I = E_{1_0}^2 + E_{2_0}^2 + 2E_{1_0}E_{2_0} \cos(2\pi f_s t + 2k_0y \sin(\theta/2) + \phi_1 - \phi_2). \quad (3.17)$$

The fringes in the interference pattern now move with velocity  $v_s = d_f f_s$  in the positive  $y$ -direction. As a result, a detector sees intensity variations with a frequency

$$f_s + \frac{v}{d_f} = f_s + \frac{2 \sin(\theta/2)}{\lambda_0} |\vec{v}| \sin \alpha = f_D, \quad (3.18)$$

which is identical to Eq (3.13), the result obtained using the Doppler theory.

### 3.2.5 Amplitude bias

Durao and Whitelaw [1979] have shown experimentally that there is a relationship between the amplitude of a Doppler burst and the particle velocity. Their study revealed that there is a tendency for low-speed particles to produce high-amplitude Doppler bursts, and vice versa. Through this mechanism low-velocity particles have (on the average) a

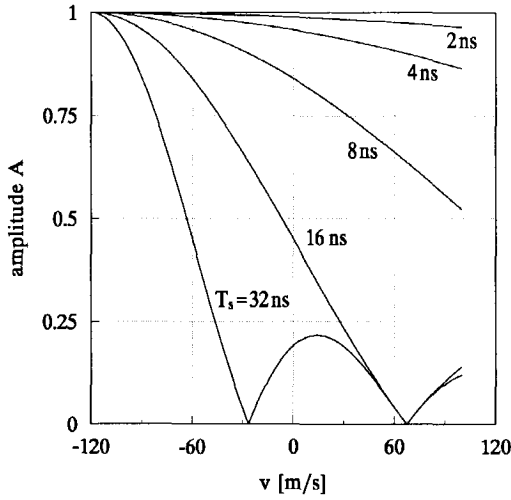


Figure 3.5: The amplitude  $A$  versus the velocity  $v$  for several values of  $T_s$  ranging between 2 ns and 32 ns.

larger probability of being detected and validated by the LDA signal processor than high-velocity particles. This bias towards low velocities was termed “amplitude bias” by Durao and Whitelaw. They argued that the amplitude bias was due to the fact that fast moving particles (on the average) spend less time in the measuring volume than slow particles. The fast moving particles scatter less photons and, therefore, produce Doppler bursts with smaller amplitude.

It was already shown in Section 3.2.2 (Eq (3.10)) that, in principle at least, the amplitude  $A$  of a Doppler burst depends on the Doppler frequency through the term

$$A = Sa_1a_2 \frac{|\sin(\pi f_D T_s)|}{\pi f_d T_s}, \quad (3.19)$$

where  $T_s$  is the time constant of the photomultiplier and  $f_D$  is the Doppler frequency. Substitution of Eq (3.18) in Eq (3.19) yields the following expression for  $A$

$$A = Sa_1a_2 \frac{|\sin(\pi(f_s + \frac{v}{d_f})T_s)|}{\pi(f_s + \frac{v}{d_f})T_s}, \quad (3.20)$$

where  $f_s$  is the shift frequency,  $v$  is the velocity component and  $d_f$  is the fringe distance. Figure 3.5 depicts the amplitude  $A$  as a function of  $v$  for several values of the photomultiplier time constant  $T_s$  ranging between 2 ns and 32 ns. Furthermore, it is assumed that  $d_f = 3 \mu\text{m}$  and  $f_s = 40 \text{ MHz}$ . Figure 3.5 shows that the amplitude  $A$  will significantly vary with the particle velocity only when the value of  $T_s$  is large. Clearly, photomultipliers with large time constants are not suited for LDA, because such photomultipliers give rise to the amplitude bias. Figure 3.5 also shows that the amplitude  $A$  is practically constant for small values of  $T_s$ . This means that the dependence of the amplitude  $A$  on the particle velocity can be conveniently ignored when a so-called “fast response” photomultiplier is used, which is usually the case.

### 3.2.6 Particle characteristics

The light-scattering particles form an essential element of the LDA measuring system. In each application the suitability of the particles must be determined in the same way as any other element of the LDA instrumentation. In general, it is highly appreciated if the particles are cheap, easy to generate, non-corrosive and non-toxic. However, the suitability of the particles for application in LDA mainly depends on their dynamical and optical characteristics.

The optical characteristics should be such that the particles scatter light with sufficient intensity for the photodetector to generate high-quality Doppler signals. Investigations based on Mie's scattering theory, e.g. Durst [1982], show that the amplitude and the visibility of the Doppler signals are dependent on the particle diameter, the refractive index of the particle material, the wavelength of the laser light, the angle between the incident laser beams and the aperture and orientation of the receiving optics. Generally speaking, the amplitude and visibility of the Doppler signals increase with increasing particle size and increasing index of refraction.

The dynamical characteristics of particles determine their ability to accurately follow the fluctuations in the fluid velocity even at high frequencies. The motion of a rigid, spherical particle in a viscous flow is governed by the Basset-Boussinesq-Oseen (BBO) equation, see Somerscales [1981]. Solutions of the BBO equation are discussed by Hjelmfelt and Mockros [1966]. A simplified equation of motion is given by (see Somerscales [1981])

$$\rho_p \frac{\pi d_p^3}{6} \frac{du_p}{dt} = 3\pi\nu\rho_f d_p (u_f - u_p), \quad (3.21)$$

where  $\nu$  is the fluid kinematic viscosity,  $d_p$  is the particle diameter,  $u_p$  and  $u_f$  are the particle and fluid velocities and  $\rho_p$  and  $\rho_f$  are the particle and fluid densities, respectively. The equation's left-hand side represents the force to accelerate the particle. The term on the right-hand side is the drag of the particle for which Stokes' drag law is used. The validity of Eq (3.21) is restricted to large values of the density ratio  $\sigma_r \equiv \rho_p/\rho_f$  and not too large acceleration. Furthermore, the effects of, for example, centrifugal forces, electrostatic forces and gravity are ignored.

Eq (3.21) will be used here to formulate a criterion for the diameter of the particles. Following Hjelmfelt and Mockros [1966] the fluid velocity and the particle velocity are expressed in terms of Fourier components. Substitution of  $u_f = e^{i\omega t}$  and  $u_p = \eta(\omega)e^{i\omega t}$  in Eq (3.21) yields the amplitude ratio  $|\eta|$  as

$$|\eta(\omega)| = \frac{\Omega}{\sqrt{\Omega^2 + \omega^2}} \quad \text{with} \quad \Omega = \frac{18\nu}{\sigma_r d_p^2}. \quad (3.22)$$

The amplitude ratio can be interpreted as a measure for the sensitivity of the particles to changes in the fluid velocity. It is seen from Eq (3.22) that the particle motion is attenuated at high frequencies. The maximum diameter of a particle that follows the velocity fluctuations up to 1 kHz, 5 kHz and 10 kHz for  $|\eta| = 0.99$  can be determined from Eq (3.22). For a number of frequently used seed materials the thus obtained diameters are listed in Table 3.1. From these results it can be concluded that oil particles with

seed material	density ratio $\sigma_r$ (in air)	maximum diameter [ $\mu\text{m}$ ]		
		1 kHz	5 kHz	10 kHz
silicone oil	620	3.1	1.4	1.0
rizella oil	711	2.9	1.3	0.9
polystyreen	865	2.6	1.2	0.8
teflon	1800	1.8	0.8	0.6
titanium oxide	3500	1.3	0.6	0.4

Table 3.1: Maximum particle diameter for various seed materials.

a diameter of typically 1  $\mu\text{m}$  accurately track the velocity fluctuations in low-speed air flows. High-speed flows generally require smaller particles, because of the energy of the velocity fluctuations at higher frequencies. The presence of a shock wave in a supersonic flow provides a further motivation to use submicron particles. Due to the strong decelerations across the shock wave the particle velocity lags the fluid velocity. This phenomenon has been studied by Yanta et al. [1971] and more recently by Maurice [1992]. The particle lag may result in a severe overestimation of the mean velocity and the turbulence intensity at locations directly downstream of the shock wave if too large particles are used. In general, particles that accurately follow the abrupt velocity changes in supersonic flows should have diameters less than 0.3  $\mu\text{m}$ .

There are flows with practical relevance for which Eq (3.21) is invalid. In vortical flows the centrifugal forces induce a migration of particles away from the core region (for  $\sigma_r > 1$ ), thus reducing the particle concentration in the core. The particle concentration may become so low that LDA measurements in the core become almost impossible as reported by Meyers and Hepner [1988]. Details on the particle motion in vortical flows can be found in e.g. Dring and Sou [1978].

### 3.2.7 Signal processor

The principle task of a signal processor is to extract the Doppler frequency (i.e. velocity) from the photomultiplier output signal. Usually, the signal processor also measures other quantities such as the arrival time of the particles and the duration of the Doppler bursts, i.e. the transit time of the particles. Two commonly used signal processors for sparsely seeded flows are “counter processors” and “spectrum analyzers.” A detailed discussion of the characteristics of the two types of processors and a comparison between their performances is beyond the scope of this thesis. Instead, this section describes only the basic principles of one representative of the latter type of signal processor. The processor to be described is the Burst Spectrum Analyzer (BSA) which is manufactured by Dantec, and available since the late 1980s.

The BSA processor performs a spectral analysis of the bandpass-filtered output signal of the photomultiplier. The Doppler frequency then follows from the location of the peak in the computed power spectrum. The basic principles of the Dantec BSA are illustrated in Fig. 3.6. The output signal of the photomultiplier is first amplified by a factor set by the operator and then bandpass filtered to remove frequency components outside the

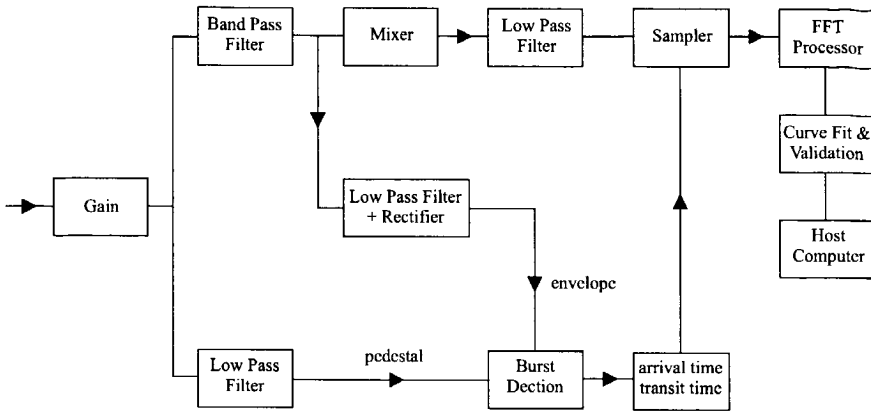


Figure 3.6: The basic principles of the Dantec BSA processor.

anticipated range of Doppler frequencies. A burst detection scheme determines whether the bandpass filtered signal contains a Doppler burst or not. Burst detection can be based on the pedestal or on the so called “envelope.” The envelope is obtained by rectifying and low-pass filtering of the bandpass filtered signal. When the envelope exceeds a 25 mV threshold, the sampler and the transit time counter are started and the arrival time is measured. The sampler is restarted each time the envelope exceeds the next higher threshold level (50 mV, 75 mV etc.). This is done to ensure that the samples are taken from the central part of the Doppler burst. The transit time counter is stopped when the envelope decreases below 12.5 mV.

While the burst detection scheme is carried out, the bandpass filtered signal is led through a mixer unit which shifts the power spectrum by a value of  $f_c$  towards lower frequencies. The aim of this shift is to increase the resolution of the computed power spectrum. The centre frequency  $f_c$  is selected by the operator in conjunction with the bandwidth  $B_w$  so that the cut-off frequencies of the bandpass filter are given by  $f_c \pm B_w/2$ . The down-shifted signal is low-pass filtered and then sampled at regular time intervals,  $t_{sam}$ . The number of samples  $n_{rec}$  is called the “record length,” and its value can be set by the operator at 8, 16, 32 or 64. The inverse of the time interval  $t_{sam}$  is called the sampling frequency  $f_{sam}$ . The resolution of the computed spectrum is proportional to  $f_{sam}/n_{rec}$ , which reduces to  $1.5B_w/n_{rec}$  because the BSA has a fixed relationship between the sampling frequency and the bandwidth:  $f_{sam} = 1.5B_w$ . A hardwired FFT processor then computes a spectrum from the samples.

In the next step a sinc function is fitted to the computed spectrum at the frequency with the highest peak and its neighbouring frequencies. The Doppler frequency follows as the frequency for which the sinc function achieves a maximum. The thus determined Doppler frequency is validated by means of a comparison between the two highest peaks in the spectrum. The Doppler frequency is validated if the primary peak of the spectrum exceeds the secondary peak by a factor of 4 or higher. After validation the Doppler frequency together with the arrival time (optional) and the transit time (optional) are transferred to a computer.

Unlike, for example, TSI counter processors, the BSA processors cannot carry out a time-coincidence test to ensure that the measured Doppler frequencies originate from the same particle in case of a multi-component measurement. However, the time-coincidence test can be performed in the software that is used to reduce the raw data, provided that for each processor the arrival times of the particles are stored on disk. Alternatively, the different BSA processors can be run in the so called "hardware-coincident mode." This mode of operation and its consequences are discussed later in this chapter.

## 3.3 The Three-Component LDA

### 3.3.1 Introduction

The interest of fluid-dynamics researchers for the three-component LDA (3-D LDA) is clear, because turbulence is a three-dimensional phenomenon and in many industrial flows even the mean flow is three-dimensional. In its early stages of development the 3-D LDA was notorious as far as the measurement accuracy of turbulence statistics was concerned. An increasing number of researchers came to the conclusion that the simultaneous measurement of three velocity components involved much more than bearing the financial burden for adding one LDA channel to an existing two-component system. The 3-D LDA poses a set of problems that are unique to this instrument. Meyers, a recognized expert in the field, sketched the development of the 3-D LDA in a paper entitled "The Elusive Third Component" [Meyers 1985]. Perhaps the title reflects the many problems encountered during the search for the right optical arrangement for the instrument. This section intends to discuss these problems and their remedies, thereby resulting in the following optical arrangement for the 3-D LDA:

- the transmitting optics are arranged such that three (nearly) orthogonal velocity components are measured by the individual LDA channels;
- the receiving optics are configured such that only light from the overlap region of the three measuring volumes is collected;
- the three signal processors are operated in a "hardware-coincident mode," i.e. the Doppler signals are processed only when these signals show (partial) overlap in time on all three channels, otherwise the processor is inhibited.

The discussion of the 3-D LDA will be limited to the dual-beam configuration, because of its superior signal-to-noise ratio.

### 3.3.2 Orthogonality requirement

Each channel of the 3-D LDA measures the velocity component in a direction that is determined by the orientation of the corresponding beam pair in space. In general, these primary or colour components are non-orthogonal and they do not coincide with one of the cartesian velocity components  $u$ ,  $v$  or  $w$ . Therefore, the primary velocity components that are measured by the 3-D LDA must be transformed into the cartesian coordinate

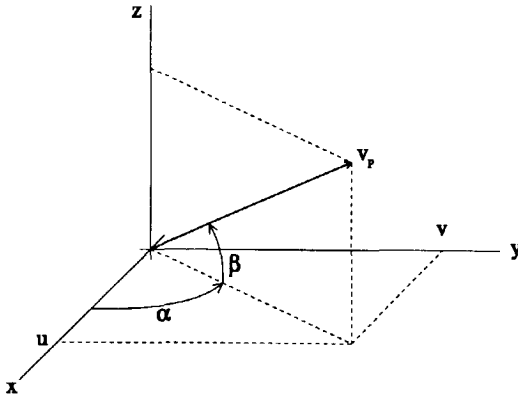


Figure 3.7: The orientation of a primary velocity component.

system. In this section the propagation of uncertainties in the primary velocities into the cartesian velocity components is investigated. The analysis of the transformation matrix will show that the orientation of the three beam pairs should be such that the primary velocity components are as close to orthogonal as possible.

Figure 3.7 portrays a primary velocity component  $v_p$  that is measured by one of the LDA channels. The orientation of this velocity component in the  $x, y, z$ -coordinate system is given by the angles  $\alpha$  and  $\beta$ . A 3-D LDA gives rise to the following set of equations:

$$\begin{aligned} v_g &= u \cos \beta_g \cos \alpha_g + v \cos \beta_g \sin \alpha_g + w \sin \beta_g \\ v_b &= u \cos \beta_b \cos \alpha_b + v \cos \beta_b \sin \alpha_b + w \sin \beta_b \\ v_v &= u \cos \beta_v \cos \alpha_v + v \cos \beta_v \sin \alpha_v + w \sin \beta_v, \end{aligned} \quad (3.23)$$

where  $u, v$  and  $w$  are the components of the velocity in the orthogonal coordinate system and  $v_g, v_b$  and  $v_v$  are the primary velocity components measured by the green, blue and violet LDA channels, respectively. If, for reasons of simplicity, it is assumed that the blue and green channels form an orthogonal two-component LDA ( $\alpha_b = \alpha_g - \pi/2$ ) that senses velocity components in the  $xy$ -plane ( $\beta_g = \beta_b = 0$ ) then Eq (3.23) reduces to

$$\begin{aligned} v_g &= u \cos \alpha_g + v \sin \alpha_g \\ v_b &= u \sin \alpha_g - v \cos \alpha_g \\ v_v &= u \cos \beta_v \cos \alpha_v + v \cos \beta_v \sin \alpha_v + w \sin \beta_v. \end{aligned} \quad (3.24)$$

Without loss of generality it may also be assumed that  $\alpha_v = \pi/2$ , so that the third component,  $w$ , can be expressed in terms of the primary velocities as

$$w = \frac{\cos \alpha_g}{\tan \beta_v} v_b - \frac{\sin \alpha_g}{\tan \beta_v} v_g + \frac{v_v}{\sin \beta_v}. \quad (3.25)$$

This equation shows that the coefficients of the primary velocities become large for small values of  $\beta_v$ . This causes the third component  $w$  to be very sensitive to uncertainties in

the measured primary velocities caused by, for example, calibration errors or processor inaccuracies. In case the third component is measured directly, i.e.  $\beta_v = \pi/2$ , this extreme sensitivity is absent. So, ideally the transmitting optics of the 3-D LDA should be configured such that the device senses nearly-orthogonal velocity components.

In a more detailed analysis of the coordinate transform, Morrison et al. [1990] showed that the uncertainty propagation into the third component is even more severe for higher-order statistics, such as the Reynolds stress  $\overline{w'^2}$ , than it is for the mean velocity  $\bar{w}$ . They conclude that the tilt angle  $\beta_v$  should be at least  $30^\circ$  to keep the error propagation within reasonable limits. This requirement on the tilt angle poses a number of practical problems. Because many researchers do not know how to solve these problems (or are simply unaware of the orthogonality requirement), most operational 3-D LDAs are of the non-orthogonal type with small  $\beta_v$ . The practical problems are as follows. First, a large tilt angle requires optical access to the experimental facility from two adjacent sides which is difficult to realize in many existing wind tunnels. The second problem has to do with the alignment of the three beam pairs. The conventional procedure to align the beam pairs involves either a small pinhole or a microscope objective [Absil 1995]. Both methods can still be applied to the 3-D LDA as long as the tilt angle  $\beta_v$  remains small, say  $\beta_v < 15^\circ$ , but they cannot be used for larger tilt angles. Consequently, the orthogonal 3-D LDA requires a new alignment procedure. Appendix A gives full details on an alignment method for the orthogonal 3-D LDA. The method centres around an extremely thin pinhole with a  $50 \mu\text{m}$  diameter that allows simultaneous passage of three beam pairs for tilt angles up to  $\beta_v = 90^\circ$ . The procedure is quick, reliable and can be used in both gases and liquids.

### 3.3.3 Virtual particles

In a study of the accuracy of a 3-D LDA, Boutier et al. [1985] found that some of the measured Reynolds stresses were systematically high, due to a phenomenon that they called "virtual particles." The phenomenon is a consequence of the fact that any 3-D LDA has at least one measuring volume that does not fully overlap the other two. Only partial overlap of the measuring volumes can be achieved because the different optical axes cannot all coincide in 3-D LDA. This is in contrast to the two-component LDA where both measuring volumes usually share a single optical axis. The typical situation for a 3-D LDA is sketched in Fig. 3.8 where the optical axes of measuring volumes *A* and *B* include an angle  $\beta$ . One of these measuring volumes actually consists of two fully overlapping volumes that is formed by two beam pairs (but that is not essential here.) Assume that each measuring volume senses a velocity component that lies in the plane spanned by the optical axes of measuring volumes *A* and *B*.

Now consider the following "multiple-particle" event. Volume *A* measures a particle with velocity component  $v_a$  at time  $t_a$  whereas a particle with velocity component  $v_b$  is measured by volume *B* at time  $t_b$ . To verify whether the measurements on the two LDA channels stem from a single particle, it is common to apply a simultaneity criterion. In other words: if the arrival times  $t_a$  and  $t_b$  satisfy the criterion  $|t_a - t_b| < \tau_w$ , where  $\tau_w$  is a user-selected time-coincidence window, then it is assumed that both measurements stem from a single particle. The LDA subsequently produces the velocity pair  $(v_a, v_b)$  as



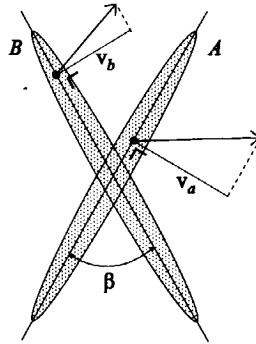


Figure 3.8: The virtual-particle phenomenon in 3-D LDA.

if it represents the velocity components of a single particle. However, in the case of the multiple-particle event sketched in Fig. 3.8, the arrival times  $t_a$  and  $t_b$  may satisfy the simultaneity criterion, but they do not originate from the same particle. As a result, a “virtual particle” with velocity components  $(v_a, v_b)$  is created, which will cause erroneous velocity statistics.

Boutier reasoned that the virtual-particle phenomenon was a complicated function of the tilt angle  $\beta$ , the time-coincidence window  $\tau_w$ , the local flow conditions and the seed density. However, a solution to the problem was not given. Intuitively, it is clear that lowering the seed density will decrease the probability that virtual particles will occur, but it will not eliminate the problem. The only sensible way to circumvent the virtual-particle phenomenon is to collect data only from the region in space that is common to all (three) measuring volumes, which can be achieved by the positioning of small pinholes in front of the photomultipliers in conjunction with a large (near  $90^\circ$ ) off-axis light-collection angle. This “spatial filtering” also happens to be the remedy for the geometry-bias problem that will be discussed below.

### 3.3.4 Geometry bias

In an attempt to quantify the findings of Boutier’s investigation, Brown [1989] simulated the operation of a typical 3-D LDA using a Monte-Carlo approach. The results of this study confirmed the existence of the virtual-particle phenomenon, and showed that, as expected, the probability of a virtual-particle occurrence increases with increasing seed density. Recall from the previous section that the virtual particles were able to pass the simultaneity criterion, thereby causing erroneous velocity statistics. Brown’s study showed that even without virtual particles, which was easy to realize in the simulation, the velocity statistics as measured by the 3-D LDA were in error. As a result, the study revealed a previously unidentified error source. This error was termed the “geometry bias,” and it is a direct result of the 3-D LDA measuring-volume geometry in conjunction with the concept of a time-coincidence window.

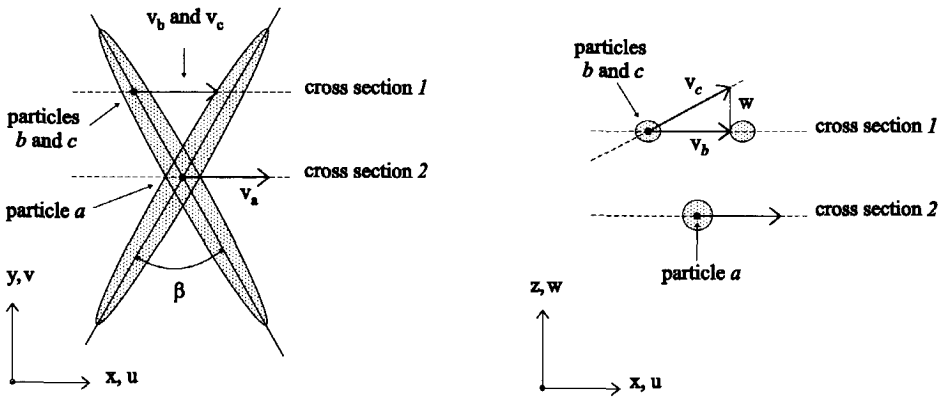


Figure 3.9: The geometry bias in 3-D LDA.

Figure 3.9 depicts the measuring-volume geometry that was used in Brown's study. The geometry is identical to that shown in Fig. 3.8 for a tilt angle  $\beta = 60^\circ$ . Consider particle *a* that passes through the overlap region of the measuring volumes. For simplicity it is assumed that its velocity component in the *y*-direction is zero. Clearly, this particle will satisfy the time-coincidence criterion regardless of the magnitude of the velocity components *u* and *w*. This is not the case for particles *b* and *c* which do not pass through the overlap region. Particle *b* is assumed to have zero *w*-component and it will satisfy the time-coincidence criterion only if the in-plane velocity component *u* is sufficiently large. Particle *c* is supposed to have a non-zero *w*-component and it cannot pass the time-coincidence test if the *w*-component is large compared to the *u*-component, simply because it will not arrive at the other measuring volume. This illustrates that the 3-D LDA measuring-volume geometry in combination with the time-coincidence window will cause a bias towards high in-plane velocity components and small out-of-plane velocity components.

The time-coincidence concept, which works very satisfactorily for a conventional two-component LDA, is inadequate for the 3-D LDA. To circumvent the geometry bias, Brown [1989] suggested a new mode of operation for the LDA signal processors known as the "channel-blanking mode" or the "hardware-coincident mode." In this mode of operation each signal processor will process a Doppler burst only when Doppler bursts are also present on the other two channels, in the sense that the three Doppler bursts (partially) overlap in time. If this is not the case, the signal processors are inhibited. Due to the hardware-coincident mode, data will be acquired only from the overlap region of the three measuring volumes, so that particle *a* will be measured by the 3-D LDA while particles *b* and *c* are ignored<sup>1</sup>.

The hardware-coincident mode removes the geometry bias, which is a single-particle event. But it does not eliminate the virtual-particle phenomenon, because this is a

<sup>1</sup>In practice the same result can be obtained using the conventional simultaneity criterion, if the time coincidence window is (much) smaller than the transit time of the particles as suggested by Benedict [1995].

multiple-particle event. To eliminate both error sources, the 3-D LDA requires both the channel-blanking mode and the collection of scattered light from the overlap region only, as mentioned in the previous section. The beneficial effect of these measures is that the spatial resolution of the 3-D LDA is high compared to that of a conventional two-component LDA. The latter is usually operated in the (off-axis) forward-scatter or backward-scatter mode, resulting in a sensitive region with relatively large dimensions. The sensitive region for the 3-D LDA is reduced to the overlap region of the three measuring volumes. This more-or-less spherical region has a characteristic length equal to the diameter of the individual measuring volumes which is typically 10 times smaller than the length of the measuring volumes. On the other hand, the smaller measuring volume of the 3-D LDA will result in a much lower mean data rate as compared to the two-component LDA for the same seed density.



## Chapter 4

# Research on the LDA Sampling Process

### 4.1 Introduction

Most measurement techniques acquire samples at equidistant time intervals. For example, the hot-wire anemometer takes velocity samples at a constant rate which is set by the operator. The mean velocity and the variance of the velocity fluctuations can be computed from the equidistant samples through simple arithmetic averages. Also, the spectral density function can be computed from the equidistant samples by using the fast Fourier transform (FFT). However, LDA is a measurements technique that naturally operates with *random* sampling times. The objective of this chapter is to discuss two important consequences of the random sampling in LDA.

Section 4.2 considers the case where the instantaneous data rate is assumed to be correlated with the instantaneous velocity, giving rise to a much debated and controversial phenomenon known as the “velocity bias.” Attention will be given to the possible dependence of the velocity bias on the mean data rate, and the ability of existing detection methods to verify the presence of the velocity bias for LDA measurements at low mean data rate. In addition, the different correction methods for the computation of relatively simple statistics, such as the mean velocity and the variance of velocity fluctuations, are evaluated.

Section 4.3 discusses the calculation of the autocorrelation function and the spectral density function from the randomly sampled LDA data, initially only for the relatively simple case in which the instantaneous data rate is not correlated with the instantaneous fluid velocity. Even in the absence of the velocity bias, special data-processing methods are required because of the randomness of the sampling times. It will be shown that existing methods for the estimation of spectral density functions from randomly sampled LDA data exhibit a large statistical scatter at high frequencies. The statistical variability is so large that it obscures the behaviour of the spectral density function in the high-frequency range, thereby making it practically impossible to study the small time scales of

the turbulent velocity fluctuations. A new data-processing method for the estimation of the spectral density function is proposed that overcomes some of the variability problems.

## 4.2 Velocity Bias

LDA measures the velocity of small particles when they move through the measuring volume. Because the particles are randomly distributed in space, the sampling times are random as well. A frequently used model for the interarrival times, i.e. the times between consecutive samples, assumes that these times obey Poisson statistics. The probability density function of the interarrival times,  $\Delta t$ , is then given by

$$p(\Delta t) = \nu e^{-\nu \Delta t}, \quad (4.1)$$

where  $\nu$  is the “rate parameter” of the Poisson process. The rate parameter can be interpreted as the mean number of samples per unit time, or, in other words,  $\nu$  is the mean data rate.

In the early days of LDA it was assumed that velocity statistics, like the mean velocity and the variance of the velocity fluctuations, could be computed from the LDA velocity samples through simple arithmetic averages as in hot-wire anemometry. Several researchers, see e.g. George [1978], have shown theoretically that this is indeed correct if the interarrival times obey Poisson statistics without any correlation between the instantaneous data rate and the instantaneous velocity of the fluid. However, McLaughlin and Tiederman [1973] recognized that there is a correlation between the instantaneous data rate and the instantaneous fluid velocity when LDA measurements are made in time-varying flows. This correlation is commonly referred to as “velocity bias”, and it leads to erroneous velocity statistics if the LDA velocity samples are processed as arithmetic averages. It is important to realize that the velocity bias itself does not cause the errors in the velocity statistics. The errors occur only when the statistical quantities are computed as arithmetic averages. Furthermore, the velocity bias is absent in equidistant sampling because in that case there is no correlation between the instantaneous velocity and the instantaneous data rate. Arithmetic averages can then be used to compute the velocity statistics.

To explain the velocity bias consider a measuring volume that is placed in a time varying flow as depicted in Fig. 4.1. The projection of the measuring volume on the plane normal to the instantaneous velocity vector,  $\vec{v}$ , is denoted by  $A_p$ . The expected number of particles that pass through the measuring volume per unit time is then given by

$$\lambda = |\vec{v}| A_p M. \quad (4.2)$$

Here,  $M$  is the particle concentration (the number of particles per unit volume), which is supposed to be constant in flows with constant density. Note that  $\lambda = |\vec{v}| A_p M$  is a time varying quantity. It is seen from Eq (4.2) that  $\lambda$  is proportional to the volume flux through the measuring volume. Hence, the probability of measuring a particle with a high velocity is higher than the probability of measuring a low-velocity particle. As a result, the histogram of measured velocity samples will be biased towards high velocities

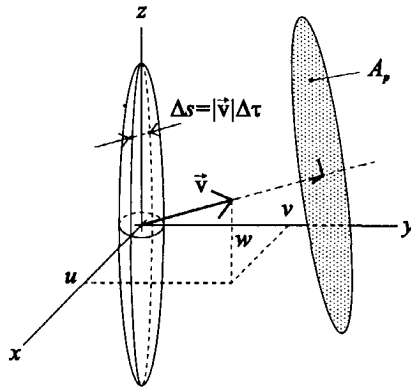


Figure 4.1: The measuring volume in a time-varying flow.

and statistical quantities that are computed as arithmetic averages will be erroneous. For the mean velocity this can be illustrated as follows. Consider a one-dimensional flow with mean velocity  $\bar{u}$  and variance  $\overline{u'^2}$ . If it is assumed that the instantaneous data rate is proportional to the instantaneous volume flux, as in Eq (4.2), then the arithmetic average  $u_r$  of the velocity samples is a measure for

$$u_r = \frac{\overline{u(t)\lambda}}{\bar{\lambda}} = \frac{\overline{u(t)|u(t)|A_p M}}{\overline{|u(t)|A_p M}} = \frac{\overline{u(t)|u(t)|}}{\overline{|u(t)|}}, \quad (4.3)$$

because  $A_p$  does not vary with time in a one-dimensional flow and  $M$  is constant. For low turbulence intensity, i.e.,  $\overline{u'^2} \ll \bar{u}^2$ , this reduces to

$$u_r = \frac{\overline{u(t)^2}}{\overline{|u(t)|}} = \bar{u} + \frac{\overline{u'^2}}{\bar{u}}, \quad (4.4)$$

which shows that the arithmetic average  $u_r$  is higher than the true mean velocity  $\bar{u}$ . Furthermore, Eq (4.4) illustrates that the effects of the velocity bias increase with increasing turbulence intensity.

### 4.2.1 Correction methods

It was stated in Section 4.2 that the calculation of the velocity statistics by means of arithmetic averages is incorrect in the presence of velocity bias. Instead, data-processing methods should be used that take the effects of the velocity bias into account. Such data-processing methods are called "correction methods" in the literature. Even though the terminology "correction method" is somewhat inconsistent (perhaps "correct method" is more appropriate), it will be maintained here for compatibility with the existing literature on this subject. The correction methods can be divided into two categories, namely sampling techniques and weighting factors.

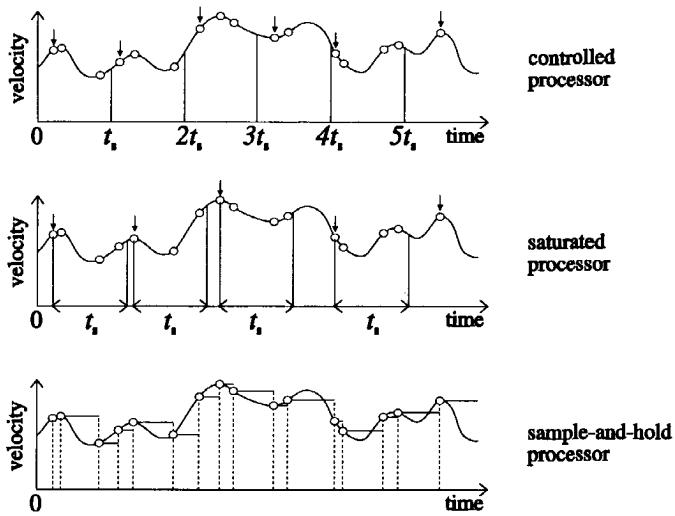


Figure 4.2: Three frequently used sampling techniques. The arrows mark the samples used by the controlled processor and the saturated processor.

### Sampling techniques

Sampling techniques attempt either to reconstruct the original velocity signal or to sample the velocity at approximately equidistant times, thereby eliminating the correlation between the sampling process and the instantaneous velocity. There are three sampling techniques, which are usually referred to as “processors,” because they can be implemented in both software and hardware. For all sampling techniques (and some of the weighting factors) the “data density” plays a crucial role. The data density is defined as the product of the mean data rate  $\nu$  and a characteristic time scale of the velocity, such as the Taylor time scale  $\lambda_t$ . Sometimes, the integral time scale  $T_u$  is used as a characteristic time scale.

#### 1. controlled processor:

The time axis is divided into equal intervals of length  $t_s$ , see Fig. 4.2 (top). Only the first sample on each interval is used to compute the velocity statistics. For high data density,  $\nu\lambda_t > 5$ , and small time intervals,  $t_s < \lambda_t$ , an equidistant sampling scheme is approximated [Edwards 1987]. Unbiased velocity statistics can then be computed using the arithmetic average of the (nearly) equidistant velocity samples.

#### 2. saturated processor:

The processor is inhibited during a time span  $t_s$  after a velocity sample is taken, as shown in Fig. 4.2 (middle). Under the same conditions as for the controlled processor ( $\nu\lambda_t > 5$  and  $t_s < \lambda_t$ ) a nearly equidistant time series is generated from which unbiased statistics can be computed as indicated by Edwards et al. [1987].

#### 3. sample-and-hold processor:

A continuous signal is constructed by holding the last velocity value until the next



sample is taken. In variations on this method linear and higher-order polynomials are fitted to the measured velocity values. The continuous signal is resampled at regular time intervals. The set of equidistant velocity samples is subsequently used to compute the velocity statistics. The sample-and-hold processor will work properly for high data densities only:  $\nu\lambda_t > 10$  as indicated by Edwards et al. [1987].

The sample-and-hold processor can be seen as a representative of the much wider class of "reconstruction techniques." The essence of all reconstruction methods is to replace the discrete, randomly-sampled time series by a continuous signal that is subsequently resampled at regular time intervals. The use of reconstruction techniques has become widespread nowadays because, if successful, the reconstruction not only eliminates the velocity bias, but it also enables the spectral analysis of the equidistant data to be carried out efficiently with the FFT algorithm. On the other hand, it is widely known [Adrian and Yao 1987] that reconstruction methods require very high sampling rates. For LDA measurements in gas flows it is seldom possible to achieve sufficiently high sampling rates, so that reconstruction techniques are of limited importance there.

### Weighting factors

The weighting factors form the second category of correction methods. Weighting factors are used to compensate for the effect of the velocity bias during the processing of the velocity samples. For simple statistical quantities, such as the mean velocity and the variance of the velocity fluctuations, the processing methods take the following form

$$\bar{u} = \frac{\sum_{i=1}^N u_i \omega_i}{\sum_{i=1}^N \omega_i} \quad (\text{mean velocity}) \quad \overline{u'^2} = \frac{\sum_{i=1}^N u_i'^2 \omega_i}{\sum_{i=1}^N \omega_i} \quad (\text{variance}) \quad (4.5)$$

Here, the subscript  $i$  denotes the  $i$ -th velocity sample,  $N$  is the total number of velocity samples and  $\omega$  is the weighting factor. Note that  $\omega = 1$  corresponds to the unweighted, arithmetic average. Weighting methods in use are:

#### 1. inverse-velocity:

Inspection of Eq (4.2) shows that the inverse of the volume flux can be used as a weighting factor in flows with constant density. (The limitation to constant-density flows is due to the assumption  $M = \text{constant}$ .) This is better known as the inverse-velocity weighting [McLaughlin and Tiederman 1973]

$$\omega = \frac{1}{A_p |\vec{v}|} = \frac{1}{A_p \sqrt{u^2 + v^2 + w^2}}. \quad (4.6)$$

The above weighting factor requires some knowledge of the shape of the measuring volume to evaluate the projected area  $A_p$ . For an ellipsoidal measuring volume with its long axis parallel to the  $z$ -direction, Eq (4.6) reduces to [McDougall 1980]

$$\omega = \frac{1}{\sqrt{u^2 + v^2 + (d/l)^2 w^2}}, \quad (4.7)$$

where  $d/l$  is the diameter-to-length ratio of the ellipsoid. For a cylindrical measuring volume with its axis along the  $z$ -axis, the weighting factor becomes [Johnson et al. 1984]

$$\omega = \frac{1}{\sqrt{u^2 + v^2 + \frac{\pi}{4}(d/l)|w|}} \quad (4.8)$$

The weighting factors given by Eqs (4.7) and (4.8) are known as 3D inverse-velocity weighting, because all three components of the velocity vector have to be measured simultaneously in order to compute the value of the weighting factor for each velocity sample. The latter requirement is often not met and it is common practice to approximate Eqs (4.7) and (4.8) by the 2D inverse-velocity weighting, given by

$$\omega = \frac{1}{\sqrt{u^2 + v^2}} \quad (4.9)$$

Due to the omission of one of the instantaneous velocity components, this weighting factor will be systematically high, resulting in a tendency to over-correct the velocity bias. On the other hand, in many practical cases  $d/l \approx 0.1$  so that ignoring the contribution of the third velocity component is not unreasonable. However, the over-correction will be much more severe when two of the three velocity components are omitted as in the 1D inverse-velocity weighting, i.e.  $\omega = 1/|u|$ . Therefore, it is generally accepted that the 1D inverse-velocity weighting should not be used.

Nakayama [1985] incorporated the effect of the unmeasured third component in Eqs (4.7) and (4.8) through an estimate of its mean value. For example, the weighting factor for the ellipsoidal measuring volume, Eq (4.7), is approximated by Nakayama as

$$\omega = \frac{1}{\sqrt{u^2 + v^2 + (d/l)^2(\bar{w}^2 + \overline{w'^2})}} \quad (4.10)$$

which, for a two-dimensional flow with  $\bar{w} = 0$ , reduces to

$$\omega = \frac{1}{\sqrt{u^2 + v^2 + (d/l)^2 \overline{w'^2}}} \quad (4.11)$$

Furthermore, Nakayama approximated the value of  $\overline{w'^2}$  as  $(\overline{u'^2} + \overline{v'^2})/2$  in the boundary layer and the wake of an airfoil. The weighting factor given by Eq (4.11) is referred to as 2D<sup>+</sup> weighting. A beneficial consequence of the inclusion of the additional term is that the weighting factor can no longer produce infinite weights when both the  $u$  and  $v$  velocity components are zero simultaneously, whereas the additional term has negligible influence for higher velocities as was shown by Petrie et al. [1988].

## 2. transit-time weighting:

Hoesel and Rodi [1977] proved mathematically that weighting with the inverse volume flux according to Eq (4.6) is equivalent to weighting with the mean time for particles to pass through the measuring volume for a given velocity vector, defined as

$$tr_e = \frac{1}{A_p} \int_{A_p} tr \, dA_p, \quad (4.12)$$

where  $tr$  is the time that an individual particle spends in the measuring volume, see Fig. 4.1. However, the mean transit time  $tr_e$  is an unmeasurable quantity. Therefore, Hoesel and Rodi [1977] and Buchhave et al. [1979] suggested to use the transit time of each individual particle,  $tr$ , instead of  $tr_e$ . In other words, they suggested the following weighting factor:

$$\omega = tr. \quad (4.13)$$

Petrie et al. [1988] argued that the transit times of the particles are dependent on the trajectory of the particle through the measuring volume. As a result, the individual transit times exhibit a large scatter around their mean value,  $tr_e$ . However, for large numbers of particles the scatter is expected to average out, because the particle trajectory is not correlated to the magnitude of the velocity vector. Still, the weighting with the transit times of the particles according to Eq (4.13) will cause an increased statistical variability as compared to weighting with the inverse velocity, Eq (4.6).

## 3. interarrival-time weighting:

Another frequently used weighting factor is the time between successive samples or the interarrival time [Barnett and Bentley 1974], [Dimotakis 1976]

$$\omega = \Delta t_i \equiv t_{i+1} - t_i. \quad (4.14)$$

This will be referred to as IT weighting. Some researchers do not interpret the IT weighting as a correction method. For example, Barnett and Bentley [1974] consider the definition of the time-averaged velocity  $u_T$ :

$$u_T = \frac{1}{T} \int_0^T u(t) dt, \quad (4.15)$$

and approximate this expression for  $u_T$  as

$$u_T \approx \frac{\sum_{i=1}^{N-1} u_i(t_{i+1} - t_i)}{\sum_{i=1}^{N-1} (t_{i+1} - t_i)}. \quad (4.16)$$

Clearly, this is identical to the IT weighting. Note that Eq (4.16) reduces to the arithmetic mean  $u_r$  for equidistant samples. An important advantage of the interarrival time weighting over the inverse-velocity weighting is that it can be used

when the particle concentration is correlated with the instantaneous velocity. In that case the inverse-velocity weighting will fail, because it is based on the assumption that the particle concentration  $M$  is constant. The results of the IT weighting are closely related to those of the sample-and-hold processor. The IT weighting yields unbiased results for high data densities only. Edwards et al. [1987] give the following criterion for the data density

$$\nu\lambda_t > 10, \quad (4.17)$$

where  $\nu$  is the mean data rate and  $\lambda_t$  is the Taylor time scale. Application of the interarrival time weighting for lower data densities results in a reduction of the effects of the velocity bias, but it does not eliminate the bias. Often the Taylor time scale  $\lambda_t$  in Eq (4.17) is replaced by the integral time scale,  $T_u$ , resulting in a less strict criterion for the mean data rate, because  $\lambda_t \ll T_u$ . As shown by Winter et al. [1991] this new criterion is sufficient to guarantee bias free results for statistics such as the mean velocity. However, it is often not realized that the relaxed condition  $\nu T_u > 10$  does not yield unbiased results for other statistical quantities, such as the autocorrelation function, as was shown by Tummers et al. [1992].

#### 4.2.2 Relationship between velocity bias and mean data rate

More than 20 years after McLaughlin and Tiederman [1973] published their findings there is still controversy on the velocity bias. The controversy is not just on the type of correction procedure that should be applied, but even on the fundamental issue whether velocity bias correction schemes should be applied at all. The controversy exists because a number of investigators claim that the velocity bias vanishes at low data rates, see e.g. Barnett and Bentley [1974]. They argue that long time delays between samples destroy any correlation between the instantaneous velocity and the instantaneous data rate, thereby eliminating the velocity bias. If this is true, then the application of velocity bias correction schemes to low data rate LDA measurements could actually introduce a bias error in an otherwise unbiased result.

The claim that the velocity bias depends on the mean data rate seems to be supported by an experiment performed by Adams [1984]. Adams investigated the dependence of the arithmetic average of the velocity samples,  $u_r$ , on the mean data rate,  $\nu$ . The results given in Fig. 4.3 show a decrease of  $u_r$  with decreasing mean data rate, indicating a decrease of the effects of the velocity bias with decreasing mean data rate. However, Adams himself indicated that the results shown in Fig. 4.3 should be interpreted with some reserve, because during the experiment the mean data rate was varied by varying the laser power instead of varying the particle seeding rate. This may have affected the measuring system causing the observed trend in the measured data shown in Fig. 4.3.

Johnson et al. [1984] also investigated the dependence of the velocity bias on the mean data rate. An important result of their investigation is given in Fig. 4.4. From this graph Johnson et al. [1984] concluded that the arithmetic mean,  $u_r$ , was independent of the mean data rate over a wide range of  $\nu$ . This means that the velocity bias is independent of the mean data rate as well. The decrease of  $u_r$  for data rates higher than 3000 Hz

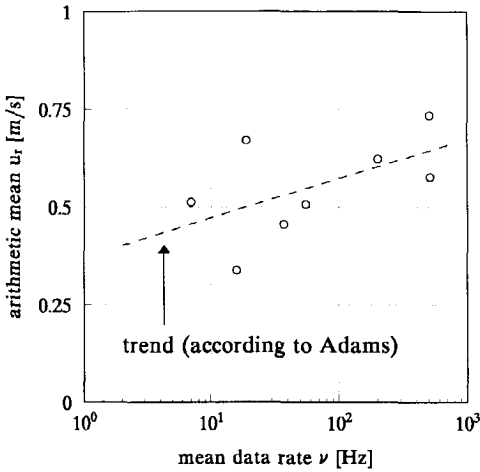


Figure 4.3: Arithmetic average as a function of the mean data rate. (Taken from Adams [1984].)

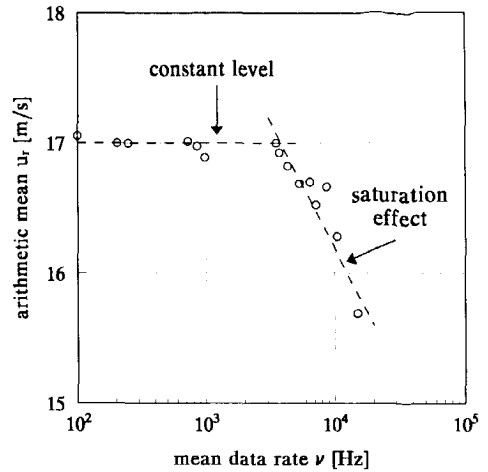


Figure 4.4: Arithmetic average as a function of the mean data rate. (Taken from Johnson et al. [1984].)

is likely to be caused by the relatively large ( $60 \mu\text{s}$ ) cycle time of the data-acquisition system, in the sense that for higher mean data rates the system increasingly acts like a saturated processor. Clearly, the findings of Johnson et al. [1984] contradict those of Adams [1984]. Still, the view that the velocity bias is absent, or at least strongly reduced, at low data rates is held by many. It is one of the reasons why a great deal of published LDA data are uncorrected for the velocity bias. The other reason is the possible coexistence of other bias sources that may (partially) compensate for the effects of the velocity bias. As discussed in Section 3.2.5, the amplitude bias may cause a reduced visibility of the Doppler bursts of fast moving particles. In that case, the probability of measuring a high-velocity particle is smaller than that of a low-velocity particle, thereby causing some degree of compensation for the effects of velocity bias (in case there is no frequency shift). Because of the compensating effects of the amplitude bias, or other bias sources, it has been suggested in the literature that the degree of velocity bias should first be determined from a velocity bias detection method before any correction method is applied. Of course, this suggestion implies that the velocity bias correction methods should not be used if the detection methods indicate that the velocity bias is absent. In the following section it will be shown that this may have adverse consequences for the computed velocity statistics.

### 4.2.3 Detection methods

Adams [1984] introduced a simple detection method that uses the inverse of the interarrival times as a measure for the instantaneous data rate. In Adams' method the velocity range is divided into a number of intervals, and for each interval the mean interarrival time is computed from the samples. A graph of the mean interarrival time as a func-

tion of the velocity displays the correlation between the instantaneous data rate and the instantaneous velocity. A decreasing trend would indicate the presence of velocity bias, while the histogram is flat in case the velocity bias is absent. Note that there is a clear link between this detection method and the interarrival time weighting, because both use the interarrival times to model the instantaneous data rate. As a consequence, it can be expected that Adams' detection method requires a high data density.

Instead of detecting the velocity bias from the inspection of a graph, one may also compute a correlation between the instantaneous data rate and the instantaneous velocity. For Adams' method the correlation coefficient  $\rho_A$  is computed as

$$\rho_A = \frac{1}{N\sigma_{s,A}\sigma_{t,A}} \sum_{i=1}^N \left( \sqrt{u_i^2 + v_i^2 + w_i^2} - s_r \right) \left( \nu - \frac{1}{\Delta t_i} \right), \quad (4.18)$$

where  $N$  is the number of samples,  $\nu$  is the mean data rate,  $\Delta t_i$  is the interarrival time of the  $i$ -th velocity sample and  $s_r$  is the arithmetic average of all values of  $\sqrt{u_i^2 + v_i^2 + w_i^2}$ . Of course, the instantaneous particle speed  $\sqrt{u_i^2 + v_i^2 + w_i^2}$  must be approximated when a two-component LDA is used. The quantities  $\sigma_{s,A}$  and  $\sigma_{t,A}$  are defined as

$$\sigma_{s,A}^2 = \frac{1}{N} \sum_{i=1}^N \left( \sqrt{u_i^2 + v_i^2 + w_i^2} - s_r \right)^2 \quad \text{and} \quad \sigma_{t,A}^2 = \frac{1}{N} \sum_{i=1}^N \left( \nu - \frac{1}{\Delta t_i} \right)^2 \quad (4.19)$$

A slightly more complicated detection method was introduced by Meyers [1988]. As in Adams' method, the velocity range is divided in a number, say 10, intervals. Then a time scale,  $\lambda_m$ , defined as the average time that consecutive samples remain in one velocity interval, is computed. This time scale represents a coherence time of the velocity signal and it is closely related to the Taylor time scale,  $\lambda_t$ . Next, the time axis is divided into intervals of length  $\lambda_m$ , and two velocity histograms are formed. The first histogram contains only the first measured velocity samples on each time interval, similar to the procedure followed in the controlled processor. The remaining or additional velocity samples on each time interval are used to construct the second histogram. In a final step, the height of each column of the second histogram is divided by the height of the corresponding column of the first histogram. This yields a third histogram which indicates the "average number of additional velocity samples per time interval  $\lambda_m$ " as a function of velocity. According to Meyers [1988] the third histogram displays the instantaneous data rate as a function of the instantaneous velocity, thereby indicating the degree of velocity bias. As in Adams' method, it is possible to quantify the degree of correlation between the instantaneous data rate and the instantaneous velocity through a correlation coefficient  $\rho_M$  defined by Meyers as

$$\rho_M = \frac{1}{N_{int}\sigma_{u,M}\sigma_{m,M}} \sum_{l=1}^{N_{int}} (u_l - u_r)(m_l - m), \quad (4.20)$$

where  $N_{int}$  is the number of divisions of the time axis ( $N_{int} = T/\lambda_m$ ),  $u_l$  is the arithmetic average of the velocities in the  $l$ -th time interval and  $u_r$  is the conventional arithmetic average of all ( $N$ ) velocity samples. Furthermore,  $m_l$  is the number of samples on the  $l$ -th

time interval and  $m$  is the average number of samples per time interval ( $m = N/N_{int}$ ). The quantities  $\sigma_{u,M}$  and  $\sigma_{m,M}$  are defined by

$$\sigma_{u,M}^2 = \frac{1}{N_{int}} \sum_{l=1}^{N_{int}} (u_l - u_r)^2 \quad \text{and} \quad \sigma_{m,M}^2 = \frac{1}{N_{int}} \sum_{l=1}^{N_{int}} (m_l - m)^2. \quad (4.21)$$

Tummers et al. [1992] clearly show that both detection methods require a high data density. At low data density neither detection method can be used to prove the presence, or absence, of the velocity bias. Ironically, most LDA experiments in air are carried out at low data density. This precludes the application of the above-mentioned detection methods to low data density measurements, because the detection methods may falsely indicate that the velocity bias is absent. As a result, there still is a need for detection methods that are independent of the data density, so that the degree of velocity bias can be established at low data densities as well.

#### 4.2.4 Experimental investigation of the velocity bias

This section summarizes the findings of a detailed experimental investigation of the velocity bias that was performed by the present author in partial fulfillment of the requirements for the M.Sc. degree at the Low-Speed Aerodynamics Laboratory (LSA) of Delft University of Technology in 1992. The experiments were aimed at clearing some of the controversies surrounding the velocity bias. The investigation focused on the possible influence of the mean data rate on the velocity bias and an evaluation of different velocity bias correction and detection techniques. All experiments were performed in the wake of a flat plate in adverse pressure gradient along a lateral traverse located at 360 mm downstream of the trailing edge. This traverse was chosen because of the presence of regions with mean flow reversal and high turbulence intensities so that the effects of the velocity bias are expected to be severe. The experimental set-up used in the velocity-bias investigation was, in principle, identical to that used in the investigation of the wake in an adverse pressure gradient that is described in Section 5.1 of this thesis.

The summary of the findings presented here provides sufficient insight into the velocity bias to decide on a proper method for the processing of LDA data as given in Section 5.1. More details of the velocity bias investigation are reported in Tummers [1992], Tummers et al. [1992] and Absil [1995].

##### Velocity bias and mean data rate

A series of measurements was performed at different mean data rates to examine the dependence of the velocity bias on this quantity. The mean data rate was varied between 20 Hz and 400 Hz by changing the seed density while all other measurement parameters were kept constant. During each run  $10^4$  velocity samples were acquired. For each run the arithmetic mean,  $u_r$ , was computed and the results are shown in Fig. 4.5. It is seen that the statistical scatter of  $u_r$  increases with increasing data rate, which is caused by the shorter measuring times. Figure 4.5 shows a  $4\sigma$ -band centered around the mean of

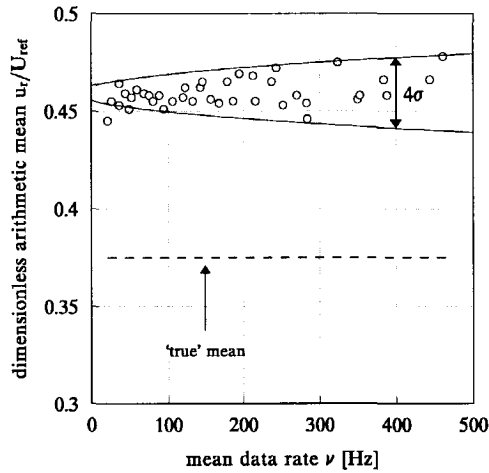


Figure 4.5: Arithmetic average as a function of the mean data rate. The dashed line represents the 'true' mean that is computed from the  $2D^+$  weighting.

all measured  $u_r$  values to indicate the expected statistical scatter. The value of  $\sigma^2$  is computed from [George 1978]

$$\sigma^2 = \frac{2T_u}{T} \overline{u'^2} + \frac{\overline{u'^2}}{\nu T}, \quad (4.22)$$

where  $T$  is the measuring time and  $T_u$  is the integral time scale of  $u(t)$ . For a Gaussian distribution the  $4\sigma$ -band should contain about 97% of the estimates. It can be concluded from the results in Fig. 4.5 that, within the experimental uncertainty, the arithmetic average  $u_r$  is independent of the mean data rate. This is an important conclusion because it implies that the velocity bias is independent of the mean data rate. It should be mentioned that this conclusion is not just based on the results shown in Fig. 4.5. The measurements were repeated at several other locations on the traverse and the same conclusion could be drawn from each of these measurements.

The outcome of the experiment confirms the findings of Johnson et al. [1984], and is, therefore, in clear disagreement with the assertion of Barnett and Bentley [1974] that the velocity bias vanishes at low data rates, see Section 4.2.2. Note that Barnett and Bentley's reasoning contains an erroneous assumption. Of course, long time delays will destroy the correlation between the velocity samples because of the finite time scale of turbulence. However, the velocity bias has to do with the correlation between the instantaneous data rate and the instantaneous velocity, and not with the correlation between the velocity at two different times. Irrespective of the mean data rate, the probability of measuring high-velocity particles is higher than the probability of measuring low-velocity particles, because more fluid is swept through the measuring volume at high velocities than at low velocities. This means that the effects of the velocity bias are independent of the mean data rate, which is confirmed by the present experiment.



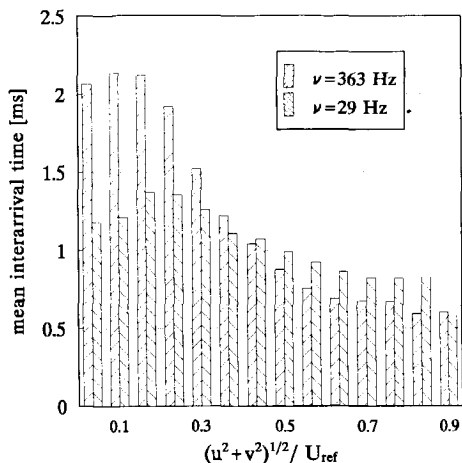


Figure 4.6: Results of Adams' detection method at two different mean data rates.

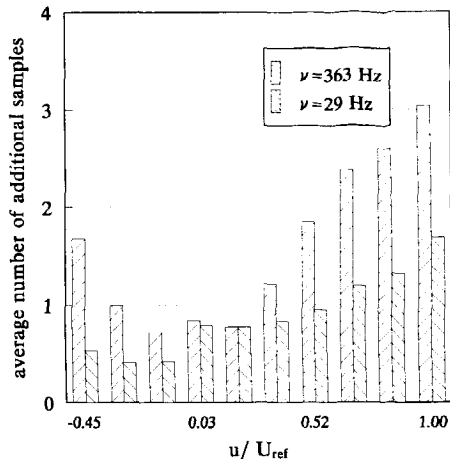


Figure 4.7: Results of Meyers' detection method at two different mean data rates. The "average number of additional samples" is a quantity defined by Meyers [1988].

### Bias detection methods

The bias detection methods proposed by Adams [1984] and Meyers [1988] were evaluated at several locations in the flow. Attention was focused on the ability of the methods to detect the velocity bias at low data densities. Therefore, a number of measurements was performed at different mean data rates. The results of these measurements are presented in Fig. 4.6 for Adams' method and in Fig. 4.7 for Meyers' method. Both methods indicate a strong correlation between the instantaneous velocity and the instantaneous data rate for the measurement with the high mean data rate ( $\nu = 363$  Hz). The correlation is much smaller at low mean data rate ( $\nu = 29$  Hz). To quantify the degree of correlation between the instantaneous data rate and the instantaneous velocity, the correlation coefficients were computed for Adams' method, Eq (4.18), and for Meyers' method, Eq (4.20). The correlation coefficients are given in Fig. 4.8 for a series of measurements at different mean data rates. These results confirm the decrease of the correlation with decreasing mean data rate. It can be observed that the correlation reaches an asymptotic value at  $\nu \approx 300$  Hz, which corresponds to a data density of  $\nu T_u \approx 10$ .

Recall that Fig. 4.5 indicated that the effect of the velocity bias on the arithmetic average,  $u_r$ , is independent of the mean data rate  $\nu$ . Therefore, the findings in Figs. 4.6 and 4.7 demonstrate that neither detection method can be used to prove the presence, or absence, of the velocity bias at low data density, because *the detection methods themselves, and not the velocity bias, are dependent on the mean data rate*. Neither method is able to accurately describe the instantaneous data rate at low data density, and the detection methods only give meaningful results for data densities  $\nu T_u \geq 10$ .

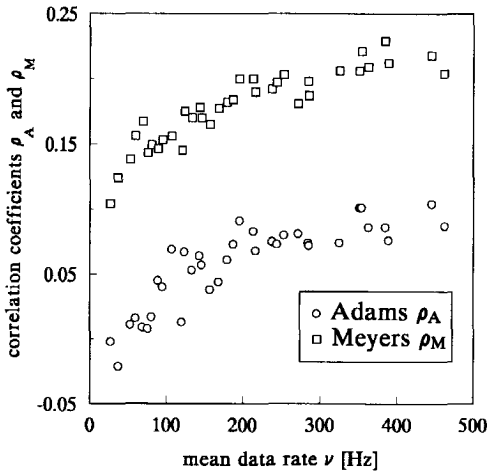


Figure 4.8: The correlation coefficients as determined with the Adams' method and the Meyers' method versus the mean data rate.

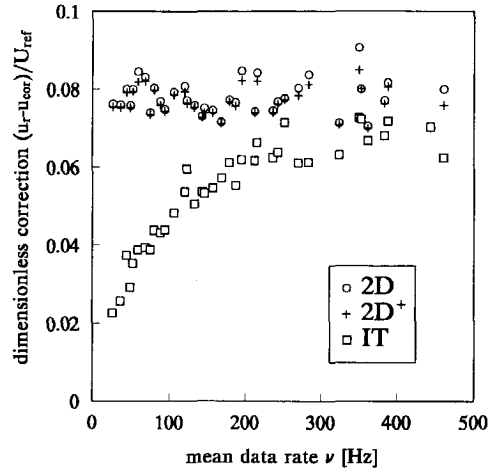


Figure 4.9: The amount of correction for three different correction schemes.

### Correction methods

To evaluate the different correction methods it is convenient to introduce "the amount of correction"  $\Delta u$ :

$$\Delta u = u_r - u_{cor}. \quad (4.23)$$

Here,  $u_{cor}$  represents a corrected mean velocity using, for example,  $2D$ ,  $2D^+$  or  $IT$  weighting. Figure 4.9 presents the amount of correction,  $\Delta u$ , for three different correction schemes. It can be seen that the  $2D$  weighting and the  $2D^+$  weighting give almost identical results. Any significant difference between the results of these methods is caused by the overweighting of the  $2D$  correction method when both the  $u$  and  $v$  velocity components are close to zero simultaneously. Therefore, the  $2D^+$  weighting is preferred over the standard  $2D$  weighting.

Figure 4.9 also shows that, as expected, the interarrival time weighting depends on the mean data rate. The amount of correction increases with increasing data rate, and reaches an asymptotic value at approximately  $\nu = 350$  Hz, which corresponds to a data density of  $\nu T_u \approx 11$ . Under these circumstances the results of the interarrival time weighting are nearly identical to those of the  $2D^+$  weighting. This is further demonstrated in Fig. 4.10, which shows the distribution of the measured velocity samples together with the distributions that result from application of the interarrival time weighting at high mean data rate and the  $2D^+$  weighting. Figure 4.10 also illustrates that a correction method based on the inverse volume flux, such as the  $2D^+$  weighting, does not cause significant over-compensation at high turbulence levels as has been suggested in the literature.

Figure 4.11 shows the results of the controlled processor and the saturated processor for three different data densities  $\nu T_u$ . It can be seen that both sampling techniques

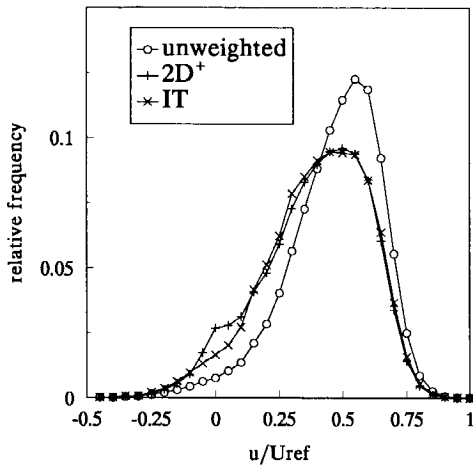


Figure 4.10: The influence of  $2D^+$  weighting and IT weighting on the distribution of the velocity samples.

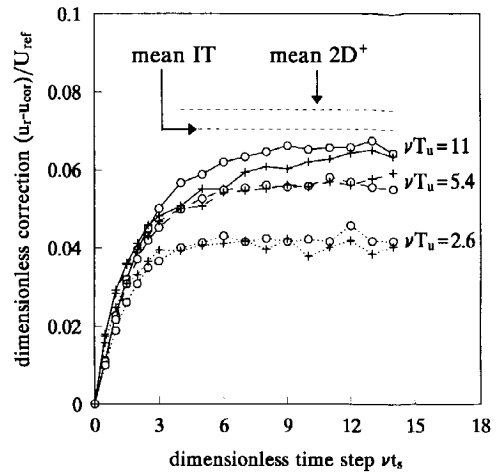


Figure 4.11: Amount of correction for the controlled ( $\circ$ ) and the saturated processor ( $+$ ) versus  $\nu t_s$  for three data densities.

give nearly identical results, and that the amount of correction increases with increasing value of the parameter  $\nu t_s$ , which is the average number of velocity samples per time interval  $t_s$ , see Fig 4.2. For a constant data density, the amount of correction reaches an asymptotic value at  $\nu t_s \geq 10$ . However, the asymptotic value increases with increasing data density, which illustrates that a partial correction for the velocity bias is achieved if the sampling techniques are used at too low data densities. A full correction for the velocity bias is achieved only if both  $\nu t_s \geq 10$  and  $\nu T_u \geq 10$ . In that case the sampling techniques yield results that are equivalent to the IT weighting.

### 4.2.5 Concluding remarks

The main findings of the research on the velocity bias can be summarized as follows:

- Experiments show that the arithmetic mean  $u_r$  is independent of the data density, implying that the velocity bias is independent of the data density;
- The detection methods of Adams and Meyers require a high data density ( $\nu T_u \geq 10$ ). Both methods falsely indicate that the velocity bias is absent at low data density;
- The IT weighting and the sampling techniques (controlled processor and saturated processor) require a high data density ( $\nu T_u \geq 10$ ). In addition, the sampling techniques require a high value of the sampling parameter, i.e.  $\nu t_s \geq 10$ . A partial correction for the velocity bias is obtained at lower data density;
- The 3D weighting is preferred when all three velocity components are measured simultaneously as in 3D LDA. For two-component measurements (2D LDA), the

$2D^+$  weighting is preferred over the  $2D$  weighting in order to prevent the occurrence of "infinite weights" when both measured velocity components are near zero simultaneously.

The velocity-bias investigation was carried out in a low-speed wake with relatively large integral time scales ( $T_u \approx 50$  ms). Therefore, a high data density could be achieved at a relatively low mean data rate. However, in many practical situations it is extremely difficult to achieve the required data density of  $\nu T_u \geq 10$ , because much smaller integral time scales are found in many turbulent flows, and the mean data rate is inherently low in reverse flow regions. As a result, the interarrival time weighting and the sampling techniques often cannot be used. However, weighting methods that are based on the inverse volume flux, such as the  $2D^+$  weighting and the  $3D$  weighting, are excellent alternatives, provided the flow is incompressible and there is no further correlation between velocity and particle concentration. Since the transit-time weighting is equivalent to the inverse-volume flux weighting, see Section 4.2.1, the transit times can also be used to compensate for the velocity bias.

### 4.3 Spectral Analysis of LDA Data

The autocorrelation function (acf) of the velocity fluctuation  $u'(t)$  was introduced in Chapter 2 as

$$\rho(\tau) = \frac{R(\tau)}{R(0)}, \quad (4.24)$$

where  $R(\tau) = \overline{u'(t)u'(t+\tau)}$  is the autocovariance function and  $\tau$  is the lag time. In general terms, the acf is a measure for the similarity between a realization of  $u'(t)$  and the same realization shifted over time  $\tau$ . In fluid mechanics  $\rho(\tau)$  is used to determine a number of time scales of the turbulent flow, such as the Taylor time scale,  $\lambda_t$ , and the integral time scale  $T_u$  defined by Eq (2.37) and Eq (2.38), respectively. The *normalized* spectral density function (sdf) is defined as the Fourier transform of  $\rho(\tau)$ , which reduces to a cosine transform because  $\rho(\tau)$  is an even function:

$$S(\omega) = \frac{1}{2\pi} \int_{-\infty}^{\infty} \rho(\tau) e^{-i\omega\tau} d\tau = \frac{1}{\pi} \int_0^{\infty} \rho(\tau) \cos \omega\tau d\tau. \quad (4.25)$$

The estimation of the acf or the sdf from LDA data poses unique data-processing problems. The random sampling times in LDA preclude the use of the methods for equidistant sampling. Spectral estimators for randomly sampled data were developed by e.g. Mayo [1974], and Gaster and Roberts [1975] [1977]. The work of these investigators revealed that the random sampling causes an additional (in comparison to equidistant sampling) statistical scatter of the spectral estimates that obscures the behaviour of the sdf in the high-frequency range. The maximum frequency at which reliable estimates can be made is usually much less than the mean data rate. For LDA measurements in gas flows, the mean data rate is often small compared to the highest frequencies of the turbulent velocity fluctuations. As a consequence, the small scales of the turbulent fluctuations cannot

be studied from the estimated sdfs with the presently available data-processing methods. The objective of this section is to modify an existing data-processing method such that information on the spectral density function can be revealed at higher frequencies. The modified estimator is applied to two types of simulated data to illustrate its performance. The spectral analysis in this section largely pertains to the relatively simple case where the velocity bias is absent, although the effects of the velocity bias on the acf are briefly addressed in Section 4.3.5.

### 4.3.1 Spectral estimation using the correlation method

The conventional method to compute the discretized autocovariance function from the random samples is known as the slotting technique. This technique can be described by the following algorithm [Mayo 1974]

$$\hat{R}(k\Delta\tau) = \frac{\text{sum}\{u'_i u'_j\}(k\Delta\tau)}{H(k\Delta\tau)} \quad \text{with } k = 0, 1, \dots, M - 1, \quad (4.26)$$

where  $\text{sum}\{u'_i u'_j\}(k\Delta\tau)$  denotes the sum of all cross-products  $u'(t_i)u'(t_j)$  having a lag time in the interval  $(k - \frac{1}{2})\Delta\tau < t_i - t_j < (k + \frac{1}{2})\Delta\tau$ . This interval is usually called a "slot." The slot width  $\Delta\tau$  is determined from  $\Delta\tau = \tau_{m_0}/(M - 1)$ , where  $M$  is the number of slots and  $\tau_{m_0}$  is the maximum lag time.  $H(k\Delta\tau)$  is the number of cross products within a slot. Self-products, i.e., cross-products with zero lag time are excluded from the algorithm. In case of Poisson sampling the expected number of cross products per slot is given by

$$\overline{H(k\Delta\tau)} = \nu N \Delta\tau \left(1 - \frac{k\Delta\tau}{T}\right), \quad (4.27)$$

which shows that the Poisson sampling process provides cross products at all lag times, including the smallest lag times. An expression for the statistical variance of the autocovariance estimates  $\hat{R}$  is derived by Scott [1974]

$$\text{var}\{\hat{R}(k\Delta\tau)\} = \frac{R^2(0) + R^2(k\Delta\tau)}{H(k\Delta\tau)} + \frac{4}{T} \int_0^\infty R^2(\mu) d\mu, \quad (4.28)$$

where  $T$  is the measuring time. The first term on the right-hand side of Eq (4.28) is the statistical variability caused by the finite number of cross products per slot. The second term on the right-hand side of Eq (4.28) is inversely proportional to the measuring time  $T$ . It gives rise to a smooth, but incorrect, estimate of the autocovariance function, and is sometimes called the run-to-run variance. For a given value of the slot width  $\Delta\tau$ , the value of  $H(k\Delta\tau)$  can be increased by increasing the mean data rate  $\nu$  or by increasing the number of samples  $N$ , see Eq (4.27). However, when the number of samples  $N (= \nu T)$  is fixed, for example, because of limited storage capacity, than an increase of the mean data rate results in a decrease of the measuring time, which in turn will increase the magnitude of the second term. Therefore, a reduction of the variance of the  $\hat{R}(k\Delta\tau)$

values requires both an increase of the mean data rate and longer measuring times. The discretized autocorrelation function  $\hat{\rho}(k\Delta\tau)$  can be computed from

$$\hat{\rho}(k\Delta\tau) = \frac{\hat{R}(k\Delta\tau)}{\overline{u'^2}} \quad \text{with } k = 0, 1, \dots, M-1, \quad (4.29)$$

where  $\hat{R}(k\Delta\tau)$  is given by Eq (4.26) and  $\overline{u'^2} = R(0)$  is the variance of the process  $u(t)$ , which is usually estimated from

$$\overline{u'^2} = \frac{1}{N} \sum_{i=1}^N u'(t_i)^2. \quad (4.30)$$

Once the discretized acf is available, a spectral estimate can be formed from [Gaster and Roberts 1975]

$$S_1(\omega) = \frac{\Delta\tau}{\pi} \left\{ \frac{1}{2} \hat{\rho}(0) + \sum_{k=1}^{M-1} \hat{\rho}(k\Delta\tau) w(k\Delta\tau) \cos(k\omega\Delta\tau) \right\}, \quad (4.31)$$

where  $w(t)$  is a lag-window function. The numerical integration over  $\tau$  is performed using the trapezoidal rule. Due to the discretization of the lag-time axis, and the subsequent smearing of the time information, the slot width must be chosen sufficiently small so that the aliasing error is negligible. In absence of an exact mathematical expression for the variance of  $S_1$ , Gaster and Roberts [1975] suggested to use the following expression

$$\text{var}\{S_1(\omega)\} = \frac{c\tau m_0}{T} \left\{ S^2(\omega) + \frac{S(\omega)}{\pi\nu} + \left( \frac{1}{2\pi\nu} \right)^2 \right\}, \quad (4.32)$$

which is based on a mathematical analysis of the variance of a closely related spectral estimator (see Gaster and Roberts [1975] for details). In Eq (4.32),  $\nu$  is the mean data rate and the constant  $c$  depends on the lag window function, e.g.  $c = 3/4$  for the Tuckey-Hanning window. The first term between the brackets is also found in the expression for the variance in case of periodically sampled data (see e.g. Priestley [1981]). The second and third term represent the extra variability of the spectral estimates due to the random sampling. The third term,  $(2\pi\nu)^{-2}$ , will dominate at high frequencies. When LDA measurements are performed in gas flows it is seldom possible to obtain mean data rates that are sufficiently high to neglect this term. In that case the extra variability will obscure the behaviour of  $S(\omega)$  at high frequencies, as will be illustrated in Section 4.3.4.

### 4.3.2 Improved spectral estimation

A new spectral estimator will now be proposed that overcomes some of the variability problems at high frequencies. This estimator is a modified version of  $S_1(\omega)$ , the estimator that is based on the slotting technique. The modification consists of two elements. First, the discretized autocorrelation function,  $\hat{\rho}(k\Delta\tau)$ , is replaced by a *locally scaled* version,  $\hat{\rho}(k\Delta\tau)$ , see Tummers et al. [1994] or Tummers and Passchier [1996b]. Secondly, the width of the lag window is varied with frequency as proposed by Gaster and Roberts

[1975]. It is important to note that each of these modifications alone is insufficient to improve the spectral estimate at high frequencies significantly. The combination of the two, however, is found to yield the desired result.

### Local normalization of the slotted covariance function

Because  $u'(t)$  is a stationary process  $(u'(t)^2 \overline{u'(t + \tau)^2})^{1/2}$  is equivalent to  $\overline{u'^2}$ . Therefore, the discrete autocovariance  $\hat{R}(k\Delta\tau)$  can be scaled alternatively with a discretized version of  $(u'(t)^2 \overline{u'(t + \tau)^2})^{1/2}$ , i.e.

$$J(k\Delta\tau) = \frac{\sqrt{\text{sum}\{u_i'^2\}(k\Delta\tau) \text{sum}\{u_j'^2\}(k\Delta\tau)}}{H(k\Delta\tau)}, \quad (4.33)$$

where  $H(k\Delta\tau)$  is defined as in Eq (4.26) and  $\text{sum}\{u_i'^2\}$  and  $\text{sum}\{u_j'^2\}$  are the sums of the squares of the samples  $u'(t_i)$  and  $u'(t_j)$  for which the lag time is in the interval  $(k - \frac{1}{2})\Delta\tau < t_i - t_j < (k + \frac{1}{2})\Delta\tau$ . This means that for each time interval a separate estimate of the variance of the velocity fluctuations is made, involving only those samples that contribute to the sum of the cross-products in that slot. The slotted autocorrelation function then follows from<sup>1</sup>

$$\tilde{\rho}(k\Delta\tau) = \frac{\hat{R}(k\Delta\tau)}{J(k\Delta\tau)} = \frac{\text{sum}\{u_i' u_j'\}(k\Delta\tau)}{\sqrt{\text{sum}\{u_i'^2\}(k\Delta\tau) \text{sum}\{u_j'^2\}(k\Delta\tau)}}. \quad (4.34)$$

The advantage of the local normalisation is that at very small lag times, i.e. when the autocorrelation is near 1, the use of Eq (4.34) to scale  $\hat{R}(k\Delta\tau)$  leads to a significant reduction of the variance of the correlation values as compared to the conventional scaling of  $\hat{R}(k\Delta\tau)$  with  $\overline{u'^2}$  as in Eq (4.29). This characteristic enables a direct determination of the Taylor time scale from the curvature of a measured acf at zero lag time, as was shown by Tummers et al. [1994]. To the author's knowledge, there is no theoretical derivation of an expression for the statistical variance of the locally scaled autocorrelation values  $\tilde{\rho}(k\Delta\tau)$ . In absence of such a derivation, one can use the following empirical expression:

$$\text{var}\{\tilde{\rho}(k\Delta\tau)\} = \frac{(1 - |\tilde{\rho}(k\Delta\tau)|)^2}{\overline{u'^2}} \text{var}\{\hat{R}(k\Delta\tau)\}, \quad (4.35)$$

where  $\text{var}\{\hat{R}(k\Delta\tau)\}$  is given by Eq (4.28).

Another advantage of the local normalization is that the  $\tilde{\rho}(k\Delta\tau)$  values cannot become larger than 1. This is because the same samples that are used to compute the autocovariance function  $\hat{R}(k\Delta\tau)$  are also used for the computation of the scale factor  $J(k\Delta\tau)$  in such a way that  $\hat{R}(k\Delta\tau) \leq J(k\Delta\tau)$  for all  $k$ .

<sup>1</sup>Note that the normalization of  $\hat{R}(k\Delta\tau)$  with the local variance  $J(k\Delta\tau)$  shows a resemblance to the scaling of a two-point covariance function,  $u'(x)u'(x + \Delta x)$ , with the variance of velocity fluctuations computed from the samples acquired at both measuring locations  $(u'(x)^2 \overline{u'(x + \Delta x)^2})^{1/2}$ .

### Variation of the window width with frequency

The selection of the width of the window is a trade-off between the smoothness and the resolvability of the spectral estimates. An increase of the width of the spectral window decreases the variance of the spectral estimates. If the window width is chosen such that the narrowest peak in the sdf can be resolved then there is more than enough resolution at all frequencies. In regions where the sdf is relatively flat, the excess resolution can be used to increase the width of the window without creating a large bias error. This forms the basis for the variable window [Priestley 1981].

In the following, a Tuckey-Hanning window will be used

$$w(\tau) = 1/2 + 1/2 \cos\left(\frac{\pi\tau}{\tau_m}\right) \quad (4.36)$$

with  $\tau < \tau_m$ . The width of this window can be conveniently varied with frequency by varying the value of  $\tau_m$  with frequency as

$$\frac{\tau_m(\omega)}{\tau_{m0}} = \kappa \frac{\omega_0}{\omega} \quad \text{with} \quad \omega_0 = \frac{2\pi}{\tau_{m0}}. \quad (4.37)$$

Here,  $\tau_{m0}$  is the maximum lag time and  $\kappa$  is approximately equal to the ratio of the centre frequency  $\omega$  and the width of the spectral window. As a result of the variation of  $\tau_m$  with the frequency, the resolvability will be relatively low at high frequencies. However, when the sdf does not have sharp peaks or troughs in the high frequency range, the variation of the window width with frequency works satisfactory.

Combining the locally normalized autocorrelation  $\tilde{\rho}(k\Delta\tau)$  with the variable window width, yields the following spectral estimator

$$S_2(\omega) = \frac{\Delta\tau}{\pi} \left\{ \frac{1}{2} \tilde{\rho}(0) + \sum_{k=1}^{M-1} \tilde{\rho}(k\Delta\tau) w(k\Delta\tau) \cos(k\omega\Delta\tau) \right\}, \quad (4.38)$$

where  $\tilde{\rho}(k\Delta\tau)$  is given by Eq (4.34), the window  $w(\tau)$  is given by Eq (4.36) and  $\tau_m$  is varied with frequency as in Eq (4.37).

### 4.3.3 Application to simulated data

To asses the two spectral estimators  $S_1$  and  $S_2$ , simulated data were generated on a computer using the methods given in Appendix B. The simulated data have known sdfs, thereby enabling a direct verification of the ability of each estimator to infer the correct sdf from the data. Second-order autoregressive (AR(2)) data have the following spectral density (see e.g. Priestley [1981])

$$S(\omega) = \frac{1}{\pi} \frac{\alpha_1 \alpha_2}{\alpha_1^2 \omega^2 + (\alpha_2 - \omega^2)^2}. \quad (4.39)$$

The coefficients  $\alpha_1$  and  $\alpha_2$  can be used to prescribe two time scales that characterize the simulated data, such as the Taylor time scale  $\lambda_t$  and the integral time scale  $T_u$ . This is discussed in detail in Appendix B. When plotted on double-log axes, the sdf of an AR(2) process has fixed slopes of  $-2$  and  $-4$ . It may be argued that this does not represent a



realistic behaviour of the sdfs that are found in fluid mechanics. Therefore, the use of AR(2) data as the only test case for the assessment of the different spectral estimators may be insufficient. To meet some of this criticism, the spectral estimators should also be applied to simulated data with a more realistic behaviour of the sdf at high frequencies. For this the following spectral density was chosen

$$S(\omega) = \frac{T_u}{\pi \left(1 + \left(\frac{\omega}{\beta_1}\right)^{\frac{5}{3}}\right) \left(1 + \left(\frac{\omega}{\beta_2}\right)^{\frac{16}{3}}\right)}. \quad (4.40)$$

The constant  $\pi$  has been introduced in the denominator so that  $S(0) = T_u/\pi$  in accordance with Eq (4.25). For high frequencies  $S(\omega)$  behaves as  $\omega^{-5/3}$  and then falls off as  $\omega^{-7}$  as suggested by Heisenberg, see Hinze [1975].

Two data records were generated. Both records consist of  $2 \times 10^5$  samples and have a duration of 200 s. Record *I* was generated with the AR(2) model. The constants in Eq (4.39) were chosen as  $\alpha_1 = 10^4$  rad/s,  $\alpha_2 = 2/9 \times 10^6$  rad<sup>2</sup>/s<sup>2</sup>, resulting in a Taylor time scale of 3.0 ms and an integral scale of 45.0 ms. Furthermore, the record has variance  $\bar{u}^2 = 1$  m<sup>2</sup>/s<sup>2</sup> and zero mean. Record *II* was generated using Heisenberg's spectral density, Eq (4.40). The constants in Heisenberg's sdf were set at  $\beta_1 = 20.7$  rad/s and  $\beta_2 = 1500.0$  rad/s, while the integral time scale was chosen as  $T_u = 40.0$  ms. This resulted in a Taylor time scale of approximately 6.0 ms. The mean and variance are identical to those of record *I*.

#### 4.3.4 Performance of the new estimator

Figure 4.12 gives a detailed view of the acf in the region near zero lag time for the conventional slotting technique, Eq (4.29), and the locally scaled variant, Eq (4.34), as computed from record *I*. The corresponding results for record *II* are shown in Fig. 4.13. In both figures the slot width equals  $25\mu\text{s}$ . The error bar at  $\tau = 1.5$  ms has length  $4\sigma$ , where  $\sigma^2$  is the variance of the  $\hat{\rho}(k\Delta\tau)$  estimates as calculated from Scott's formula, Eq (4.28). Recall that the  $4\sigma$ -band contains approximately 97% of the  $\hat{\rho}(k\Delta\tau)$  estimates for a Gaussian distribution. Even though there is no theoretical expression for the variability of the  $\hat{\rho}(k\Delta\tau)$  values, it is clear from Figs. 4.12 and 4.13 that the local scaling results in a dramatic decrease of the variability. The local scaling enables an accurate description of the acf. The beneficial effect of the local scaling is most pronounced at the smallest lag times, i.e. in the region where the value of the correlation coefficient is near 1. The scatter increases with decreasing correlation, and in the limiting case of zero correlation, e.g. at very large lag times, the variability of  $\hat{\rho}(k\Delta\tau)$  becomes equal to that of  $\hat{\rho}(k\Delta\tau)$ .

Figure 4.14 shows the results of the conventional spectral estimator  $S_1$  for record *I*. The estimator  $S_1$  used the Tuckey-Hanning window and the maximum lag time was set at  $\tau_{m_0} = 1$  s. The lag-time axis was divided into  $10^5$  intervals of  $10\mu\text{s}$ . The spectral density for which the variance of  $S_1$  exceeds  $\delta^2 S^2(\omega)$  as determined from Eq (4.32) is  $S_\delta = 2.92 \times 10^{-5}$  s at  $\omega = 570$  rad/s for  $\delta = \frac{1}{3}$ . This value compares reasonably well with the experimentally observed value of  $S_{\delta=1/3} = 1.24 \times 10^{-5}$  s at  $\omega = 820$  rad/s in Figure 4.14. It illustrates that Eq (4.32) can be used to predict the lowest spectral density that can be accurately estimated with  $S_1$ . Note that the frequency  $\omega = 820$  rad/s corresponds

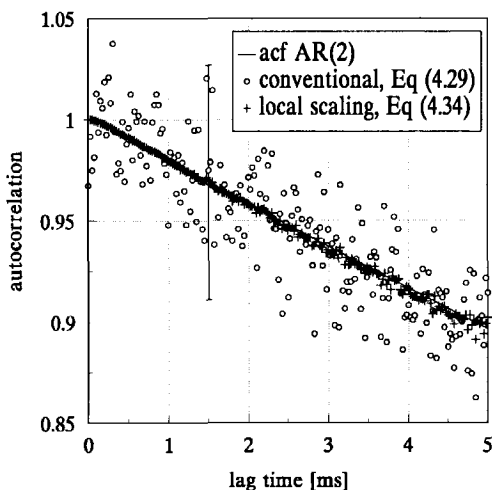


Figure 4.12: The influence of local scaling on the acf for record *I*. The error bar denotes the  $4\sigma$ -band as computed from Scott's formula, Eq (4.28).

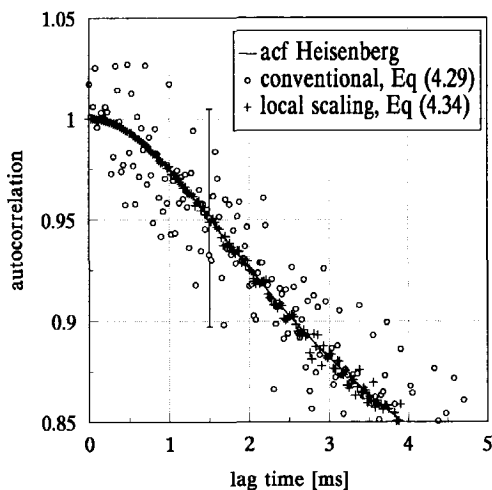


Figure 4.13: The influence of local scaling on the acf for record *II*. The error bar denotes the  $4\sigma$ -band as computed from Scott's formula, Eq (4.28).

to approximately  $1/8$  of the mean data rate. For higher frequencies the spectral density function becomes increasingly obscured by the variability of the estimates.

The *individual* effects of the local scaling and the variation of the window width on the spectral density are also shown in Figure 4.14. First, the standard autocorrelation  $\hat{\rho}(k\Delta\tau)$  in Eq (4.31) was replaced by the locally scaled autocorrelation  $\tilde{\rho}(k\Delta\tau)$ . Theoretically, this should lead to some improvement, but this is not noticeable from the results. Apparently, the reduction of the scatter of the autocorrelation values near  $\tau = 0$  had negligible influence on the calculated spectral density function, because the integration in Eq (4.25) is performed up to the maximum lag time, i.e.  $\tau = \tau_{m_0}$ . As indicated by Gaster and Roberts [1975], the use of the variable window alone alleviates some of the variability problems. The value of  $S_{\delta=1/3}$  was determined as  $2.0 \times 10^{-6}$  s at  $\omega = 1600$  rad/s.

Figure 4.15 shows the results of the  $S_1$  estimator together with the results of the new spectral estimator  $S_2$  when applied to record *I*. The latter estimator combines the locally scaled autocorrelation  $\tilde{\rho}(k\Delta\tau)$  and the variable window. The width of the window is varied according to Eq (4.37) with  $\kappa = 6$ . The choice of the value of  $\kappa$  is not critical. As shown by Tummers and Passchier [1996a] a variation of  $\kappa$  between 3 and 9 did not yield significant differences in the results. Both spectral estimators used the Tuckey-Hanning window and the maximum lag time was  $\tau_{m_0} = 1$  s. The lag-time axis was again divided into  $10^5$  slots each having a width of  $10 \mu\text{s}$ . The estimator  $S_1$  gives reliable estimates up to  $\omega = 820$  rad/s. The variability of  $S_2$  is much lower; the value of  $S_{\delta=1/3}$  was determined as  $1.8 \times 10^{-7}$  s at  $\omega = 4660$  rad/s. Now, advantage is taken of the smaller variance of the autocorrelation values near  $\tau = 0$ , because the upper limit of the integration in Eq (4.25) decreases with frequency. The use of  $S_2$  results in a gain of about 2 decades in the spectral density. The same result could have been achieved with  $S_1$  if  $2 \times 10^9$  instead of

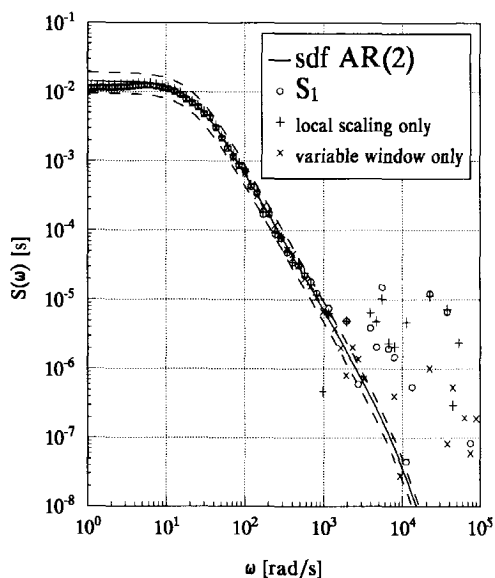


Figure 4.14: The individual influences of the local scaling and the variable window on the spectral density for record *I*. The dashed lines represent  $(1 \pm 1/3)S(\omega)$ .

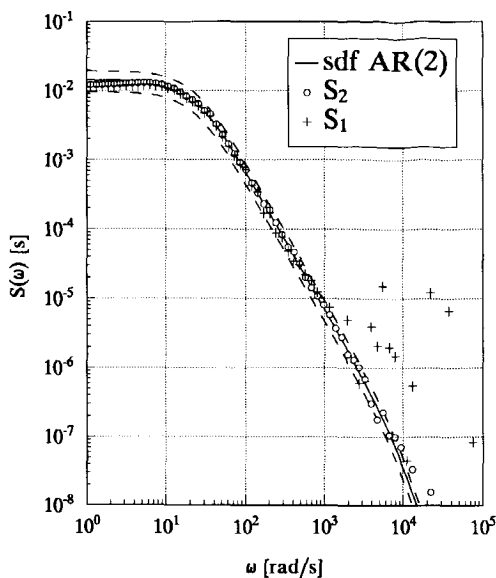


Figure 4.15: Comparison between the spectral estimators  $S_1$  (slotted correlation method) and the new spectral estimator  $S_2$  for record *I*. The dashed lines represent  $(1 \pm 1/3)S(\omega)$ .

$2 \times 10^5$  samples were processed.

Figure 4.16 shows the results for  $S_1$  and  $S_2$  when applied to record *II*. Both estimators used the Tuckey-Hanning window and  $S_2$  employed  $\kappa = 6$ . The maximum lag time,  $\tau_{m_0}$ , was set at 1 s and the width of the time slots was  $10 \mu\text{s}$ . The variance of the  $S_1$  estimates exceeds  $\delta^2 S(\omega)^2$  at  $\omega = 610 \text{ rad/s}$  for  $\delta = \frac{1}{3}$ . The equivalent frequency for  $S_2$  is determined as  $\omega = 2000 \text{ rad/s}$ . Through the use of  $S_2$  instead of  $S_1$  about 1.5 decades in spectral density are gained. In particular, the estimator  $S_2$  is able to reveal the change of the slope from  $-5/3$  to  $-7$  in the Heisenberg sdf.

### 4.3.5 Lifting the model restrictions

The preceding spectral analysis implicitly assumed that the LDA measuring volume was infinitely small, that the time at which particles passed through the measuring volume could be determined exactly, that the velocities were measured without error, and that the sampling process was independent of the process being sampled, i.e. there was no velocity bias. To some extent all these assumptions are violated in practice. It is the aim of this section to reveal some of the consequences of the model restrictions. First, the model requirements will be somewhat relaxed by the allowance of velocity errors in the form of uncorrelated noise. Secondly, the influence of the velocity bias on the acf will be studied. Some consequences of ignoring the velocity bias will be revealed, and ways are

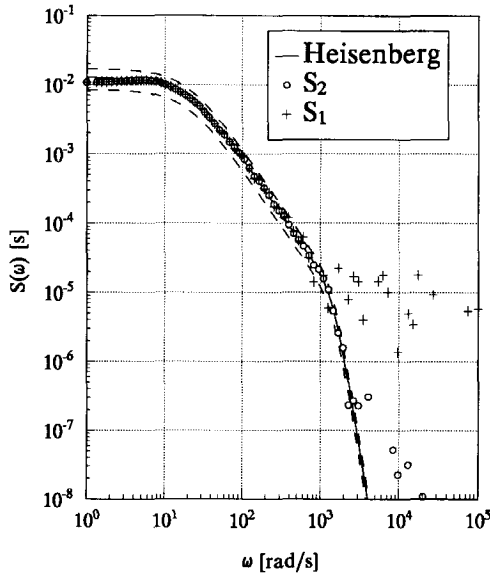


Figure 4.16: Comparison between the spectral estimators  $S_1$  (slotted correlation method) and the new spectral estimator  $S_2$  for record II). The dashed lines represent  $(1 \pm 1/3)S(\omega)$ .

indicated to correct for the velocity bias. This is followed by a discussion on the effects of the limited spatial resolution.

### Effects of uncorrelated noise

In practice a measured velocity fluctuation  $u'_m$  consists of the true velocity fluctuation  $u'$  and an error  $n$ , which is modeled here as uncorrelated noise

$$u'_m(t) = u'(t) + n(t). \quad (4.41)$$

The subscript  $m$  denotes a measured value. If it is assumed that the velocity and the noise are uncorrelated then the measured autocovariance function will, in theory at least, not be affected by the noise:

$$\begin{aligned} \overline{u'_m(t)u'_m(t+\tau)} &= \overline{u'(t)u'(t+\tau)} + \overline{u'(t)n(t+\tau)} \\ &+ \overline{n(t)u'(t+\tau)} + \overline{n(t)n(t+\tau)} \\ &= \overline{u'(t)u'(t+\tau)}, \end{aligned} \quad (4.42)$$

for  $\tau \neq 0$ . However, the variance of the measured velocity fluctuations will be too high because it contains self products, i.e. zero lag time products, of the noise

$$\overline{u'_m(t)^2} = \overline{u'(t)^2} + 2\overline{u'(t)n(t)} + \overline{n(t)^2} = \overline{u'^2} + \overline{n^2}. \quad (4.43)$$

When the measured variance is used to scale the autocovariance function  $R(\tau)$ , the resulting autocorrelation function  $\rho(\tau)$  exhibits a discontinuity at zero lag time with

magnitude (see, for example, Absil et al. [1990])

$$\Delta\rho = \frac{\overline{n^2}}{u'^2 + \overline{n^2}}. \quad (4.44)$$

The locally scaled autocorrelation function  $\tilde{\rho}(k\Delta\tau)$  that is used in the spectral estimator  $S_2$  will also exhibit a discontinuity at zero lag time, because it utilizes self products of the noise component for the scaling of the  $\hat{R}(k\Delta\tau)$  values. Note that  $\hat{R}(k\Delta\tau)$  is not directly affected by the uncorrelated noise, because the algorithm given by Eq (4.26) excludes all self products. The magnitude of the discontinuity  $\Delta\rho$  can be determined accurately if the  $\tilde{\rho}(k\Delta\tau)$  values reveal the behaviour of the autocorrelation function near zero lag time in detail. As pointed out earlier, the discrete autocorrelation function  $\tilde{\rho}(k\Delta\tau)$ , as determined with the local normalisation according to Eq (4.34), has a very small statistical variance in regions where the (absolute) value of  $\tilde{\rho}(k\Delta\tau)$  is near 1. This property enables a reliable determination of  $\Delta\rho$  from the experimental data, if the noise level  $\overline{n^2}/u'^2$  is small, say  $\overline{n^2}/u'^2 < 0.05$ . For large values of  $\overline{n^2}/u'^2$  the measured values of  $\tilde{\rho}(k\Delta\tau)$  near  $k\Delta\tau = 0$  are significantly smaller than 1 due to the discontinuity. As a result, the statistical variance of the  $\tilde{\rho}(k\Delta\tau)$  values near  $k\Delta\tau = 0$  will be relatively large, so that it is difficult to determine  $\Delta\rho$  from the measured values of  $\tilde{\rho}(k\Delta\tau)$  (despite the use of the local scaling). If the value of  $\Delta\rho$  is determined accurately then the discontinuity in  $\tilde{\rho}(k\Delta\tau)$  can be eliminated as in

$$\tilde{\rho}_c(k\Delta\tau) = \frac{\tilde{\rho}(k\Delta\tau)}{1 - \Delta\rho} \quad \text{with} \quad k = 0, 1, \dots, M - 1. \quad (4.45)$$

Here, the subscript  $c$  denotes a "noise-corrected" value. After rescaling according to Eq (4.45), the discrete autocorrelation function  $\tilde{\rho}_c(k\Delta\tau)$  can be used in the spectral estimator  $S_2$  instead of  $\tilde{\rho}(k\Delta\tau)$ .

From the preceding it is clear that the signal-to-noise ratio (SNR) defined as

$$SNR = \frac{\overline{u'^2}}{\overline{n^2}}, \quad (4.46)$$

should be as high as possible. A high SNR results in a small discontinuity at  $\tau = 0$ , since

$$\Delta\rho = \frac{\overline{n^2}}{u'^2 + \overline{n^2}} = \frac{1}{1 + SNR}. \quad (4.47)$$

Apart from the spike at zero lag time, the uncorrelated noise also has another, more subtle, effect on the spectral estimates. In deriving Eqs (4.42) and (4.43) the ensemble averaging causes correlations, such as  $u'(t)n(t)$ , to vanish. In practice, however, the averaging process is based on a finite number of samples. As a consequence, the cross correlations will not vanish completely, and this effectively increases the statistical variability of  $\hat{R}(k\Delta\tau)$  and  $\tilde{\rho}(k\Delta\tau)$ , thereby increasing the statistical variability of the spectral estimates. This again illustrates the importance of increasing the SNR.

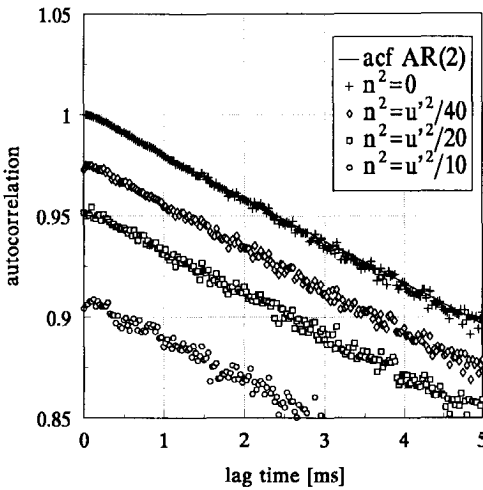


Figure 4.17: The effects of uncorrelated noise on the acf of the AR(2) process.

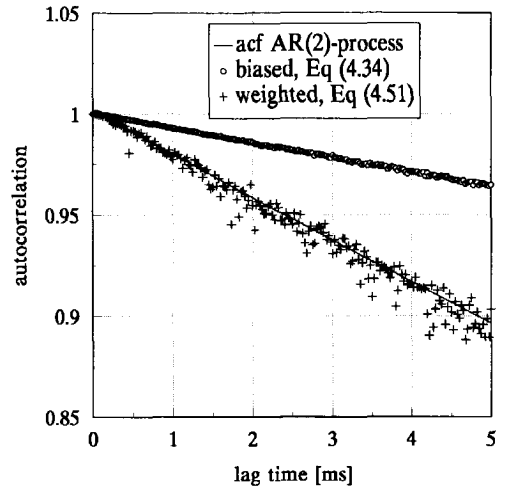


Figure 4.18: Inference of the AR(2)-process acf from a biased data record.

### Effects of velocity bias on the autocorrelation function

The standard slotting technique, Eq (4.29), and its locally normalised version, Eq (4.34), can only be used to estimate the acf from randomly sampled data if there is no correlation between the sampling process and the velocity. Since this correlation is inherent to the LDA measurement technique, it should be taken into account when processing measured data.

Buchhave et al. [1979] were the first to warn for the effects that ignoring the velocity bias has on the measured acf. It remained unclear what these effects were until the simulations of Edwards and Kolodzy [1986] revealed that the computed acf could rise above 1 at small lag times, which is physically unrealistic because the true acf is always less than 1. This physically unrealistic behaviour was also observed by Van Strien [1988] for measurements in a stirred vessel, and by Tummers [1992] for measurements in a low-speed turbulent wake. For the simple case of a one-dimensional flow with low turbulence intensity and a Gaussian velocity distribution, it is easy to show that the velocity bias causes  $\hat{\rho}(k\Delta\tau)$  to become larger than 1 [Tummers 1992]

$$\lim_{k\Delta\tau \rightarrow 0} \hat{\rho}(k\Delta\tau) = \frac{1 + \overline{u'^2}/\bar{u}^2}{1 - \overline{u'^2}/\bar{u}^2} > 1. \quad (4.48)$$

Here,  $\bar{u}$  is the mean velocity and  $\overline{u'^2}$  is the variance of the velocity fluctuations. Clearly, this abnormal behaviour of  $\hat{\rho}(k\Delta\tau)$  at small lag times will have adverse consequences for the spectral density  $S_1$ . This indicates that there is a strong need to modify the existing algorithms for the estimation of the acf such that the effects of velocity bias are taken into account. Buchhave et al. [1979] argued that the autocorrelation function  $\hat{\rho}(k\Delta\tau)$  should be corrected for the velocity bias by weighting each cross-product  $u'_i u'_j$  with the

transit times of the particles according to

$$\hat{R}(k\Delta\tau) = \frac{\text{sum}\{u'_i u'_j \omega_i \omega_j\}(k\Delta\tau)}{\text{sum}\{\omega_i \omega_j\}(k\Delta\tau)}, \quad (4.49)$$

where  $\omega_i$  is the transit time of the  $i$ -th particle. The autocorrelation function  $\hat{\rho}(k\Delta\tau)$  then follows from  $\hat{R}(k\Delta\tau)$  by scaling with the corrected variance

$$\overline{u'^2} = \sum_{i=1}^N u_i'^2 \omega_i / \sum_{i=1}^N \omega_i. \quad (4.50)$$

Instead of the transit times other quantities, such as the time between successive particle arrivals (i.e. the particle interarrival times) or the inverse of the instantaneous volume flux, can be considered to construct a suitable weighting factor  $\omega$ , as explained in Section 4.2.1.

Van Strien [1988] noted that the rise above 1 of  $\hat{\rho}(k\Delta\tau)$  could be avoided by scaling  $\hat{R}(k\Delta\tau)$  with a "local variance" similar to Eq (4.34). Even though  $\tilde{\rho}(k\Delta\tau)$  does not exhibit the unrealistic behaviour, it is incorrect to assume that  $\tilde{\rho}(k\Delta\tau)$  is insensitive to the effects of velocity bias. On the contrary, as shown by Van Maanen and Tummens [1996] the values of  $\tilde{\rho}(k\Delta\tau)$  are affected by the velocity bias at all lag times, except at  $\tau = 0$ . Fortunately, the locally normalized autocorrelation  $\tilde{\rho}(k\Delta\tau)$  can be modified to yield unbiased values as follows [Tummens and Passchier 1996a]

$$\tilde{\rho}(k\Delta\tau) = \frac{\text{sum}\{u'_i u'_j \omega_i \omega_j\}(k\Delta\tau)}{\sqrt{\text{sum}\{u_i'^2 \omega_i \omega_j\}(k\Delta\tau) \text{sum}\{u_j'^2 \omega_i \omega_j\}(k\Delta\tau)}}. \quad (4.51)$$

This reduces to Eq (4.34) for  $\omega = 1$ . Figure 4.18 clearly illustrates that the algorithm given by Eq (4.51) with the transit times of the particles as a weighting factor, infers the correct acf from a "biased" data record<sup>2</sup>, albeit at the cost of a small increase of the statistical scatter as can be seen from a comparison between the results in Figs (4.18) and (4.12). Processing the biased data record as if the velocity bias was absent, by using Eq (4.34) instead of Eq (4.51), results in severe errors. Ignoring the effects of the velocity bias has resulted in an acf that is too "flat" for small lag times, which results in a too high a value of the Taylor time scale. However, this is not a general conclusion, because the effects of the velocity bias on the computed acf depend on the relative turbulence intensity. A detailed study on the effects of the velocity bias on the acf, and various methods to correct the acf for the velocity bias, is given by Tummens and Passchier [1999].

It is worth noting that the velocity bias itself does not cause errors in statistical quantities. The errors arise when the LDA user applies algorithms that ignore the existence of the velocity bias. However, the velocity bias further complicates the already inefficient processing algorithms, and often additional information is needed (e.g. in the form of two or three velocity components or the transit times of the particles) to take the bias into account. If this information is not available, it is inevitable that errors will result.

<sup>2</sup>Methods to generate "biased" simulated velocity data and the transit times of particles are briefly described in appendix B.

### Effects of spatial averaging

The spatial averaging for the (individual-realization) LDA is radically different from that for the hot-wire anemometer. In case of a hot-wire anemometer, all parts of the wire contribute to a certain extent to the *instantaneous* output of the device. So, the *instantaneous* velocity measured by the hot wire is the result of an averaging process over the complete wire. In contrast, the LDA measures the velocity of a single particle that passes through the otherwise empty measuring volume. Therefore, the spatial resolution of a LDA is limited only by the distance that the particle travels through the measuring volume during the time span that the signal processor needs to analyze the Doppler burst. The *instantaneous* velocity measured by a LDA thus resembles a "point measurement," unaffected by the size of the measuring volume. However, it should not be concluded from this that the LDA has a near perfect spatial resolution, because during the process of inferring statistical quantities from the velocity samples, significant spatial averaging may take place. Whether or not the spatial averaging is relevant depends on the dimensions of the measuring volume, the local properties of the turbulence field and on the statistical quantity that is under consideration<sup>3</sup>.

There is considerable confusion among the LDA users on the nature of the volume averaging in case of an (individual realization) LDA. This has resulted in different approaches in formulating a mathematical model for the spatial averaging. Below, a procedure is put forward that takes the "point measurements" into account. The analysis is presented for the simple case of a measuring volume of zero width and length  $l$ . The analysis for a more realistic shape, such as a cylinder or an ellipsoid, is straightforward but it involves a much larger algebraic effort, while hardly yielding any additional insight into the effects of the spatial averaging, as was shown by Kraan [1995].

Let  $l$  be the length of a measuring volume that is oriented along the  $z$ -axis. Furthermore, it will be assumed that the turbulence is homogeneous in  $z$ -direction. Consider two velocity fluctuations; one measured at location  $z = z_1$  on time  $t$  and another measured at location  $z = z_2$  on time  $t + \tau$ . Each individual velocity fluctuation is assumed to be uninfluenced by the length the measuring volume. The product of the two velocity fluctuations  $u'(z_1, t)u'(z_2, t + \tau)$  is an estimate of the autocovariance function  $R(\tau)$  only if  $z_1 = z_2$ . This condition is not fulfilled in practice, because of the finite extent of the measuring volume. As a consequence, the cross product  $u'(z_1, t)u'(z_2, t + \tau)$  should be considered an estimate of the space-time covariance  $R(\tau, z_2 - z_1)$ . Recall that the slotting technique (see Eq (4.26)) involves the summing of such cross products, so that some degree of spatial averaging is incurred when the autocovariance function is calculated from the samples. The autocovariance  $\hat{R}(\Delta\tau)$  is a measure for

$$R_{va}(\tau) = \int_{-l/2}^{l/2} \int_{-l/2}^{l/2} \overline{u'(z_1, t)u'(z_2, t + \tau)p(z_1)p(z_2)} dz_1 dz_2, \quad (4.52)$$

where the subscript  $va$  denotes a volume-averaged quantity and  $p(z)$  is the probability

<sup>3</sup>In addition to the spatial resolution, there is the related issue of temporal resolution. In practice all signal processors calculate some average Doppler frequency during the passage of a particle through the measuring volume. Therefore, the shape of the acf will be obscured for lag times smaller than the mean transit time of the particles. If the mean transit time is larger than the Kolmogorov scale, then it is inevitable that some information on the turbulence is lost.



density that a particle will pass through the measuring volume between  $z$  and  $z + dz$ . For simplicity it is assumed here that  $p$  is uniformly distributed, i.e.

$$p(z) = \begin{cases} 1/l & \text{if } -l/2 \leq z \leq l/2 \\ 0 & \text{otherwise.} \end{cases} \quad (4.53)$$

Because of the homogeneity of the flow in  $z$ -direction, only the difference  $\Delta z = z_2 - z_1$  is of relevance, so that Eq (4.52) reduces to

$$R_{va}(\tau) = \int_{-l}^l \overline{u'(z, t)u'(z + dz, t + \tau)} P(\Delta z) d\Delta z. \quad (4.54)$$

The probability density function of  $\Delta z$  is given by (e.g. Papoulis [1991])

$$P(\Delta z) = \begin{cases} 1/l - |\Delta z|/l^2 & \text{if } -l \leq \Delta z \leq l \\ 0 & \text{otherwise.} \end{cases} \quad (4.55)$$

Expanding the velocity fluctuation  $u'(z + \Delta z, t + \tau)$  in a Taylor series around  $t, z$  and integrating yields [Kraan 1995]

$$\begin{aligned} R_{va}(\tau) &= \overline{u'^2} - \frac{1}{12} \overline{\left(\frac{\partial u'}{\partial z}\right)^2} l^2 + \mathcal{O}(l^4) \\ &+ \frac{1}{12} \overline{u' \frac{\partial^3 u'}{\partial t \partial z^2}} \tau l^2 + \mathcal{O}(l^4) \\ &- \frac{1}{2} \overline{\left(\frac{\partial u'}{\partial t}\right)^2} \tau^2 + \frac{1}{24} \overline{u' \frac{\partial^4 u'}{\partial t^2 \partial z^2}} \tau^2 l^2 + \mathcal{O}(l^4) \\ &\vdots \end{aligned} \quad (4.56)$$

The right-hand side of this equation is organised as follows. The first line gives the constant terms, while the second (third) line gives the terms which are linear (quadratic) in  $\tau$ . The Taylor expansion of the true autocorrelation function  $R(\tau)$  reads [Hinze 1975]

$$R(\tau) = \overline{u'^2} + \sum_{n=1}^{\infty} \left(\frac{-1}{2n!}\right)^n \overline{\left(\frac{\partial^n u'}{\partial t^n}\right)^2} \tau^{2n} = \overline{u'^2} - \frac{1}{2} \overline{\left(\frac{\partial u'}{\partial t}\right)^2} \tau^2 + \mathcal{O}(\tau^4). \quad (4.57)$$

A comparison between Eq (4.56) and Eq (4.57) shows that the finite size of the measuring volume has resulted in unwanted constant, linear and higher-order terms that may obscure the behaviour of the true autocovariance function. In particular, it is seen that the finite size of the measuring volume causes a too low covariance at small lag times. To a first approximation the discrepancy is given by

$$R(0) - \lim_{\tau \rightarrow 0} R_{va}(\tau) = \frac{1}{12} \overline{\left(\frac{\partial u'}{\partial z}\right)^2} l^2 = \frac{\overline{u'^2} l^2}{6\lambda_z^2}, \quad (4.58)$$

where  $\lambda_z$  is the Taylor length scale for the  $z$ -direction.

Using the same procedure as for the covariance function, an expression can be derived for the effects of volume averaging on the variance of the velocity fluctuations  $\overline{u'^2}$ . The

outcome of the calculation is simply  $\overline{u'^2}_{va} = \overline{u'^2}$ , indicating that the size of the measuring volume has no effect on the measured value of the variance in homogeneous turbulence. This is in agreement with the findings of an experimental investigation carried out by Luchik and Tiederman [1985], and it illustrates the fundamental difference between the effects of spatial averaging for an (individual realization) LDA and instruments such as the hot-wire anemometer.

Once it is known that the variance  $\overline{u'^2}$  is unaffected by the spatial averaging, it follows from Eq (4.56) that the imperfect resolution of the measuring volume causes a discontinuity in the measured acf. Combining the influences of the spatial averaging and the uncorrelated noise (see Section 4.3.5), yields the following expression for the magnitude of the discontinuity of the measured acf at zero time lag

$$\Delta\rho = \frac{\overline{n^2} + \overline{u'^2}C_1}{\overline{n^2} + \overline{u'^2}} \quad \text{with} \quad C_1 = \frac{l^2}{6\lambda_z^2}. \quad (4.59)$$

Tummers et al. [1995] give the magnitude of the discontinuity in case the measuring volume is modeled as a cylinder with diameter  $d$  and length  $l$ :

$$\Delta\rho = \frac{\overline{n^2} + \overline{u'^2}C_3}{\overline{n^2} + \overline{u'^2}} \quad \text{with} \quad C_3 = \frac{d^2}{8\lambda_x^2} + \frac{d^2}{8\lambda_y^2} + \frac{l^2}{6\lambda_z^2}, \quad (4.60)$$

where  $\lambda_x$ ,  $\lambda_y$  and  $\lambda_z$  are the Taylor length scales for the  $x$ ,  $y$  and  $z$ -direction, respectively. Eqs (4.59) and (4.60) illustrate the dilemma that one faces when measuring acfs using LDA. To avoid the occurrence of a large spike at zero lag time, the dimensions of the measuring volume should be small compared to the corresponding Taylor length scale. This often necessitates that the light-collection optics are placed in a plane perpendicular to the axis of the transmitting optics, i.e. a side-scatter configuration should be used to reduce the effective length of the measuring volume. However, in that case the intensity of the received light is small compared to the intensity that can be received in forward or backward scatter. This will reduce the signal-to-noise ratio (SNR) of the Doppler signals, thereby increasing the noise component  $n(t)$  of the individual samples. It is seen from Eqs (4.59) and (4.60) that this will increase the magnitude of the discontinuity. Therefore, it can be concluded that the measurement of an acf is a trade-off between the effects of the uncorrelated noise and the spatial averaging.

### Experiment on the effects of spatial averaging on the acf

To investigate the effects of spatial averaging, Tummers et al. [1995] measured a large number of autocorrelation functions in the turbulent near wake of a flat plate with different pinholes placed in front of the photomultipliers. Scattered light was collected using a side-scatter configuration. The effective length of the measuring volume could be varied by using pinholes with different diameters. The resulting effective length of the measuring volume was equal to the pinhole diameter, because the magnification factor of the receiving optics was nearly 1. For each pinhole 40 blocks of  $10^4$  samples were acquired at an average rate of 1 kHz. The increase of the mean data rate caused by the increase of the pinhole diameter was compensated for by lowering the seed rate. All

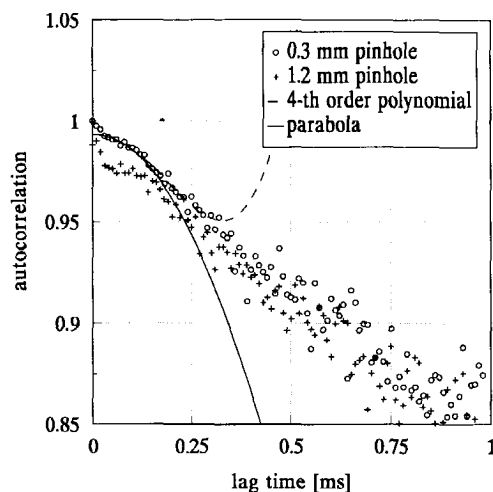


Figure 4.19: The effect of the effective measuring-volume length on the measured acf.

other parameters, like the settings of the BSA signal processors and the photomultiplier gain, were the same for each measurement.

The results of the experiment for pinhole diameters of 0.3 mm and 1.2 mm are given in Fig. 4.19. The transit times are used as a weighting factor to compensate for the effects of the velocity bias. (The acfs reported in Tummers et al. [1995] were computed as arithmetic averages.) The results for the small pinhole reasonably approximate the expected parabolic behaviour for small lag times, except for the smallest lag times, i.e.  $\tau \leq 20 \mu\text{s}$ , where the results are affected by the limited temporal resolution of the measurement. The results for the large pinhole do not show a parabolic behaviour at all, indicating the need for a small effective measuring volume. Therefore, all acfs that are reported in this thesis were measured using a small pinhole in conjunction with the side-scatter arrangement. The larger measuring volume length apparently obscured the expected parabolic behaviour of the acf as indicated by the simple theory presented above. Eq (4.60) predicts a discontinuity of magnitude  $\Delta\rho = 0.03186$ , assuming  $l = 1.2 \text{ mm}$ ,  $\lambda_x = 3.9 \text{ mm}$ , isotropic relations between the length scales and a negligible contribution of the uncorrelated noise. The discontinuity reduces to  $\Delta\rho = 0.0023$  for  $l = 0.3 \text{ mm}$ . These values are in good agreement with the values observed in Fig. 4.19.

#### 4.3.6 Concluding remarks

The main findings of the research on the spectral estimation can be summarized as follows. It is shown that the conventional spectral estimator  $S_1$  exhibits a large statistical scatter due to the randomness of the sampling process. As a result, this estimator is unable to reveal the spectral density at high frequencies. A new spectral estimator,  $S_2$ , is proposed that overcomes some of the variability problems. This estimator combines a window of variable width and a locally normalized autocorrelation function  $\hat{\rho}$ .

At small lag times the local normalisation strongly reduces the statistical variability

of the autocorrelation estimates compared to  $\hat{\rho}$ , the estimates resulting from the standard slotting technique. The characteristics of the locally-scaled autocorrelation function  $\tilde{\rho}$  were investigated regarding the effects of (1) uncorrelated noise, (2) velocity bias and (3) spatial averaging.

1. Uncorrelated noise: a low signal-to-noise ratio of the Doppler signals causes an increase of the error in the individual velocities measured by the LDA. These noise errors are presumed to be uncorrelated with the velocity and result in a discontinuity of  $\tilde{\rho}$  at zero lag time.
2. Velocity bias: the correlation between the instantaneous velocity and the sampling probability is inherent to the use of LDA and should therefore be taken into account. An algorithm (Eq (4.51)) is given to compute the correct autocorrelation function from a biased time series while using the local normalisation.
3. Spatial resolution: the effects of the spatial averaging for an individual realization LDA are fundamentally different from that of an instrument such as the hot wire. A method is proposed that can be used to investigate the effects of spatial averaging for an individual realization LDA. The model indicates that the finite size of the measuring volume distorts the shape of the autocorrelation function. In particular, the measured autocorrelation function shows a discontinuity at zero lag time of which the magnitude depends on the size of the measuring volume relative to the Taylor length scale.

The new spectral estimator  $S_2$  was applied to two types of simulated data, i.e. the AR(2) process and the Heisenberg spectral density. The new spectral estimator proved to be superior to the existing estimator  $S_1$ . It was shown that approximately two decades in spectral density were gained through the use of  $S_2$ . Also, the spectral estimator  $S_2$  can be used to compute the spectral density function from a biased data record when the locally scaled autocorrelation function  $\tilde{\rho}$  is computed from Eq (4.51).

## Chapter 5

# Investigation of the Adverse Pressure Gradient Wake

The first section of this chapter provides information on the experimental aspects of the investigation of the adverse pressure gradient wake. It includes a description of the wind-tunnel facility, the model, the instrumentation and the measurement programme. The description of the instrumentation has an emphasis on the different optical arrangements of the LDA. The numerical investigation of the wake in adverse pressure gradient is outlined in the second section. It consists of a brief description of the turbulence models and the numerical procedures.

### 5.1 Experimental Investigation

#### 5.1.1 Wind tunnel and model

The experimental facility used is an open-circuit wind tunnel at the Low-Speed Aerodynamics Laboratory of Delft University of Technology. A centrifugal fan accelerates the air which passes through a diffusing section, the settling chamber and the contraction (1:8) before it reaches the test section with dimensions  $400 \times 400 \text{ mm}^2$ . The test section is followed by a plane diffuser that is made from perspex to allow optical access. The diffuser has a length of 920 mm and the side walls include a  $15^\circ$  angle. The large pressure rise in the diffuser causes a rapid growth of the boundary layers along the diffuser walls. This might cause the diffuser flow to stall if adequate measures were not taken. To prevent boundary-layer separation along the diffuser walls, a screen was placed at the outlet of the channel and the diffuser walls were equipped with regularly spaced slots. A straight duct with a length of 1000 mm was placed between the diffuser and the screen. The screen induces an over-pressure inside the channel which causes the boundary layers that develop on the diffuser walls to be blown out through the slots. The absence of flow separation at the diffuser walls was confirmed with tufts and by a flow visualization using a laser sheet and oil smoke.

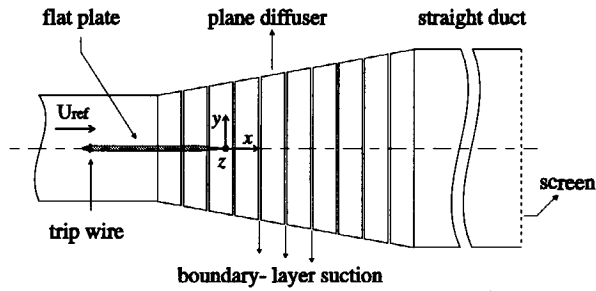


Figure 5.1: Top view of the test configuration for the investigation of the wake in adverse pressure gradient.

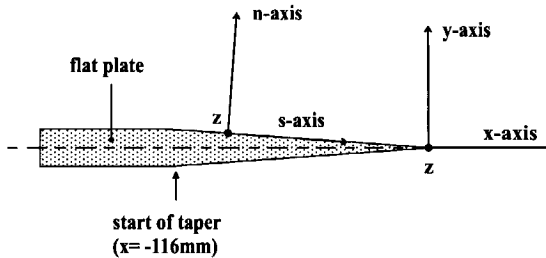


Figure 5.2: Definition of the two coordinate systems in the trailing-edge region of the plate.

An airfoil-like flat plate with a 600 mm chord and a thickness of 18 mm served as a wake generator. The plate has an elliptic nose and the last 116 mm was tapered to form a sharp trailing edge with a thickness of approximately 0.2 mm. The change in the surface contour from the constant-thickness region of the plate to the tapered region was rounded to avoid flow separation. The model was placed at zero incidence in the test section of the wind tunnel, and the aft portion of the plate (50% chord) was located in the diffuser as shown in Fig. 5.1. The boundary layers on both sides of the plate were tripped with wires to ensure uniform transition across the span. The wires had a diameter of 1 mm and were positioned at 6 % chord from the leading edge. The divergence of the diffuser and the width of the slots in the diffuser walls were tuned such that the turbulent boundary layers at the trailing edge of the plate were nearly separated ( $H = 2.91$ ). This simulates the flow field on the suction side of a highly loaded airfoil in the trailing-edge region.

An orthogonal coordinate system  $(x, y, z)$  was defined having its origin at the trailing edge of the plate at mid span, see Fig. 5.2. The  $x$ -coordinate is measured along the wind tunnel axis and taken positive in the streamwise direction. The  $z$ -coordinate is measured in the spanwise direction and taken positive in the upward direction. A second orthogonal system  $(s, n, z)$  is used for measurements in the boundary layer on the tapered region of the plate. The  $z$ -coordinate is identical to the one mentioned above. The  $n$ -coordinate is measured normal to the plate surface.

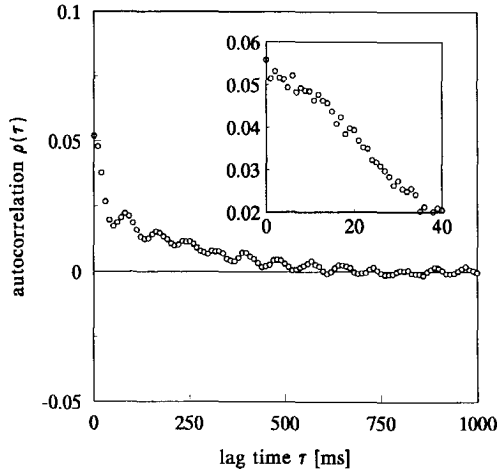


Figure 5.3: Autocorrelation function in the empty test-section (with detailed view for small lag times).

### 5.1.2 Flow quality

Ideally, the flow in the empty test section of a wind tunnel is uniform and has no fluctuations in time. Also, the mean flow about the flat plate should be perfectly two-dimensional. However, this is not the case in the real world. At the onset of the investigation the quality of the flow was investigated in a number of ways.

- The uniformity of the flow across the empty test section was examined with Pitot-tube measurements;
- Time-resolved measurements of the streamwise velocity component were performed in the empty test section (using a one-component LDA) to determine the intensity of the free-stream disturbances and their spectral distribution;
- A number of spanwise traverses were made in the turbulent wake of the plate (using a one-component LDA) to determine the degree of two-dimensionality.

First, total pressures were measured across the empty test section using Pitot tubes. These measurements indicated that the deviations in total pressure were negligibly small. Secondly, a one-component LDA (to be described in Section 5.1.3) was used to perform time-resolved measurements of the streamwise velocity component. Figure 5.3 shows the autocorrelation function of the velocity fluctuations measured on the wind-tunnel axis near the junction of the test-section and the diffuser. The root-mean-square value of the velocity fluctuations was computed as  $u'_{rms} = 3.61 \times 10^{-2}$  m/s at a free stream velocity of approximately 10.2 m/s. However, Fig. 5.3 shows that the measured autocorrelation has a very large discontinuity at zero lag time. As discussed in Section 4.3.5, this indicates that the measured mean-square value of the velocity fluctuations is much higher than its true value due to a large contribution of uncorrelated noise. In other words, the accuracy

with which the LDA measured the extremely small velocity fluctuations in the empty test section was relatively low. This resulted in a too high a value of  $\overline{u'^2}$ . The detail in Fig. 5.3 shows the measured autocorrelation value at zero lag time as 0.053. By using the simple theory presented in Section 4.3.5, in particular Eq (4.44), a much more accurate value of  $\overline{u'^2}$  can be computed:  $\overline{u'^2} = 6.89 \times 10^{-5} \text{m}^2/\text{s}^2 \Rightarrow u'_{rms} = 0.83 \times 10^{-2} \text{m/s}$ , corresponding to a relative turbulence intensity of 0.11% which is an acceptable value. Interestingly, the autocorrelation in Fig. 5.3 reveals a periodic component of 12.2 Hz. Since the wind-tunnel fan revolves at a frequency of  $12.3 \pm 0.2$  Hz, the presence of the periodic component is probably caused by an imperfection of one of the six blades of the fan or a mechanical vibration of the fan. Autocorrelation functions that were measured at more downstream locations on the diffuser axis revealed the same periodic component. However, spectral density functions of turbulent velocity fluctuations that are measured in the wake of the flat plate are not affected by the small amount of energy in the 12.2 Hz component.

The two-dimensionality of the mean flow was examined by performing spanwise traverses with a one-component LDA, measuring the velocity component in the  $x$ -direction. The spanwise traverses were carried out at a station 175 mm downstream of the trailing edge at three lateral locations:  $y = 0$ ,  $y = 47$  mm and  $y = 100$  mm. The latter position is near the edge of the wake, whereas  $y = 47$  mm is the location of the maximum kinetic energy,  $k$ . The spanwise coordinate,  $z$ , was varied between  $z = -28$  mm and  $z = +35$  mm. This range of  $z$  values corresponds to about 16 % of the span of the flat plate. In the following,  $z = 0$  can be seen as a reference, because all subsequent measurements were performed in this mid-span plane. For each measurement run the mean velocity  $\bar{u}$  and the rms value of the velocity fluctuations  $u'_{rms}$  were calculated as arithmetic averages, because bias corrections are irrelevant when assessing the variation of  $\bar{u}$  and  $u'_{rms}$  in  $z$ -direction.

Figure 5.4 shows the spanwise variation of the mean-velocity component,  $\bar{u}$ . At  $y = 100$  mm the maximum variation of  $\bar{u}$  is small, i.e. less than 1.0 % of the edge velocity  $U_e$ . Somewhat larger variations of  $\bar{u}$  occur at  $y = 0$  and  $y = 47$  mm. In particular, at  $y = 47$  mm the mean velocity has a tendency to increase with increasing values of the spanwise coordinate. However, the change of  $\bar{u}$  with  $z$  remains within 3.0 % of the edge velocity. Figure 5.5 shows the rms value of the velocity fluctuations,  $u'_{rms}$ , as a function of the spanwise coordinate. At station  $y = 0$ ,  $z = 0$  three measurements were taken to indicate the amount of statistical scatter in the results. It is seen that the change of  $u'_{rms}$  with  $z$  is slightly larger than the statistical scatter. The smallest variation of  $u'_{rms}$  with  $z$  occurs again near the edge of the wake at  $y = 100$  mm. The largest variation in  $u'_{rms}$  occurs at  $y = 47$  mm and equals 9.6 % of the maximum value of  $u'_{rms}$  at station  $x = 175$  mm. On the basis of the results shown in Figs. 5.4 and 5.5 it was concluded that there are no major three-dimensionalities in the mean flow.

### 5.1.3 Optical arrangements and instrumentation

#### Set-up 1: single-point statistics

The single-point statistics were measured with a three-component LDA system that was built according to the guidelines for a 3-D LDA given in Section 3.3. The complete LDA



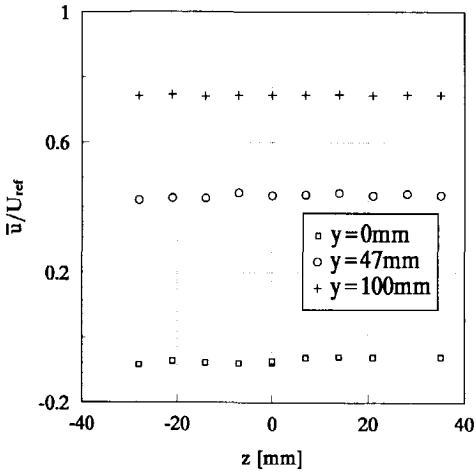


Figure 5.4: The mean velocity  $\bar{u}/U_{ref}$  versus the spanwise coordinate  $z$ .

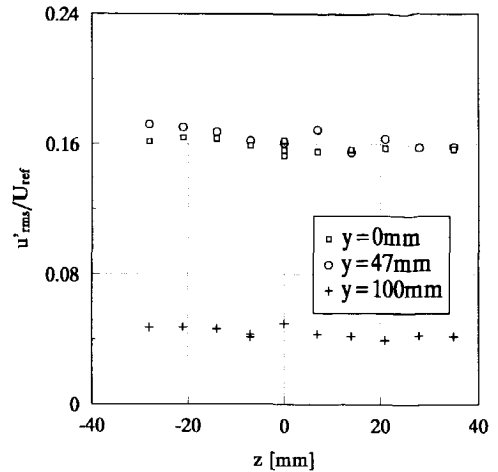


Figure 5.5: The rms of the velocity fluctuations  $u'_{rms}/U_{ref}$  versus  $z$ .

was mounted on a rigid frame that spans the wind tunnel, see Fig. 5.6. A traversing mechanism enabled displacements of the frame in steps of  $5 \mu\text{m}$ . The green (514.5 nm), blue (488.0 nm) and violet (476.5 nm) colours of a 5 W argon-ion laser were used to measure the three components of the velocity simultaneously. A modular-optics TSI system employed the blue and green colours to measure two velocity components in the  $x, y$ -plane that were oriented at  $+45^\circ$  and at  $-45^\circ$  with respect to the  $x$ -axis, so that (on the average) the blue and green channels measured velocities of comparable magnitude. One beam of each colour was frequency shifted over 40 MHz by Bragg cells to enable detection of instantaneous flow reversals. A beam expander ( $3.75\times$ ) together with a 750 mm focal-length lens were used to create two overlapping measuring volumes each having a length of 1.3 mm and a diameter of 0.11 mm. A fibre-optic Dantec LDA used the violet colour to measure the velocity component in the  $z$ -direction, i.e. the spanwise velocity component. This LDA channel also included a Bragg cell to introduce an optical shift of 40 MHz. Both violet beams passed through separate beam expanders before intersecting. The length and diameter of the violet measuring volume were 1.7 mm and 0.12 mm, respectively.

The three fringe patterns have a nominally orthogonal orientation. The fringe spacings and the precise orientation of the fringe patterns in the  $x, y, z$ -coordinate system were determined with a theodolite using procedures similar to those described by Absil [1995]. Recall from Section 3.3 that the advantage of the orthogonality, as compared to the situation for non-orthogonal fringe patterns, lies in the strongly reduced sensitivity of the measured velocity components to small calibration errors. On the other hand, the orthogonal 3-D LDA poses a number of practical problems with regard to the alignment of the transmitting and receiving optics. The solutions to these problems are discussed in Appendix A.

The receiving optics were placed in a plane perpendicular to the optical axes of the

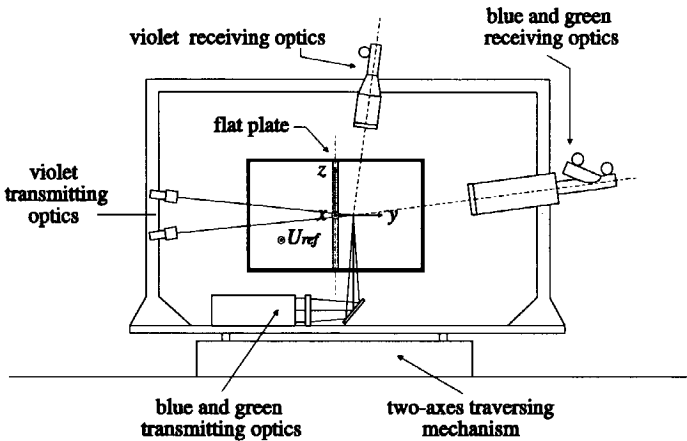


Figure 5.6: Experimental set-up for 3-D single-point statistics.

transmitting optics, i.e. a side-scatter configuration was used for each channel. This was done to collect scattered light from the overlap region of the three measuring volumes only. However, in case of a side-scatter configuration the intensity of the scattered light is small compared to the intensity that could have been obtained if forward-scattered light were collected. In the present set-up, the loss of light intensity was partly compensated for by the use of large-aperture lenses in the receiving optics. The blue and green channel used the same 145 mm aperture lens to collect scattered light. The collected light was separated using a dichroic mirror before it was focused on separate photomultipliers. Each photomultiplier was equipped with a small pinhole which resulted in a reduction of the effective length of the measuring volumes to 0.2 mm. The receiving optics for the violet channel included a 110 mm aperture lens and a small pinhole was placed in front of the photomultiplier to reduce the effective length of the violet measuring volume to about 0.2 mm. Cross talk between the blue, green and violet channels was eliminated by narrow-band optical filters placed in front of each photomultiplier. Note that the small pinholes in conjunction with the side-scatter configuration act as spatial filters that limit the probe size of the 3-D LDA to  $0.2 \times 0.2 \times 0.2 \text{ mm}^3$ .

The photomultiplier output signals were electronically down-mixed to an effective frequency pre-shift of 5 MHz and then fed to one Dantec BSA model 57N10 (clock master) and two BSAs model 57N35 (clock slaves). These processors were operated in the "hardware coincident mode," which means that the Doppler signals were processed only when signals were detected on all three channels simultaneously. Recall, that it is explained in Section 3.3 that this mode of operation is needed to ensure that each BSA analyses Doppler bursts that originate from the same particle. Some of the Doppler bursts that pass this hardware-coincidence test are rejected by the internal validation procedures performed by each processor. Since the processors apply the internal validation test independently of each other, it is possible that from triplets of hardware coincident Doppler bursts only one or two bursts are validated. Therefore, a conventional (software) time-coincidence window has to be applied during the later data reduction on a computer.

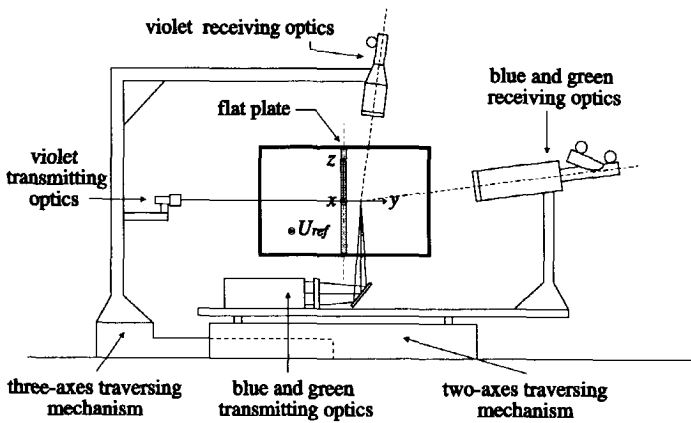


Figure 5.7: Experimental set-up for two-point statistics.

### Set-up 2: autocorrelation functions

Most of the autocorrelation functions were measured with a Dantec one-component fibre-optic LDA that is almost identical to the fibre-optic channel described in "set-up 1." The laser beams were oriented to measure the streamwise component of the velocity. The measuring volume length and diameter were 1.7 mm and 0.12 mm respectively. Scattered light was collected using a side-scatter configuration. A small pinhole positioned in front of the photomultiplier reduced the effective length of the measuring volume to 0.2 mm.

The photomultiplier output signals were electronically downmixed and subsequently processed by the model 57N10 BSA. The Doppler frequency and the arrival time of each particle were stored on disk. The transit times, i.e. the duration of each Doppler burst, were also measured to enable a velocity bias correction for this one-component measurement as explained in Section 4.2.

### Set-up 3: two-point statistics

The spatial correlation functions were measured with a TSI two-component modular-optics LDA in conjunction with a Dantec one-component fibre-optics LDA, see Fig. 5.7. Both LDA channels are nearly identical to the ones described in "set-up 1." Only the relevant differences are described here. The fringe pattern of the one-component channel was oriented to measure the streamwise component of the velocity and it was mounted on a manual  $x, y, z$ -traversing mechanism. The two-component channel, which measured the velocity components in the  $x, y$ -plane, could be traversed in  $x$  and  $y$ -direction by the computer-controlled traversing mechanism. For spatial correlation measurements with the separation vector in the  $xy$ -plane, the one-component LDA channel formed the fixed probe and the two-component channel was traversed in small steps. The situation was reversed for separations in the  $z$ -direction.

A special 50  $\mu\text{m}$  pinhole (see Appendix A) positioned at the measurement location was used to align the beams of both channels at "zero" separation. Side-scattered light was collected and small pinholes were used in the receiving optics to limit the effective length

of each measuring volume to 0.2 mm. The BSA processors were used in the “hardware coincident mode” to ensure that the two LDA channels acquired time-coincident velocity samples.

#### 5.1.4 Additional instrumentation

The barometric pressure and the temperature were measured to determine the density of air,  $\rho$ , using the equation of state of a perfect gas. The temperature was also used to calculate the dynamic viscosity,  $\mu$ , from Sutherland’s formula, see e.g. Schlichting [1987]. The difference between the static pressure in the settling chamber and in the test section, was measured using a manometer with an inaccuracy of  $\pm 0.3$  Pa. This pressure difference together with the contraction ratio of the wind tunnel and the density of the air, were used to determine the test-section speed,  $U_{ref}$ . The velocity  $U_{ref}$  is used to make all measured data dimensionless. The experiments were performed at a constant chord-based Reynolds number of  $4 \times 10^5$ , corresponding to a test-section speed of about 10.2 m/s. When atmospheric conditions changed, small adjustments of the test-section speed were made in between measurement runs (but not during the runs) to maintain the constant Reynolds number.

The Doppler bursts were monitored on an oscilloscope to verify that high quality bursts are generated by each LDA channel. The simultaneous visualisation of Doppler bursts produced by two LDA channels allowed the detection of small misalignments in streamwise direction of the corresponding measuring volumes from a time lag between the bursts. An air-blast atomizer was used to seed the flow with small oil droplets (Rizella oil). The size distribution of the droplets was measured [Plomp 1986], and found to have an average value of  $0.98 \mu\text{m}$ , while 95 % of the particles were smaller than  $2.0 \mu\text{m}$ . The droplets were injected into the flow upstream of the centrifugal fan to ensure a homogeneous distribution in space.

#### 5.1.5 Measuring programme and data reduction

Single-point statistics (set-up 1) were measured in the wake of the plate on a grid consisting of a centreline traverse and 6 lateral traverses located between  $x = 17$  mm and  $x = 175$  mm. In addition, the boundary layer in the trailing-edge region was surveyed with 5 traverses located between  $x = -137$  mm and the trailing edge ( $x = 0$  mm). Each wake traverse consisted of approximately 60 measurement stations, whereas the number of stations per boundary layer traverse was slightly less, about 50. At each measurement location at least  $2 \times 10^4$  velocity samples were acquired with the 3-D LDA. During these measurements the mean data rate varied between 200 Hz in the outer regions of the shear layer and 25 Hz near the centreline or close to the walls. The velocity samples were used to calculate the following statistical quantities

- the mean velocity components  $\bar{u}$ ,  $\bar{v}$  and  $\bar{w}$ .
- the Reynolds stresses  $\overline{u'^2}$ ,  $\overline{v'^2}$ ,  $\overline{w'^2}$  and  $\overline{u'v'}$ .
- the triple-velocity correlations  $\overline{u'^3}$ ,  $\overline{u'v'^2}$ ,  $\overline{u'w'^2}$ ,  $\overline{v'u'^2}$ ,  $\overline{v'^3}$  and  $\overline{v'w'^2}$ .

The overall uncertainty in the measured statistical quantities is as follows (see Ab-sil [1995] for a detailed analysis of the various error sources). The mean-velocity components are accurate up to  $\pm 1\%$  of  $U_{ref}$ . The Reynolds normal stresses and the Reynolds shear stress are accurate up to  $\pm 5\%$  and  $\pm 8\%$  of their local maximum values, respectively. The uncertainty in the triple-velocity correlations is about  $\pm 20\%$  of the local maximum value.

Autocorrelation functions (set-up 2) of the streamwise velocity component were measured in the wake along the contour of maximum kinetic energy (10 locations) and along the centreline (9 locations). Furthermore, the wake traverse at  $x = 30$  mm (and  $x = 130$  mm) was surveyed at 7 (8) locations. At each measurement station the one-component LDA acquired  $4.5 \times 10^5$  samples at a mean data rate of about 1 kHz. These conditions were selected to obtain accurate estimates of the acf at small lag times, thereby enabling the determination of the Taylor time scales.

Spatial correlation functions (set-up 3) were measured at a limited number of locations in the wake, mainly along the contour of maximum kinetic energy and along the centreline. Most of the spatial correlations concerned the streamwise velocity component, but spatial correlations of the lateral and spanwise velocity components were also measured to assess the degree of anisotropy of the turbulence. Integral length scales were not measured, because priority was given to the small scale behaviour of the scfs to determine the Taylor length scales.

The merits of the different velocity bias correction methods were extensively discussed in Chapter 4. The algorithms that were used to compute statistical quantities in the present study are given below. All single-point statistics were calculated using the 3D inverse-velocity weighting. For example, the mean velocity in  $x$ -direction is calculated from

$$\bar{u} = \frac{\sum_{i=1}^N u_i \omega_i}{\sum_{i=1}^N \omega_i}, \quad (5.1)$$

while the 3D inverse-velocity weighting factor was evaluated as

$$\omega_i = \frac{1}{\sqrt{u_i^2 + v_i^2 + w_i^2}}, \quad (5.2)$$

because the three velocity components were measured simultaneously in an approximately spherical measuring volume. The remaining mean-velocity components, the Reynolds stresses and the triple-velocity correlations were evaluated from expressions similar to Eq (5.1). The autocorrelation functions were computed using the local normalisation procedure:

$$\bar{\rho}(k\Delta\tau) = \frac{\text{sum}\{u'_i u'_j \omega_i \omega_j (k\Delta\tau)\}}{\sqrt{\text{sum}\{u_i'^2 \omega_i \omega_j\}(k\Delta\tau) \text{sum}\{u_j'^2 \omega_i \omega_j\}(k\Delta\tau)}}. \quad (5.3)$$

The weighting factor  $\omega_i$  again accounts for the effects of the velocity bias. Because the acfs were measured with a one-component LDA, the use of the inverse-velocity weighting is inappropriate. The transit times were used as a weighting factor, i.e.  $\omega_i = tr_i$ .

The spatial correlation function of the streamwise velocity component with a streamwise spatial separation  $\Delta x$  was computed as

$$\rho_{11}(\Delta x_1, 0, 0) \equiv \rho_{11}(\Delta x) = \frac{\sum_{i=1}^N u'_i(x)u'_i(x + \Delta x)}{(\sum_{i=1}^N u'_i(x)^2 \sum_{i=1}^N u'_i(x + \Delta x)^2)^{1/2}}, \quad (5.4)$$

Similar expressions were used for the spatial correlation functions of different velocity components and different spatial separations. Note that the spatial correlation function  $\rho_{11}(\Delta x_1, 0, 0)$  is not corrected for the effects of the velocity bias.

An executable of the program *BURSTware* (version 3.0) developed by Dantec was used during the data acquisition stage. The further reduction of the raw data files to the various statistical quantities was done using the software developed by Passchier [1992].

## 5.2 Numerical Investigation

A detailed comparison between the experimental data and the numerical solutions of the Reynolds-averaged Navier-Stokes equations can be used to trace the deficiencies in existing turbulence models. The comparison may also suggest ways to improve these models for predictions in turbulent wakes with strong adverse pressure gradients. In the present investigation the continuity equation, Eq (2.8), and the Reynolds-averaged NS equations, Eq (2.9), were numerically solved for the two-dimensional, turbulent near wake in adverse pressure gradient. Two turbulence models were considered; the two-equation  $k-\epsilon$  model of Launder and Sharma [1974] and the (differential) Reynolds-stress transport model of Hanjalić et al. [1992]. These two models yielded excellent results for the near wake of the flat plate in zero pressure gradient, see Section 2.2.2 for details. However, the standard  $k-\epsilon$  model is known to be inaccurate in flows with adverse pressure gradients. It is therefore unrealistic to expect this model to perform well in the near wake that is subjected to a strong adverse pressure gradient. The expectations regarding the performances of the RSTM in the near wake in adverse pressure gradient are higher. Details on both turbulence models are given below.

### Low-Reynolds-number $k-\epsilon$ model

The use of the  $k-\epsilon$  model was first reported by Jones and Launder [1972]. Since then, the model has been applied to a wide variety of flows in both industry and research, and it may be considered as the most popular two-equation turbulence model today. The  $k-\epsilon$  model employs the Boussinesq approximation, which relates the Reynolds stresses to the mean strain rate according to

$$-\overline{u'_i u'_j} = \nu_t \left( \frac{\partial \overline{u}_i}{\partial x_j} + \frac{\partial \overline{u}_j}{\partial x_i} \right) - \frac{2}{3} k \delta_{ij}. \quad (5.5)$$

The eddy viscosity,  $\nu_t$ , has dimensions *length*  $\times$  *velocity*. As discussed in Section 2.1.4, the  $k-\epsilon$  model derives the length scale and the velocity scale from the turbulence kinetic

energy,  $k$ , and the dissipation,  $\epsilon$ . More specific:  $k^{1/2}$  is used as the velocity scale and the length scale is given by  $k^{3/2}/\epsilon$ . This yields the following expression for the eddy viscosity

$$\nu_t = c_\mu f_\mu \frac{k^2}{\epsilon}. \quad (5.6)$$

The kinetic energy  $k$  and the turbulent energy dissipation  $\epsilon$  are described by the following two differential equations

$$\frac{\partial k}{\partial t} + \bar{u}_j \frac{\partial k}{\partial x_j} = \frac{\partial}{\partial x_j} \left[ \left( \nu + \frac{\nu_t}{\sigma_k} \right) \frac{\partial k}{\partial x_j} \right] + \nu_t \left( \frac{\partial \bar{u}_i}{\partial x_j} + \frac{\partial \bar{u}_j}{\partial x_i} \right) \frac{\partial \bar{u}_i}{\partial x_j} - \epsilon + D, \quad (5.7)$$

and

$$\frac{\partial \epsilon}{\partial t} + \bar{u}_j \frac{\partial \epsilon}{\partial x_j} = \frac{\partial}{\partial x_j} \left[ \left( \nu + \frac{\nu_t}{\sigma_\epsilon} \right) \frac{\partial \epsilon}{\partial x_j} \right] + E + c_{\epsilon_1} f_1 \frac{\epsilon}{k} P_k - c_{\epsilon_2} f_2 \frac{\epsilon^2}{k}. \quad (5.8)$$

The above equations for  $\nu_t$ ,  $k$  and  $\epsilon$  are essentially identical to the corresponding equations given in Section 2.1.4, i.e. Eq (2.18), Eq (2.19) and Eq (2.21), respectively. However, the latter equations do not include the low-Reynolds-number functions  $f_\mu$ ,  $f_1$ ,  $f_2$ ,  $D$  and  $E$ . These functions are introduced in the turbulence model to bring into account the effects of wall proximity and viscosity. An overview of different low-Reynolds-number formulations is given by Patel et al. [1985]. In the present investigation the formulation of Launder and Sharma [1974] is adopted, i.e.

$$\begin{aligned} f_\mu &= \exp \left( \frac{-3.4}{(1 + Re_t/50)^2} \right), \\ f_1 &= 1.0, \\ f_2 &= 1.0 - 0.3 \exp(-Re_t^2), \\ D &= -2\nu \frac{\partial \sqrt{k}}{\partial x_j} \frac{\partial \sqrt{k}}{\partial x_j}, \\ E &= 2\nu \nu_t \frac{\partial^2 \bar{u}_i}{\partial x_j \partial x_k} \frac{\partial^2 \bar{u}_i}{\partial x_j \partial x_k}, \end{aligned} \quad (5.9)$$

where  $Re_t$  is the turbulent Reynolds number, defined as

$$Re_t = \frac{k^2}{\nu \epsilon}. \quad (5.10)$$

The high-Reynolds-number closure coefficients have the standard values [Launder and Sharma 1974]:

$$c_\mu = 0.09, \quad c_{\epsilon_1} = 1.44, \quad c_{\epsilon_2} = 1.92, \quad \sigma_k = 1.0 \quad \text{and} \quad \sigma_\epsilon = 1.3. \quad (5.11)$$

### Reynolds-stress transport model

The Reynolds-stress transport model (RSTM) has its origin in the exact transport equation for the Reynolds stresses, Eq (2.10). After a rearrangement of its terms, the exact

transport equation for  $\overline{u'_i u'_j}$  reads

$$\begin{aligned} \frac{\partial \overline{u'_i u'_j}}{\partial t} + \overline{u_k} \frac{\partial \overline{u'_i u'_j}}{\partial x_k} &= - \left( \overline{u'_i u'_k} \frac{\partial \overline{u_j}}{\partial x_k} + \overline{u'_j u'_k} \frac{\partial \overline{u_i}}{\partial x_k} \right) + \frac{\partial}{\partial x_k} \nu \frac{\partial \overline{u'_i u'_j}}{\partial x_k} \\ &+ D_{ij}^t + \Phi_{ij} - \epsilon_{ij}, \end{aligned} \quad (5.12)$$

where

$$D_{ij}^t = \frac{\partial}{\partial x_k} \left[ -\overline{u'_i u'_j u'_k} - \frac{1}{\rho} \overline{p' u'_i} \delta_{jk} - \frac{1}{\rho} \overline{p' u'_j} \delta_{ik} \right], \quad (5.13)$$

$$\Phi_{ij} = \frac{p'}{\rho} \left( \frac{\partial \overline{u'_i}}{\partial x_j} + \frac{\partial \overline{u'_j}}{\partial x_i} \right), \quad (5.14)$$

$$\epsilon_{ij} = 2\nu \frac{\partial \overline{u'_i}}{\partial x_l} \frac{\partial \overline{u'_j}}{\partial x_l}. \quad (5.15)$$

As explained in Section 2.1.3, the quantities  $D_{ij}^t$ ,  $\Phi_{ij}$ ,  $\epsilon_{ij}$  contain unknown correlations that have to be modeled. The remainder of this section describes the RSTM as proposed by Hanjalić et al. [1992].

The triple-velocity correlations,  $\overline{u'_i u'_j u'_l}$ , and the pressure-velocity correlations,  $(\overline{p' u'_i} \delta_{jl} + \overline{p' u'_j} \delta_{il})/\rho$ , are taken together and modeled using the generalized gradient-diffusion hypothesis [Daly and Harlow 1970], i.e.

$$D_{ij}^t \equiv \frac{\partial}{\partial x_k} \left[ C_s \frac{k}{\epsilon} \overline{u'_k u'_l} \frac{\partial \overline{u'_i u'_j}}{\partial x_l} \right], \quad (5.16)$$

where  $C_s$  is a closure coefficient with value 0.22. Note that the modeling of the turbulent diffusion is very similar to the approach followed in the  $k - \epsilon$  model, see Eq (2.20). The pressure-strain correlation,  $\Phi_{ij}$ , is commonly split into two parts,

$$\Phi_{ij} = \Phi_{ij,1} + \Phi_{ij,2}, \quad (5.17)$$

which are known as the slow pressure strain and the rapid pressure strain, respectively. The slow pressure strain,  $\Phi_{ij,1}$ , is modeled using Rotta's "return-to-isotropy hypothesis," i.e.

$$\Phi_{ij,1} = -C_1 \epsilon a_{ij}, \quad (5.18)$$

where  $a_{ij}$  is the Reynolds-stress anisotropy tensor, defined as

$$a_{ij} = \frac{\overline{u'_i u'_j}}{k} - \frac{2}{3} \delta_{ij}. \quad (5.19)$$

The rapid-strain term,  $\Phi_{ij,2}$ , is modeled using the "isotropization-of-production hypothesis" [Launder et al. 1975]

$$\Phi_{ij,2} = -C_2 \left( P_{ij} - \frac{2}{3} P_k \delta_{ij} \right), \quad (5.20)$$



where  $P_k = \frac{1}{2}P_{ii}$  is the production of the turbulence kinetic energy,  $k$ . The  $C_1$  and  $C_2$  that appear in Eq (5.18) and Eq (5.20), respectively, are functions of the turbulent Reynolds number,  $Re_t$ , and parameters derived from the Reynolds-stress anisotropy tensor, such as the "flatness,"  $A$ , defined by

$$A = 1 - \frac{9}{8}(A_2 - A_3), \quad (5.21)$$

where  $A_2 = a_{ij}a_{ji}$  and  $A_3 = a_{ij}a_{jk}a_{ki}$  are the first and second invariants of the Reynolds-stress anisotropy tensor,  $a_{ij}$ . The values of  $C_1$  and  $C_2$  depend on  $Re_t$ ,  $A_2$  and  $A_3$  as suggested by Launder and Shima [1989], i.e.

$$C_2 = 0.75 A^{1/2}, \quad (5.22)$$

$$C_1 = 1 - f_s + 2.58AA_2^{1/4} [1 - \exp(-0.0067Re_t^2)], \quad (5.23)$$

where  $f_s$  is a low-Reynolds-number function given by

$$f_s = \frac{1}{(1 + 0.1 Re_t)}. \quad (5.24)$$

The RSTM as formulated by Hanjalić et al. [1992] contains expressions for the effects of the wall reflections of the pressure fluctuations on the pressure-strain correlation. For compactness, these expressions are omitted here, because the wall-reflection terms are set to zero for computations in the wake.

The dissipation tensor  $\epsilon_{ij}$  is modeled as

$$\epsilon_{ij} = f_s \epsilon_{ij}^* + (1 - f_s) \frac{2}{3} \delta_{ij} \epsilon, \quad (5.25)$$

where

$$\epsilon_{ij}^* = \frac{\epsilon}{k} \left[ \frac{\overline{u'_i u'_j} + f_s (\overline{u'_i u'_k n_j n_k} + \overline{u'_j u'_k n_i n_k} + \overline{u'_k u'_l n_k n_l n_i n_j})}{1 + \frac{3}{2} \frac{\overline{u'_p u'_q} n_p n_q}{k} f_s} \right]. \quad (5.26)$$

Here,  $\vec{n}$  is the unit-vector normal to the wake centreline, i.e.  $n_2 = 1$ ,  $n_1 = n_3 = 0$ . For fully turbulent and isotropic flow  $f_s = 0$ , so that the dissipation tensor  $\epsilon_{ij}$  obtains its isotropic value

$$\epsilon_{ij} = \frac{2}{3} \delta_{ij} \epsilon. \quad (5.27)$$

The Hanjalić RSTM employs the following differential equation for the isotropic dissipation  $\epsilon$

$$\begin{aligned} \frac{\partial \epsilon}{\partial t} + \overline{u_k} \frac{\partial \epsilon}{\partial x_k} &= \frac{\partial}{\partial x_k} \left[ \left( \nu + C_\epsilon \frac{k}{\epsilon} \overline{u'_i u'_j} \right) \frac{\partial \epsilon}{\partial x_l} \right] - C_{\epsilon_1} f_{\epsilon_1} \frac{\epsilon}{k} \overline{u'_i u'_j} \frac{\partial \overline{u_i}}{\partial x_j} \\ &- C_{\epsilon_2} f_{\epsilon_2} \frac{\epsilon \bar{\epsilon}}{k} + C_{\epsilon_3} \nu \frac{k}{\epsilon} \overline{u'_j u'_k} \frac{\partial^2 \overline{u_i}}{\partial x_j \partial x_l} \frac{\partial^2 \overline{u_i}}{\partial x_k \partial x_l} + S_{\epsilon_4}, \end{aligned} \quad (5.28)$$

where  $\tilde{\epsilon}$  is given by

$$\tilde{\epsilon} = \epsilon - 2\nu \left( \frac{\partial \sqrt{k}}{\partial x_j} \right)^2, \quad (5.29)$$

so that  $\epsilon = 0$  is prescribed at a solid wall. In its original formulation [Hanjalić et al. 1992] the equation for  $\epsilon$  did not include the term  $S_{\epsilon_4}$ . This term was later added by Jakirlić et al. [1994] to improve the numerical prediction of flows with strong streamwise pressure gradients. For a two-dimensional flow  $S_{\epsilon_4}$  is given by

$$S_{\epsilon_4} = C_{\epsilon_4} \frac{\epsilon}{k} \left( \overline{v'^2} - \overline{u'^2} \right) \frac{\partial \bar{u}}{\partial x}, \quad (5.30)$$

where  $C_{\epsilon_4}$  is a closure coefficient. The inclusion of  $S_{\epsilon_4}$  is meant to differentiate the effects of the “rotational strains” and the “irrotational strains” on the source dissipation, as suggested by Hanjalić and Launder [1980]. Note that  $(\overline{v'^2} - \overline{u'^2}) \partial \bar{u} / \partial x$  is the production of kinetic energy by the working of Reynolds stresses against an irrotational strain. This type of production is sometimes called the “normal production.” The term  $S_{\epsilon_4}$  favours the increase of dissipation in response to normal production above the increase due to “shear production,” when it is used in conjunction with a positive value of the closure coefficient  $C_{\epsilon_4}$ . This means that the value of the closure coefficient  $C_{\epsilon_1}$  in the source term of Eq (5.28), is adapted depending on the type of strain that causes the increase of  $P_k$ .

The high-Reynolds-number closure coefficients in Eq (5.28) have the following values [Hanjalić et al. 1992]

$$C_\epsilon = 0.18, C_{\epsilon_1} = 1.44, C_{\epsilon_2} = 1.92, C_{\epsilon_3} = 0.5 \quad \text{and} \quad C_{\epsilon_4} = 1.16. \quad (5.31)$$

The low-Reynolds-number functions are given by

$$f_{\epsilon_1} = 1.0 \quad \text{and} \quad f_{\epsilon_2} = 1.0 - \frac{0.52}{1.92} \exp(-(Re_t/6)^2). \quad (5.32)$$

### Numerical procedure

To solve the equations numerically, the spatial derivatives in the equations are discretized with the finite volume method on a staggered grid. A Cartesian grid was used with a strong refinement in the  $y$ -direction near the centreline, whereas the grid was equidistant in the  $x$ -direction. The inlet (west) and the outlet (east) of the computational domain were located at  $x = 17$  mm and  $x = 600$  mm, respectively. The outer edge (north) of the domain was located at  $y = 200$  mm. Only one wake half was calculated because flow symmetry is assumed with respect to the centreline at  $y = 0$  mm (south). The convection terms are discretized with the second-order accurate upwind scheme. An unsteady fully implicit time integration is performed to obtain the steady solution at large time. At each new time level the discrete systems belonging to each of the transport equations are iteratively solved by a line Gauss-Seidel method. Alternating Gauss-Seidel sweeps from the west to the east side and from the east to the west side of the computational domain are performed. After each sweep the pressure is calculated from the discretized

Poisson equation for the pressure-correction by using a conjugate gradient solver. The calculation was started with a certain initial solution at  $t = 0$  and the time integration is performed until a steady final solution is reached.



## Chapter 6

# Results of the Investigation of the Wake

Chapter 6 reports the results of both the experimental and the numerical investigations of the adverse pressure gradient wake. Section 6.1 presents the experimental results regarding the mean flow and the turbulence statistics. This section also provides an in-depth analysis to aid the interpretation of the experimental results. Section 6.2 reports on the comparison between the experimental findings and the outcome of the computations in the wake. Section 6.3 presents the results of the spatial correlation measurements. The outcome of the spectral measurements is given in Section 6.4. Finally, Section 6.5 discusses explanations for some of the findings of the investigation.

### 6.1 Results of the Single-Point Measurements

#### 6.1.1 Pressure distribution

Pressure measurements were performed in the undisturbed flow outside the wake using a static pressure probe. The measurements were taken along a line given by  $y = 130.0 + 0.14x$ , where  $x$  and  $y$  were measured in mm. This is approximately a streamline well outside the wake. The static pressures were also measured along a number of lines  $x = \text{constant}$  to determine the lateral pressure gradient. The measurements allowed an accurate interpolation of the static-pressure distribution along the edge of the computational domain at  $y = 200$  mm. Static pressures were not measured in the wake itself, because of the high local turbulence intensities.

The distribution of the static-pressure coefficient,  $C_p \equiv 2(\bar{p} - \bar{p}_{ref})/(\rho U_{ref}^2)$ , along the line  $y = 200$  mm is shown in Fig. 6.1. It is seen that the adverse pressure gradient gradually decreases in the downstream direction, but it remains positive over the complete region of investigation.

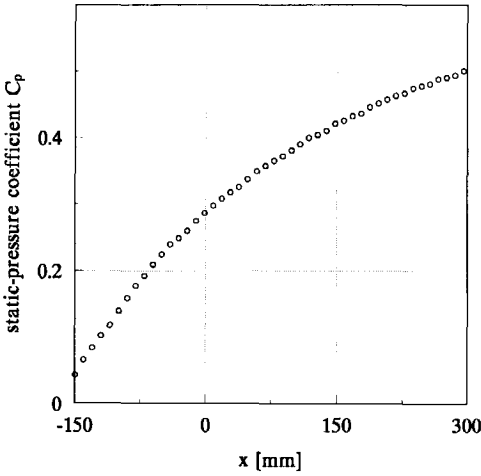


Figure 6.1: Static-pressure distribution at  $y = 200$  mm.

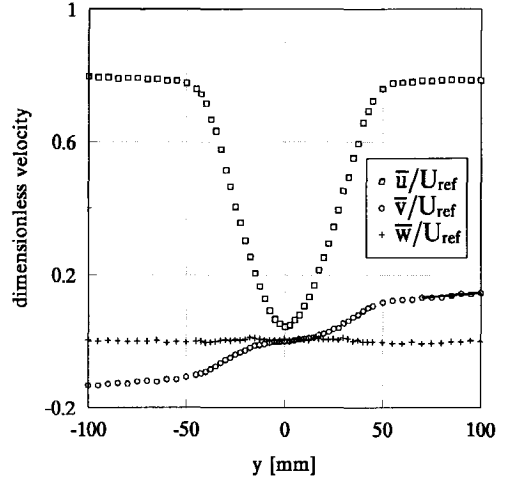


Figure 6.2: Components of the mean velocity at  $x = 53$  mm. The line drawn between  $70 < y < 100$  is the  $\bar{v}$  distribution that is computed from the static pressure measurements and the continuity equation.

## 6.1.2 Mean-flow characteristics

### Mean-velocity components and integral parameters

Figure 6.2 shows the three components of the mean velocity measured at station  $x = 53$  mm. The centreline velocity is small, but there is not yet mean-flow reversal at this station. Outside the wake, the transverse component shows an increase in the positive  $y$ -direction. This is a consequence of the flow developing in a diffusing tunnel section, because according to the continuity equation, Eq (2.8), a decrease of  $\bar{u}$  in the  $x$ -direction causes an increase of  $\bar{v}$  in the  $y$ -direction. The continuity equation together with the measured static-pressure distribution were used to compute the value of  $\partial\bar{v}/\partial y$  at location  $x = 53$  mm,  $y = 100$  mm. The solid line in Fig. 6.2 shows the inferred distribution of  $\bar{v}$  (matched at  $y = 100$  mm) outside the wake, i.e.,

$$\begin{aligned}\bar{v} &= \bar{v}_m + \frac{\partial\bar{v}}{\partial y}y \\ &= \bar{v}_m - \frac{y}{\rho\bar{u}_m} \frac{\partial\bar{p}}{\partial x},\end{aligned}\tag{6.1}$$

where the subscript  $m$  denotes a measured value at location  $x = 53$  mm,  $y = 100$  mm. The good agreement between the measured and the inferred  $\bar{v}$ -distribution indicates two-dimensional flow. The spanwise velocity,  $\bar{w}$ , is smaller than 1.6 % of the edge velocity at all locations. This is another indication for two-dimensional flow. Furthermore, it is seen that the mean flow is reasonably symmetric.

The streamwise development of the  $x$ -component of the mean velocity is shown in Fig. 6.3. The five stations in the upper half of the graph were measured in the boundary

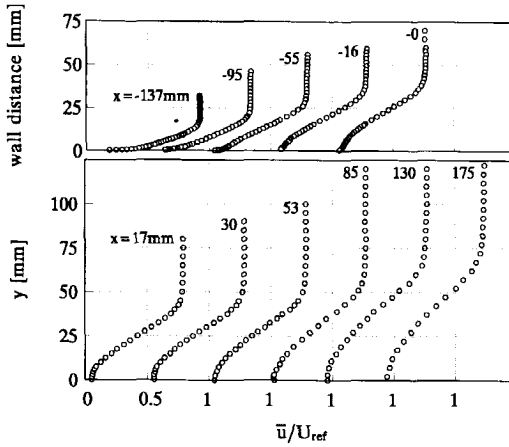


Figure 6.3: Streamwise development of the  $x$ -component of the mean velocity. *top*: boundary layer, *bottom*: wake.

layer of the plate. The boundary layer at the station furthest upstream ( $x = -137$  mm) has a displacement thickness  $\delta^* = 3.7$  mm and a shape factor  $H = 1.62^1$ . The thickness of the boundary layer rapidly increases owing to the large pressure rise, and near the trailing edge the velocity profiles develop an inflexion point. The boundary layer is still attached at the trailing edge. There, the characteristics of the mean-velocity profile are  $H = 2.91$  and  $\delta^* = 18.9$  mm.

A more detailed view of the streamwise development of the integral parameters,  $H$ ,  $\delta^*$  and  $\theta$  is given in Figs. 6.4 and 6.5. After a steady rise in the boundary layer, the shape factor remains at a more or less constant value of about 3.2 in the wake up to  $x = 85$  mm. The nearly constant value of  $H$  indicates a nearly constant centreline velocity in that region. For larger values of  $x$  the shape factor increases again. Clearly, for trailing-edge distances up to  $x = 175$  mm, the present wake shows no tendency to attain a self-similar behaviour, which is characterized by a constant shape factor.

The momentum thickness increases towards the trailing edge due to the effects of the skin friction and the adverse pressure gradient. The latter alone causes the increase of the momentum thickness in the wake. The integral momentum equation was used to assess the self-consistency of the experimental data, despite the fact that the integral momentum equation is based on the “thin-shear layer” approximation so that its accuracy is questionable in this particular flow. The integral momentum equation

$$\frac{d\theta}{dx} = -(2 + H) \frac{dU_e}{dx} \frac{\theta}{U_e} + \frac{C_f}{2} + \frac{1}{U_e^2} \frac{d}{dx} \int_0^\infty (\overline{u'^2} - \overline{v'^2}) dy, \quad (6.2)$$

was integrated with respect to  $x$  using the experimental values of the shape factor  $H$ , the static-pressure coefficient  $C_p$  and the skin-friction coefficient  $C_f$ . Details on the measurement of the skin friction will be discussed shortly. The constant of integration

<sup>1</sup>As described in Section 2.2.2, the values of the integral parameters  $\delta^*$  and  $\theta$  are determined directly from their definitions, Eq (2.50) and Eq (2.51), respectively.

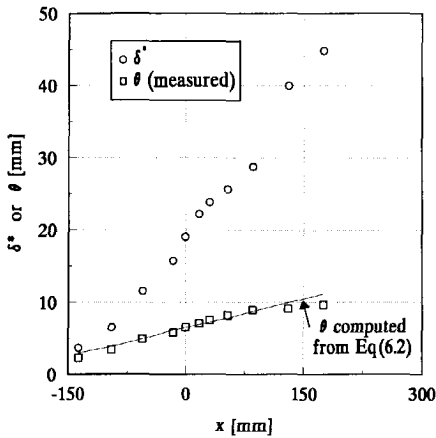


Figure 6.4: Streamwise development of integral parameters  $\delta^*$  and  $\theta$ .

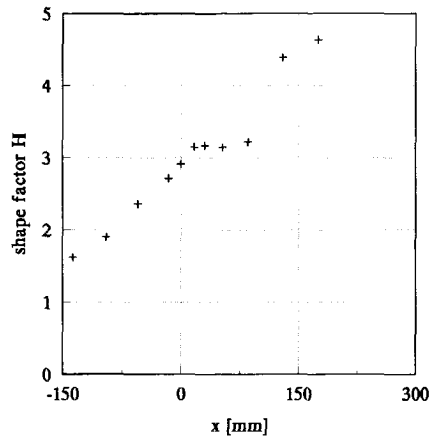


Figure 6.5: Streamwise development of the shape factor  $H \equiv (\delta^*/\theta)$ .

was chosen such that the inferred distribution of  $\theta$  matched the measured distribution at the trailing edge  $x = 0$ . The results of this procedure are shown in Fig. 6.4 as a solid line. Two comments on the development of the momentum thickness are in place. First, the inclusion of the last term on the right-hand side of Eq (6.2), i.e. the term that incorporates the effect of the streamwise development of Reynolds stresses, is important in this wake. Without this term the computed values of  $\theta$  would increase at a much slower rate than in the experiments. Secondly, the pressure-gradient term is much larger than the skin-friction term in the region of the flow that is covered by the experiments. As a result, the contribution of the skin friction to the growth rate of  $\theta$  is very small, which is essentially different from the zero-pressure-gradient boundary layer.

### Skin-friction data

The skin-friction coefficient  $C_f$  was determined by means of the Clauser-chart method as described in Section 2.1.6. Figure 6.6 portrays the Clauser charts for each boundary-layer station. It is well known that errors in the determination of the wall distance of the LDA measuring volume can have large effects on the outcome of the Clauser-chart method. In the present experiment the wall distance could be determined with an accuracy of  $\pm 0.03$  mm. The error bars in the Clauser chart for station  $x = -137$  mm indicate that a  $\pm 0.03$  mm error will have a negligible effect on the outcome of the matching procedure. Also shown in the Clauser chart for  $x = -137$  mm are the curves for  $C_f = 0.0026 \pm 0.0002$  to indicate the sensitivity of the matching procedure to variations in the selected value of  $C_f$ .

For  $x = -137$  mm it is seen that Reichardt's formulation of the law of the wall,

$$u^+ = \frac{1}{\kappa} \ln(1 + \kappa y^+) + \frac{C\kappa - \ln\kappa}{\kappa} \left( 1 - e^{-\frac{y^+}{11}} - \frac{y^+}{11} e^{-0.33y^+} \right), \quad (6.3)$$

agrees well with the experimental data up to  $y^+ \approx 50$ . This range of  $y^+$  values does not



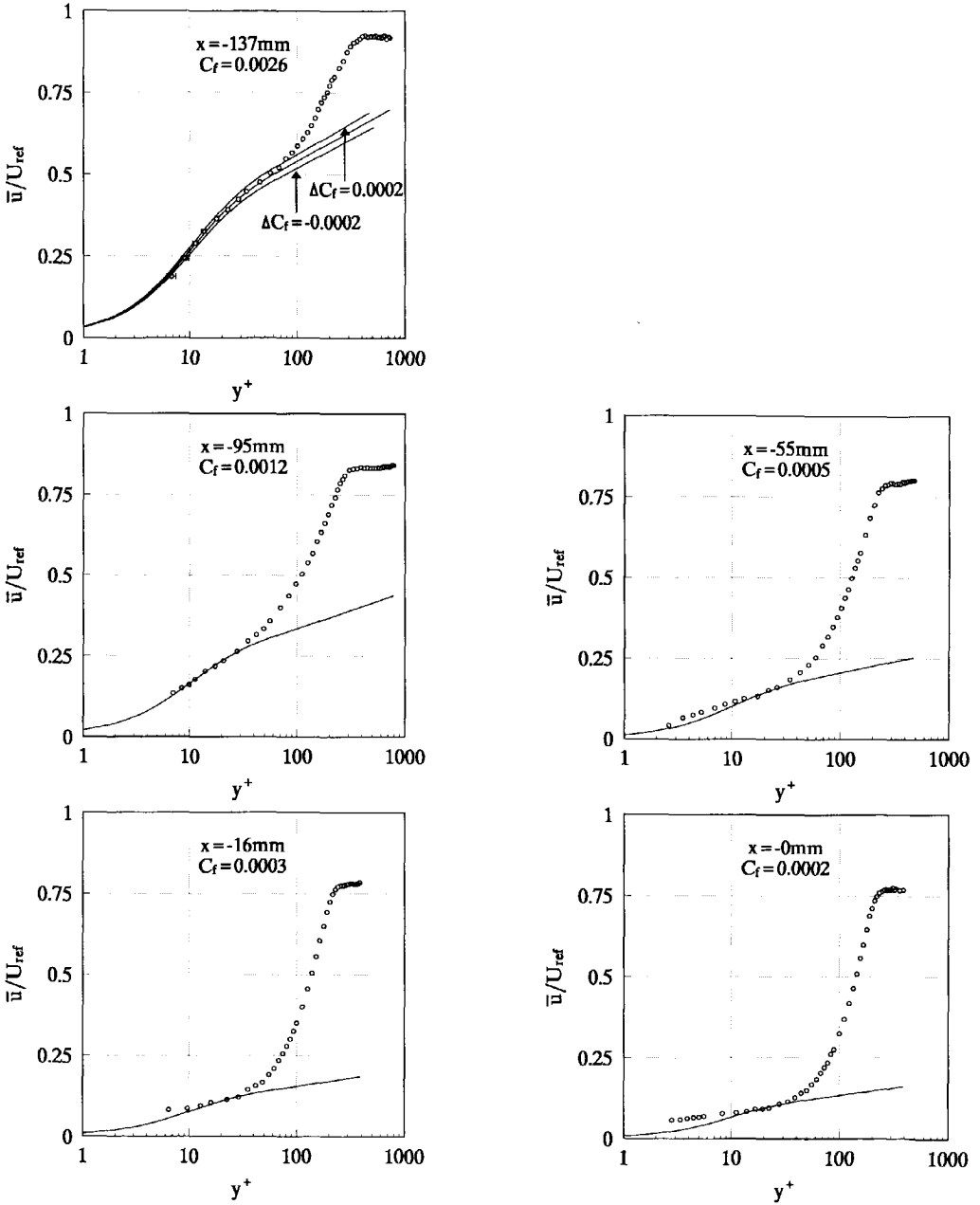


Figure 6.6: Clauser charts for different boundary-layer stations.

include the logarithmic region of Reichardt's mean-velocity distribution. The absence of any noticeable logarithmic behaviour of the measured mean-velocity profile is not surprising considering the relatively small value of  $R_\theta$ . At  $x = -137$  mm the value of  $R_\theta$  is 1430. It is known from both experiments and DNS studies [Spalart 1988] that the boundary layer of a flat plate in zero pressure gradient has only a small logarithmic region at this Reynolds number. In addition to the effect of the low-Reynolds number, there is the effect of the adverse pressure gradient. As can be seen from Fig. 6.6, the discrepancy between Reichardt's mean-velocity distribution and the experimental data increases when approaching the trailing edge. The discrepancy increases especially near the outer region, and it has a tendency to propagate into the inner region. For example, at  $x = -95$  mm there is good overlap up to  $y^+ = 30$ , but at the trailing edge ( $x = -0$  mm) it has become practically impossible to match Reichardt's velocity distribution to the experimental data. This underlines the basic weakness of the Clauser-chart method: the reliance on the validity of the law of the wall. It is unrealistic to expect that the mean-velocity distribution in a boundary layer that is in strong non-equilibrium can be described by a law of the wall. Consequently, the skin-friction coefficients that follow from the Clauser charts become increasingly unreliable when moving towards the trailing edge. Unfortunately, it was not possible to determine the friction velocity directly from the slope of the mean-velocity profiles at the wall, because the minimum wall distance for the boundary-layer traverses is approximately 0.3 mm, corresponding to  $y^+ \approx 6$ . No further attempts were made to determine the skin friction.

### Centreline velocity

It is seen from Fig. 6.3 that, in addition to an increase of the width of the wake, the wake defect increases in the downstream direction. A detailed view of the mean velocity on the wake centreline,  $\bar{u}_{cl}$ , is shown in Fig. 6.7. The graph shows that there is an initial increase of the centreline velocity in the region between the trailing edge (where  $\bar{u}_{cl} = 0$ ) and the first measuring point at  $x \approx 2$  mm. This is followed by a gradual decrease of the centreline velocity and a backflow region is formed downstream of  $x \approx 80$  mm. The centreline velocity decreases to about  $-0.15U_e$  at the measurement station farthest downstream. There, the lateral extent of the backflow region has grown to approximately 29 mm. Because the pressure gradient relaxes beyond  $x \approx 400$  mm, the mean velocity will increase somewhere further downstream. Unfortunately, this region was not covered by the present experiment.

Also plotted in Fig. 6.7 are the results for the zero-pressure-gradient wake measured by Starke [2000], who used the same wake generator and experimental facility as in the present investigation. Starke's data clearly show a logarithmic behaviour of the centreline velocity for large trailing-edge distances. This common feature of the constant-pressure wake of a flat plate was discussed in some detail in Section 2.2.1. A qualitative explanation for the large differences between the two wakes follows from the Reynolds-averaged momentum equation, Eq (2.9). For the  $x$ -direction this equation reads

$$\bar{u} \frac{\partial \bar{u}}{\partial x} + \bar{v} \frac{\partial \bar{u}}{\partial y} = -\frac{1}{\rho} \frac{\partial \bar{p}}{\partial x} - \frac{\partial \overline{u'^2}}{\partial x} - \frac{\partial \overline{u'v'}}{\partial y} + \nu \frac{\partial^2 \bar{u}}{\partial x^2} + \nu \frac{\partial^2 \bar{u}}{\partial y^2}. \quad (6.4)$$

Of course,  $\bar{v} = 0$  along the centreline. Furthermore, the viscous terms can be neglected

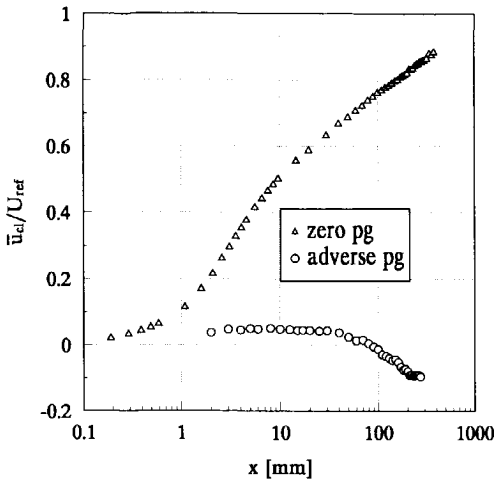


Figure 6.7: Mean velocity on the centreline for two pressure gradients.

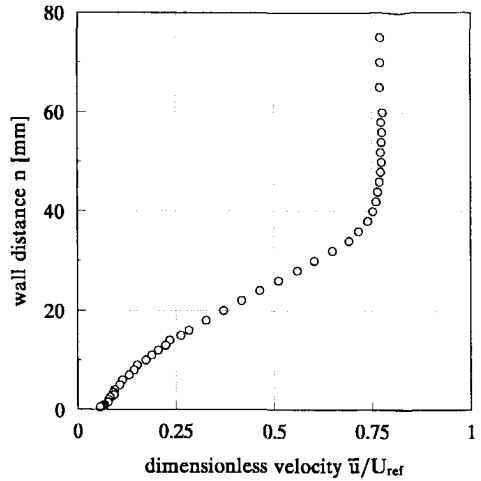


Figure 6.8: Mean-velocity distribution at the trailing edge ( $x = -0$  mm).

some distance from the trailing edge. In the zero-pressure-gradient wake the centreline velocity rapidly increases owing to the large gradient in Reynolds shear stress. The shear stress gradient is smaller in the adverse-pressure-gradient wake. In addition, the adverse pressure gradient stimulates the streamwise growth of the Reynolds normal stress. This opposes the tendency of the shear-stress gradient to accelerate the mean flow. In the present wake, the combined effects of the adverse pressure gradient and the two Reynolds-stress gradients have resulted in an increase of the maximum velocity defect instead of the decrease that is found in case of a mild adverse or zero pressure gradient.

Interestingly, the mean-flow reversal begins some distance downstream of the trailing edge at  $x \approx 80$  mm. This means that “free separation” takes place, since the recirculation zone is detached from the surface of the plate. Clearly, the mean-flow reversal occurs because the adverse pressure gradient increases the maximum velocity defect of the wake. The decrease of the centreline velocity is preceded by an initial increase directly downstream of the trailing edge. The explanation for this initial increase of the centreline velocity follows from Fig. 6.8, which shows the mean velocity in the boundary layer at the trailing edge ( $x = -0$  mm). As mentioned before, this boundary layer is close to separation. The mean-velocity profile has a wake-like shape, except for a thin region directly above the wall. In this region, the mean velocity rapidly increases from zero at the wall to  $0.07U_e$  at  $n \approx 2$  mm. The relatively high turbulent viscosity in this region is also responsible for the increase of the centreline velocity directly downstream of the trailing edge. Therefore, one may speculate that if the flow were separated at the trailing edge, then there would not have been an initial rise of the centreline velocity. Consequently, a more conventional recirculation zone would have occurred with negative centreline velocities occurring immediately downstream of the trailing edge of the plate.

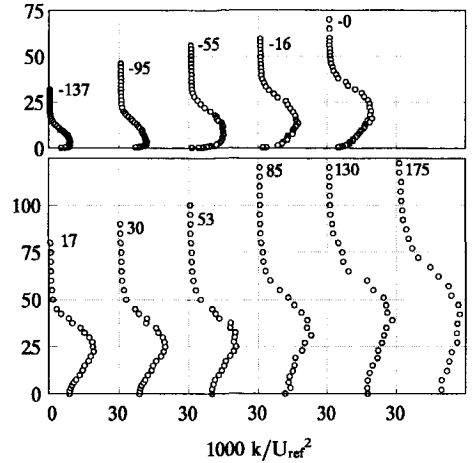
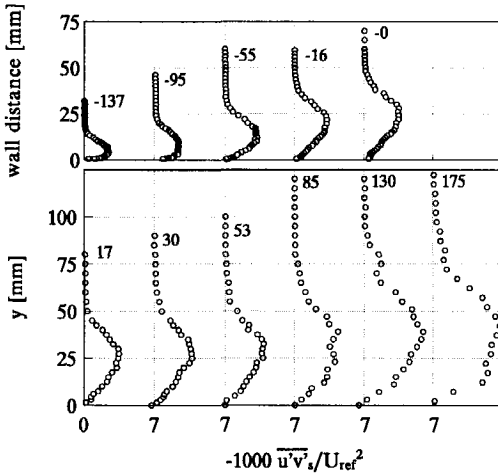


Figure 6.9: Streamwise development of the Reynolds stress  $-\overline{u'v'_s}$ . *top*: boundary layer, *bottom*: wake.

Figure 6.10: Streamwise development of the kinetic energy  $k$ . *top*: boundary layer, *bottom*: wake.

### 6.1.3 Turbulence quantities

#### Reynolds stresses

Recall from Section 5.1 that two coordinate systems are used in the experiments. In the boundary layer the  $s, n, z$ -coordinate system is used with axes parallel and normal to the plate surface. The wind-tunnel axes  $(x, y, z)$  are used as a coordinate system in the wake. The (kinematic) Reynolds shear stress,  $-\overline{u'v'}$ , is dependent on the orientation of the coordinate system. One obvious consequence is the unrealistic variation in the measured shear-stress profiles at the trailing edge, where the coordinate system changes from wall orientation to tunnel-axis orientation. This may complicate the interpretation of the measured data. To avoid these problems, the Reynolds stresses were transformed into local streamline coordinates according to (see Cutler and Johnston [1984])

$$\overline{u'v'_s} = \overline{u'v'} \cos(2\alpha) - \frac{1}{2} (\overline{u'^2} - \overline{v'^2}) \sin(2\alpha), \tag{6.5}$$

where  $\alpha$  is the angle between the mean velocity vector and the  $x$ -axis given by  $\alpha = \tan^{-1}(\overline{v}/\overline{u})$ . The development of  $-\overline{u'v'_s}$  is shown in Fig. 6.9. For the most upstream station, there is little difference between  $\overline{u'v'_s}$  and  $\overline{u'v'}$ , because there the boundary layer thickens only slowly. However, near the trailing edge and in the wake the growth rate of the shear layer has increased dramatically, so that  $\overline{u'v'_s}$  and  $\overline{u'v'}$  are quite different.

The Reynolds normal stresses were summed as  $(\overline{u'^2} + \overline{v'^2} + \overline{w'^2})/2$  to yield the kinetic energy of the velocity fluctuations,  $k$ . Of course,  $k$  is an invariant quantity so that a coordinate transformation similar to Eq (6.5) is unnecessary. The streamwise development of  $k$  is shown in Fig. 6.10. At station  $x = -137$  mm the distribution of  $k$  has its maximum value very close to the wall. This peak gradually moves away from the surface as the flow approaches the trailing edge. This is a common phenomenon in a turbulent

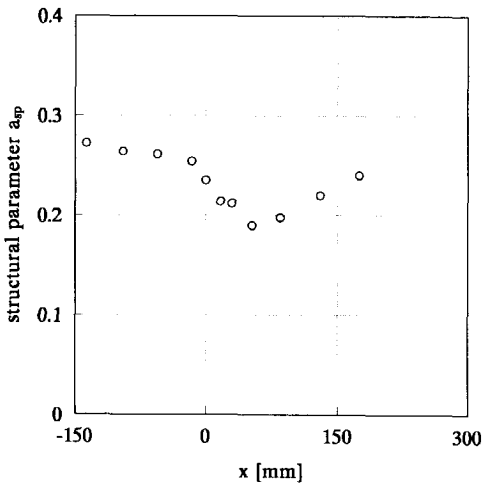


Figure 6.11: The maximum value of the “structural parameter” for various stations in the boundary layer and the wake.

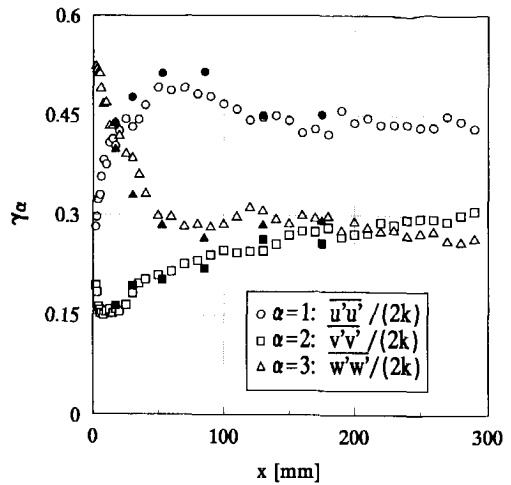


Figure 6.12: The contribution of different Reynolds normal stresses to the kinetic energy along the centreline. The full symbols followed from the lateral traverses at the intersection with the centreline.

boundary layer approaching separation, see e.g. Simpson et al. [1981]. The locations of the peaks practically coincide with the inflexion point of the mean-velocity profiles. As the flow moves past the trailing edge, the kinetic energy continues to rise in the downstream direction. Such a substantial growth of the kinetic energy is not observed in the constant-pressure wake of a flat plate. Usually, there is a slight initial increase of  $k$  when moving downstream of the trailing edge, but the “overshoot” is generally small [Hayakawa and Iida 1992]. The explanation for the large increase of the kinetic energy in the present wake is discussed on page 107, where the balance of the kinetic energy is considered.

A comparison of the results in Figs. 6.9 and 6.10 suggests that there is a similarity between the growth of the shear-stress profiles and the kinetic-energy profiles. The degree of similarity can be expressed by a “structural parameter,” defined as

$$a_{sp} = \frac{-\overline{u'v'_s}}{k} \quad (6.6)$$

Experiments in zero-pressure-gradient boundary layers, see e.g. Townsend [1976], suggest that  $a_{sp} = 0.3$ . For the present experiment the maximum value of  $a_{sp}$  for various stations in the boundary layer and the wake is plotted in Fig. 6.11. The value of  $a_{sp}$  is less than 0.3 for the range of  $x$  values that is covered by the experiments. However, it is likely that  $a_{sp}$  asymptotes to 0.3 for  $x \ll -137$  mm. The decrease of  $a_{sp}$  below 0.3 is common in adverse-pressure-gradient flows.

### Reynolds-stress anisotropy

The contribution of the different Reynolds normal stresses to the kinetic energy can be defined as  $\gamma_\alpha = \overline{u'_\alpha{}^2}/(2k)$ . The quantity  $2(\gamma_\alpha - 1/3)$  is a direct measure for the degree of anisotropy of the Reynolds stress  $\overline{u'_\alpha{}^2}$ , as discussed in Section 5.2, Eq (5.19). Figure 6.12 gives the values of  $\gamma_\alpha$  as determined from the centreline traverse. The full symbols followed from the lateral traverses at the intersection with the centreline. Note that the tunnel-axis coordinates and the streamline coordinates coincide on the centreline of the wake, because of flow symmetry. As a result, there is no need for a transformation of the Reynolds stresses into local streamline coordinates.

It is seen in Fig. 6.12 that the contribution of the lateral fluctuations,  $\overline{v'^2}$ , to the kinetic energy is small close to the trailing edge. In the same region the spanwise velocity fluctuations,  $\overline{w'^2}$ , are dominant. Some of these observations can be explained as follows. Near the plate surface the lateral velocity fluctuations,  $\overline{v'^2}$ , are small compared to the streamwise fluctuations,  $\overline{u'^2}$ , and the spanwise fluctuations,  $\overline{w'^2}$ , owing to the surface boundary conditions. Therefore, the contribution of  $\overline{v'^2}$  to  $k$  at the trailing edge is small. However, this contribution is expected to increase in the wake once the wall constraint is removed at the trailing edge. Consistent with this reasoning, Fig 6.12 indicates a small value of  $\overline{v'^2}/(2k)$  near  $x \approx 0$ , with an increasing trend in the streamwise direction after an initial decay. It should be noted, however, that the reason for this initial decrease of  $\overline{v'^2}/(2k)$  is not known. Also unclear is the reason for the large contribution of the spanwise fluctuations  $\overline{w'^2}$  to  $k$  close to the trailing edge.

### Triple-velocity correlations

The triple-velocity correlations were grouped as  $\overline{u'q'} \equiv (\overline{u'^3} + \overline{u'v'^2} + \overline{u'w'^2})/2$  and  $\overline{v'q'} \equiv (\overline{u'v'^2} + \overline{v'^3} + \overline{v'w'^2})/2$ . As such,  $\overline{u'q'}$  and  $\overline{v'q'}$  are the  $x$ - and  $y$ -components of a vector which is related to the kinetic-energy transport. More precisely:

$$T_k = \frac{\partial(-\overline{u'q'})}{\partial x} + \frac{\partial(-\overline{v'q'})}{\partial y} \quad (6.7)$$

is the transport of turbulence kinetic energy by velocity fluctuations. In the present study all six triple-velocity correlations were measured, so that the components of the transport vector could be determined accurately<sup>2</sup>.

The streamwise development of  $-\overline{u'q'}$  and  $-\overline{v'q'}$  is depicted in Fig. 6.13. The graph on the left-hand side shows that there is a strong growth of  $-\overline{u'q'}$  in the streamwise direction. This indicates that the  $x$ -derivative of  $-\overline{u'q'}$  in Eq (6.7) may not everywhere be negligible compared to the  $y$ -derivative of  $-\overline{v'q'}$ , as is often assumed within the framework of the

<sup>2</sup>In many studies the spanwise velocity component is not measured. In these cases it is sometimes assumed, see e.g. Nakayama and Kreplin [1994], that the triple-velocity correlations that include the unmeasured spanwise velocity correlations  $w'$  can be approximated by

$$\overline{u'w'^2} \approx \frac{1}{2} (\overline{u'^3} + \overline{u'v'^2}) \quad \text{and} \quad \overline{v'w'^2} \approx \frac{1}{2} (\overline{v'u'^2} + \overline{v'^3}).$$

These expressions mimic the well-known approximation for the variance of the spanwise velocity fluctuations  $\overline{w'^2} = (\overline{u'^2} + \overline{v'^2})/2$ . In the present investigation it was found that the above expressions yield inaccurate results, especially for the more downstream stations.

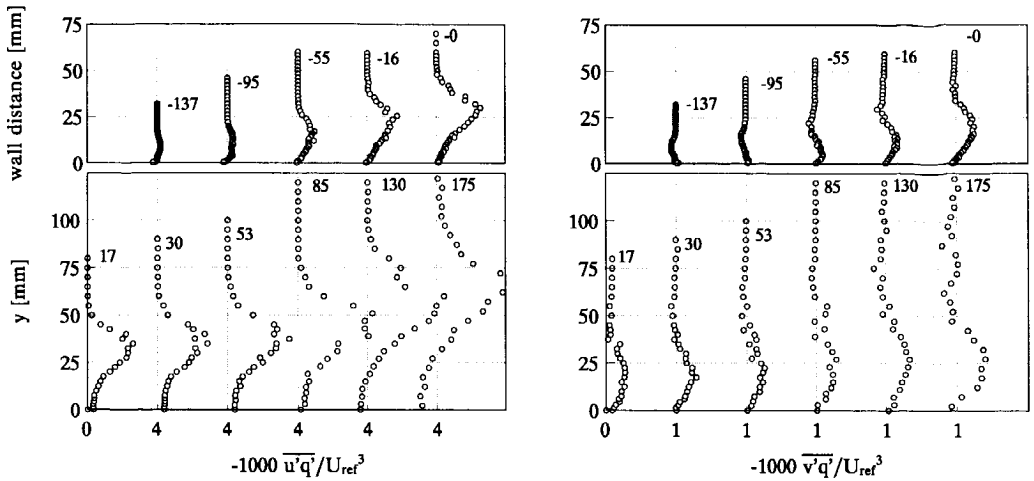


Figure 6.13: Streamwise development of  $-\overline{u'q'}$  (left) and  $-\overline{v'q'}$  (right). *top*: boundary layer, *bottom*: wake. The measured values of  $-1000\overline{v'q'}$  at station  $x = 17$  mm are shifted over 0.1.

boundary-layer approximation. Another observation in Fig. 6.13 concerns the ability of gradient-diffusion models to predict the qualitative behaviour of the triple-velocity correlations in the present flow. For example, in the  $k - \epsilon$  model described in Section 5.2 the following model for the triple-velocity correlations is used

$$-\overline{u'q'} = \frac{\nu_t}{\sigma_k} \frac{\partial k}{\partial x}, \quad (6.8)$$

for the  $x$ -direction, and

$$-\overline{v'q'} = \frac{\nu_t}{\sigma_k} \frac{\partial k}{\partial y}, \quad (6.9)$$

for the  $y$ -direction. In these expressions the effect of the pressure-velocity correlations on the transport of kinetic energy is neglected. Figure 6.13 reveals slightly negative values of  $-\overline{u'q'}$  near the wake centreline for  $x > 130$  mm. This indicates counter-gradient transport, because the kinetic energy  $k$  continuously increases along the centreline. Apart from this small region near the centreline, the measured values of  $-\overline{u'q'}$  are in qualitative agreement with Eq (6.8). However, the situation is different for transport in the  $y$ -direction. In large parts of the wake and boundary layer the signs of the measured values of  $-\overline{v'q'}$  are opposite to those predicted by the gradient-diffusion model, Eq (6.9). The only exceptions are the most upstream stations, where the boundary layer is still thin. There, the lateral transport of kinetic energy is described reasonably well by the gradient-diffusion model (qualitatively, at least) and the streamwise transport of kinetic energy is small compared to the lateral transport.

### Balance of the momentum equation

Once the mean-velocity components and the Reynolds stresses are known from the experiment, one may attempt to evaluate the terms in the Reynolds-averaged momentum

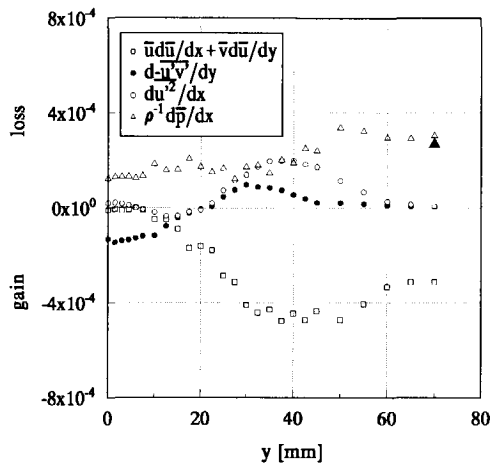


Figure 6.14: Balance of the Reynolds-averaged momentum equation for the  $x$ -direction at station  $x = 30$  mm. The full triangle represents the streamwise pressure gradient as determined from the static-pressure measurements outside the wake.

equation, Eq (6.4). To obtain the different lateral derivatives in Eq (6.4), polynomials were least-squares fitted to the measured profiles. Two successive  $y$ -traverses were used to determine the streamwise derivatives. The results of both wake halves were averaged to reduce the experimental scatter.

The individual terms in the momentum equation are shown in Fig 6.14 for station  $x = 30$  mm. The pressure-gradient term followed from the balance. Unfortunately, the variation in  $y$ -direction of this term could not be checked from independent measurements, because static pressures were not measured across the wake. The full triangle in Fig. 6.14 gives the streamwise pressure gradient as determined from the static-pressure measurements outside the wake, see Section 6.1.1. It is seen that this pressure gradient agrees well with that found from the balance.

The sum of the two Reynolds-stress gradients is locally larger than the pressure-gradient term. Therefore, the present wake is neither dominated by pressure forces nor is it dominated by turbulent stresses. The balance shows that both Reynolds-stress gradients are of equal importance. The effect of the Reynolds normal stress,  $-\overline{u'^2}$ , cannot be neglected compared to the effect of the Reynolds shear stress  $-\overline{u'v'}$ . Furthermore, it is seen that the streamwise growth of  $\overline{u'^2}$  opposes the acceleration of the mean velocity near the centreline. There, all terms of the momentum equation have roughly the same magnitude and accurate modeling of the Reynolds stresses is required to predict the correct mean flow behaviour.



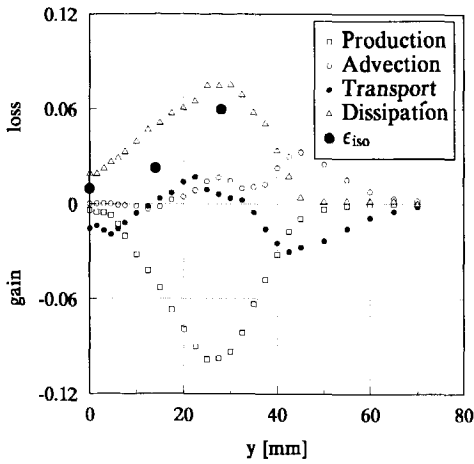


Figure 6.15: Balance of the kinetic energy equation at  $x = 30$  mm. The large bullets are the isotropic values of the dissipation  $\epsilon_{iso}$ , see Section 6.3.

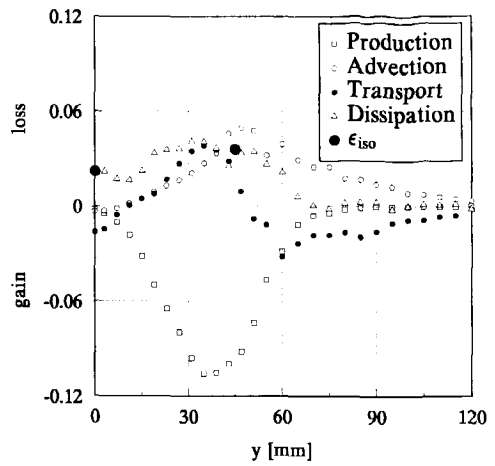


Figure 6.16: Balance of the kinetic energy equation at  $x = 130$  mm. The large bullets are the isotropic values of the dissipation  $\epsilon_{iso}$ , see Section 6.3.

### Balance of the kinetic-energy equation

It is possible to use the experimental data to evaluate the terms in the kinetic-energy equation. The equation for the kinetic energy,  $k$ , is given by

$$\bar{u}_j \frac{\partial k}{\partial x_j} = -\overline{u'_i u'_j} \frac{\partial \bar{u}_i}{\partial x_j} + \frac{\partial}{\partial x_j} \left[ -\frac{1}{2} \overline{u'_i u'_i u'_j} - \frac{1}{\rho} \overline{p' u'_j} + \nu \frac{\partial k}{\partial x_j} \right] - \epsilon \quad (6.10)$$

Figures 6.15 and 6.16 show the balances of the kinetic-energy equation at  $x = 30$  mm and  $x = 130$  mm, respectively. The effects of the molecular diffusion and the pressure diffusion on the transport of  $k$  are neglected. The viscous term is small in the wake so that its neglect has no serious consequences. As noted before, all six triple-velocity correlations were measured in the present study, so that the transport by the velocity fluctuations is described with reasonable accuracy. The dissipation  $\epsilon$  was determined from the balance. At both stations the shear production is zero at the centreline due to flow symmetry, whereas the normal production is small due to the slowly varying mean velocity on the centreline. Integration of the transport profiles between  $y = 0$  mm and the edge of the wake yields a non-zero value. This is the result of the streamwise derivatives of the triple-velocity correlations. Close to the centreline, the gain caused by the transport is balanced by the dissipation. The transport also causes the increase of the kinetic energy along streamlines near the edge of the wake.

It is seen from Figs. 6.15 and 6.16 that the approximate relation  $\epsilon = P_k$  holds in the outer region of the wake. However, this relation underestimates the dissipation near the centreline and it overestimates the dissipation near the location of maximum production. The overestimation is especially large for the more downstream station. Both balances indicate that the wake is in strong non-equilibrium, because the production-to-dissipation

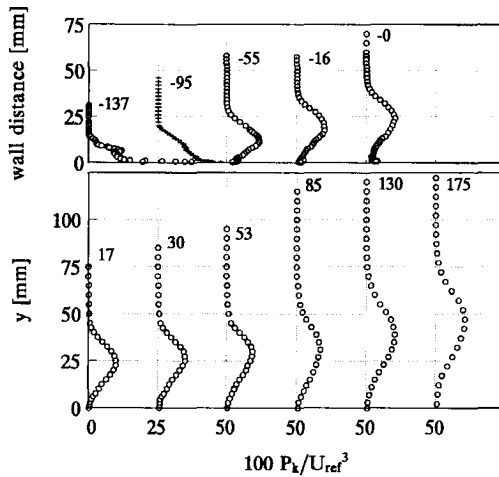


Figure 6.17: Streamwise development of the production of turbulence kinetic energy,  $P_k$ .

ratios are significantly larger than one. Near the location of maximum production the ratios were determined as  $P_k/\epsilon = 1.3$  for station  $x = 30$  mm and  $P_k/\epsilon = 2.6$  for station  $x = 130$  mm. The development of the production of kinetic energy, as given in Fig. 6.17, goes some way in explaining the large increase of the production-to-dissipation ratio. (Note that a different symbol type is used in Fig. 6.17 for station  $x = -95$  mm to avoid confusion with the neighbouring stations.) Figure 6.17 shows that the peak values of  $P_k$  remain nearly constant in the wake. However, the total production of the kinetic energy, defined as the integral of  $P_k$  across the wake, continues to rise in the streamwise direction due to the widening of the  $P_k$  profiles. It appears that the increase of the production is not matched by a similar growth of the dissipation. Since the transport cannot cause an overall increase or decrease of the kinetic energy, it is inevitable that  $k$  steadily increases in the downstream direction.

A few comments on the accuracy of the kinetic energy balances should be made. First, the effect of the pressure-velocity correlation on the balance is neglected, because it cannot be measured. Secondly, the extraction of the transport term from the experimental data involves the differentiation of triple-velocity correlations. This is not an easy task considering the relatively high statistical scatter ( $\pm 20\%$ ) in these correlations. However, at station  $x = 30$  mm the inferred  $\epsilon$  is positive everywhere and it has no unexpected indentations. At station  $x = 130$  mm the  $\epsilon$  distribution has unrealistic indentations at  $y \approx 10$  mm and  $y \approx 45$  mm. Also,  $\epsilon$  becomes negative near  $y = 70$  mm. These errors are believed to be caused mainly by uncertainties in the transport term.

## 6.2 Numerical Results

The continuity equation, Eq (2.8), and the (elliptical) Reynolds-averaged momentum equations, Eq (2.9), are numerically solved for both a  $k - \epsilon$  model [Launder and Sharma

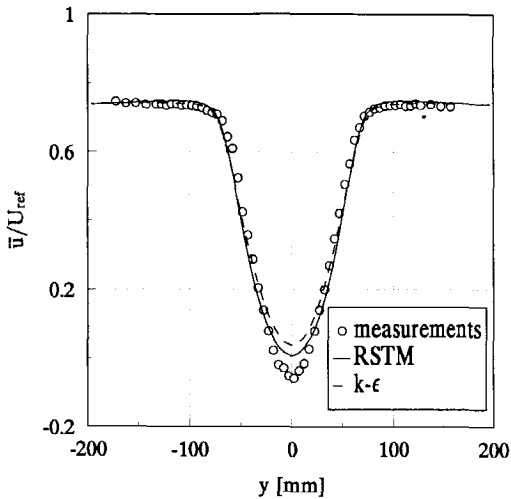


Figure 6.18: Measured and calculated mean velocity at  $x = 175$  mm.

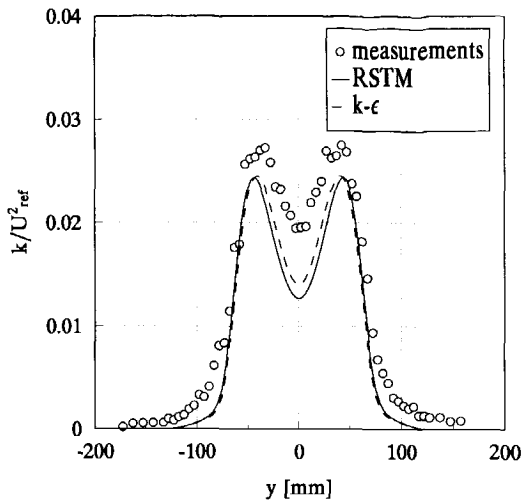


Figure 6.19: Measured and calculated kinetic energy at  $x = 175$  mm.

1974] and a differential Reynolds stress transport model (RSTM) [Hanjalić et al. 1992] using the procedures described in Section 5.2.

The boundary conditions for the calculations in the wake were specified as follows. The calculation is started at a distance of 17 mm behind the trailing edge of the plate. There, the measured mean-velocity profiles and the turbulence profiles are prescribed, whereas the initial  $\epsilon$  profile is guessed by assuming a local equilibrium of production and dissipation of turbulent kinetic energy, i.e.  $\epsilon = P_k$ . The consequences of this somewhat inaccurate assumption regarding the initial  $\epsilon$  profile will be discussed at the end of Section 6.2.1. Furthermore, the effects of the term  $S_{\epsilon_4}$  in the transport equation of the isotropic part of the dissipation in the RSTM, were neglected in the initial calculations (i.e.,  $C_{\epsilon_4}$  was set to zero). The effects of the term  $S_{\epsilon_4}$  on the numerical predictions are discussed in Section 6.2.2.

At the outer edge of the wake ( $y = 200$  mm) the measured static pressure is prescribed. Homogeneous Neumann conditions are prescribed for all turbulence quantities. Varying the position of the wake outer edge was verified to have negligible effect on the solution. Symmetry was assumed at the wake centreline ( $y = 0$  mm). Therefore, only one half of the wake was calculated. Zero streamwise gradients were assumed at the end of the computational domain ( $x = 600$  mm). Varying the location of the end of the domain between  $x = 600$  mm and  $x = 1200$  mm was checked to have negligible effect on the numerical solution in the region where experimental data were available. Results were obtained on a coarse grid consisting of  $50 \times 50$  points and on a fine grid with  $100 \times 100$  points. The differences in the results on these two grids are negligibly small, indicating that almost grid-independent solutions were obtained.

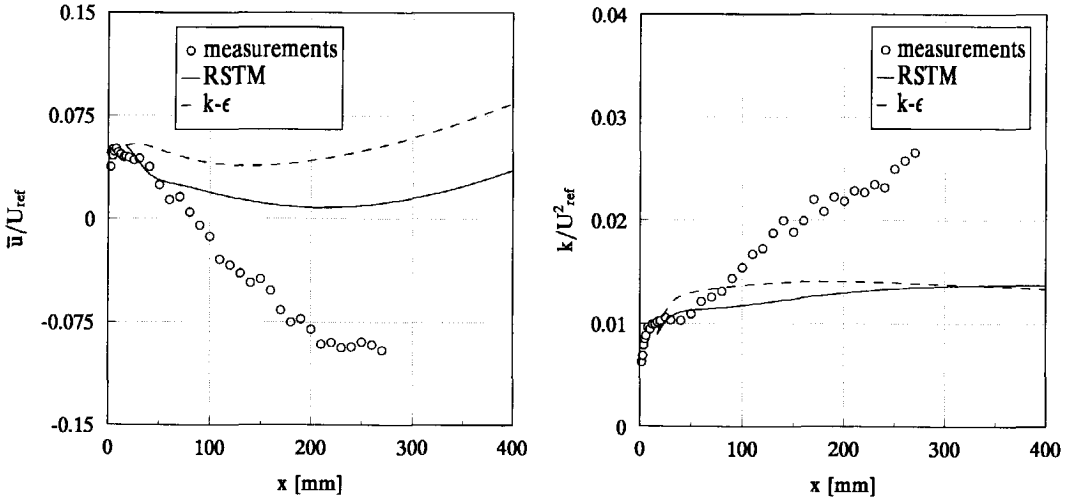


Figure 6.20: Measured and calculated mean velocity (left) and kinetic energy (right) along the centreline.

### 6.2.1 Mean velocity and kinetic energy

Figures 6.18 and 6.19 show the measured and calculated  $x$ -component of the mean velocity  $\bar{u}$  and the kinetic energy  $k$  at station  $x = 175$  mm. The width of the wake appears to be well predicted. However, at the edge of the wake the measured kinetic energy is higher than the computed values. This may be caused by the intermittent behaviour of the interface that separates turbulent from non-turbulent air<sup>3</sup>. There are also large discrepancies between the experiments and the predictions near the centreline of the wake. This is further illustrated in Fig. 6.20 which shows the mean velocity and the kinetic energy along the centreline. The graph shows that neither model is able to reproduce the measured mean-flow reversal. As far as the mean velocity is concerned, the RSTM is only slightly more accurate than the  $k - \epsilon$  model.

It may be argued, however, that the size and position of regions of reversed flow are often sensitive to the strength of the pressure gradient, so that a slight inaccuracy in the prescribed static-pressure distribution at the outer edge of the wake ( $y = 200$  mm) may alter the mean flow significantly. For the present flow this sensitivity was investigated by means of a comparison of the numerical solutions for slightly different pressure gradients. The results of the analysis are given in Fig. 6.21. The curve for  $\bar{p} = \bar{p}_m$  is the numerical solution of the RSTM for the measured static-pressure distribution. Of course, the curves for  $\bar{p} = \bar{p}_m$  are identical to those shown in Fig. 6.20. The other two curves are the results for  $\bar{p} = c\bar{p}_m$ , where  $c$  was varied between 0.95 and 1.05 to simulate an error in the measured static-pressure distribution. It is seen that a 5% error in the static pressure has only a small effect on the mean velocity on the wake centreline. The difference between

<sup>3</sup>An explicit modeling of the effects of the intermittency, as suggested by e.g. Cho and Chung [1992], may reduce the discrepancies between the measurements and the computations near the edge of the wake. However, the effects of such a modification of the turbulence models were not explored in the present investigation.

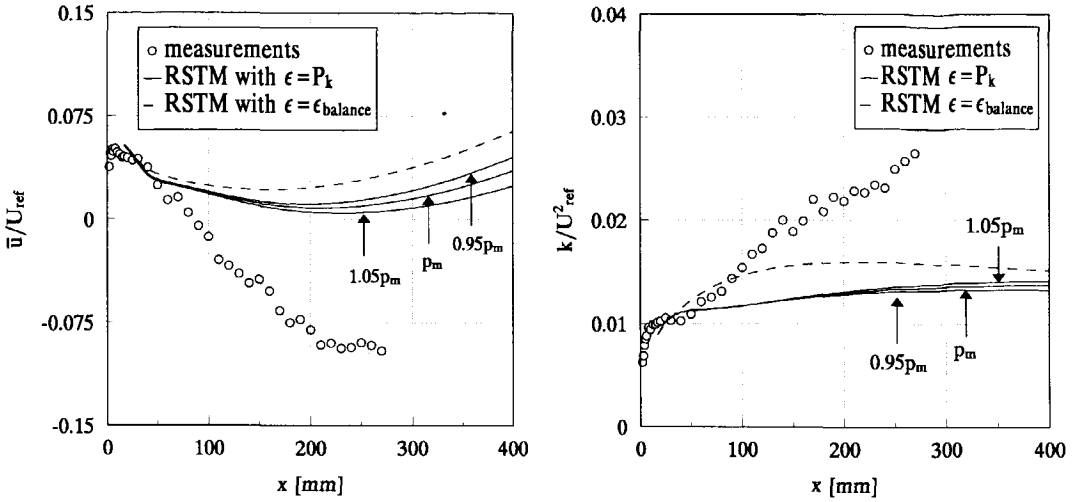


Figure 6.21: The effect of static-pressure variations and the initial  $\epsilon$  profile on the outcome of the RSTM.

the measured and the calculated mean velocity on the centreline is much larger and cannot be explained from a possible error in the measured static pressure distribution. Figure 6.21 also indicates that a 5% error in the static pressure has negligible effect on the kinetic-energy level on the centreline.

Another point of concern is the effect of an inaccurate boundary condition for the dissipation. The results presented so far pertain to the initial condition  $\epsilon = P_k$ , that is, a local equilibrium of production and dissipation is assumed. However, the balance of the kinetic-energy equation shown in Fig. 6.15, indicates that, apart from the region near the edge of the wake, the assumption  $\epsilon = P_k$  is inaccurate. It seems therefore more realistic to use the dissipation profile that was determined from the balance of the kinetic-energy equation at  $x = 30$  mm, denoted by  $\epsilon = \epsilon_{balance}$ , as a boundary condition for the dissipation. The results of the RSTM for this new boundary condition are shown in Fig. 6.21 (dashed lines). It is seen that the new boundary condition for  $\epsilon$  has resulted in a generally higher kinetic energy level, although the computed level is still much lower than the measured values of  $k$  at large trailing-edge distances. Also, the mean velocity on the centreline has slightly increased. So, despite the more realistic boundary condition of the dissipation, there is no overall improvement of the numerical prediction. The same conclusion was drawn from the predictions of the  $k - \epsilon$  model with  $\epsilon = \epsilon_{balance}$  as a boundary condition. These results are not shown here for brevity.

### 6.2.2 Effect of the $S_{\epsilon_4}$ term in the RSTM

The transport equation for the isotropic part of the dissipation tensor in the RSTM, see Eq (5.28), contains the term  $S_{\epsilon_4}$ , given by

$$S_{\epsilon_4} = C_{\epsilon_4} \frac{\epsilon}{k} (\overline{v'^2} - \overline{u'^2}) \frac{\partial \bar{u}}{\partial x}, \quad (6.11)$$

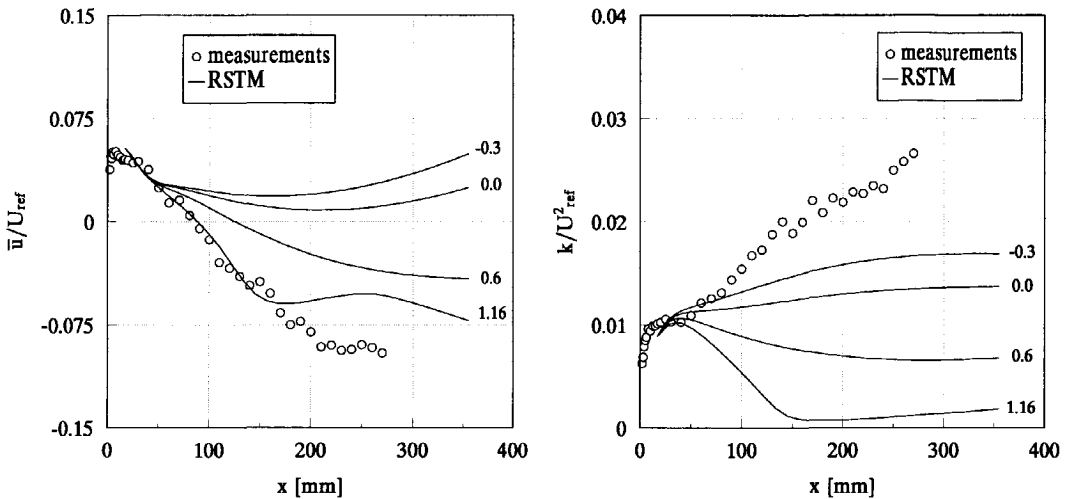


Figure 6.22: Effects of the  $S_{\epsilon_4}$  term on the mean velocity (left) and the kinetic energy (right) for various values of the closure coefficient  $C_{\epsilon_4}$ .

with  $C_{\epsilon_4} = 1.16$ . Figure 6.22 visualizes the effect of  $S_{\epsilon_4}$  on the development of the mean velocity (left) and the kinetic energy (right) along the centreline of the wake for various values of  $C_{\epsilon_4}$ . Note that the curves for  $C_{\epsilon_4} = 0$  are identical to the results that were reported in the previous section. In the adverse-pressure-gradient wake with  $\partial\bar{u}/\partial x < 0$  and  $\overline{v'^2} < \overline{u'^2}$ , the additional term  $S_{\epsilon_4}$  will be positive for positive values of  $C_{\epsilon_4}$ , thereby increasing the dissipation while reducing the kinetic energy. The smaller kinetic energy together with the larger dissipation reduces the eddy viscosity, which in turn reduces the mean velocity on the centreline. Figure 6.22 shows that the inclusion of  $S_{\epsilon_4}$  (with  $C_{\epsilon_4} > 0$ ) improves the agreement between measurements and computations as far as the mean velocity is concerned. However, the price paid for this improvement is a worsening of the numerical predictions of the kinetic energy. For the standard value of  $C_{\epsilon_4} = 1.16$ , the extra term in the dissipation equation causes a dramatic decrease of  $k$  along the centreline, so that the flow nearly relaminarizes. Such a behaviour is not in accordance with the experiments.

Summarizing, the results of Fig. 6.22 show that it is impossible to find a value of  $C_{\epsilon_4}$  with which one can achieve both a decrease of the centreline velocity and an increase of the kinetic energy on the centreline. For completeness it is remarked here that the same conclusion can be drawn if  $\epsilon = \epsilon_{balance}$  is used as a boundary condition at  $x = 17$  mm instead of  $\epsilon = P_k$ . It is not clear why the inclusion of  $S_{\epsilon_4}$  has not resulted in an improvement of the numerical prediction of the adverse-pressure-gradient wake, especially since it is known to work very well in wall boundary layers subjected to adverse pressure gradients, see Henkes [1997].

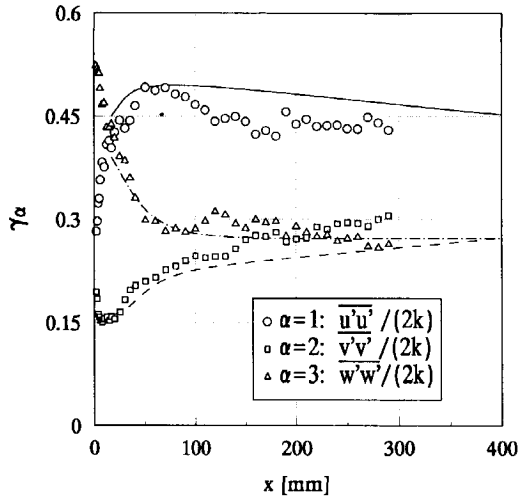


Figure 6.23: Measured and computed values of the anisotropy parameter  $\gamma_\alpha$  on the centreline. The symbols represent the measurements; the lines are the results for the RSTM.

### 6.2.3 Prediction of the Reynolds-stress anisotropy

It is seen in Fig. 6.20 that the kinetic energy on the centreline is strongly underpredicted. However, the distribution of the kinetic energy over the different Reynolds normal stresses, as found with the RSTM, agrees quite well with the experiments. This can be observed in Fig. 6.23 which shows the measured and the computed values of  $\gamma_\alpha = \overline{u_\alpha'^2}/(2k)$  on the wake centreline.

### 6.2.4 Predictions of Reynolds shear stress and kinetic energy

Figure 6.24 compares the measured and the calculated Reynolds shear stress,  $-\overline{u'v'_s}$ , for the  $k-\epsilon$  model (left) and the RSTM (right). The  $k-\epsilon$  model overpredicts the shear-stress values everywhere. This is hardly surprising, considering the well-known characteristic of the standard  $k-\epsilon$  model to produce too high Reynolds shear stresses in flows with adverse pressure gradients. This characteristic is usually attributed to deficiencies in the  $\epsilon$ -equation. However, even if the mean-velocity field, the  $k$  values and the  $\epsilon$  values were somehow known exactly, the  $k-\epsilon$  model would still produce too high Reynolds shear stresses due to the Boussinesq hypothesis, Eq (2.14), which fixes the relationship between the mean strain rates and the Reynolds stresses.

The RSTM, on the other hand, does not rely on the Boussinesq hypothesis, but instead solves a transport equation for each Reynolds stress. It is seen in Fig. 6.24 (right) that the RSTM yields significantly better predictions of the Reynolds shear stress profiles than the  $k-\epsilon$  model. However, the RSTM also tends to overpredict the Reynolds shear stress. The predicted gradients of  $-\overline{u'v'_s}$  in  $y$ -direction on the centreline are larger than the measured gradients, especially for the upstream stations. This is a serious shortcoming, because too high Reynolds-shear-stress gradients result in a too fast increase of the mean velocity on the centreline. The consequences of this can be observed in Fig. 6.20.

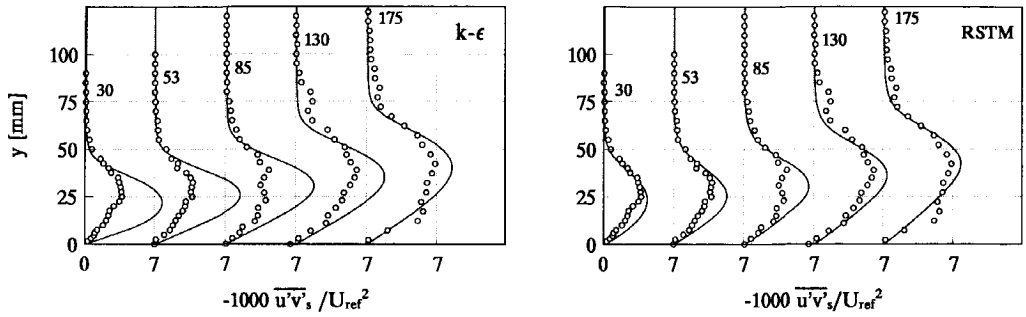


Figure 6.24: Measured and computed Reynolds shear-stress profiles for the  $k - \epsilon$  model (left) and the RSTM (right).

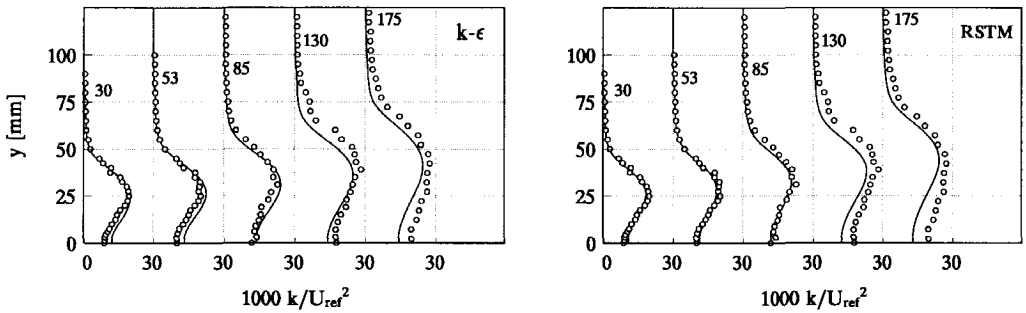


Figure 6.25: Measured and computed kinetic-energy profiles for the  $k - \epsilon$  model (left) and the RSTM (right).

Even though the RSTM gives much better predictions of the Reynolds shear stress than the  $k - \epsilon$  model, there is not much difference between the two models as far as the kinetic energy is concerned. As seen in Fig. 6.25, the RSTM is slightly more accurate for the measuring stations close to the trailing edge, but both models tend to underpredict the kinetic-energy levels farther in the wake.

The severe overprediction of the Reynolds shear stress by the  $k - \epsilon$  model is an indication that this model will also overpredict the production of kinetic energy  $P_k$ . That this is indeed the case is illustrated in Fig. 6.26. The computed  $P_k$  is much larger than the measured values at the upstream stations in the wake. However, the agreement between the measured and the computed values of  $P_k$  is very good for the station farthest downstream. The RSTM gives a more realistic behaviour of  $P_k$  than the  $k - \epsilon$  model, because the severe overprediction of  $P_k$  at the upstream stations is absent. On the other hand, the computed values of  $P_k$  are consistently higher than the measured values, but the differences are relatively small.



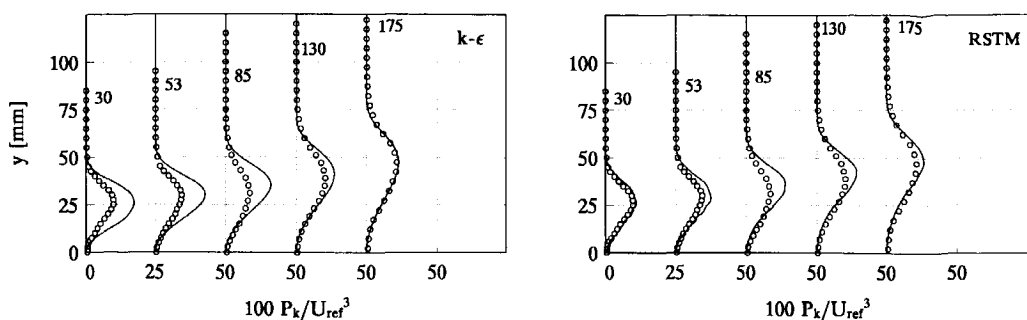


Figure 6.26: Measured and computed kinetic-energy production profiles for the  $k - \epsilon$  model (left) and the RSTM (right).

### 6.2.5 The computed kinetic-energy balances

Figures 6.27 and 6.28 depict the measured and computed balances of the kinetic-energy equation at station  $x = 30$  mm for the  $k - \epsilon$  model and the RSTM, respectively. A comparison of the two graphs clearly shows the superiority of the RSTM over the  $k - \epsilon$  model. Both the dissipation and the production of kinetic energy are strongly overestimated by the  $k - \epsilon$  model, but the predictions of the RSTM agree well with the experimental results. The ratio of production and dissipation  $P_k/\epsilon$ , determined at the location of maximum production, is 1.61 for the  $k - \epsilon$  model and 1.27 for the RSTM. Recall that the measurements indicated  $P_k/\epsilon = 1.3$ .

The RSTM also produces better results for the transport terms than the  $k - \epsilon$  model. Still, even with the RSTM there are significant differences between the experiment and the predictions of the transport terms. More specifically, neither the  $k - \epsilon$  model nor the RSTM reproduces the significant advection of  $k$  near the edge of the wake caused by the transport by turbulent velocity fluctuations. As a result, both turbulence models fail to predict the relatively high kinetic-energy levels near the edge of the wake as observed in Fig. 6.19.

Figures 6.29 and 6.30 show the measured and computed kinetic-energy balances as determined at  $x = 130$  mm for the  $k - \epsilon$  model and the RSTM, respectively. Several interesting observations can be made. First, as was seen above in the kinetic-energy balance at station  $x = 30$  mm, neither model predicted the significant transport of  $k$  by the turbulent velocity fluctuations near the edge of the wake. Secondly, both computed balances are very similar at station  $x = 130$  mm. For example, both models computed almost the same values of the production of turbulence kinetic energy  $P_k$  (and these values are slightly larger than the measured values). However, the most important observation is that both models predicted a much too high dissipation level. Neither model has predicted the large decrease of the measured dissipation in between  $x = 30$  mm and  $x = 130$  mm. Instead, both models predicted relatively small changes of the dissipation levels in the streamwise direction. It can therefore be concluded that, even though the computed production of kinetic energy  $P_k$  is nowhere smaller than the measured  $P_k$ , the computations yield too low levels of  $k$ , because the computed dissipation of turbulence kinetic energy is too high.

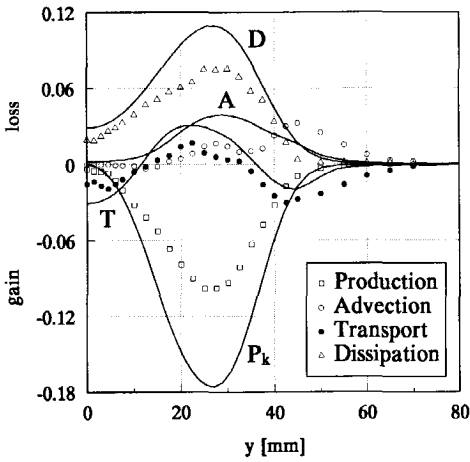


Figure 6.27: Measured and computed kinetic energy balance at station  $x = 30$  mm. The lines are the results for the  $k - \epsilon$  model.

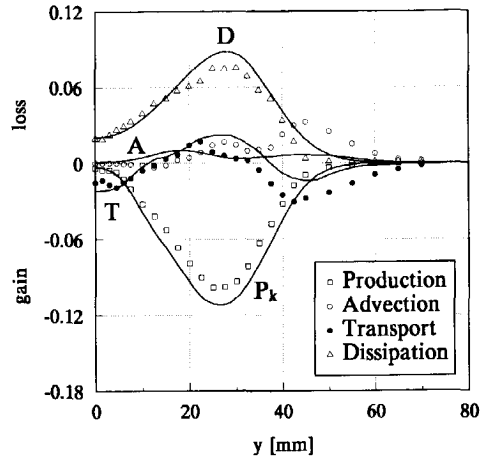


Figure 6.28: Measured and computed kinetic energy balance at station  $x = 30$  mm. The lines are the results for the RSTM.

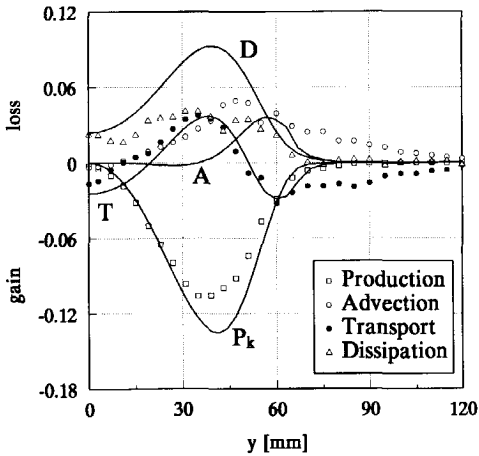


Figure 6.29: Measured and computed kinetic energy balance at station  $x = 130$  mm. The lines are the results for the  $k - \epsilon$  model.

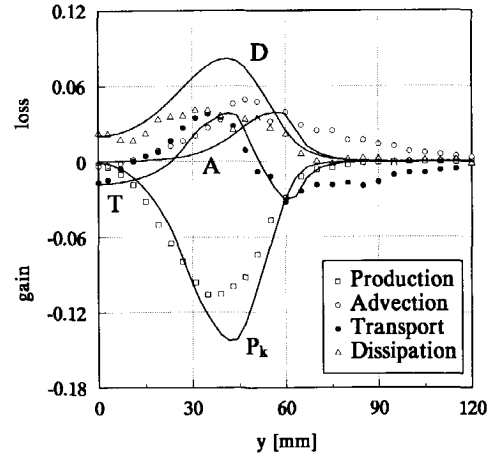


Figure 6.30: Measured and computed kinetic energy balance at station  $x = 130$  mm. The lines are the results for the RSTM.

### 6.2.6 Concluding remarks on the computations

Whenever major differences occurred between the predictions of the  $k - \epsilon$  model and the RSTM, the latter proved to be superior. For example, the RSTM predicted much more accurate Reynolds shear stresses than the  $k - \epsilon$  model. The RSTM was also able to predict the anisotropy of the Reynolds normal stresses with good accuracy. Still, the overall performance of the RSTM is not better than that of the standard  $k - \epsilon$  model for the present wake flow. Neither model was able to predict the measured large increase of the kinetic energy on the wake centreline together with the mean flow reversal that occurred some distance downstream of the trailing edge.

The comparison between the measured and the computed kinetic energy balances indicated that *both* models computed too high dissipation levels at the more downstream station. This is an indication that the inability of the turbulence models to accurately predict the large increase of  $k$  is caused by a deficiency in the transport equation for the dissipation  $\epsilon$ . Recall that the transport equation for the dissipation in the  $k - \epsilon$  model, Eq (5.8), and the transport equation for the isotropic part of the dissipation in the RSTM, Eq (5.28), are very similar. For example, in both equations the production of  $\epsilon$  is directly linked to the production of turbulence kinetic energy  $P_k$ . If this model for the production of  $\epsilon$  is inaccurate in the present wake flow, then the natural superiority of the RSTM over the standard  $k - \epsilon$  model is negated by the use of an improper scale-providing  $\epsilon$ -equation.

At this stage it is not clear if, and how, the transport equations in the turbulence models can be adapted to realize both an increase of the turbulence kinetic energy and a decrease of the mean velocity on the wake centreline, because increased turbulence kinetic energy will generally increase the mean velocity as well. Further experimentation in the adverse present gradient wake may indicate directions for improvement of the turbulence models. This is reported in the following sections.

## 6.3 Results of the Spatial Correlation Measurements

### 6.3.1 Correlation values for small separations

Spatial correlation functions were measured in the adverse pressure gradient wake of the flat plate using experimental set-up 3 described in Section 5.1. As an example, Fig. 6.31 shows the scf  $\rho_{11}(\Delta x)$  measured at station  $x = 130$  mm,  $y = 0$  mm. Starting at zero separation, one probe was traversed in small steps (initially  $25\mu\text{m}$ ) in the  $x$ -direction. In total, 32 measurement runs cover a separation range of 1.1 mm. During each run approximately  $3 \times 10^3$  hardware-coincident velocity pairs were acquired. Clearly visible in Fig. 6.31 is the bump in the correlation values in the overlap region as discussed in Appendix C. Information on the scf is obtained only when the measuring volumes are completely separated, which in this particular set-up amounts to a minimum separation of about 0.1 mm. At zero separation the mean data rate was about 400 Hz, which is relatively high as a result of "single particles" crossing the overlap region, see Appendix C for details. When the separation between the measuring volumes was increased, the mean data rate remained nearly constant in the range  $\Delta x < 0.1$  mm. As the separation was

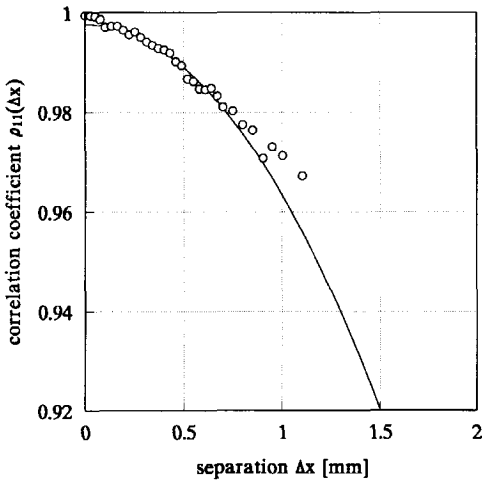


Figure 6.31: The spatial correlation function  $\rho_{11}(\Delta x)$  measured at station  $x = 130$  mm,  $y = 0$  mm. The parabola is least squares fitted to a subset of the measured coefficients.

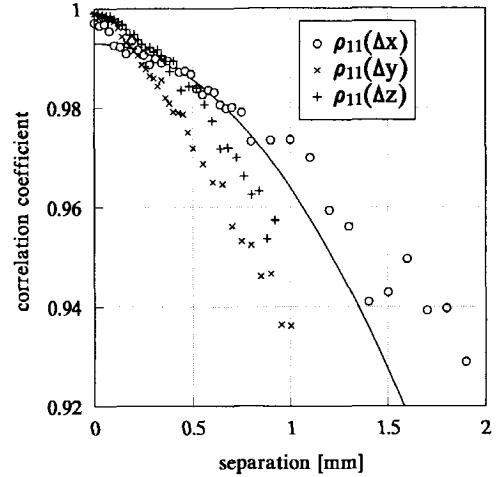


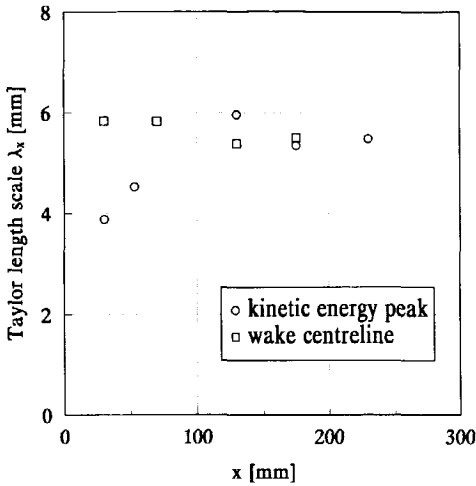
Figure 6.32: The spatial correlation function for separations in three directions at station  $x = 30$  mm,  $y = 0$  mm. The parabola is least squares fitted to a subset of the measured coefficients  $\rho_{11}(\Delta x)$ .

further increased, the mean data rate suddenly dropped to about 25 Hz, and this value remained nearly constant during the remainder of the measurement.

Figure 6.32 shows the longitudinal correlation  $\rho_{11}(\Delta x)$  together with the two lateral correlations  $\rho_{11}(\Delta y)$  and  $\rho_{11}(\Delta z)$  measured at station  $x = 30$  mm,  $y = 0$  mm. Note that the value of  $\rho_{11}(\Delta x = 0)$  is relatively low, indicating a relatively low signal-to-noise ratio of the Doppler signals for this particular measurement. This may be the result of an imperfect alignment of the optical components. Furthermore, the bump in the correlation values is less pronounced for the separation in the  $z$ -direction than for the other two directions; the reason for this is not known. Despite these shortcomings, Fig. 6.32 clearly reveals that the small scale part of the turbulence is anisotropic at this measurement station, because  $\rho_{11}(\Delta y)$  decays more rapidly than  $\rho_{11}(\Delta z)$  for small separations.

### 6.3.2 Determination of Taylor length scales

The Taylor length scales were estimated from the spatial correlation functions using the following procedure. First, the measured correlation values were replotted as  $\rho(\Delta x)$  versus  $\Delta x^2$ . This graph was then used to determine an upper limit of a range in which the replotted data showed a nearly linear behaviour. Of course, the data points inside this interval will show a nearly quadratic behaviour when plotted on linear axes. The reason for the intermediate step is that it proved to be easier to detect a linear behaviour of data points instead of a quadratic behaviour. Then, a lower limit of this range was selected to prevent the inclusion of correlation values that lie within the overlap region



measurement station (coordinates in [mm])	$\lambda_x$ [mm]	$\epsilon_{iso}/U_{ref}^3$ [ $m^{-1}$ ]
$x = 30, y = 0$	5.8	0.010
$x = 70, y = 0$	5.8	0.013
$x = 30, y = 14$	5.2	0.023
$x = 30, y = 28$	3.9	0.060
$x = 53, y = 29$	4.5	0.046
$x = 175, y = 0$	5.5	0.024
$x = 130, y = 0$	5.4	0.022
$x = 130, y = 45$	6.0	0.036
$x = 175, y = 47$	5.4	0.046
$x = 230, y = 60$	5.5	0.052

Figure 6.33: The development of the Taylor length scale  $\lambda_x$  in the streamwise direction.

of the measuring volumes. A fourth order polynomial  $a_0 + a_1\Delta x^2 + a_2\Delta x^4$  was subsequently “least squares” fitted to the measured correlation coefficients that lie within the selected range of  $\Delta x$  values. The fourth order term served as a correction for the errors introduced when some of the selected data points lie just outside the region where the spatial correlation function can be closely approximated by a parabola. The parabolic part of the polynomial was then used to determine the Taylor length scale, while the value of  $1 - a_0$  indicated the magnitude of the discontinuity of the measured scf at zero spatial separation.

In practice, it can be difficult to determine the Taylor length scale from the measured correlation values. For example, in Fig. 6.32 the scf for the  $y$ -direction decays so rapidly that a significant part of the parabolic region is obscured by the bump in the overlap region of the measuring volumes. This makes an estimate of the Taylor length scale for the  $y$ -direction speculative. On the other hand, the turbulence scales in the  $x$ -direction are much larger so that it is well possible to determine the Taylor length scale for the  $x$ -direction with reasonable accuracy.

### 6.3.3 Variation of Taylor length scales in streamwise direction

Figure 6.33 presents the values of the Taylor length scales  $\lambda_x$  as determined from the scf  $\rho_{11}(\Delta x)$  for various locations in the wake. The bullets were measured on the contour of maximum kinetic energy, whereas the squares were measured along the centreline of the wake. These results indicate an increase of the Taylor length scale  $\lambda_x$  in the streamwise direction on the contour of maximum kinetic energy. Along the centreline there is negligible variation of  $\lambda_x$ . The table on the right of Fig. 6.33 lists the Taylor length scales that were measured at several locations in the wake. Also given in this table are the estimates of the dissipation of kinetic energy that were obtained from the

assumption of local isotropy (see Section 2.1.5 for details):

$$\epsilon_{iso} = 15\nu \overline{\left(\frac{\partial u'}{\partial x}\right)^2} = 30\nu \frac{\overline{u'^2}}{\lambda_x^2}. \quad (6.12)$$

The values of  $\epsilon_{iso}$  are plotted in the balances of the kinetic energy at  $x = 30$  mm (Fig. 6.15) and at  $x = 130$  mm (Fig. 6.16) as large bullets. For the lateral traverse at  $x = 130$  mm there is good agreement between  $\epsilon_{iso}$  and the values of the dissipation that follow from the balance,  $\epsilon_{balance}$ . For the lateral traverse at  $x = 30$  mm the values of  $\epsilon_{iso}$  are systematically lower than that of  $\epsilon_{balance}$ . The difference may be caused by deviations from the assumption of local isotropy. Figure 6.32 indicates that this is indeed the case for measurement station  $x = 30$  mm,  $y = 0$  mm. Furthermore, the measured Taylor length scales may be subject to a systematic error because the spatial correlation functions are not corrected for the effects of the velocity bias. Despite these possible uncertainties, the measured values of  $\epsilon_{iso}$  confirm the earlier important finding that the dissipation of turbulence kinetic energy decreases with increasing trailing edge distance between stations  $x = 30$  mm and  $x = 130$  mm.

## 6.4 Spectral Measurements

### 6.4.1 Small-scale characteristics of the autocorrelation function

The small scale temporal behaviour of the velocity fluctuations in the  $x$ -direction was studied at two stations in the wake at  $x = 30$  mm (7 measurement locations ranging between the centreline and  $y = 42$  mm) and at  $x = 130$  mm (8 measurement locations ranging between the centreline and  $y = 63$  mm). The shear-layer thickness  $\delta_{0.95}$  is 45 mm at station  $x = 30$  mm and  $\delta_{0.95} = 70$  mm at station  $x = 130$  mm. At each location  $4.5 \times 10^5$  velocity samples were acquired at a mean data rate of about 1 kHz using the one-component LDA described in Section 5.1.3 (experimental set-up 2). The transit times of the particles,  $tr$ , were also measured to enable a correction for the effects of the velocity bias. The acfs were computed using the local normalisation algorithm, Eq (4.51), with weighting factor  $\omega_i = tr_i$ .

The acfs measured at stations  $x = 30$  mm and  $x = 130$  mm are shown in Figs. 6.34 and 6.35, respectively. Two acfs are shown for location  $x = 30$  mm,  $y = 42$  mm to indicate the effect of the velocity bias on the computed acf. Figure 6.34 indicates a small decrease of the (downward) curvature of the acf at zero lag time towards the centreline of the wake. This indicates a small increase of the Taylor time scale towards the centreline. The same trend can be observed in Fig. 6.35, but the change of the (downward) curvature in the  $y$ -direction is even less here, suggesting that the Taylor time scale remains nearly constant across the wake at  $x = 130$  mm. Furthermore, it is seen that there is hardly any difference between the two acfs that are measured on the centreline, indicating that the small scale (temporal) behaviour of the velocity fluctuations doesn't change along the centreline in between both measurement stations.

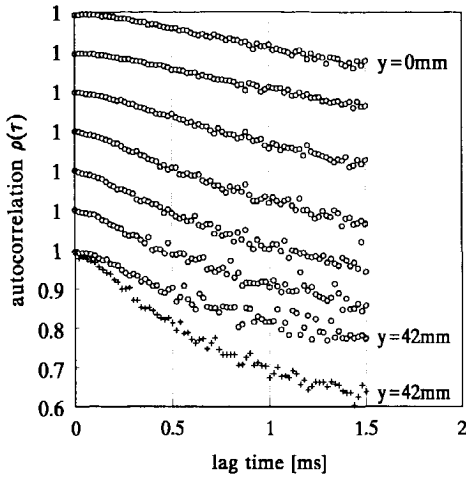


Figure 6.34: Detailed view of the autocorrelation functions measured at cross-section  $x = 30$  mm. The  $y$ -range is divided into equal steps of 7 mm. The crosses (+) are the biased acf at  $y = 42$  mm.

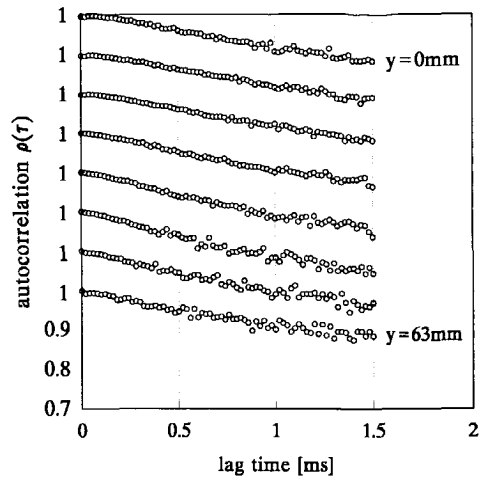


Figure 6.35: Detailed view of the autocorrelation functions measured at cross-section  $x = 130$  mm. The  $y$ -range is divided into equal steps of 9 mm.

### 6.4.2 Spectral density functions in the wake

Spectral density functions (sdfs) of the velocity fluctuations in the  $x$ -direction were measured at various locations in the wake. The sdfs for nine locations on the centreline between  $x = 30$  mm and  $x = 255$  mm are shown in Fig. 6.36. The sdfs measured on a lateral traverse at  $x = 130$  mm are given in Fig. 6.37. This lateral traverse comprises eight measurement locations between  $y = 0$  mm (centreline) and the edge of the wake at  $y = 63$  mm.

Each graph shows the sdf as computed from both the standard spectral estimator  $S_1$  (+ marker) and the improved spectral estimator  $S_2$  (o marker). The characteristics of the two estimators are extensively discussed in Section 4.3. Here, only the results for the improved spectral estimator  $S_2$  will be considered. The spectral density functions computed from  $S_2$  are accurate up to a frequency of approximately 2000 rad/s. This value for the upper frequency is based on the results of the simulated velocity data as discussed in Section 4.3.4. The upper frequency may vary slightly at the different measuring locations due to, for example, small variations in the mean data rate.

The results in Fig. 6.36 indicate that there is little change in the high frequency part of the sdfs along the centreline of the wake. This is consistent with the observations made in Figs. 6.34 and 6.35. A striking feature of the sdfs is the presence of a “bump” for frequencies lower than approximately 25 rad/s. This low-frequency bump is relatively strong at  $x = 30$  mm and gradually weakens farther downstream. Consequently, the integral time scale decreases in the downstream direction along the centreline (although the integral time scale has a maximum value at station  $x = 53$  mm and not at  $x = 30$  mm). The low-frequency bump is also visible in the sdfs measured on the lateral

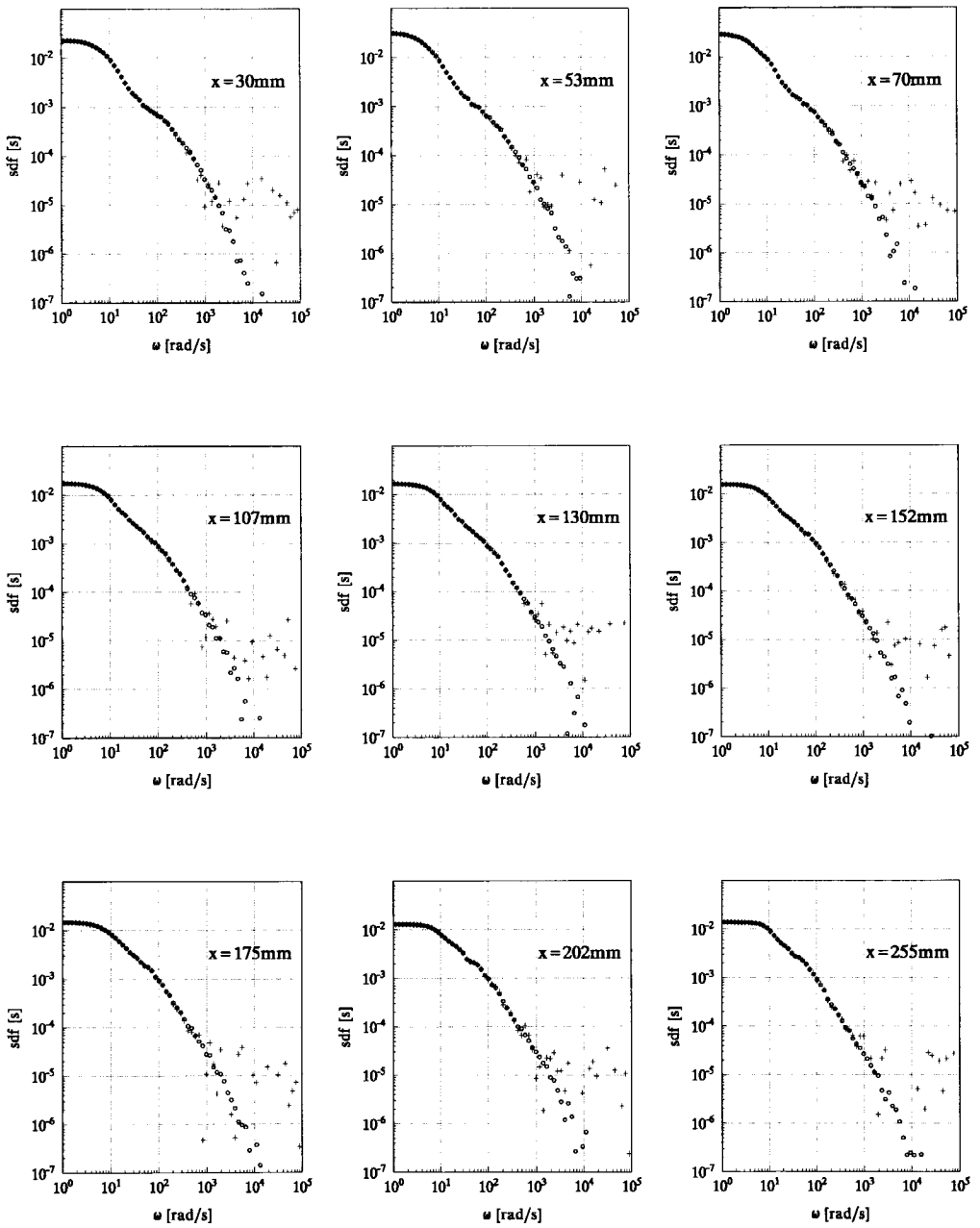


Figure 6.36: Spectral density functions measured at various stations along the wake centreline. The crosses (+) result from the standard spectral estimator  $S_1$  and the open bullets ( $\circ$ ) result from the modified spectral estimator  $S_2$ , see Section 4.3 for details.



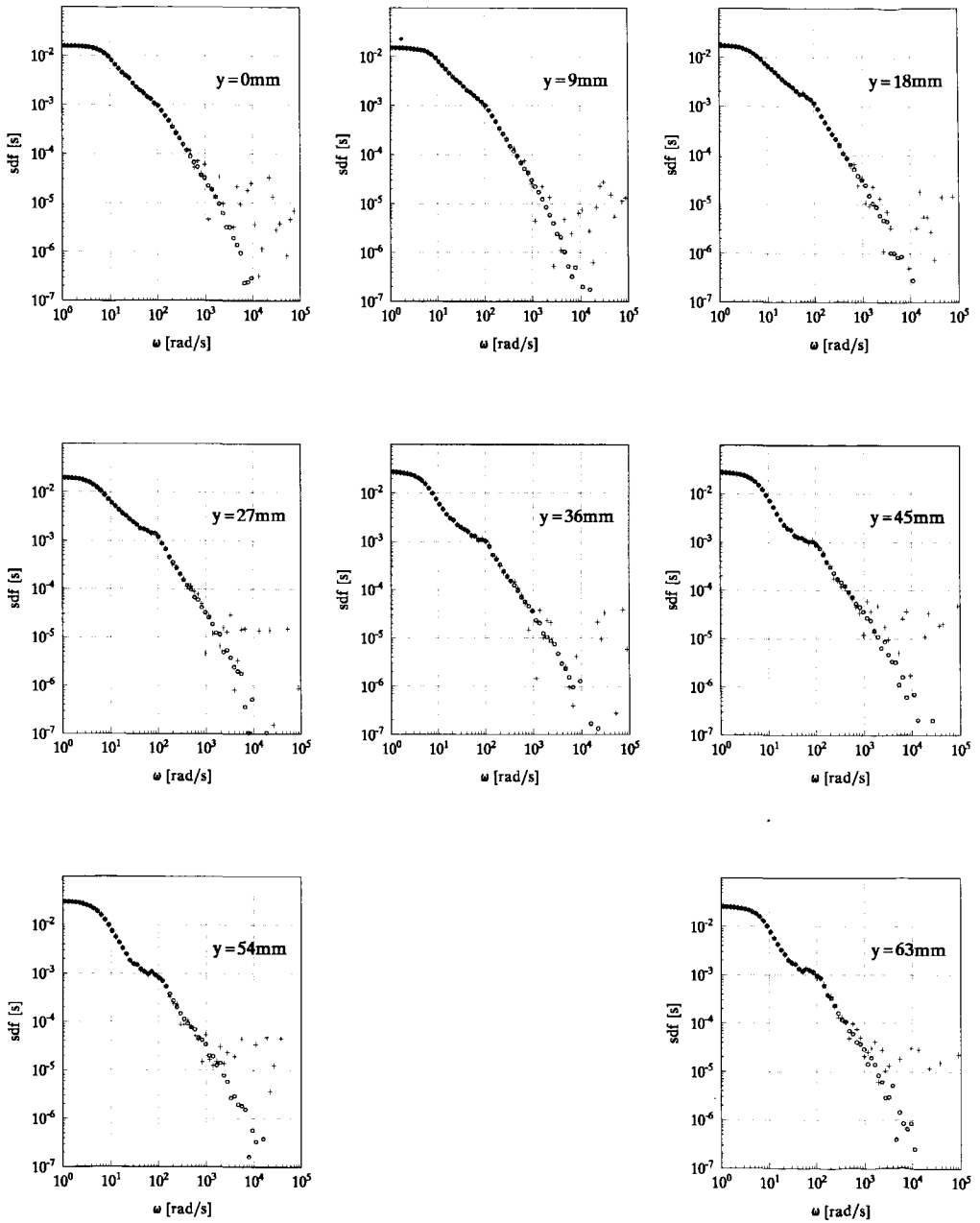


Figure 6.37: Spectral density functions measured at station  $x = 130$  mm. The crosses (+) result from the standard spectral estimator  $S_1$  and the open bullets (o) result from the modified spectral estimator  $S_2$ , see Section 4.3 for details. The local shear-layer thickness  $\delta_{0.95}$  is approximately 70 mm.

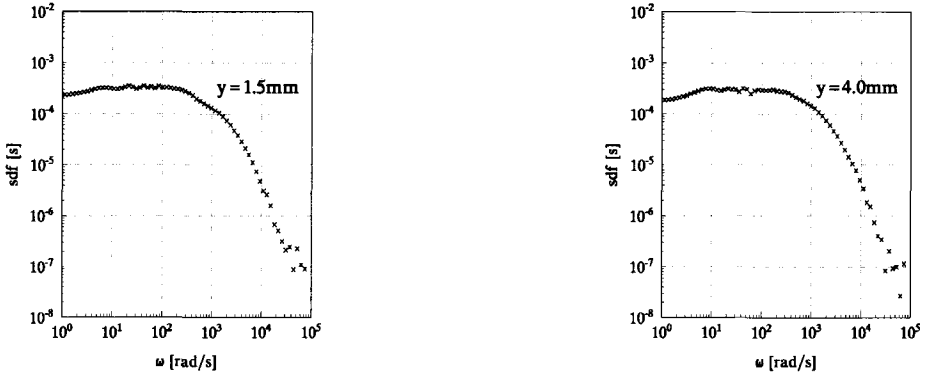


Figure 6.38: Spectral density functions (computed using the estimator  $S_2$ ) measured in the *zero-pressure-gradient* wake at a station 10.01 mm downstream of the trailing edge. The shear-layer thickness  $\delta_{0.95}$  at this particular station is approximately 14 mm.

traverse at  $x = 130$  mm, see Fig 6.37. The strength of the bump appears to increase with increasing values of the  $y$ -coordinate, i.e. with increasing distance from the wake centreline.

It is interesting to explore the origin of the low-frequency content of the measured sdfs. If the largest turbulence structures of approximate size  $\delta_{0.95}$  move past the measuring volume with velocity  $U_e$ , then this gives rise to a frequency of  $\omega_1 = 2\pi U_e / \delta_{0.95} = 6.6 \times 10^2$  rad/s, when  $U_e = 7.4$  m/s and  $\delta_{0.95} = 70$  mm (these values pertain to station  $x = 130$  mm). However, there are frequencies lower than  $\omega_1$  in a turbulent wake or boundary layer due to the presence of an interface that separates the turbulent air from the non-turbulent air. The location of the interface changes with time so that a (stationary) measuring volume is sometimes in the turbulent air and sometimes in the non-turbulent air. This intermittent behaviour of the flow results in frequencies as low as  $\omega_2 = 0.1 \times \omega_1 = 6.6 \times 10^1$  rad/s, see e.g. Antonia et al. [1987]. Clearly, even the lower frequency  $\omega_2$  is well outside the range of frequencies where the bump occurs:  $\omega < 25$  rad/s. It can therefore be concluded that the intermittency of the flow cannot explain the observed low-frequency behaviour. For completeness, it is remarked here that the low-frequency bump in the sdfs is not an artifact of the experimental facility or the data-processing method. This follows from Fig. 6.38 which shows two sdfs measured in the near wake of the flat plate in zero pressure gradient using the same experimental facility and data-processing algorithm as in the present investigation.

## 6.5 Discussion

In a further attempt to explain the low-frequency content of the spectral density functions it is useful to consider the effects of streamline curvature. Concave curvature can have

large effects on a turbulent boundary layer, see Bradshaw [1973] for details. The degree of curvature is usually measured by the curvature parameter  $\delta/r$ , where  $\delta$  is the local thickness of the boundary layer and  $r$  is the local radius of curvature of the streamlines. According to Bradshaw [1973] concave curvature tends to destabilize the flow and its effects are already noticeable for values of  $\delta/r$  as small as 0.01.

The effects of concave curvature on the structure of a turbulent boundary layer were investigated by Jeans and Johnston [1982] and Barlow and Johnston [1988]. In their experiments a turbulent boundary layer that developed on a flat wall in a nominally zero-pressure-gradient was led through a  $90^\circ$  bend with a constant radius of curvature of  $r = 1.36$  m. The curvature parameter  $\delta/r$  varied between zero at the start of the bend and 0.088 at a station  $60^\circ$  into the bend. The Reynolds number based on  $\theta$  at the latter station was  $R_\theta = 1680$ . Flow visualisation with a laser light sheet and dye revealed that the concave curvature induced the formation of large scale "roll cells" in the turbulent boundary layer with their axis in the mean flow direction. These roll cells have their origin in the same centrifugal-instability mechanism that leads to the formation of Taylor-Görtler vortices in a concave laminar boundary layer. Clearly, if such roll cells have a stationary location in the turbulent boundary layer, they will give rise to a periodic variation in the spanwise direction of time-averaged quantities, i.e. a three-dimensional mean flow will occur. However, the experiments of Jeans and Johnston [1982] and Barlow and Johnston [1988] showed that the roll cells did not have a stationary behaviour. Instead, the roll cells grew, merged, disappeared and wandered in spanwise direction in a random manner so that long-term time averages were two-dimensional. However, the presence of the large-scale roll cells in the turbulent boundary layer introduced velocity fluctuations with very large time scales. More precisely, the spectral measurements of Barlow and Johnston [1988] showed that the differences between the flat and the curved boundary layer were confined to the very low frequency range. The high-frequency content of the power spectra was hardly affected by the concave curvature.

In the present experiment in the adverse pressure gradient wake, the surface of the wake generating plate is not curved except for a small region with convex curvature where the tapered trailing edge begins. However, the streamlines in the trailing-edge region are curved as a result of the rapid increase of the shear-layer thickness. The local radius of curvature of the streamlines  $r$  can be determined from the mean-velocity measurements using the following approximate expression (see Fig. 6.39):

$$r = \frac{\sqrt{(x_b - x_a)^2 + (y_b - y_a)^2}}{\tan(\gamma_b - \gamma_a)}. \quad (6.13)$$

Here,  $\gamma_a$  ( $\gamma_b$ ) is the angle between the mean-velocity vector at location  $A$  ( $B$ ) and the  $x$ -axis. The numerator in Eq (6.13) is the distance between  $A$  and  $B$ . For example, with  $A$  located on the boundary layer traverse at  $x = -95$  mm and  $B$  located at  $x = -55$  mm, a typical value of the radius of curvature was determined as  $r \approx 1.1$  m. This yields a curvature parameter  $\delta/r \approx 0.025$  when  $\delta$  is evaluated as the average value of  $\delta_{0.95}$  at stations  $x = -95$  mm and  $x = -55$  mm. Figure 6.40 shows the (dimensionless) angular momentum  $r(\bar{u}^2 + \bar{v}^2)^{1/2}/U_{ref}$  in the boundary layer at station  $x = -95$  mm. It is seen that the angular momentum decreases towards the wall, i.e. the angular momentum decreases in the direction away from the centre of curvature as is the case in concave

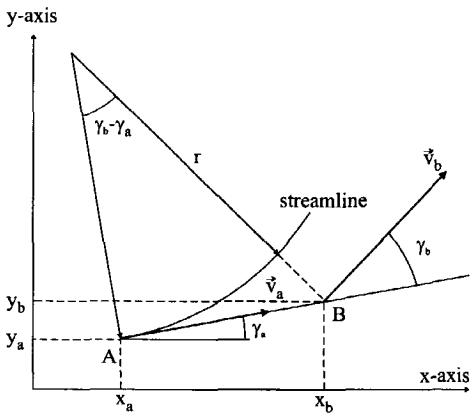


Figure 6.39: Determination of local radius of curvature from mean-velocity measurements.

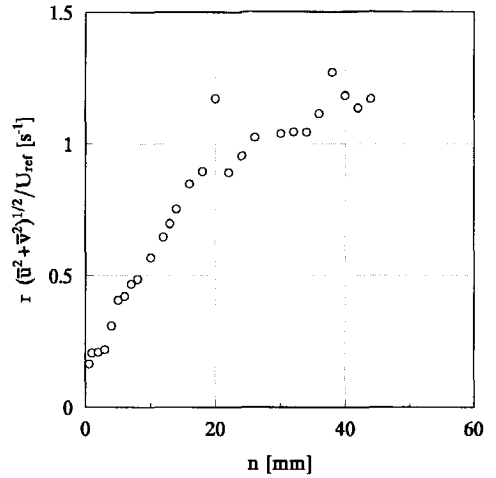


Figure 6.40: The dimensionless angular momentum  $r(\bar{u}^2 + \bar{v}^2)^{1/2}/U_{ref}$  as a function of the wall distance at boundary layer station  $x = -95$  mm.

curvature. This concave curvature tends to destabilize the flow. Furthermore, a curvature parameter with a value of 0.025 can be interpreted as a moderate degree of curvature [Bradshaw 1973].

An analysis of the mean-velocity data indicated that the streamlines were concavely curved at the other boundary layer stations as well. Interestingly, the radius of curvature changes sign downstream of the trailing edge of the plate. For example, in between the wake stations  $x = 30$  mm and  $x = 53$  mm the curvature parameter is  $\delta/r \approx -0.019$ . There, the curvature of the streamlines is convex and tends to stabilize the flow. The effects of convex curvature on the flow are much smaller than that of concave curvature [Bradshaw 1973]. Farther downstream the radius of curvature changes sign again; the value of  $\delta/r$  in between stations  $x = 85$  mm and  $x = 130$  mm was determined as approximately 0.011.

It is now reasonable to speculate as follows. The rapid increase of the thickness of the boundary layer towards the trailing edge of the plate has resulted in streamlines with concave curvature. The concave curvature (with  $\delta/r \approx 0.025$  in between station  $x = -95$  mm and  $x = -55$  mm) may have affected the structure of the boundary layer in the trailing-edge region through the formation of roll cells. The roll cells contain a significant amount of low-frequency energy, which appears in the measured spectral density functions as a bump in the low-frequency range, see Figs. 6.36 and 6.37.

Just downstream of the trailing edge the streamline curvature is convex so that there is no drive for the formation of roll cells. Also, the streamline curvature on the wake centreline is zero because of flow symmetry. This may explain the change in shape of the sdfs that were measured on the centreline (shown in Fig. 6.36). The bump in the low-frequency range gradually decreases with increasing distance from the trailing edge,

indicating the gradual fading of the roll cells along the centreline. The sdfs that were measured on the lateral traverse at  $x = 130$  mm (shown in Fig. 6.37) indicate that the relatively small bump in the low-frequency range at  $y = 0$  mm increases with increasing  $y$ . This suggests that the remnants of the roll cells that were formed in the boundary layer are convected downstream by the mean flow. As a result, the roll cells also appear in the near wake especially in the outer regions, and, for sufficiently small trailing-edge distances, the rolls cells even appear at the wake centreline.

It was concluded in Section 6.2.6 that the cause for the discrepancies between the computations and the measurements is the failure of the length-scale supplying, transport equations for  $\epsilon$  to predict the measured decrease of the dissipation levels in the downstream direction. The relation between the inability of the turbulence models to predict the decrease of the dissipation and the presence of the rolls cells will now be discussed.

Although the presence of roll cells in the trailing-edge region of the plate is speculative (the rolls cells are not visualised), the measured sdfs clearly indicate the presence of turbulence structures that are characterised by very low frequencies. Such turbulence structures are absent in the trailing-edge region of the flat plate in case of a zero pressure gradient as can be seen from the sdfs in Fig. 6.38. Because the near wake of the flat plate in zero pressure gradient can be accurately predicted by the standard  $k - \epsilon$  model and the RSTM (see Section 2.2.2), it is plausible to assume that the failure of the same models to accurately predict the present wake is caused by the low-frequency turbulence structures (which are thought to be roll cells).

In the present wake in adverse pressure gradient a significant amount of the produced turbulence kinetic energy ends up as low-frequency velocity fluctuations. Unaware of this phenomenon, the transport equation for  $\epsilon$  in both turbulence models interprets all of the kinetic energy that is produced as conventional, well-behaved turbulence and produces  $\epsilon$  at a rate proportional to  $P_k$  through the source term:  $C_{\epsilon_1} P_k \epsilon / k$ . It appears that this is an inaccurate model in the present flow, because a large part of the produced turbulence kinetic energy accumulates in the low-frequency range of the spectrum, and, as a consequence, the energy transfer to the high-frequency, dissipation range of the spectrum takes place at a rate that is lower than  $C_{\epsilon_1} P_k \epsilon / k$ . Therefore, both turbulence models predict too high dissipation levels. A possible solution to this problem would be the use of a multi-scale model in which the energy containing region of the spectrum is split into two parts. The turbulence in both parts of the spectrum can then be modelled in different ways.



# Chapter 7

## Conclusions

In this chapter the conclusions are presented in regard to the objectives that were formulated in Section 1.2. The primary objective was to gain better understanding of the complex flow that results when a strong adverse pressure gradient is imposed on the wake of an “airfoil-like” flat plate. Secondary objectives concerned the operation of the three-component LDA, the velocity bias and the high statistical scatter in the power spectra that are measured with LDA.

### Conclusions regarding the flow

The experiments in the turbulent trailing-edge flow of the flat plate in an adverse pressure gradient indicate a rapid growth of the shear-layer thickness in the streamwise direction. The boundary layer on the plate remains fully attached, although it is close to separation at the trailing edge. After a slight initial increase, the mean velocity on the centreline decreases so that a region with mean-flow reversal is formed some distance downstream of the trailing edge. The turbulence kinetic energy steadily rises in the downstream direction on the centreline. The measured balances of the kinetic energy equation show the importance of transport by turbulent velocity fluctuations in the present wake, especially near the edges. The balances also indicated a significant decrease of the dissipation in the streamwise direction while the production of turbulence kinetic energy remains nearly constant. Power spectra measured in the wake revealed the presence of a significant amount of turbulence kinetic energy in the very-low frequency range; a phenomenon not seen in the zero pressure gradient wake of the same flat plate. It is speculated (but not proved) that this is caused by the formation of “roll cells” in the turbulent shear layer as a result of concave streamline curvature.

The comparison between the experiments and the numerical solutions of the Reynolds-averaged Navier-Stokes equations for a  $k - \epsilon$  model and a differential Reynolds-stress transport model, show that neither model reproduces the measured mean-flow reversal together with the large increase of the turbulence kinetic energy on the wake centreline. Both turbulence models also fail to predict the measured decrease of the dissipation in the streamwise direction, indicating a deficiency in the transport equations for the dissipation, which are rather similar in both turbulence models. The response of the

source term of the dissipation equation to the production of turbulence kinetic energy is to produce dissipation. In the present flow this is not the correct response because a significant portion of the produced kinetic energy ends up in the very-low frequency range and is not dissipated at this stage.

### Conclusions regarding the measurement technique

The use of a three-component LDA (3D LDA) poses a number of problems that are not encountered in the more conventional one- or two-component LDA. The angle between the “third velocity component” and the plane spanned by the other two velocity components should be at least  $30^\circ$  otherwise all statistical quantities that involve this third velocity component are extremely sensitive to small inaccuracies of the signal processor or small inaccuracies in, for example, the calibration factors. Furthermore, the statistical quantities measured by the 3D LDA can be in error due to so-called “virtual particles” [Boutier et al. 1985] and the “geometry bias” [Brown 1989]. The analysis of the different problems related to the 3D LDA, and the remedies to these problems, has resulted in the following recommendation for the arrangement of the 3D LDA:

- the transmitting optics should be arranged such that three (nearly) orthogonal velocity components are measured by the individual LDA channels. This removes the extreme sensitivity of the third velocity component to the various small errors;
- the receiving optics should be configured such that only light from the overlap region of the three measuring volumes is collected. This eliminates the virtual particles;
- the three signal processors should be operated in the “hardware-coincident mode.” In conjunction with the previous item, this eliminates the geometry bias.

To realize the desired optical configuration (items 1 and 2) a new alignment procedure is introduced that centers around a “thin” pinhole.

Irrespective of the number of velocity components being measured, the LDA measurement technique naturally operates with particles that are randomly distributed in space. As a result, the times at which the velocity is sampled are also random. The random sampling times give rise to two major problems which were thoroughly investigated in this thesis: (1) the correlation between the instantaneous data rate and the instantaneous velocity (velocity bias) and (2) the high statistical scatter in the power spectra and the autocorrelation functions that are computed from the LDA data. The outcome of the investigations is as follows:

- The existence of the velocity bias is confirmed experimentally and it is found to be independent of the data density (defined as the product of the mean data rate  $\nu$  and the integral time scale  $T_u$ ). The velocity-bias detection methods developed by Adams [1984] and Meyers [1988] are shown to be valid only at high data density ( $\nu T_u > 10$ ). Both detection methods falsely indicate the absence of the velocity bias at low data density.



Various velocity-bias correction methods are evaluated. The different sampling techniques and the interarrival time weighting all require high data densities ( $\nu T_u > 10$ ). A partial correction for the effects of the velocity bias is observed when these correction methods are applied at low data densities. The 3D inverse-velocity weighting is preferred when all three velocity components are measured simultaneously as in 3D LDA. In case only two velocity components are measured, the 3D inverse-velocity weighting can be approximated by the 2D<sup>+</sup> inverse-velocity weighting, which was found to yield good results. The 1D inverse-velocity weighting should never be used. If only one velocity component is measured it is better to resort to the transit time weighting.

- Using simulated turbulence data it is confirmed that existing spectral estimators for randomly sampled data, like the one developed by Gaster and Roberts [1975], exhibit a large statistical scatter in the high-frequency range of the power spectrum. A new spectral estimator [Tummers and Passchier 1996b] is evaluated and found to yield significant improvements. The new spectral estimator combines a window function of variable width and a "locally scaled" autocorrelation function. At small lag times the local scaling results in a strong reduction of the statistical scatter of the autocorrelation values as compared to those calculated with the standard "slotting technique." This characteristic enables the direct determination of Taylor time scales from the curvature of the acf at zero lag time. The effects of uncorrelated noise, velocity bias and spatial averaging on the locally scaled autocorrelation function are also investigated. The results of this investigation stress the importance of using small measuring volumes while maintaining Doppler signals with high signal-to-noise ratios. Furthermore, a correction scheme is given that enables the computation of unbiased, locally scaled autocorrelation values from biased LDA data.



## Appendix A

# Alignment of the 3-D LDA

The unique problems of three-component LDA measurements were discussed in Section 3.3. The remedies to these problems imposed in a number of demands on the optical arrangement of the 3-D LDA, including the orthogonality requirement. However, details on how to realize the desired optical arrangement were not given. This appendix describes practical aspects of the alignment of the orthogonal 3-D LDA. The calibrating procedure of the 3-D LDA, i.e. the determination of the crossing angles of the beams and the orientation of each beam in space, is described in detail by Absil [1995].

The alignment of the orthogonal 3-D LDA is carried out in two steps

1. manipulation of six incident laser beams to create three measuring volumes with (nominally) orthogonal fringe patterns that share a common region in space.
2. positioning of the receiving optics such that scattered light is collected only from the overlap region of the three measuring volumes.

First, the transmitting optics of, say, the blue and green beams are manipulated to form two completely overlapping measuring volumes with orthogonal fringe patterns using the procedures as described by Absil [1995]. (The complete overlapping implies that the blue and green beam pairs have the same optical axis.) Then a small pinhole is placed at the centre of the two overlapping measuring volumes at a  $45^\circ$  orientation as shown in Fig. A.1. The aim of the pinhole is to allow simultaneous passage of the three beam pairs even if the axis of the violet beam pair and the axis of the blue and green beam pairs include a  $90^\circ$  angle. The pinhole has a  $50\ \mu\text{m}$  diameter, which is somewhat smaller than the nominally 0.1 mm waists of the laser beams. The simultaneous passage of the six beams requires that the thickness of the pinhole is much smaller than its diameter. Commercially available pinholes do not meet this requirement. Therefore, an extremely thin pinhole was produced. The pinhole consists of a glass plate with a  $0.1\ \mu\text{m}$  aluminium layer coated on one of its surfaces. An etching technique is used to remove the aluminium in an elliptical region having a short axis of  $50\ \mu\text{m}$  and a long axis of  $71\ \mu\text{m}$  as illustrated in Fig. A.2. The  $71/50$  ( $\approx \sqrt{2}$ ) ratio was chosen so that the opening appeared circular when viewed from a  $45^\circ$  angle.

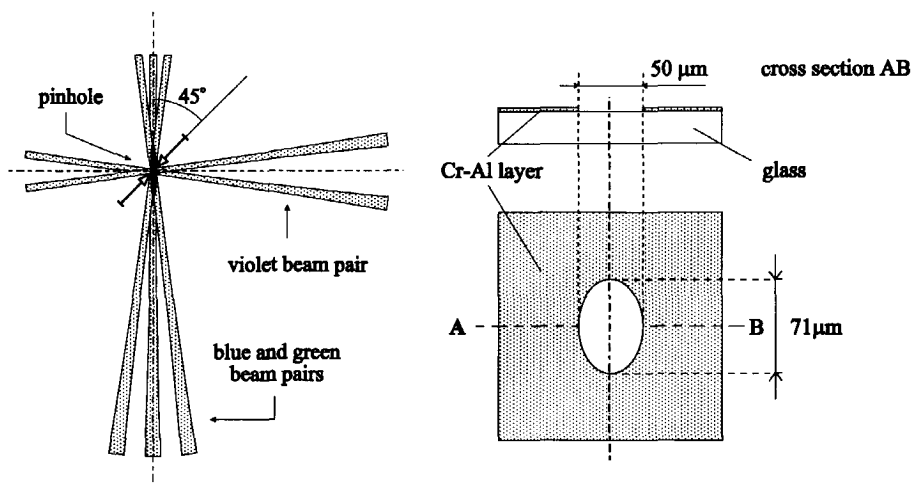


Figure A.1: The pinhole at 45° orientation. Figure A.2: Detailed view of the pinhole.

To place the pinhole in the centre of the overlapping blue and green measuring volumes, the pinhole position is adjusted until all four beams pass through the opening and are visible on a screen. Fine adjustments of the pinhole position in the  $x$ ,  $y$  and  $z$ -direction are made to maximize the light intensity of the four beam kernels on the screen. The pinhole can be positioned very accurately in the measuring volume centre, because displacements in the plane perpendicular to the optical axis as small as  $10\ \mu\text{m}$  cause a noticeable change in light intensity of the beam kernels on the screen. Of course, displacements along the optical axis are less sensitive. Then the violet beams are passed through the pinhole so that two violet beams are visible on a second screen. Finally, the orientation of violet beams is fine adjusted to maximize the light intensity of both violet kernels, while the pinhole location is fixed.

The above procedure results in three measuring volumes with nominally orthogonal fringe patterns that share a common region in space, as illustrated in Fig. A.3. The next step is to align the receiving optics such that scattered light is collected only from the overlap region of the three measuring volumes. To achieve this, the violet receiving optics are placed on the solid angle  $\kappa$ . This angle is chosen close to  $90^\circ$  so that side-scattered light is collected. A small, conventional pinhole placed in front of the photomultiplier acts as a spatial filter, thereby reducing the effective length of the violet measuring volume. Ideally, the diameter of this pinhole is chosen such that the effective length matches the size of the overlap region. The same procedure is followed for the collection optics of the blue and green channels. The angle  $\kappa$  should be near  $90^\circ$  to collect side-scattered light, and small pinholes in front of the photomultipliers limit the effective length of the blue and green measuring volumes to collect scattered light from the overlap region only.

A thin transparent foil placed in the overlap region of the three measuring volumes is used to align the receiving optics. The foil acts as a light-scattering source and is used as a target for the light collection optics. Therefore, it is important to position the foil

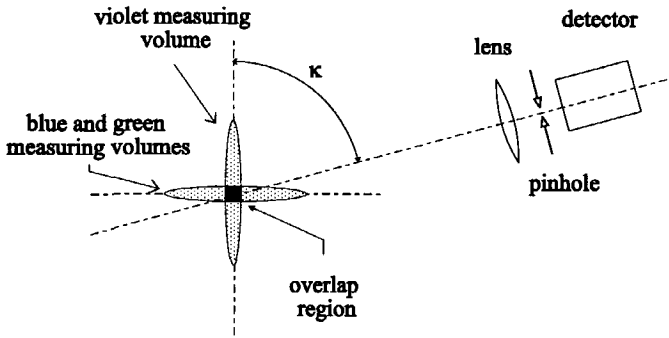


Figure A.3: Side-scatter arrangement for the receiving optics.

very accurately. To achieve this the foil may be viewed with a telescope. If the foil is not properly positioned, six beam crossings can be seen on the foil. In that case the location of the foil, should be fine adjusted until the different beam crossing converge into a single spot.



# Appendix B

## Generation of Simulated Data

### B.1 Introduction

The numerical generation of simulated turbulence data on a computer is an important step in the development of new spectral estimators. The desired property of the simulated data is the fact that their spectral density function (sdf) is known exactly, which is not the case for measured LDA data. This property enables the evaluation of different spectral estimators through a simple comparison between the computed spectral estimates and the exact sdf, as in Section 4.3.

In this appendix two methods are presented for the generation of simulated data. The first method can be found in, for example, Priestley [1981] and it can be used to generate second-order autoregressive ( $AR(2)$ ) data. This method is computationally inexpensive, but only little variation of the shape of the sdf is possible, because its characteristics are largely fixed by the  $AR(2)$  model. In this method a primary signal is created at closely spaced, equidistant time instants. Then a set of Poisson-distributed sampling times  $t_i$  is generated. The simulated velocity at time  $t_i$  then follows from linear interpolation in the primary signal. The second method is given by Shinozuka [1974] and it can be used to generate simulated velocity data with an arbitrary sdf that is sampled at Poisson distributed sampling times. This method is very time consuming, because it requires a large amount of computation.

### B.2 Poisson Distributed Sampling Times

Consider the random variable  $x$  which is uniformly distributed on the interval  $0 \leq x \leq 1$ . By definition, this means that the probability density function of  $x$  is given by [Papoulis 1991]

$$p(x) = \begin{cases} 1 & \text{if } 0 \leq x \leq 1 \\ 0 & \text{otherwise.} \end{cases} \quad (\text{B.1})$$

The random variable  $x$  is the starting point for the generation of Poisson-distributed sampling times. Press et al. [1989] give a good overview of practical methods to generate

uniformly-distributed numbers on a computer. A new random variable,  $\Delta t$ , can be computed from the random variable  $x$  using the following transformation:

$$\Delta t = -\frac{1}{\nu} \ln(x), \quad (\text{B.2})$$

where  $\nu$  is a positive constant. The probability density functions of  $\Delta t$  and  $x$  are related as [Papoulis 1991]:

$$q(\Delta t) = p(x) \left| \frac{dx}{d\Delta t} \right|. \quad (\text{B.3})$$

Combining Eq (B.2) and Eq (B.3) yields the probability density function of  $\Delta t$

$$q(\Delta t) = \nu e^{-\nu \Delta t} \quad 0 \leq \Delta t < \infty, \quad (\text{B.4})$$

indicating that the values of  $\Delta t$  are Poisson distributed. This means that Poisson-distributed arrival times  $\Delta t$  can be computed from Eq (B.2) once the value of the constant  $\nu$  is prescribed. Clearly,  $\nu$  is the mean data rate which is related to the measuring time  $T$  and the total number of samples  $N$  as  $\nu = N/T$ .

### B.3 Generation of AR(2) Data

The discrete parameter process  $U_t$  is called second-order autoregressive, AR(2), if it satisfies the following difference equation [Priestley 1981]

$$U_t + a_1 U_{t-1} + a_2 U_{t-2} = \epsilon_t, \quad (\text{B.5})$$

where  $\epsilon_t$  is a Gaussian random process with zero mean. The coefficients  $a_1$  and  $a_2$  are yet to be determined.  $U_t$  is the discrete parameter form of the continuous parameter process  $U(t)$  that satisfies the second-order differential equation

$$\frac{d^2 U(t)}{dt^2} + \alpha_1 \frac{dU(t)}{dt} + \alpha_2 U(t) = \epsilon(t). \quad (\text{B.6})$$

The coefficients  $\alpha_1$  and  $\alpha_2$  are related to  $a_1$ ,  $a_2$  and the equi-spaced time step  $\Delta t$  as (see Priestley [1981] for details)

$$\alpha_1 = \frac{-(a_1 + 2a_2)}{a_2 \Delta t} \quad \text{and} \quad \alpha_2 = \frac{(1 + a_1 + a_2)}{a_2 \Delta t^2}. \quad (\text{B.7})$$

The time step  $\Delta t$  of the process  $U_t$  is chosen such that there is negligible power at frequencies higher than  $1/\Delta t$ . The autocorrelation function  $\rho(\tau)$  of the continuous parameter process  $U(t)$  is given by [Priestley 1981]

$$\rho(\tau) = \frac{c_2}{c_2 - c_1} e^{c_1 |\tau|} - \frac{c_1}{c_2 - c_1} e^{c_2 |\tau|}, \quad (\text{B.8})$$

where the coefficients  $c_1$  and  $c_2$  are the roots of the polynomial  $g(x) = x^2 + \alpha_1 x + \alpha_2$ . The spectral density function of  $U(t)$  is simply the Fourier transform of  $\rho(\tau)$

$$S(\omega) \equiv \frac{1}{\pi} \int_0^\infty \rho(\tau) \cos \omega \tau \, d\tau = \frac{1}{\pi} \frac{\alpha_1 \alpha_2}{\alpha_1^2 \omega^2 + (\alpha_2 - \omega^2)^2}. \quad (\text{B.9})$$



Beyond its first edge frequency, this sdf behaves as  $\omega^{-2}$  until the second edge frequency is reached, after which the spectral density falls-off as  $\omega^{-4}$ , as shown in Fig. B.1

The specification of the coefficients  $c_1$  and  $c_2$  fixes the  $AR(2)$  autocorrelation function. As a result, the specification of  $c_1$  and  $c_2$  also fixes the value of several time scales that characterise  $U(t)$ , such as the Taylor time scale  $\lambda_t$  and the integral time scale  $T_u$ , which are defined by Eq (2.38) and Eq (2.37), respectively. It is easy to show that the relationship between  $\lambda_t$ ,  $T_u$  and the coefficients  $c_1$  and  $c_2$  is given by

$$\lambda_u^2 = \frac{2}{c_1 c_2} \quad \text{and} \quad T_u = \frac{-(c_1 + c_2)}{c_1 c_2}. \quad (\text{B.10})$$

Furthermore, the relationship between the variance of the simulated velocities  $\overline{u'^2}$  and the variance of the Gaussian random process  $\overline{\epsilon_t^2}$  is given by

$$\overline{u'^2} = \frac{(1 + a_2)\overline{\epsilon_t^2}}{(1 - a_2)(1 - a_1 + a_2)(1 + a_1 + a_2)}. \quad (\text{B.11})$$

The procedure to generate the simulated velocity data is as follows. First, the Taylor time scale  $\lambda_t$  and the integral time scale  $T_u$  are specified. This yields the coefficients  $c_1$  and  $c_2$ , which in turn yield the values of  $\alpha_1$  and  $\alpha_2$  from the polynomial  $g$ . For a chosen time step,  $\Delta t$ , the values of  $a_1$  and  $a_2$  follow from Eq (B.7). A closely spaced primary time series is subsequently generated from the difference equation Eq (B.5) after specification of the initial conditions, e.g.  $U_1 = U_2 = 0$ . Then a set of Poisson distributed sampling times,  $t_i$ , is created using Eq (4.1) and the simulated velocities  $U(t_i)$  follow from linear interpolation in the primary time series.

## B.4 The Shinozuka Method

Shinozuka [1974] describes a method that generates velocity samples from

$$U(t) = \sum_{k=1}^{k_{max}} \sqrt{4S(k\Delta\omega)\Delta\omega} \cos(k\Delta\omega t + \theta_k), \quad (\text{B.12})$$

where  $S(\omega)$  is an arbitrary spectral density function and  $\Delta\omega$  is the frequency spacing. The values of  $\theta_k$  are uniformly distributed on the interval  $[0, 2\pi]$ . The summation in Eq (B.12) can be evaluated for any value of the time  $t$ . Therefore, simulated velocity data can be created at Poisson-distributed sampling times. The advantage of this method is that it can be used for arbitrary sdfs, but, as mentioned in the introduction, it is much slower than the previous method, because the value of  $k_{max}$  is usually very large, for example  $10^5$ .

Shinozuka's method can be used to generate velocity data with a more realistic behaviour at high frequencies than the  $AR(2)$  data. As an example, one may use the "Pao-like" spectral density function given by [Hinze 1975]

$$S(\omega) = \frac{aT_u e^{-\frac{3}{2}a(\omega/\omega_d)^{4/3}}}{a\pi + (\omega/\omega_d)^{\frac{5}{3}}}. \quad (\text{B.13})$$

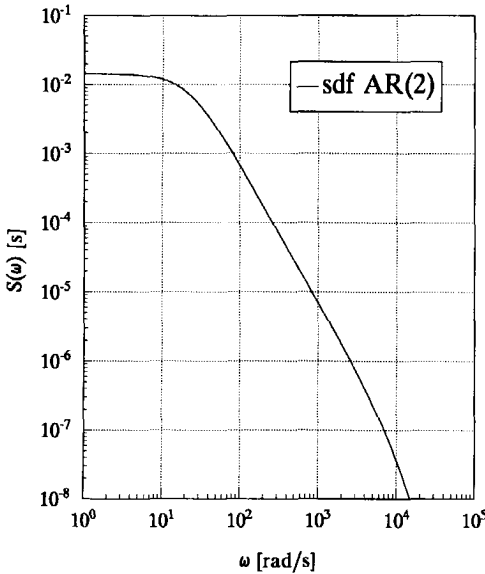


Figure B.1: The sdf of the AR(2) process for  $\alpha_1 = 10^4$  rad/s and  $\alpha_2 = 2/9 \times 10^6$  rad<sup>2</sup>/s<sup>2</sup>, corresponding to  $\lambda_t = 3.0$  ms and  $T_u = 45.0$  ms.

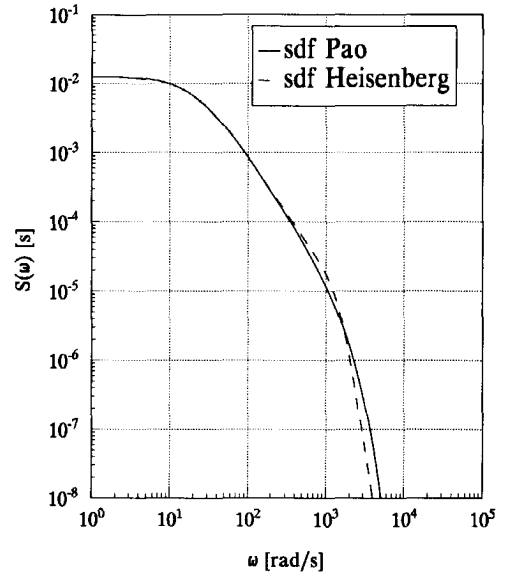


Figure B.2: The Pao-like sdf for  $a = 0.02$  and  $\omega_d = 112$  rad/s and the Heisenberg sdf for  $\beta_1 = 20.7$  rad/s and  $\beta_2 = 1500.0$  rad/s. In both cases:  $\lambda_t = 6.0$  ms and  $T_u = 40.0$  ms.

The constant  $\pi$  has been introduced in the denominator so that  $S(0) = T_u/\pi$  in accordance with Eq (4.25). For large frequencies  $S(\omega)$  behaves as  $\omega^{-5/3}$  and then decreases exponentially as suggested by Pao [1965]. An alternative is formed by the Heisenberg spectral density function [Hinze 1975]

$$S(\omega) = \frac{T_u}{\pi(1 + (\omega/\beta_1)^{5/3})(1 + (\omega/\beta_2)^{16/3})}. \quad (\text{B.14})$$

For high frequencies this sdf behaves as  $\omega^{-5/3}$  and then falls off as  $\omega^{-7}$  as suggested by Heisenberg, see Hinze [1975]. Both the Pao-like sdf and the Heisenberg sdf are shown in Fig. B.2.

## B.5 Simulated Data and Velocity Bias

Section B.2 described how to generate a set of Poisson distributed sampling times. If the simulated velocities  $U$  are computed at these Poisson distributed sampling times, then there is no correlation between the instantaneous velocity and the sampling process. This means that the simulated data are free of velocity bias, or, in other words: the simulated data are “unbiased.” These unbiased data are a good approximation for flows with low turbulence intensity. However, if the turbulence intensity is high, the effects of the velocity bias are likely to be significant, so that the unbiased data should not be

used. Section B.5.1 discusses how the velocity bias can be introduced in the simulated data. Section B.5.2 describes the simulation of the transit times of the particles. The transit times can be used as a weighting factor in bias correction methods.

### B.5.1 Generation of Biased Velocity Data

To introduce the velocity bias in the simulated data, the *distance* between the particles, rather than the *time* between successive particle arrivals is assumed to be Poisson distributed. In the so called conveyer-belt method [Tropea 1987] the arrival times  $t_i$  follow from

$$\Delta x_i = \int_{t_{i-1}}^{t_i} |\vec{V}(t)| dt, \quad (\text{B.15})$$

where  $\vec{V}(t)$  is the instantaneous velocity vector, which can be replaced by the velocity component  $U(t)$  when a one-dimensional flow is considered. Clearly,  $U(t)$  can be obtained from either the Priestley method or from Shinozuka's method. The distances  $\Delta x$  between consecutive particles can be generated from

$$p(\Delta x) = \gamma e^{-\gamma \Delta x}, \quad (\text{B.16})$$

using the procedure given in Section B.2. To assure the correct mean data rate  $\nu (= N/T)$ , the above Poisson process should have rate parameter  $\gamma = \nu/V_t$ , where  $V_t$  is the time average of the absolute velocity:

$$V_t = \frac{1}{T} \int_0^T |\vec{V}(t)| dt. \quad (\text{B.17})$$

The simulated velocities  $U$  determined at the times  $t_i$  now form a biased time series. Note that  $V_t$  reduces to the time average of  $V(t)$  if there are no instantaneous flow reversals.

### B.5.2 Generation of Particle Transit Times

To generate the transit times of the particles, it is necessary to make an assumption about the shape of the measuring volume. Here, it is assumed that the measuring volume is an ellipsoid with diameter  $d$  and length  $l$ :

$$\left(\frac{2x}{d}\right)^2 + \left(\frac{2y}{d}\right)^2 + \left(\frac{2z}{l}\right)^2 = 1. \quad (\text{B.18})$$

In a one-dimensional flow with the velocity in the  $x$ -direction, a particle travels over a distance

$$D = d \left( 1 - \left(\frac{2y_p}{d}\right)^2 - \left(\frac{2z_p}{l}\right)^2 \right)^{1/2} \quad (\text{B.19})$$

inside the measuring volume, when  $y_p$  and  $z_p$  are the  $y$ - and  $z$ -coordinates of the location where the particle enters the measuring volume. For simplicity it is assumed that the values of  $y_p$  and  $z_p$  are uniformly distributed on the intervals

$$-\frac{d}{2} \leq y_p \leq \frac{d}{2}, \quad (\text{B.20})$$

and

$$-\frac{l}{2} \left( 1 - \left( \frac{2y_p}{d} \right)^2 \right)^{1/2} \leq z_p \leq \frac{l}{2} \left( 1 - \left( \frac{2y_p}{d} \right)^2 \right)^{1/2}, \quad (\text{B.21})$$

respectively. Note that the boundaries for the random variable  $z_p$  are dependent on the value of  $y_p$ . Once the values of  $y_p$  and  $z_p$  are generated, the distance  $D$  can be computed from Eq (B.19) and the transit time  $tr$  of the  $i$ -th particle follows simply from

$$tr_i = \frac{D}{|U(t_i)|}. \quad (\text{B.22})$$

## Appendix C

# Measurement of Spatial Correlation Functions using LDA

### C.1 Introduction

Apart from accurate values of relatively simple statistics, such as the mean velocity, Reynolds stresses and triple velocity products, the development of turbulence models also requires knowledge of more complex quantities, for example, the dissipation of the turbulence kinetic energy. Since information on the dissipation is contained in the spatial correlation function (see Section 2.1.5), this quantity has been the subject of many investigations.

Most research on spatial correlation functions is based on hot-wire anemometry. However, this technique suffers from the drawback that a physical probe has to be inserted into the flow, thereby disturbing the flow field. In case of simultaneous measurements at two nearby locations, the interference between the probes further complicates the problem. Also, the results of hot-wire anemometry are reliable only for relatively low turbulence levels ( $< 20\%$ ). LDA solves these problems because of its non-intrusive character and the possibility to measure flow reversal. However, length-scale measurements based on LDA are still rare, because of the complexity of such experiments. Reliable measurements of spatial correlation functions often require small measurement volume dimensions and a high signal-to-noise ratio of the Doppler signals. The first requirement often necessitates that the receiving optics are oriented nearly perpendicular to the transmitting optical axes (side scatter). However, in that case the intensity of the received light is low compared to the intensity of the light that is scattered in forward or backward direction. It is possible to obtain Doppler signals with high signal-to-noise ratios when side scatter is used, but it makes high demands upon the quality of the alignment of both the transmitting and the receiving optics.

Despite the experimental difficulties, spatial correlations were measured by a number

of researchers. In as early as 1971 Morton and Clark measured longitudinal and lateral scfs in a turbulent pipe flow using two single component LDAs, while Schäfer [1982] has reported on the measurement of longitudinal scfs in a turbulent axisymmetric jet. These early correlation studies primarily presented correlation coefficients that were measured at rather coarse spacings, i.e. the measurements only revealed the large scale structure of the turbulence. Absil et al. [1990] were the first to report on detailed measurements of spatial correlation functions that yielded information on the small scale behaviour of the turbulence. Their study also revealed a number of previously unidentified bias sources that hamper the measurement of the small scale part of scfs.

Section C.2 aims to introduce these bias phenomena by means of a brief discussion of the research of Absil et al. [1990], Tummers et al. [1995], both from Delft University of Technology, and Benedict [1995] from North Carolina State University. Section C.2 is not meant to present a complete review of spatial correlation measurements that are based on LDA. The conclusions regarding the measurement of spatial correlation functions using LDA are given in Section C.3.

## C.2 Problems Related to the Measurement of Spatial Correlation Functions

### C.2.1 The cylinder wake

#### Experimental set-up

Absil et al. [1990] and Absil [1995] have reported on the measurement of scfs in the turbulent wake of a circular cylinder ( $D = 2$  mm) in air at a free stream velocity of 10 m/s. The scfs were measured using a technique in which light was collected from two distinct regions in a single elongated measuring volume formed by the green line (514.5 nm) of an Argon laser. The measuring volume had a length of 31 mm and a diameter of 0.6 mm. Scattered light was collected  $90^\circ$  off-axis, i.e. a side-scatter arrangement was used. The side-scattered light was then led through a semi-reflecting mirror, which was positioned such that the reflected light and the transmitted light had equal intensity. Each halve of the scattered light was subsequently focused on a separate photomultiplier. The pinholes placed in front of the photomultipliers had a diameter of 0.3 mm resulting of a pinhole image of about 0.2 mm (the magnification factor of the receiving optics was calibrated and found to be 1.54). In this way measurements could be obtained from two different locations in the measuring volume. The distance between the two measurement locations could be varied by traversing one of the pinhole images along the axis of the measuring volume.

The photomultiplier output signals were processed by two TSI counter processors (model 1990) operated in the  $N$ -cycle mode with 8 required fringe crossings and a 1 % comparison setting. The master time-interface was operated in the non-priority coincidence mode and the time-coincidence window was set at 50  $\mu$ s. The orientation of the fringe pattern was such that the streamwise velocity component,  $u$ , was measured with the spatial separation vector in the spanwise direction, ( $z$ ). Of course, this technique can only be used to measure lateral scfs; longitudinal or crosswise scfs cannot be measured.

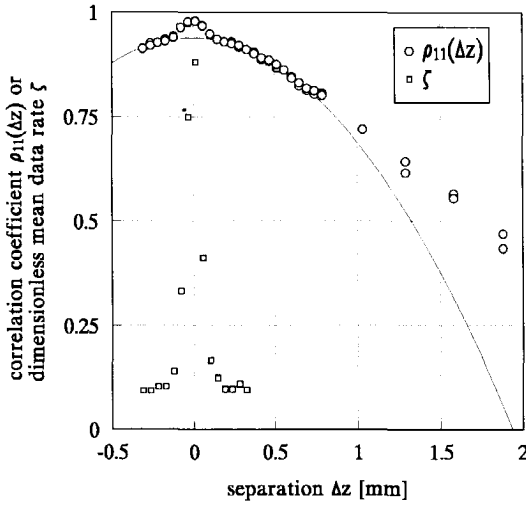


Figure C.1: The spatial correlation function  $\rho_{11}(\Delta z)$  at station  $x/D = 125$  and  $y/D = -2$  as measured by Absil et al. [1990]. The parabola is least squares fitted to (a subset of) the measured coefficients. The symbol  $\zeta$  is the dimensionless mean data rate.

**Effects of uncorrelated noise and overlapping pinhole images**

The spatial correlation coefficient at separation  $\Delta z$  was computed from

$$\rho_{11}(\Delta z) = \frac{\sum_{i=1}^N u'_i(z)u'_i(z + \Delta z)}{\left(\sum_{i=1}^N u'_i(z)^2 \sum_{i=1}^N u'_i(z + \Delta z)^2\right)^{1/2}}, \tag{C.1}$$

where the subscript  $i$  denotes the  $i$ -th velocity pair and  $N$  is the total number of velocity pairs. At each separation about  $5 \times 10^3$  time-coincident velocity pairs were acquired. Figure C.1 shows the small scale part of a scf measured by Absil in the cylinder wake at station  $x/D = 125$  and  $y/D = -2$ , which is the location of the maximum of the Reynolds normal stress  $\overline{u'^2}$ . The results in Fig. C.1 show that the measured scf is less than 1 at zero spatial separation. Absil et al. [1990] argued that the uncorrelated noise is largely responsible for this phenomenon. They assumed that the fluctuating velocity measured on each channel was the sum of the true velocity fluctuation  $u'$  and an uncorrelated noise contribution  $n$ , i.e.  $u_m = u' + n$ , where the subscript  $m$  denotes a measured value. Based on the experimental observation that the mean-square value of the uncorrelated noise  $\overline{n^2}$  is independent of the local flow conditions, they suggested the following (empirical) expression for the measured correlation coefficient at zero separation  $\rho_{11}(\Delta z = 0)_m$ :

$$\rho_{11}(\Delta z = 0)_m = \frac{\overline{u'_s(z)u'_t(z)}}{\left(\overline{u'_s(z)^2} \overline{u'_t(z)^2}\right)^{1/2}} \approx \frac{\overline{u'_s(z)u'_t(z)}}{\overline{u'_s(z)u'_t(z)} + (\overline{n_s^2} \overline{n_t^2})^{1/2}}, \tag{C.2}$$

where the subscript  $t$  ( $s$ ) refers to the traversable (stationary) measurement location. Eq (C.2) gave excellent predictions of the measured values of  $\rho_{11}(\Delta z = 0)$  in Absil's experiment.

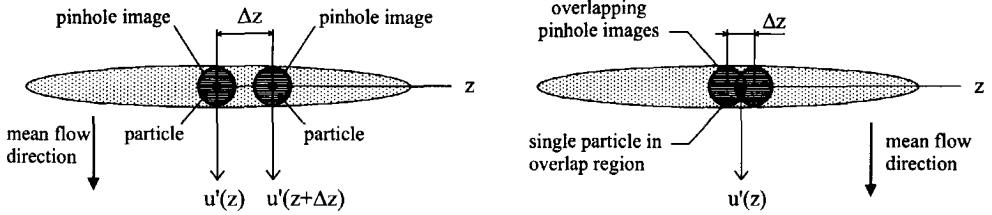


Figure C.2: The two pinhole images for a separation without overlap (left) and with overlap (right).

Furthermore, Fig. C.1 indicates that the measured correlation coefficients exhibit a bump for very small separations. This region with the relatively high correlation coefficients roughly coincides with the overlap region of the two 0.2 mm pinhole images (see Absil et al. [1990] for details). The overlapping of the pinhole images apparently obscures the shape of the scf for very small separations, which may hamper the determination of the Taylor length scale. Absil gave two possible explanations for the presence of the bump:

- Velocity errors that affect both channels, like phase fluctuations due to multiple particle signals or distortions of the fringe pattern. These errors, which are known as “correlated noise,” will artificially increase the correlation coefficients;
- Particles that transit the overlap region of the two pinhole images are observed on both channels. Velocity pairs that originate from these particles will be highly correlated in time as well as in space.

The latter explanation refers to a bias mechanism that is related to the particle arrival statistics. Figure C.2 illustrates this bias mechanism for the measurement of  $\rho_{11}(\Delta z)$ . In Absil’s experiment the separation  $\Delta z$  is normal to the mean flow direction ( $x$ ) and the local turbulence intensity is low ( $\approx 3\%$ ). The measurement system acquires a velocity pair  $u'(z)u'(z + \Delta z)$  only when both counter processors validate the Doppler signals and the time-coincidence criterion is satisfied. It is important to realize that for the situation depicted in Fig. C.2 (left) the velocity pair will be the result of a “two particle event,” because the velocity fluctuations  $u'(z)$  and  $u'(z + \Delta z)$  are produced by two different particles. In case of a two particle event it is theoretically impossible to acquire truly simultaneous velocity pairs due to the random nature of the particle arrivals. The time-coincidence window is used to acquire nearly simultaneous velocity pairs. By doing so, the measured scf actually resembles a space-time correlation function that is averaged over the duration of the coincidence window  $\tau_w$ . Clearly, the value of  $\tau_w$  should be sufficiently small so that the measured space-time correlation function is close to the spatial correlation function.



By definition, the velocity pair  $u'(z)u'(z + \Delta z)$  is the result of a "single particle event" when the velocity fluctuations  $u'(z)$  and  $u'(z + \Delta z)$  are produced by one particle that is sampled on both LDA channels. Figure C.2 (right) depicts the situation in which the pinhole images partly overlap. In that case the vast majority of the velocity pairs acquired by the measurement system originate from "single particles" that transit the overlap region, because the single-particle events are much more likely to occur than two-particle events<sup>1</sup>. The single-particle velocity pairs are perfectly correlated in space and naturally satisfy the time-coincidence criterion, thereby causing relatively high correlation values.

### C.2.2 The flat plate wake

#### Experimental set-up

Tummers et al. [1995] have reported on the measurement of scfs in the wake of a flat plate subjected to an adverse pressure gradient. Full details on the experimental set-up are given in Section 5.1, but some relevant data on the instrumentation will be given here also to achieve a degree of self-containment of this appendix.

The violet (476.5 nm) line of an Argon laser was used to create a measuring volume with a length of 1.7 mm and a diameter of 0.12 mm. The fringe pattern was oriented to measure the velocity component in either the  $x$ -direction ( $u$ ) or the  $y$ -direction ( $v$ ). Light was collected using a side-scatter configuration and a pinhole mounted in front of the photomultiplier reduced the effective length of the measuring volume to 0.2 mm. The green (514.5 nm) and the blue (488.0 nm) lines were used to create two fully overlapping measuring volumes each 1.3 mm in length and 0.11 mm in diameter. The fringe patterns were oriented to measure two velocity components in the  $x, y$ -plane, at  $+45^\circ$  and  $-45^\circ$  with respect to the  $x$ -axis. This enabled the simultaneous measurement of both  $u$  and  $v$ , but only  $u$  was used during the spatial correlation measurements. The 2D LDA formed the traversable probe during the measurements, whereas the 1D LDA served as the stationary probe. The photomultiplier output signal of the blue channel was processed using a (Dantec) BSA processor which acted as the time master. The green and violet channels were processed by two time-slave BSA processors. The BSA processors were operated in the "hardware-coincident mode," also known as the "channel blanking mode."

#### Effect of overlapping measuring volumes

The longitudinal scf of the streamwise velocity fluctuations  $\rho_{11}(\Delta x)$  was measured at several locations in the wake. Attention was focused on the correlation values at small spatial separation to obtain information on the Taylor length scales. Starting at zero separation the 2D LDA was traversed in the streamwise direction in steps of  $25 \mu\text{m}$ . For each separation  $3 \times 10^3$  velocity pairs were acquired at an average rate of 25 Hz. The

<sup>1</sup>This can also be observed from Fig. C.1. The squares represent the dimensionless mean data rate which is defined as the ratio of the coincident mean data rate and the mean data rate of the individual channels.

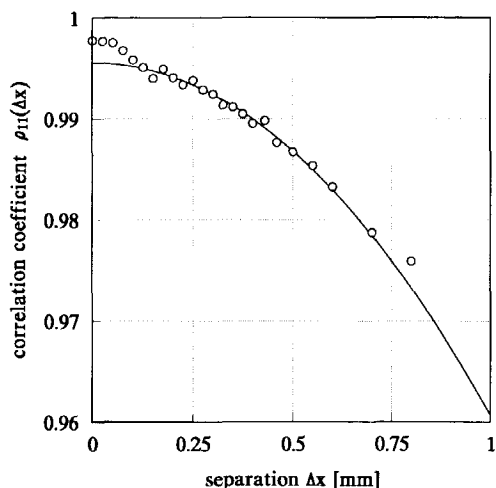


Figure C.3: The spatial correlation function  $\rho_{11}(\Delta x)$  at station  $x = 175$  mm,  $y = 47$  mm as measured by Tummers et al. [1995]. The parabola is least squares fitted to a subset of the measured coefficients.

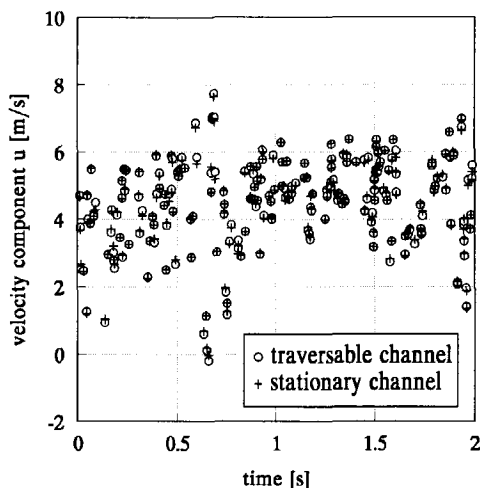


Figure C.4: Instantaneous velocities measured by the stationary and the traversable probe at station  $x = 175$  mm,  $y = 47$  mm for  $\Delta x = 0$ .

spatial correlation coefficient was then computed from

$$\rho_{11}(\Delta x) = \frac{\sum_{i=1}^N u'_i(x)u'_i(x + \Delta x)}{\left(\sum_{i=1}^N u'_i(x)^2 \sum_{i=1}^N u'_i(x + \Delta x)^2\right)^{1/2}}. \quad (\text{C.3})$$

Figure C.3 shows a typical result of a measurement. At zero separation the measured correlation value is high; approximately 0.998. This indicates that both LDA channels measured almost identical instantaneous velocities, i.e. the errors in the instantaneous velocities due to uncorrelated noise were very small (see Eq (C.2)). This is illustrated in Fig. C.4 which shows a number of instantaneous velocities as measured by the two LDA channels.

Another interesting detail in Fig. C.3 is the presence of a small bump for separations less than about 0.1 mm, similar to that observed by Absil et al. [1990]. Tummers et al. [1995] explained the bump as follows.

- For separations  $\Delta x < 0.1$  mm the measured correlation coefficients are too high as a result of the partial overlap of the effective measuring volumes. The BSA processors are operated in the hardware coincident mode so that data is acquired only during the time span that Doppler signals are present on all channels simultaneously. This requirement is most likely met when particles transit the overlap region of the measuring volumes. In that case, however, the effective spatial separation remains zero, even when the centres of the measuring volumes are a distance  $\Delta x$  apart. Therefore, the measured spatial correlation coefficients are incorrect as long as the measuring volumes (partly) overlap.

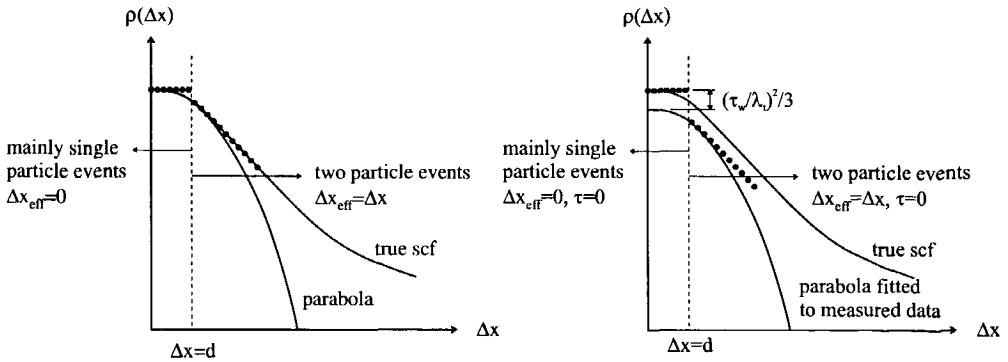


Figure C.5: The explanation of the bump in the measured scf as given by Tummers et al. [1995] (left) and the improved explanation (right) that takes the lag time into account.

The above explanation for the relatively high correlation coefficients is based on the phenomenon that the single particles that transit the overlap region have an effectively zero spatial separation although the physical centre of the measuring volumes do not coincide. Because of its influence on the effective spatial separation this phenomenon will be termed “separation bias.” Although Benedict [1995] accepted that this phenomenon was real, he noted that it did not fully explain all the characteristics of the bump as seen in Figs. C.1 and C.3. This criticism is fair because according to the above explanation the measured correlation value at zero separation  $\rho_{11}(\Delta x = 0)$  should equal the extrapolated value of the parabola that is tangent to the true scf at  $\Delta x = 0$ , as illustrated in Fig. C.5 (left). However, the results in Fig. C.3 show that  $\rho_{11}(\Delta x = 0)$  is above the “least-squares fitted” parabola at zero separation, so that the explanation given above needs to be improved.

The explanation may be improved by considering the issue of correlation loss due to the (small) difference in particle arrival time in case of a two-particle event. The single particles that move through the overlap region produce exactly time coincident velocity pairs. However, the particles are lagging in time in case of a two-particle event, with the maximum lag time determined by the time-coincidence window<sup>2</sup>. For separations without overlap this results in a reduction of the measured correlation coefficients as compared to the situation with overlapping measuring volumes. The reduction of the measured spatial correlation values due to the lag times between the velocity samples can be estimated as the mean value of  $1 - \rho(\tau)$ , where  $\rho$  is the (temporal) autocorrelation function of the velocity fluctuations in  $x$ -direction,  $u'$ . The lag time  $\tau$  between the velocity samples will vary between 0 and  $\tau_w$ . Recall that for small values of  $\tau$  the quantity  $1 - \rho(\tau)$  can be

<sup>2</sup>The time-coincidence window  $\tau_w$  is relevant when the BSA processors are operated in the time-coincidence mode, or when conventional TSI counter processors are used. When the BSA processors are operated in the hardware-coincidence mode, the time-coincidence window  $\tau_w$  should be replaced by the record interval  $n_{rec}/f_{sam}$ , see Section 3.2.7.

approximated as

$$1 - \rho(\tau) = \left( \frac{\tau}{\lambda_t} \right)^2, \quad (\text{C.4})$$

where,  $\lambda_t$  is the Taylor time scale of the velocity fluctuations  $u'$ . The mean value of  $1 - \rho(\tau)$  will be

$$\frac{1}{3}(\tau_w/\lambda_t)^2, \quad (\text{C.5})$$

when it is assumed that the values of  $\tau$  are uniformly distributed on the interval  $0 \leq \tau \leq \tau_w$ . When the spatial correlation measurement is based on two-particle events only, this reduction of the measured correlation coefficients will be constant for separations without overlap ( $\Delta x > d$ ). Consequently, the correlation coefficients for  $\Delta x < d$  appear too high as depicted in Fig. C.5 (right).

It is interesting to test this assertion by application to measured data. The scf in Fig. C.3 pertains to a measurement station with a Taylor time scale of 1.1 ms. Furthermore, the BSA signal processors were operated in the hardware-coincident mode with the record interval  $n_{rec}/f_{sam}$  set at  $5.3 \mu\text{s}$ . Substitution of these values in Eq (C.5) gives

$$\frac{1}{3} \left( \frac{n_{rec}/f_{sam}}{\lambda_t} \right)^2 = \frac{1}{3} \left( \frac{5.3 \times 10^{-6}}{1.1 \times 10^{-3}} \right)^2 = 7.7 \times 10^{-6}, \quad (\text{C.6})$$

which is negligible compared to the value of 0.0021 that is observed in Fig. C.3. Now consider the scf measured by Absil et al. [1990] in Fig. C.1. The observed correlation loss due to the lag time is much larger here; about 0.0405. The time coincidence window  $\tau_w$  for these measurements is  $50 \mu\text{s}$  and the Taylor time scale is about 0.34 ms [Steenbergen 1988], which gives

$$\frac{1}{3} \left( \frac{\tau_w}{\lambda_t} \right)^2 = \frac{1}{3} \left( \frac{50 \times 10^{-6}}{0.34 \times 10^{-3}} \right)^2 = 7.2 \times 10^{-3}, \quad (\text{C.7})$$

The computed values are very much smaller than the measured values in both cases. Clearly, the correlation loss due to the non-zero lag times between velocity samples is a real effect, but this effect alone cannot be responsible for the experimental observations. Other effects must be considered to explain all details of the bump in the measured spatial correlation function. One such effect is the correlated noise due to, for example, multiple particle signals as suggested by Absil et al. [1990]. If more particles are inside the overlap region of the measuring volumes, then both channels, say channel  $a$  and channel  $b$ , may produce velocity errors that are correlated. This means that the mean value of the cross-products of the velocity errors will no longer vanish, i.e.  $\overline{n_a n_b} \neq 0$ . In that case artificially high correlation coefficients are produced in the overlap region.

Another effect is the variation with the separation  $\Delta x$  of the mean-square value of the uncorrelated noise  $\overline{n^2}$  on both channels. This effect pertains to the measurement of spatial correlation functions using BSA processors that are operated in the hardware-coincident mode. It will therefore not provide an explanation for Absil's measurements. The effect will be discussed below and it is illustrated in Fig. C.6. Recall that when the

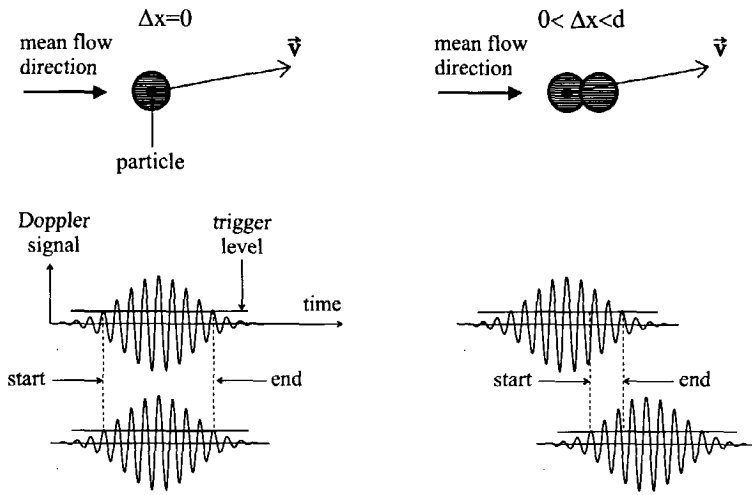


Figure C.6: Doppler signals for different spatial separations.

signal processors are operated in the hardware-coincident mode the processors acquire data only during the time span that Doppler signals are detected on all channels. For separations with (partial) overlap, i.e.  $0 \leq \Delta x \leq d$  where  $d$  is the diameter of the measuring volume, the system will acquire data mainly from single particles that move through the overlap region. Assume that the signal processors are able to determine the Doppler frequency with great accuracy when both measuring volumes perfectly overlap at  $\Delta x = 0$ . In that case  $\overline{n^2}$  will be small for both channels. For  $0 < \Delta x < d$  the measuring volumes partially overlap and the hardware coincidence mode effectively forces the signal processors to take measurements from the tails of the Doppler signals. The relatively low signal-to-noise ratio in these tails will increase the noise contribution on both channels, which results in a decrease of the measured correlation coefficients as compared to the situation for  $\Delta x = 0$ . The largest noise contributions are expected when both measuring volumes are almost separated. For  $\Delta x > d$  there is no overlap region and the hardware coincidence mode ensures that data are acquired only from two-particle events. However, the two particles will not enter the measuring volumes at exactly the same time and their transit times will also be different, due to the random distribution of the particles in space. It is therefore still possible that the signal processor will acquire data from the tails of the (hardware-coincident) Doppler signals, but this will generally not be the case. As a result, the mean-square value of the noise  $\overline{n^2}$  will on both channels be smaller than that for  $\Delta x < d$ , but larger than that for perfect overlap at  $\Delta x = 0$ .

**The correlation-geometry bias**

From the previous discussion it has become clear that single particles that transit the overlap region (in conjunction with the use of the hardware-coincidence mode) induce erroneous correlation coefficients because of the "separation bias." In addition to the separation bias, the single particles give rise to another error source even if the measuring

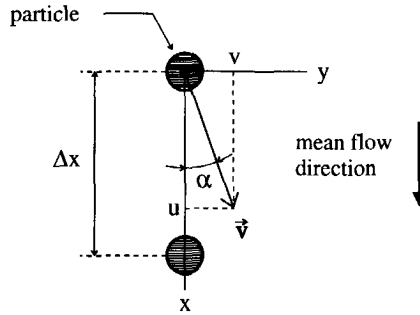


Figure C.7: The correlation-geometry bias for the measurement of  $\rho_{11}(\Delta x)$ .

volumes do not overlap. This error will be called “correlation-geometry bias,” because of its similarity to the conventional geometry bias in 3D LDA measurements as discussed in Section 3.3.4. The correlation-geometry bias is illustrated in Fig. C.7, which shows a top view of two measuring volumes each with diameter  $d$ . The centres of the measuring volumes are separated by a distance  $\Delta x$ . The separation is in the mean flow direction and  $\Delta x$  is larger than  $d$  so that there is no overlap. Consider a particle that moves through the upstream measuring volume with velocity vector  $\vec{v} = (u, v, w)$ . For simplicity, it may be assumed that  $w = 0$  so that the particle moves in the  $x, y$ -plane. If the velocity vector of the particle is such that  $\alpha > \tan^{-1}(d/\Delta x)$  then the particle will not reach the downstream measuring volume, irrespective of the velocity magnitude  $|\vec{v}|$ . It is obvious that this (single) particle cannot produce a velocity pair during a spatial correlation measurement. However, if the direction of  $\vec{v}$  is such that  $\alpha < \tan^{-1}(d/\Delta x)$  then the particle will reach the downstream measuring volume. The single particle will produce a velocity pair only if it can bridge the distance  $\Delta x$  within the duration of the time-coincidence window,  $\tau_w$ . Clearly this produces a bias towards high velocity components in the  $x$ -direction and small velocity components in the  $y$ -direction. The severity of this bias is a complicated function of the local flow conditions, like the mean flow direction and the turbulence intensity, the size and relative orientation of the measuring volumes, the duration of the coincidence window, and the value of the separation  $\Delta x$ . For example, when  $\Delta x \gg d$  then it is unlikely that a particle that transits the upstream measuring volume will also transit the downstream measuring volume because of the turbulent velocity fluctuations. In that case nearly all the velocity pairs will be the result of two-particle events and the geometry bias will not influence the results. Furthermore, for the situation sketched in Fig. C.7 the geometry bias is not expected to have a significant influence on the results if  $\Delta x \ll d$  and if the turbulence intensity is very low, because, in that case, nearly all the single particles will transit both measuring volumes within the time-coincidence window. However, bias problems are expected for the “intermediate” separations, see Benedict and Gould [1999].

To eliminate the correlation-geometry bias for both intermediate and large separations, Tummers et al. [1995] operated their BSA signal processors in the so-called hardware-coincident mode. This means that the Doppler signals were processed only when the signals were detected on all three channels simultaneously, otherwise the pro-

processors were inhibited. In other words: the processors were only able to acquire data from Doppler bursts that overlapped in time, see Section 3.3.4. Clearly, the hardware-coincidence mode eliminates the correlation-geometry bias completely for all separations without overlap, because it is no longer possible to produce velocity pairs from single particle events. Instead, all velocity pairs will be the result of two-particle events. However, Tummers et al. realized that the occurrence of single particles is unavoidable for situations with (partial) overlap. So, even when the channel blanking method is implemented the separation bias and the correlation-geometry bias will affect the results of the measurement when there is (partial) overlap. Therefore, Tummers et al. base their spatial correlation measurements exclusively on the collection of velocity pairs from two-particle events for separations without overlap, thereby accepting that the resolution of the spatial correlation measurement is effectively limited to the size of the overlap region of the measuring volumes.

### C.2.3 The backwards facing step flow

#### Experimental set-up

Benedict [1995] has reported on the measurement of scfs in the flow over a backwards facing step in a channel with area expansion ratio 1.25 and a step height  $H = 25.4$  mm at a free stream velocity of about 18 m/s. The green line (514.5 nm) of an Argon laser was used to measure the streamwise velocity component,  $u$ , directly. This LDA channel formed the stationary probe during the measurements. A second Argon laser employed either the green line (514.5 nm) or the blue line (488.0 nm) to measure the streamwise or lateral velocity component directly. This LDA could be accurately traversed in  $x$ ,  $y$  and  $z$ -direction. The measuring volumes had a length of 1.2 mm and a diameter of 0.14 mm. Both channels collected side-scattered light and the effective size of the measuring volumes was reduced to approximately 0.2 mm by means of small pinholes placed in front of the photomultipliers. The output signals of the photomultipliers were processed by two TSI counter processors (model 1990), operated in the  $N$ -cycle mode with 32 required fringe crossings and a 1% comparison. A time-coincidence window was employed to acquire nearly simultaneous velocity data and the time interface was operated in the non-priority coincidence mode. In principle, this set-up was able to measure all nine correlations  $\rho_{\alpha\alpha}(\Delta x)$ ,  $\rho_{\alpha\alpha}(\Delta y)$  and  $\rho_{\alpha\alpha}(\Delta z)$  with  $\alpha = 1, 2, 3$ , but results were only presented for  $\alpha = 1$ .

#### Increased spatial resolution

Tummers et al. [1995] eliminated the correlation-geometry bias through implementation of the channel-blanking method. The price paid for the elimination of this bias error is a reduction of the spatial resolution of the correlation measurements to the overlap region of the measuring volumes. As a result, this technique cannot be used to measure Taylor length scales when the turbulence scales are so small that the relevant part of the scf is contained in the overlap region.

Benedict [1995] claims that it is possible to measure scfs with a much higher spatial resolution. His approach is very different from that of Absil et al. or Tummers et al. Benedict aims to increase the spatial resolution by capitalizing on certain properties of

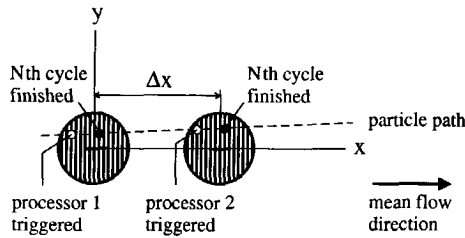


Figure C.8: Illustration of the “infinitely” high resolution for the measurement of  $\rho_{11}(\Delta x)$  in case of single particle events.

the velocity pairs that stem from single particles. To illustrate the approach, consider the measurement of  $\rho_{11}(\Delta x)$  in a flow with low turbulence intensity as depicted in Fig. C.8. The distance between the centres of the measuring volumes is  $\Delta x$ . For small separations, nearly all the particles that transit the upstream measuring volume will eventually also transit the downstream measuring volume, because the spatial separation is in the mean flow direction and the turbulence intensity is low. The interesting property of the single particle is that it moves over a distance nearly equal to  $\Delta x$  in between the times that the two Doppler bursts are processed and validated by the counter processors. For this to be true, it is required that the counter processors are operated in the  $N$ -cycle mode, the measuring volumes are identical in size and light intensity distribution and the fringe distance of both measuring volumes are equal. If these requirements are met, the spatial separation for the single particle events is (nearly) equal to the physical distance between the probe centres for small separations with and without overlap. This implies that the spatial resolution of the measurement is, in principle at least, infinitely high for the measurement of  $\rho_{11}(\Delta x)$  when  $\Delta x$  is in the mean flow direction and the turbulence intensity is low.

Several comments can be made at this stage. First, this technique will not work for the measurement of lateral and spanwise scfs, because the effective spatial separation will be zero due to the separation bias when there is partial overlap of the measuring volumes (see Benedict [1995] for details). Secondly, the turbulence intensity has to be low, otherwise a significant proportion of the velocity pairs will be the result of two-particle events, thereby negating the advantage of the high resolution. Thirdly, the use of a time-coincidence window in conjunction with the single particles will induce errors due to the correlation-geometry bias. It is not clear at this stage whether these bias errors can be made acceptably small.

### Effects of the time-coincidence window

Figure C.9 shows the small scale part of  $\rho_{11}(\Delta x)$  as measured by Benedict at station  $x/H = 3.0$  and  $y/H = 0.85$  for three values of the time-coincidence window. The graph



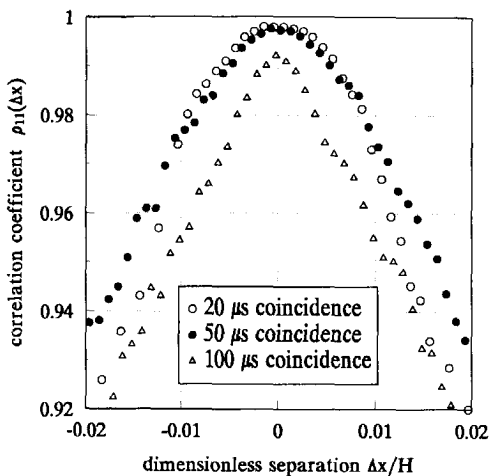


Figure C.9: The spatial correlation function  $\rho_{11}(\Delta x)$  for different coincidence windows as measured by Benedict [1995].

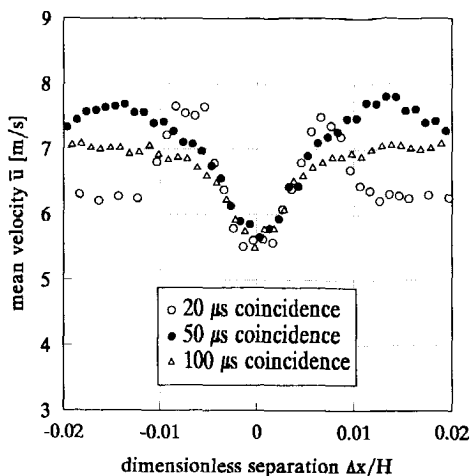


Figure C.10: The influence of the coincidence window on the mean velocity measured by the stationary probe for different coincidence windows.

shows that there is a clear dependence on the time-coincidence window. Benedict argues that the  $100\mu\text{s}$  window is too large because the measured correlation coefficients are significantly influenced by the lag times between the velocity samples. Furthermore, it is argued that the  $20\mu\text{s}$  window is too small, because it has resulted in correlation coefficients that do not exhibit a proper parabolic behaviour for small separations. The  $50\mu\text{s}$  window is considered a good compromise between the two effects.

Figure C.10 shows the mean velocity in streamwise direction as measured by the stationary probe for the correlation measurements shown in Fig. C.9. Similar graphs were presented for the variance of the velocity fluctuations at the stationary probe, but these are not included here. The graph illustrates that the geometry bias has a large effect on the measured velocity statistics for all three coincidence windows<sup>3</sup>. Benedict assumes that the geometry bias has not much influence on the correlation coefficients even though the mean velocity and the variance are strongly influenced by it. The present author doubts this assumption. It is unlikely that the correlation coefficients are unaltered by the geometry bias while all other statistics are. Awaiting further research on this topic, it appears more appropriate at this stage to assume that the correlation coefficients are also influenced by the geometry bias.

### Effect of the lag times between the samples

Benedict's method to measure the scf  $\rho_{11}(\Delta x)$  with almost infinite spatial resolution is based on the collection of velocity pairs  $u'(x)u'(x + \Delta x)$  from the single-particle events.

<sup>3</sup>It would have been interesting to see what happens when the coincidence window is further decreased below  $20\mu\text{s}$ , because when the duration is well below the transit time of the particles, the time-coincidence window acts as a channel-blanking scheme.

When certain conditions are met (discussed previously), the single particles have spatial separation  $\Delta x$ . Also, the single particles have a lag time  $\tau = \Delta x/u$ , which increases with increasing separation. This lag time will cause a small correlation loss similar to what is discussed in Section C.2.2. In Benedict's method to measure  $\rho_{11}(\Delta x)$ , it is implicitly assumed that it is possible to neglect the small correlation loss due to the non-zero lag times. It will be shown below that this is not possible.

For very small separations the scf measured using Benedict's method can be approximated as

$$\rho_{11}(\Delta x) = 1 - \left(\frac{\Delta x}{\lambda_x}\right)^2 - \left(\frac{\tau}{\lambda_t}\right)^2, \quad (\text{C.8})$$

where  $\lambda_x$  is the Taylor length scale and  $\lambda_t$  is the Taylor time scale of the velocity fluctuations in the  $x$ -direction. The first and the second term on the right-hand side of Eq (C.8) are desired terms, because they are the first and the second term in a Taylor series expansion of the scf  $\rho_{11}(\Delta x)$  around  $\Delta x = 0$ . The third term on the right-hand side of Eq (C.8) is not desired, because it is the correlation loss due to the lag times. The influence of the lag times on the measured scf can be safely neglected if the third term in Eq (C.8) is much smaller than the second term, i.e. if  $\tau^2/\lambda_t^2 \ll \Delta x^2/\lambda_x^2$ . In Benedict's method it is assumed that the turbulence intensity is small and  $\Delta x$  is in the mean-flow direction. In that case it is reasonable to use Taylor's hypothesis to convert time scales into length scales, i.e.  $\lambda_x = \lambda_t \bar{u}$ . Furthermore, the lag time  $\tau$  equals  $\tau = \Delta x/u = \Delta x/(\bar{u} + u')$ , so that Eq (C.8) can be approximated as

$$\rho_{11}(\Delta x) = 1 - \left(\frac{\Delta x}{\lambda_x}\right)^2 - \left(\frac{\Delta x}{\lambda_x}\right)^2 \left(\frac{1}{1 + u'^2/\bar{u}^2}\right). \quad (\text{C.9})$$

This means that the third term in Eq (C.8) has almost the same magnitude as the second term for all values of the separation  $\Delta x$ . As a result the measured Taylor length scales are approximately a factor  $\sqrt{2}$  too small. However, this is not a serious flaw of the method, because the factor can be taken into account when deriving the Taylor length scale from the measured spatial correlation values.

### C.2.4 Influence of spatial averaging

The subject of the spatial resolution was already touched upon during the discussion of Benedict's method to measure the scf with nearly infinite resolution by capitalizing on certain properties of the single particles. Consider Fig. C.11 for a more general treatment of the spatial resolution during scf measurements. The graph shows two measuring volumes each having length  $l$  and diameter  $d$ . The centres of the measuring volumes are a distance  $\Delta x$  apart in order to measure  $\rho(\Delta x)$ . In case of a two particle event, one particle will be measured in measuring volume 1 at time  $t_1$  and location  $(x_1, y_1, z_1)$  and the other will be measured in measuring volume 2 at time  $t_2$  and location  $(x_2, y_2, z_2)$ . For simplicity, it will be assumed that the two particles are measured at the same time, i.e.  $t_1 = t_2$  so that the correlation loss due to the lag time can be ignored. It is also assumed that both LDAs take "point measurements," which means that the individual

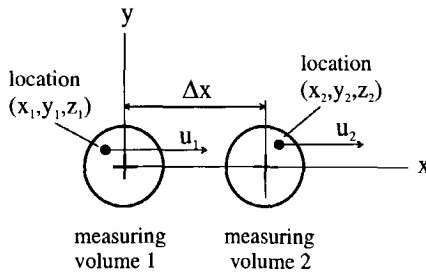


Figure C.11: Illustration of the spatial resolution for the measurement of  $\rho(\Delta x)$  in case of “two particle events.”

velocities  $u_1(x_1, y_1, z_1)$  and  $u_2(x_2, y_2, z_2)$  are unaffected by the size of the measuring volumes as explained in Section 4.3.5. The velocity product  $u_1 u_2$  is an estimate of the spatial covariance function for separation  $((x_1 - x_2)^2 + (y_1 - y_2)^2 + (z_1 - z_2)^2)^{1/2}$ . In general this separation will not be equal to  $\Delta x$  due to the finite size of the measuring volumes. Clearly, if the value of  $\Delta x$  is much larger than both the diameter and the length of the measuring volumes, than the effect of the spatial averaging on the measured spatial correlation coefficient can be neglected. However, it is not clear whether the effect of the spatial averaging can be neglected when the value of  $\Delta x$  is approximately equal to the size of the measuring volume, i.e.  $\Delta x \approx d$  or  $\Delta x \approx l$ . The actual separation between the two particles,  $((x_1 - x_2)^2 + (y_1 - y_2)^2 + (z_1 - z_2)^2)^{1/2}$ , will sometimes be larger than  $\Delta x$  and sometimes it will be smaller. Consequently, the effect of the error in the spatial separation will partly cancel when the sum of many velocity products  $u_1 u_2$  is computed. However, the effect of the error in the spatial separation will not completely cancel due to the curvature of the true scf. The quadratic term in a Taylor series expansion of the scf around  $\Delta x = 0$  can be used as an approximation of the maximum curvature of the true scf. This term is directly related to the Taylor length scale, so that the effects of the spatial averaging on the measured scf are expected to be negligible if the dimensions of the measuring volume are small compared to the Taylor length scale. This is in analogy with the effect of the spatial averaging on the autocorrelation function as discussed in Section 4.3.5.

### C.3 Concluding Remarks

Several error sources (biases) were considered for the measurement of spatial correlation functions using LDA. These error sources are related to the statistics of the particle arrivals at the different measuring volumes and are particularly important when the spatial separation between the measuring volumes is small. Some of these biases, like the geometry-correlation bias, are closely related to biases that were identified for 3D

LDA measurements. Others, like the separation bias, are unique to spatial correlation measurements.

Absil et al. [1990] used a single elongated measuring volume and ingenious receiving optics to measure the small-scale part of scfs. This method is suited for the measurement of lateral scfs. The experiments of Absil et al. also revealed the separation bias that caused too high correlation coefficients when the pinhole images were overlapping. This led to the concept of "single-particle events" and "multiple-particle events" in spatial correlation measurements based on LDA.

Tummers et al. [1995] used two separate LDA channels to measure both lateral and longitudinal scfs. The effects of the correlation-geometry bias, which has its origin in the single-particle events, were eliminated by using the channel-blanking scheme. The price paid for this advantage is that the spatial resolution is limited to the effective size of the measuring volumes, because the measured correlation coefficients are valid only for spatial separations without overlapping measuring volumes. However, this posed no problem for the measurements in the adverse-pressure-gradient wake of the flat plate, because there the smallest length scales of the turbulence were relatively large.

Benedict [1995] also used two separate LDA channels, but his approach was very different to that of either Absil et al. or Tummers et al. Instead of eliminating the effects of the correlation-geometry bias by the exclusion of the single-particles, Benedict did exactly the opposite and decided to use the single-particle events as a basis for the correlation measurements. The reason for doing so is the (theoretically) much higher spatial resolution that can be achieved with single-particle events. However, the price paid for this increased spatial resolution is the introduction of errors caused by the correlation-geometry bias. Also, the method is limited to the measurement of longitudinal scfs with the spatial separation vector in the mean-flow direction in flows with low turbulence intensity.

# Bibliography

- Absil, L.H.J. (1995) "Analysis of the Laser Doppler Measurement Technique for Application in Turbulent Flows," Phd. thesis, Delft University of Technology.
- Absil, L.H.J., Steenbergen, W., and Passchier, D.M. (1990) "Time and Spatial Correlation Measurements in the Wake of a Circular Cylinder using LDA," *Applied Scientific Research*, **47**:247-271.
- Adair, D. and Horne, W.C. (1989) "Turbulent Separated Flow over and Downstream of a Two-Element Airfoil," *Exp. Fluids*, (7):531-541.
- Adams, E.W. (1984) "Experiments on the Structure of Turbulent Reattaching Flow," Report md-43, Stanford University, Department of Mechanical Engineering.
- Adrian, R.J. and Yao, C.S. (1987) "Power Spectra of Fluid Velocities Measured by Laser Doppler Velocimetry," *Exp. Fluids*, (5):17-28.
- Alber, I.E. (1980) "Turbulent Wake of a Thin, Flat Plate," *AIAA Journal*, **18**(9):1044-1051.
- Andreopoulos, J. and Bradshaw, P. (1980) "Measurements of Interacting Turbulent Shear Layers in the Near Wake of a Flat Plate," *J. Fluid Mech.*, **100**:639-668.
- Antonia, R.A., Browne, L.W.B., and Fulachier, L. (1987) "Average Wavelength of Organised Structures in the Turbulent Far Wake of a Cylinder," *Exp. Fluids*, **5**:298-304.
- Barlow, R.S. and Johnston, J.P. (1988) "Structure of a Turbulent Boundary Layer on a Concave Surface," *J. Fluid Mech.*, **191**:137-176.
- Barnett, D.O. and Bentley, H.T. (1974) "Statistical Bias of Individual Realization Laser Velocimeters," In *Proceedings of the Second International Workshop on Laser Velocimetry*, volume 1, pp. 428-444.
- Benedict, L.H. (1995) "Direct Measurements of Turbulent Dissipation Rate in Flow over a Backwards-Facing Step using LDA," Phd. thesis, North Carolina State University.
- Benedict, L.H. and Gould, R.D. (1999) "Understanding Biases in the Near-Field Region of LDA Two-Point Correlation Measurements," *Exp. Fluids*, **26**:381-388.

- Boutier, A., Pagan, D., and Soulevant, D. (1985) "Measurements Accuracy with 3D Laser Velocimetry," Tp 171, ONERA.
- Bradshaw, P. (1973) "Effects of Streamline Curvature on Turbulent Flow," In *AGARD AG-169*.
- Bradshaw, P. (1976) "*Turbulence*," volume 12 of *Topics in Applied Physics*, chapter 1 Springer-Verlag.
- Brown, J.L. (1989) "Geometric Bias and Time Coincidence in 3-dimensional Laser Doppler Velocimeter Systems," *Exp. Fluids*, **7**:25-32.
- Buchhave, P., George, W.K., and Lumley, J.L. (1979) "The Measurement of Turbulence with the Laser-Doppler Anemometer," *Ann. Rev. Fluid Mech.*, **11**:443-503.
- Butter, D.J. (1984) "Recent Progress on Development and Understanding of High-Lift Systems," In *Improvement of Aerodynamic Performance Through Boundary Layer Control and High Lift Systems*, pp. 1.1-26.
- Cebeci, T. and Smith, A.M.O. (1974) "*Analysis of Turbulent Boundary Layers*," Academic Press.
- Chevray, R. and Kovasznay, L.S.G. (1969) "Turbulence Measurements in the Wake of a Thin Flat Plate," *AIAA Journal*, **7**(8):1641-1643.
- Cho, J.R. and Chung, M.K. (1992) "A  $k - \epsilon - \gamma$  Equation Turbulence Model," *J. Fluid Mech.*, **237**:301-322.
- Clauser, F. H. (1954) "Turbulent Boundary Layers in Adverse Pressure Gradients," *Journal of the Aeronautical Sciences*, **21**(2):91-108.
- Cutler, A.D. and Johnston, J.P. (1984) "An Experimental Investigation of the Effect of Initial Shear Stress Distribution on a Separating Turbulent Boundary Layer," In *AIAA paper 1583, 17th Fluid Dynamics, Plasma Dynamics, and Lasers Conference*.
- Daly, B.J. and Harlow, F.H. (1970) "Transport Equations of Turbulence," *Phys. Fluids*, **13**:2634-2649.
- Dimotakis, P.E. (1976) "Single Scattering Particle Laser Doppler Measurements of Turbulence," In *Applications of Non-Intrusive Instrumentation in Fluid Flow Research, AGARD CPP-193*, pp. 10.1-14.
- Dring, R.P. and Suo, M. (1978) "Particle Trajectories in Swirling Flows," *Journal of Energy*, **2**(4):233-237.
- Durao, D.F.G. and Whitelaw, J.H. (1979) "Relationship between Velocity and Signal Quality in Laser Doppler Anemometry," *J. Phys. E:Sci. Instrum.*, **12**:27-50.
- Durrani, T.S. and Greated, C.A. (1977) "*Laser Systems in Flow Measurement*," Plenum Press.

- Durst, F. (1982) "Combined Measurements of Particle Velocities, Size Distributions, and Concentrations," *Journal of Fluids Engineering*, **104**:285–296.
- Durst, F., Melling, A., and Whitelaw, J.H. (1976) "*Principles and Practice of Laser Doppler Anemometry*," Academic Press.
- Durst, F. and Stevenson, W.H. (1979) "Influence of Gaussian Beam Properties on Laser Doppler Signals," *Applied Optics*, **18**(4):516–524.
- Eaton, J.K. and Johnston, J.P. (1981) "A Review of Research on Subsonic Turbulent Flow Reattachment," *AIAA Journal*, **19**(9):1093–1100.
- Edwards, R.V. (1987) "Report of the Special Panel on Statistical Particle Bias Problems in Laser Anemometry," *Journal of Fluids Engineering*, **109**:89–93.
- Edwards, R.V. and Kolodzy, P.J. (1986) "Computation of the Autocorrelation Function of Velocity Fluctuations using a Laser Anemometer in Sparsely Seeded Flows," In *Proceedings of the Third International Symposium on Applications of Laser Technology to Fluid Mechanics*, pp. 103–112.
- Gaster, M. and Roberts, J.B. (1975) "Spectral Analysis of Randomly Sampled Signals," *Journal of the Institute of Mathematics and its Applications*, **15**:195–216.
- Gaster, M. and Roberts, J.B. (1977) "The Spectral Analysis of Randomly Sampled Records by a Direct Transform," *Proceedings of the Royal Society*, **354**:27–58.
- George, W.K. (1978) "Processing of Random Signals," In *Proceedings of the Dynamic Flow Conference*, pp. 757–793.
- Goldstein, R.J. (1983) "*Fluid Mechanics Measurements*," chapter 5 Hemisphere Publishing Company.
- Haji-Haidari, A. and Smith, C.R. (1988) "Development of the Turbulent Near Wake of a Tapered Thick Flat Plate," *J. Fluid Mech.*, **189**:135–163.
- Hanjalić, K., Jakirlić, S., Stošić, N., Vasić, S., and Hadžić, I. (1992) "Collaborative Testing of Turbulence Models 1990/1992," Report Istm 352/t/92, Universität Erlangen–Nürnberg.
- Hanjalić, K. and Launder, B.E. (1980) "Sensitizing the Dissipation Equation to Irrotational Strains," *ASME, Journal of Fluids Engineering*, **102**:34–40.
- Hayakawa, M. and Iida, S. (1992) "Behaviour of Turbulence in the Near Wake of a Thin Flat Plate at Low Reynolds Numbers," *Phys. Fluids A*, **4**(10):2282–2291.
- Henkes, R.A.W.M. (1997) "Comparison of Turbulence Models for Attached Boundary Layers Relevant to Aeronautics," *Applied Scientific Research*, **57**(1):43–65.
- Hill, P.G., Schaub, U.W., and Senoo, Y. (1963) "Turbulent Wakes in Pressure Gradients," *Journal of Applied Mechanics*, pp. 518–524.

- Hinze, J.O (1975) "*Turbulence*," McGraw-Hill, 2nd edition.
- Hjelmfelt, A.T. and Mockros, L.F. (1966) "Motion of Discrete Particles in a Turbulent Fluid," *Appl. Sci. Res.*, **16**:149-161.
- Hoesel, W. and Rodi, W. (1977) "New Biasing Elimination Method for Laser Doppler Velocimeter Counter Processing," *Rev. Sci. Instrum.*, **48**(7):910-919.
- Jakirlić, S., Hadžić, I., and Hanjalić, K. (1994) "Computation of Non-Equilibrium and Separating Flows at Transitional and High Re-Numbers with a New Low Re-Number Second-Moment Closure Model," In *Proceedings of Strömungen mit Ablösung*. AGSTAB, DGLR Congress, Erlangen, Germany.
- Jeans, A.H. and Johnston, J.P. (1982) "The Effects of Streamwise Concave Curvature on Turbulent Boundary Layer Structure," Report md-40, Thermosciences Division - Department of Mechanical Engineering, Stanford University, USA.
- Johnson, D.A., Modarres, D., and Owen, F.K. (1984) "An Experimental Verification of Laser-Velocimeter Sampling Bias and Its Correction," *Journal of Fluid Engineering*, **106**:5-12.
- Johnston, L.J. and Horton, H.P. (1986) "An Experimental Study of Turbulent Wake/Boundary Layer Mixing Flows," In *Proceedings of the International Congress of Aeronautical Sciences (ICAS)*, pp. 360-369.
- Jones, W.P. and Launder, B.E. (1972) "The Prediction of Laminarization with a Two-Equation Model of Turbulence," *Int. J. Heat and Mass Transfer*, **15**(1):301-313.
- Kraan, T.D.G. (1995) "Bepaling van Autocorrelatie Functies m.b.v. Laser Doppler Anemometrie Metingen in een Turbulente Grenslaag en Zog met Tegenwerkende Drukgradiënt," Msc. thesis, Delft University of Technology (in Dutch).
- Launder, B.E., Reece, G.J., and Rodi, W. (1975) "Progress in the Development of a Reynolds-Stress Turbulence Closure," *J. Fluid Mech.*, **68**:537-566.
- Launder, B.E. and Sharma, B.I. (1974) "Application of the Energy Dissipation Model of Turbulence to the Calculation of Flow near a Spinning Disc," *Letters in Heat and Mass Transfer*, **1**:131-138.
- Launder, B.E. and Shima, N. (1989) "Second-Moment Closure for the Near-Wall Sub-layer: Development and Application," *AIAA Journal*, **27**(10):1319-1325.
- Lock, R.C. (1981) "A Review of Methods for Predicting Viscous Effects on Aerofoils and Wings at Transonic Speeds," In *AGARD CP-291*, pp. 2.1-9.
- Lock, R.C. and Firmin, M.C.P. (1982) "*Survey of Techniques for Estimating Viscous Effects in External Aerodynamics*," Numerical Methods in Aeronautical Fluid Dynamics, ed. P.L. Roe. Academic Press.



- Luchik, T.S. and Tiederman, W.G. (1985) "Effect of Spanwise Probe Volume Length on Laser Velocimeter Measurements in Wall Bounded Turbulent Flows," *Experiments in Fluids*, **3**:339-341.
- Maanen, van H.R.E. and Tummers, M.J. (1996) "Estimation of the Auto Correlation Function of Turbulent Velocity Fluctuations using the Slotting Technique with Local Normalisation," In *Proceedings of the 8th International Symposium on Applications of Laser Techniques to Fluid Mechanics*, pp. 36.4.1-6.
- Maurice, M.S. (1992) "AIAA-92 paper 0764," In *AIAA*.
- Mayo, W.T. (1974) "A Discussion of Limitations and Extensions of Power Spectrum Estimation with Burst Counter LDV Systems," In *Proceedings of the Second International Workshop on Laser Velocimetry*, pp. 90-104. Purdue University.
- McDougall, T.J. (1980) "Bias Correction for Individual Realisation LDA Measurements," *J. Phys. E:Sci. Instrum.*, **13**:53-60.
- McLaughlin, D.K. and Tiederman, W.G. (1973) "Biasing Correction for Individual Realization of Laser Anemometer Measurements in Turbulent Flows," *Phys. Fluids*, **16**:7.
- Meredith, P.T. (1992) "Viscous Phenomena Affecting High-Lift Systems and Suggestions for Future CFD Development," In *High-Lift System Aerodynamics*, pp. 19.1-8.
- Meyers, J.F. (1985) "The Elusive Third Component," In *Proceedings of the International Symposium on Laser Anemometry*, pp. 247-254.
- Meyers, J.F. (1988) "Laser Velocimeter Data Acquisition and Real Time Processing Using a Microcomputer," In *Proceedings of the 4th International Symposium on Applications of Laser Techniques to Fluid Mechanics*, pp. 7.20.1-5.
- Meyers, J.F. and Hepner, T.E. (1988) "Measurement of Leading Edge Vortices from a Delta Wing using a Three Component Laser Velocimeter," In *Proceedings of the AIAA 15th Aerodynamic Testing Conference*.
- Morrison, G.L., Johnson, M.C., Swan, D.H., and DeOtte, R.E. (1990) "Advantages of Orthogonal and Non-Orthogonal 3-D LDA Systems," In *Proceedings of the 5th International Symposium on Applications of Laser Techniques to Fluid Mechanics*, pp. 25.2.1-6.
- Nakayama, A. (1985) "Measurements of Separating Boundary Layer and Wake of an Airfoil using Laser Doppler Velocimetry," In *AIAA paper 0181, 23rd Aerospace Sciences Meeting*.
- Nakayama, A. and Kreplin, H.P. (1994) "Characteristics of Asymmetric Turbulent Near Wakes," *Phys. Fluids*, **6**(7):2430-2439.
- Nakayama, A., Kreplin, H.P., and Morgan, H.L. (1990) "Experimental Investigation of Flow Field about a Multielement Airfoil," *AIAA Journal*, **28**:14-21.

- Nakayama, A. and Liu, B. (1990) "The Turbulent Near Wake of a Flat Plate at Low Reynolds Number," *J. Fluid Mech.*, **217**:93-114.
- Pao, Y.H. (1965) "Structure of Turbulent Velocity and Scalar Fields at Large Wave Numbers," *Phys. Fluids*, **8**:1063-1075.
- Papoulis, A. (1991) "*Probability, Random Variables, and Stochastic Processes*," McGraw-Hill, 3rd edition.
- Passchier, D.M. (1992) *private communication*.
- Patel, V.C. and Chen, H.C. (1987) "Turbulent Wake of a Flat Plate," *AIAA Journal*, **25**(8):1078-1085.
- Patel, V.C., Rodi, W., and Scheuerer, G. (1985) "Turbulence Models for Near-Wall and Low Reynolds Number Flows: A Review," *AIAA Journal*, **23**(9):1308-1319.
- Patel, V.C. and Scheuerer, G. (1982) "Calculation of Two-Dimensional Near and Far Wakes," *AIAA Journal*, **20**(7):900-907.
- Petrie, H.L., Samimy, M., and Addy, A.L. (1988) "Laser Doppler Velocity Bias in Separated Turbulent Flows," *Exp. Fluids*, **6**:80-88.
- Petrov, A.V. (1980) "Some Features of Flow Past Slotted Wings," Library translation 2050, Royal Aircraft Establishment (also *Uchenye Zapiski, TsAGI*, **8,6**, pp. 119-124, 1977).
- Plomp, A. (1986) "Characteristics of Four Aerosol Generators for Velocity Measurements in a Wind Tunnel," contract report 86/11, ECN, The Netherlands.
- Pot, P.J. (1979) "Measurements in a 2-D Wake and in a 2-D Wake Merging into a Boundary Layer," Tr-79063 u, NLR, The Netherlands.
- Press, W.H., Flannery, B.P., Teukolsky, S.A., and Vetterling, W.T. (1989) "*Numerical Recipes*," Cambridge University Press, 1th edition.
- Priestley, M.B. (1981) "*Spectral Analysis and Time Series*," Academic Press.
- Ramaprian, B.R., Patel, V.C., and Sastry, M.S. (1982) "The Symmetric Turbulent Wake of a Flat Plate," *AIAA Journal*, **20**(9):1228-1235.
- Ramjee, V., Tulapurkara, E.G., and Rajasekar, R. (1987) "Development of an Airfoil Wake in a Longitudinally Curved Stream," *AIAA Journal*, **26**(8):948-953.
- Reichardt, H. (1951) "Vollständige Darstellung der Turbulenten Geschwindigkeitsverteilung in Glatten Leitungen," *Zeitschrift für Angewandte Mathematik and Mechanik*, **31**(7):208-219.
- Reynolds, O. (1895) "On the Dynamical Theory of Incompressible Viscous Fluids and the Determination of the Criterion," *Philosophical Transactions of the Royal Society of London*, **186**(Series A):123-164.

- Rudd, M.J. (1969) "A New Theretical Model for the Laser Doppler Meter," *J. Phys. E.*, **2**:4.
- Schäfer, H.J. (1982) "Study of Coherent Structures in a High-Speed Exhaust Jet," In *Selected papers from the First Int. Symp. on Applications of LDA to Fluid Mechanics*, pp. 221-228.
- Schlichting, H. (1987) "*Boundary-Layer Theory*," McGraw-Hill, 7th edition.
- Scott, P.F. (1974) "Theory and Implementation of Laser Velocimeter Turbulence Spectrum Measurements," In *Proceedings of the Second International Workshop on Laser Velocimetry*, pp. 47-67. Purdue University.
- Shinozuka, M. (1974) "Digital Simulation of Random Processes in Engineering Mechanics with the Aid of FFT Technique," In *Stochastic Problems in Mechanics*, pp. 277-286. University of Waterloo Press.
- Simpson, R.L. (1989) "Turbulent Boundary-Layer Separation," *Ann. Rev. Fluid Mech.*, (21):205-234.
- Simpson, R.L., Chew, Y.-T., and Shivaprasad, B.G. (1981) "The Structure of a Separating Turbulent Boundary Layer. Part1: Mean Flow and Reynolds stresses.," *J. Fluid Mech.*, **113**:23-51.
- Smith, A.M.O. (1975) "High-Lift Aerodynamics," *Journal of Aircraft*, **12**(6):501-530.
- Somerscales, E.F.C. (1981) "*Fluid Dynamics*," volume 18 of *Methods of Experimental Physics*, chapter 1 Academic Press.
- Spalart, P.R. (1988) "Direct Simulation of a Turbulent Boundary Layer up to  $R_\theta = 1410$ ," *J. Fluid Mech.*, **187**:61-98.
- Starke, A.R. (2000) "A Combined Experimental and Numerical Study of the Turbulent Wake," Phd. thesis, Delft University of Technology.
- Steenbergen, W. (1988) "Noise and Spatial Resolution Effects in a LDA Measured Space and Autocorrelation of the Turbulent Cylinder Wake," Msc. thesis, Delft University of Technology.
- Strien, C. van (1988) "Invloed van Snelheidsbias op de Bepaling van de Locale Energie Dissipatie in een Geroerd Vat," Msc. thesis, Eindhoven University of Technology (in Dutch).
- Tennekes, H. and Lumley, J.L. (1972) "*A First Course in Turbulence*," The MIT Press.
- Townsend, A.A. (1976) "*The Structure of Turbulent Shear Flow*," Cambridge University Press, 2nd edition.
- Tropea, C. (1986) "A Practical Aid for Choosing the Shift Frequency in LDA," *Exp. Fluids*, **4**:79-80.

- Tropea, C. (1987) "Turbulence-induced Spectral Bias in Laser Anemometry," *AIAA Journal*, **25**:306-309.
- Tummers, M.J. (1992) "Snelheidsbias bij Laser Doppler Anemometrie," Msc. thesis, Delft University of Technology (in Dutch).
- Tummers, M.J., Absil, L.H.J., and Passchier, D.M. (1992) "An Experimental Investigation of Velocity Bias in a Turbulent Flow," In *Proceedings of the 6th International Symposium on Applications of Laser Techniques to Fluid Mechanics*, pp. 5.4.1-7.
- Tummers, M.J. and Passchier, D.M. (1996a) "Spectral Analysis of Individual Realization LDA Data," Report lr-808, Faculty of Aerospace Engineering, Delft University of Technology, The Netherlands.
- Tummers, M.J. and Passchier, D.M. (1996b) "Spectral Estimation using a Variable Window and the Slotting Technique with Local Normalization," *Meas. Sci. Technol.*, **7**:1541-1546.
- Tummers, M.J. and Passchier, D.M. (1999) "Estimation of the Autocorrelation Function from Individual Realisation LDA Data," (submitted to *Experiments in Fluids*).
- Tummers, M.J., Passchier, D.M., and Aswatha Narayana, P.A. (1994) "Three-component LDA Measurements of Mean Turbulence Quantities, Time- and Spatial Correlation Functions in the Wake of a Flat Plate in an Adverse Pressure Gradient," In *Proceedings of the 7th International Symposium on Applications of Laser Techniques to Fluid Mechanics*, pp. 25.1-7.
- Tummers, M.J., Passchier, D.M., and Aswatha Narayana, P.A. (1995) "LDA Measurements of Time- and Spatial Correlation Functions in an Adverse Pressure Gradient," In *Proceedings of the ASME/JSME Fluids Engineering and Laser Anemometry Conference*, volume 229, pp. 347-354.
- Tummers, M.J., Starke, A.R., Henkes, R.A.W.M., and Passchier, D.M. (1997) "Effects of Pressure Gradients on the Near Wake of a Flat Plate," In *Proceedings of the Seventh International Conference on Laser Anemometry, Advances and Applications*, pp. 825-832. Karlsruhe, Germany.
- Wilcox, D.C. (1993) "Turbulence Modeling for CFD," DCW Industries.
- Winter, A.R., Graham, L.J.W., and Bremhorst, K. (1991) "Effects of Time Scales on Velocity Bias in LDA Measurements using Sample and Hold Processing," *Exp. Fluids*, **11**:147-152.
- Yanta, W.J., Gates, D.F., and Brown, F.W. (1971) "The Use of a Laser-Doppler Velocimeter in Supersonic Flow," In *Proceedings of the Second International Workshop on Laser Velocimetry*, volume AIAA paper 71-287.
- Yeh, Y. and Cummins, H.Z. (1964) "Localized Fluid Flow Measurements with a He-Ne Laser Spectrometer," *Appl. Phys. Lett.*, **4**:3.

# Samenvatting

Het hoofddoel van dit onderzoek is het verkrijgen van meer begrip van de complexe stroming in het nabije zog van een vlakke plaat, dat onderworpen is aan een tegenwerkende drukgradiënt. Om dit doel te bereiken is een gecombineerd experimenteel en numeriek onderzoek verricht. Een drie-componenten LDA (3D LDA) is gebruikt om gegevens te verzamelen over gemiddelde snelheden, Reynolds spanningen en triple-producten. LDA is ook gebruikt voor het meten van vermogensspectra en plaatscorrelatie functies. Deze gegevens zijn gebruikt voor een gedetailleerde vergelijking tussen de experimenten en berekeningen gebaseerd op de Reynolds-gemiddelde Navier Stokes vergelijkingen. Twee turbulentie modellen zijn toegepast: een  $k - \epsilon$  model en een Reynolds-stress transport model. De vergelijking tussen de experimenten en de berekeningen droeg bij tot de interpretatie van de experimentele resultaten en maakte het mogelijk om onjuistheden op te sporen in de turbulentie modellen voor berekeningen van het zog in tegenwerkende drukgradiënt.

Het gebruik van een 3D LDA voor metingen in een turbulente stroming wordt gehinderd door een drietal foutenbronnen. Een algemene configuratie voor de 3D LDA is voorgesteld waarmee de drie foutenbronnen geëlimineerd worden. Verder geeft de random bemonstering bij LDA aanleiding tot problemen zoals het snelheidsbias en een hoge statistische scatter in de gemeten autocorrelatie functies en de vermogensspectra. Een experimenteel onderzoek bevestigde het bestaan van het snelheidsbias en toonde aan dat voor de invloed van het snelheidsbias gecorrigeerd kan worden door weegfactoren te gebruiken die gebaseerd zijn op de inverse van de snelheid. Het probleem van de hoge statistische scatter in de gemeten autocorrelatie functies en de vermogensspectra is opgelost door de invoering van een lokaal geschaalde versie van de 'slotting' methode en een techniek waarbij gebruik wordt gemaakt van een variabel venster.

De experimenten in de achterrandsstroming van de vlakke plaat in een tegenwerkende drukgradiënt wezen op een snelle groei van de dikte van de grenslaag en het zog, een sterke toename in stromingsrichting van de turbulente kinetische energie en de aanwezigheid van een gebied met terugstroming op enige afstand stroomafwaarts van de achterrands. De balans van de vergelijking voor de turbulente kinetische energie liet zien dat de dissipatie afneemt in stromingsrichting, terwijl de productie van turbulente kinetische energie op een hoog niveau blijft. De in het nabije zog gemeten vermogensspectra onthulden de aanwezigheid van een significante hoeveelheid turbulente kinetische energie bij (zeer) lage frequenties.

Noch het  $k - \epsilon$  model noch het Reynolds-stress transport model waren in staat om de gemeten terugstroming en de sterke toename van de kinetische energie te reproduceren. Beide turbulentie modellen berekenden een te grote dissipatie in het nabije zog. Aangetoond is dat dit het gevolg is van onjuistheden in de transportvergelijkingen voor de dissipatie, die in beide turbulentie modellen grote gelijkenis vertonen. Het blijkt dat de transportvergelijking voor de dissipatie reageert op de grote productie van kinetische energie door een hoog niveau voor de dissipatie te handhaven. Dit is echter een onjuiste respons, omdat een belangrijk deel van de geproduceerde kinetische energie in de lage frequenties blijft en niet in het nabije zog gedissipeerd wordt.

# Dankwoord

Een promotieonderzoek verricht je niet zonder hulp van anderen. Velen hebben een bijdrage geleverd aan de totstandkoming van dit proefschrift. Hiervoor wil ik hen hartelijk bedanken. Een aantal personen wil ik met name noemen.

Graag wil ik mijn promotor, professor van Ingen, bedanken voor het feit dat hij mij de gelegenheid heeft geboden om het promotieonderzoek (in alle vrijheid) te verrichten. De heer Passchier wil ik bedanken voor de begeleiding tijdens het onderzoek. U was altijd bereid om de meetresultaten uitvoerig te bespreken en na te denken over het oplossen van problemen. Ruud Henkes ben ik dank verschuldigd voor de begeleiding tijdens het verrichten van de berekeningen. De samenwerking tijdens het onderzoek heb ik als zeer prettig ervaren.

Louk Absil ben ik dankbaar voor zijn begeleiding tijdens het afstuderen, de vele discussies over het promotieonderzoek (en allerlei andere zaken) en het leveren van zinvolle kritiek op de eerdere versies van het proefschrift.

Hans Bessem, Rob Booy en Hans van Maanen ben ik zeer erkentelijk voor de interessante discussies tijdens de bijeenkomsten van de werkgroep Digitale Signaalverwerking.

De afstudeerders/stagiaires Diana van Beek, Sander de Boer, Marcel van Drunen en Ted Kraan ben ik zeer erkentelijk voor hun inspanningen tijdens de vele meetsessies en de daarop volgende verwerking van de meetgegevens. Ted Kraan verdient een speciale vermelding vanwege zijn belangrijke bijdrage aan het autocorrelatie-onderzoek.

Mijn dank gaat ook uit naar Piet Deken voor het regelmatig uitlijnen van het meetstelsel en naar Leo Molenwijk, Bertus Keus, Hein Raaymakers en Frans Bazem voor de technische adviezen tijdens de voorbereiding en het verrichten van de metingen. Verder bedank ik de overige collega's van de vakgroep Aërodynamica voor de prettige samenwerking.

Tenslotte wil ik mijn ouders bedanken voor hun steun tijdens de afgelopen jaren.

## Curriculum Vitae

Mark Jeroen Tummers werd geboren op 27 juli 1966 te Amsterdam. In 1985 behaalde hij zijn VWO diploma aan de Scholengemeenschap "De Meergronden" te Almere. In hetzelfde jaar begon hij met de studie Luchtvaart- en Ruimtevaarttechniek aan de Technische Universiteit Delft. In mei 1992 slaagde hij cum laude voor het ingenieursexamen. Het afstudeerwerk werd verricht bij de vakgroep Aërodynamica en richtte zich op het snelheidsbias bij laser Doppler anemometrie. Na het afstuderen trad hij als assistent-in-opleiding bij de vakgroep in dienst om onderzoek te verrichten naar turbulente grenslagen en zoggen met behulp van laser Doppler anemometrie. De resultaten van het onderzoek zijn in dit proefschrift beschreven. Tussen september 1997 en november 1998 werkte hij bij de groep Vaste Brandstoffen van het Energieonderzoek Centrum Nederland aan de ontwikkeling van een model voor de simulatie van stroming en verbranding in een "entrained-flow reactor." Sinds februari 1999 werkt hij weer bij de vakgroep Aërodynamica van de Faculteit Luchtvaart- en Ruimtevaarttechniek van de Technische Universiteit Delft.

